MOHAMMAD HOSSEIN SHAFIEI MAYAM

Experimental study of the turbulence structures in a boundary layer subjected to a strong adverse pressure gradient

Thèse présentée
à la Faculté des études supérieures de l'Université Laval
dans le cadre du programme de doctorat génie mécanique
pour l'obtention du grade de Philosophiae Doctor (Ph.D.)

FACULTÉ DES SCIENCES ET DE GÉNIE
UNIVERSITÉ LAVAL
QUÉBEC

2009

Abstract

The focus of this thesis is on understanding coherent structures of a turbulent boundary layer subjected to a severe adverse pressure gradient and which has also experienced an abrupt transition from strong favourable to strong adverse pressure gradients. The experimental set-up was designed to achieve flow conditions corresponding to trailing-edge stall of an airfoil. Large sets of instantaneous velocity fields are acquired by "Particle Image Velocimetry" in streamwise-wall-normal planes at three different streamwise positions in the adverse pressure gradient region. Investigation of the instantaneous velocity fields shows that the upper region of the boundary layer is densely populated with signatures of hairpin vortices and hairpin packets qualitatively similar to those encountered in zero-pressure-gradient turbulent boundary layer. Since hairpin packets propagate with small velocity dispersion, groups of hairpin vortices appear to be coherently arranged along the streamwise direction. It is found that packets of hairpin vortices sometimes extend over a length of 2δ and contain 3 to 12 vortices. In addition, both two-point spatial correlations between the swirling strength of prograde/prograde vortices and linear stochastic estimation reveal also imprints which are qualitatively similar to the hairpin packets found in the instantaneous fields. The hairpin packets average growth angle in the streamwise direction is approximately 11^o, which is more important than in the zero-pressure-gradient turbulent boundary layer. The individual hairpin vortices are also slightly more inclined with respect to the wall and more closely spaced in the adverse-pressure-gradient turbulent boundary layer. These differences of hairpin properties are consistent with the differences in the mean strain rates in both flows. The swirl intensity of hairpin heads scaled by the Zagarola-Smits time scale has higher value in the zero-pressure-gradient case in comparison to the present flow and in the lower half of the boundary layer it decreases in the streamwise direction of the present flow. The hairpin population decreases in the streamwise direction close to the wall, while it increases in the upper region. These various trends of the swirl intensity and hairpin populations are consistent with those of the Reynolds stresses and turbulence production. This is also consistent with the reported results that hairpin vortices are the major source of turbulence production. Finally, the size of vortices with respect to the boundary layer thickness decreases slightly in the streamwise direction. Since the mean flow evolves rapidly in the present flow, it is therefore possible that the turbulent structures respond with a certain delay to the changes of the mean flow.

Résumé

L'objet de cette thèse porte sur la compréhension des structures cohérentes d'une couche limite turbulente soumise à un fort gradient de pression adverse, et qui a aussi subie une transition brusque de fort gradient de pression favorable à un gradient de pression adverse. L'installation expérimentale permet d'obtenir des conditions d'écoulement correspondant au décrochage d'une aile. De grands ensembles de champs de vitesse instantanée sont acquis par "Particle Image Velocimetry" dans des plans à la paroi alignés avec l'écoulement à trois positions différentes dans la direction de l'écoulement dans la région de gradient de pression défavorable. Les investigations sur les champs instantanés de vitesse prouvent que la région supérieure de la couche limite est densément peuplée avec des signatures de tourbillons hairpin et des paquets de hairpins qualitativement semblables à ceux rencontrées dans la couche limite turbulente à gradient de pression nul. Puisque les paquets de hairpin voyagent avec la petite dispersion de vitesse, les groupes de hairpin semblent être arrangés de façon cohérente dans la direction de l'écoulement. On constate que les paquets de hairpins se prolongent parfois au-delà d'une longueur de 2δ et contiennent 3 à 12 tourbillons. En plus, l'estimation stochastique linéaire et les corrélations spatiales entre l'intensité des tourbillons "prograde/prograde" indiquent également que les empreintes sont qualitativement semblables aux paquets de hairpin trouvés dans les champs instantanés. L'angle moyen de croissance des paquets de hairpin dans la direction de l'écoulement est approximativement 11^o, ce qui est plus important que dans la couche limite turbulente à gradient de pression nul. Les hairpins individuels sont aussi légèrement plus inclinés par rapport à la paroi et plus rapprochés dans la couche limite turbulente avec gradient de pression adverse. Ces différences de propriétés de hairpin sont consistantes avec les différences de taux de déformations moyens dans les deux écoulements. L'intensité des têtes de hairpin normalisée par l'échelle de temps de Zagarola-Smits a une valeur plus élevée dans le cas à gradient de pression nul par rapport à l'écoulement présent et, dans la moitié inférieure de la couche limite diminue dans la direction de l'écoulement dans ce dernier. Tout proche de la paroi, la population de hairpins diminue dans la direction de l'écoulement, alors qu'elle augmente dans la région supérieure. Ces différentes tendances des populations et d'intensité de hairpin sont compatibles avec celles des tensions de Reynolds et de la production de turbulence. C'est également compatible aux résultats rapportés que des hairpins sont la source majeure de la production de turbulence. Finalement, la taille des tourbillons normalisée par l'épaisseur de la couche limite diminue légèrement dans la direction de l'écoulement. Puisque l'écoulement moyen évolue rapidement, il est donc possible que les structures turbulentes répondent avec un certain retard aux changements de l'écoulement moyen.

Acknowledgments

First and foremost, I would like to thank our Creator for endowing me the ability to study the wondrous world in which we all live. I hope that I will continue to get the opportunity to use my given abilities for the betterment of others.

I would like to express my sincere appreciation to of advisor, Professor Yvan Maciel, who has advised me through my Ph.D life. The guidance and support he provided during the course of this work is deeply appreciated. His professionalism and wisdom, his hard work in aiding my professional development and especially for giving me the opportunity to work on this terrific project, has steered my professional development over the past six years and my growth as a scientist. I consider myself very fortunate to have been able to work with him. I have been supported in all phases, and I have learned a lot from him, both professionally and personally.

I am also grateful to the other committee members of my thesis defence Drs Jean Lemay, Guy Dumas, Claire Deschênes and Benaïssa Azemi for their helpful critique and advices, suggestions and comments which made the thesis a more complete reference.

I would also like to thank and acknowledge:

- Ministry of Science, Research and Technology of the IRI for its financial support via its scholarship program.
- Department of Mechanical Engineering for providing me the opportunity to attend graduate school at Laval University.
- Mr Pierre Robichaud, who helped me to analyse the PIV data and made the hairpin database.
- Professors of Mechanical Engineering Department, Claire Deschênes, Benoît Lévesque and Yvan Maciel for giving me teaching assistantships to support me financially.
- Employees of Mechanical Engineering Department (Diane Moore, Sylvie Brodeur, and Hélène Fafard), who helped me and were kind to me during my Ph.D period.

Lastly and most importantly, I would like to deeply express my gratitude and respect to my wife, **"Seddigheh"**, who has provided me continual support, encouragement and understanding over the course of my studies at Laval University. She has patiently endured the many long evenings and working weekends that have been necessary to complete this work and for that I am deeply thankful. I am eternally indebted to my parents for their love and support.

À ***ma défunte mère****, qui était en attente juste pour mon appel mais est décédée avant que je l'appelle, à mon père, à ma femme, à mon garçon et à ma fille.*

This dissertation is dedicated to ***my deceased mother****, who was waiting just for my call but passed away before I called her, my father, my wife "Seddigheh" my son "Sajjad" and my daughter "Narges".*

Nomenclature

APG	Adverse pressure gradient
DNS	Direct numerical simulation
LSE	Linear stochastic estimation
TBL	Turbulent boundary layer
ZPG	Zero pressure gradient
D	Effective diameter of vortex
H	Shape factor, δ^*/θ
P_x	Random uncertainty of x
U, V	Streamwise and wall-normal mean velocity components
u, v	Streamwise and wall-normal instantaneous velocity components
U_e, V_e	Streamwise and wall-normal freestream velocity
U_c, V_c	Streamwise and wall-normal mean convection velocity
u_c, v_c	Streamwise and wall-normal instantaneous convection velocity
U_{zs}	Zagarola-Smits velocity, $U_e\delta^*/\delta$
x	Streamwise coordinate
y	Wall-normal coordinate
x_c, y_c	Coordinates of vortex center
$\langle\rangle$	Ensemble average of a variable
α	Neck angle of hairpin
β	Inclined shear layer angle
β_{zs}	Pressure gradient parameter with Zagarola-Smits scaling, $(\delta/U_{zs})dU_e/dx$
δ	Boundary layer thickness
δ^*	Displacement thickness
γ	Growth angle of hairpin packet
γ_{zs}	Velocity ratio with Zagarola-Smits scaling, U_{zs}/U_e
η	Kolmogorov length scale
λ_{ci}	Swirling strength
λ_{rms}	The root-mean-square of swirling strength
λ_{cithr}	Swirling rate after applying the thresholds
$\tilde{\lambda}_{ci}$	λ_{ci} normalized by λ_{rms}
λ_{ci}^p	Swirling strength of prograde vortices ($\lambda_{ci} < 0$)
λ_{ci}^r	Swirling strength of retrograde vortices ($\lambda_{ci} > 0$)
$\bar{\lambda}$	The arithmetic average of swirling strength in each vortex (swirl intensity)

Λ_{max}	The maximum of swirling strength value in the instantaneous field
Π	Probability of occurence of spanwise vortices
Π_p	Probability of occurence of prograde spanwise vortices
Π_r	Probability of occurence of retrograde spanwise vortices
Π_{zs}	Pressure gradient parameter, β_{zs}/γ_{zs}
θ	Momentum thickness
$\rho_{\lambda_p\lambda_p}$	Two-point correlation coefficient between prograde/prograde swirl
$\rho_{\lambda_p}(x+r)$	The two-point correlation between swirling strength and the streamwise velocity fluctuation
σ	The size of Gaussian filter window
σ_x	Standard deviation of the variable x
ω_z	Vorticity component in z direction
$\Psi_{p(r)}$	Vortex probability fractions of prograde (retrograde) spanwise vortices

Contents

List of Figures

List of Tables

Chapter 1

Motivation and Objectives

1.1 Introduction

The present chapter describes the motivation, objectives, methodology and organization of the thesis. Although understanding the behaviour of turbulent boundary layers subjected to severe adverse pressure gradients leading to separation is of great technological interest, there is little information on the corresponding turbulence structures in such flows. In the present study a turbulent boundary layer subjected to a severe adverse pressure gradients that has suffered from an abrupt transition from strong favorable to strong adverse pressure gradients is experimentally studied using Particle Image Velocimetry. The motivation, objective and methodology of the present study are explained in the following sections.

1.2 Motivation

Although our understanding of canonical turbulent wall flows (zero-pressure-gradient turbulent boundary layer, fully developed pipe and channel flows) is far from complete, our knowledge of the details of turbulence in these flows has improved steadily over the past decades. It is nowadays generally recognized that coherent structures play an important role in the turbulence production and in the transport of mass and momentum in such flows. This is why a large number of the recent research efforts focuses on better understanding the properties, dynamics and interactions of coherent structures for canonical turbulent wall flows. In contrast, not much is known about the characteristics

and behaviours of coherent structures in adverse-pressure gradient turbulent boundary layers. Studying turbulent boundary layers subjected to a strong adverse pressure gradient is no doubt of great technological interest. For instance, such flow conditions are encountered in many aerodynamic devices, such as airfoils, turbine blades and diffusers, and usually cause performance degradation. Similar studies and investigations to those done about coherent structures for the canonical turbulent wall-bounded flows can be very useful for the adverse-pressure-gradient turbulent boundary layers because of its great applications and technological interest.

The numerous studies that exist have usually focused on the statistical properties of adverse-pressure-gradient turbulent boundary layers. Recent studies of adverse-pressure-gradient turbulent boundary layers using direct numerical simulations have provided some insight into the turbulent structures found in these flows. However, these studies pertained to separation bubbles at very low Reynolds numbers with fairly rapid distortion of the upstream boundary layer. In addition, the focus was only on the near-wall structures. Thus in spite of the existence of these numerous studies on adverse pressure gradient turbulent boundary layer and on adverse pressure gradient induced separation, much still remains to be understood especially in terms of the turbulence behaviour in such flows. This is even more so for trailing edge stall of an airfoil which corresponds to the following nonequilibrium flow category: high-Reynolds-number turbulent boundary layer that has suffered from an abrupt transition from very strong favorable pressure gradient to very strong adverse pressure gradient, leading to a non-reattaching large separation zone.

The processes of interaction between turbulence structures (ejections, evolution, breakup and sweeps) in the different regions of the boundary layer are extremely complex and are not well understood for adverse pressure gradient turbulent boundary layers. It is important to mention that despite a general agreement on the layers found in zero pressure gradient turbulent boundary layers (viscous sub-layer, buffer layer, log-layer and wake layer) the layers structure of adverse pressure gradient turbulent boundary layers has not yet been unanimously established. In addition, the processes of interaction between turbulence structures in boundary layer can not be calculated at high Reynolds numbers and complex geometries even with modern computational fluid dynamics methods. They can however be investigated experimentally even if there are some difficulties in experimental methods. Since the flow is affected by large viscous zones due to the boundary layer separation and rapid growing of endwall boundary layers in such laboratory flows, the three-dimensional terms would be also more important in adverse pressure gradient turbulent boundary layers. This is because of their vorticity which is severely skewed by the presence of significant levels of transverse strain rates. So, providing the two dimensional conditions for the mean flow with the

presence of the large viscous zones in such flows, which introduce important blockage effects, needs special cares. Endwall effects can no longer be neglected in such flows. In addition, investigation of three dimensional coherent structures via two dimensional velocity fields that result from experimental measurements is not easy.

The dynamics of coherent structures is very complex. This is why progress in the understanding of turbulent structures has been slow for canonical turbulent wall flows, despite the existence of numerous experimental and numerical research works over the past decades. Indeed, there is still no generally accepted theory about the mechanisms of their generation, evolution and dissipation. This is much worse for the adverse pressure gradient turbulent boundary layer. While most previous efforts have focused on canonical wall-turbulent flows, real flows are usually subjected to adverse pressure gradient, which makes the real flows more complicated. Studying of the coherent structures in such flows could help us to discover a way to break down the complex three-dimensional and random fields of turbulent motion into simpler and more organized motions which called turbulence structures. This is why understanding the effect of pressure gradients on the coherent structures is important.

1.3 Objectives and Approach

The general objective of the thesis is to gain a better understanding of coherent structures in the outer region of a turbulent boundary layer subjected to a strong adverse pressure gradient. To achieve this objective a detailed experimental study is performed in an adverse pressure gradient turbulent boundary layer similar to those found on the suction side of airfoils in trailing-edge post-stall conditions, for which separation occurs at the trailing edge and moves upstream when the angle of attack increases.

Previous experimental and DNS studies showed that the hairpin vortex, the term hairpin is used here as a general term to represent cane, hairpin, horseshoe or arch-shaped vortices, or any deformed versions of them (see section 2.2.2 for details), is one of the most frequently encountered structure within wall bounded canonical turbulent flows. Furthermore, most of researchers agree that hairpin vortices very frequently occur in groups, and that the individuals within these groups propagate at nearly the same convective velocity, so that they form a travelling packet of hairpin vortices. Various autogeneration mechanisms have also been proposed for their formation. The characteristics of these coherent structures have not been investigated in adverse pressure gradient turbulent boundary layer. The objective of this study is to answer some specific questions in order to better understand the structures of a turbulent boundary

layer subjected to a severe adverse pressure gradient.

- The first question is, do hairpins and hairpin packets exist in such flows?
- If the hairpins and hairpin packets exist, what are the typical arrangements and orientations of individual hairpins and of hairpin packets?
- What is the size and swirl intensity of hairpin vortices?
- What is the effect of pressure gradient on hairpin and hairpin packet characteristics?
- What are the statistical characteristics of hairpin vortices and their contribution to turbulence production and Reynolds stresses?

Particle image velocimetry (PIV), an optical technique that measures velocity components in a desired region of flow, is employed to acquire the instantaneous velocity fields in streamwise/wall-normal (xy) planes. Once the instantaneous velocity fields are obtained, fluctuations, gradients, Reynolds stresses and coherent structures can also be determined. The measurements are performed at various streamwise locations across the adverse pressure gradient zone. Indeed, data are acquired from a position near the pressure peak to the separation point. This enables a comparison of the structures across the adverse pressure gradient zone. With the help of the velocity gradient tensor, vortical structures can be investigated.

1.4 Organization of the Thesis

The present thesis is organized in six chapters. Chapter one is an introductory part including motivation, objectives of this thesis and organization of the thesis. In the next chapter, previous studies on turbulence structures for wall-bounded turbulent flows are briefly presented. In chapter three, experimental setup and instrumentation are presented. The two next chapters focus on the acquired results. The results of spanwise vortices are explained and discussed in chapter four, and the results of hairpin vortices are discussed in chapter five. The conclusions of this research are described in the last chapter and some future works are also proposed in this chapter.

Chapter 2

Literature Review

2.1 Introduction

Due to motion complexity, turbulence was initially thought to contain only random fluctuations, but this idea has been changed during the past several decades by numerous research works. Now it is known that coherent structures exist in turbulent flows. Furthermore, turbulence structures play an important role in the turbulence production and Reynolds stress also centers around vortices and streaks of low speed fluid near the wall. In other words, the coherent motions are responsible for most of the production and turbulence transport in a turbulent boundary layer. For this reason, researchers are trying to better understand the behaviour of turbulence structures in different layers of turbulent wall-bounded flows.

In the present thesis, the main goal of literature review is to concentrate on the wall turbulence for two general categories of flow, i.e. canonical turbulent wall flows (zero-pressure-gradient turbulent boundary layer, fully developed pipe and channel flows), and adverse-pressure-gradient turbulent boundary layers. Over the last decades, series of experimental and numerical studies have been performed to study the characteristics of turbulence structures and their relationship with Reynolds stresses turbulence production.

2.2 Canonical Flows

Numerous researchers reported the existence of coherent structures in wall bounded turbulent boundary layers, fully developed channel flows and pipe flows during the several past decades. The reported results of coherent structures of turbulent wall-bounded flows can be categorized in two groups. The first group deals with turbulence structures in inner layer and the second describes the structures of the outer layer.

2.2.1 Inner Layer

This layer includes the viscous sublayer (corresponds roughly to $y^+ < 5$), buffer layer ($5 < y^+ < 30$) and overlap layer. Most of teams working on near-wall turbulence proposed that the regions of sweeps ($u' > 0$ and $v' < 0$) and ejections ($u' < 0$ and $v' > 0$) are the major sources of turbulence production. In the regions of sweeps, high-speed fluid away from the wall is pushed towards the wall, while in the regions of ejections the low-speed fluid close to the wall is pushed upwards.

Before presenting the previous studies, it is useful to describe a general view of the reported results and proposed categories of self-sustaining mechanisms. Over the several past decades the researchers found that (independent of the technique that they were using to study the flows such as smoke visualization, hot wire anemometer, particle image velocimetry, direct numerical simulations) the pattern of streaks and quasi-streamwise vortices are the most frequent structures in the canonical turbulent wall flows within the inner layer. In other words, streaks and quasi-streamwise vortices are universal and are almost always observed in the inner region of wall-bounded turbulent flows. Most of researchers agree that streaks contribute to the production of turbulent energy. So, two main categories are proposed for the self-sustaining mechanism of wall turbulent flows. In the first category, parent vortices interact with the wall and produce offsprings. This idea implies the existence of regeneration of turbulence structures by themselves in a close cycle. In this hypothesis, vortices produce the streaks and streaks generate vortices. In the second category, streak velocity profiles are unstable and produce vortices. In other words, a primary structure like streaks in some cases appears directly from flow disturbances and generates a vortex. The generated vortex is pushed up far from the wall and regenerates other vortex or breaks down to smaller structures.

Blackwelder (1978), Blackwelder and Eckelmann (1979) and Blackwelder (1997), described a conceptual model of wall structure before arrival of the sweep (figure 2.1). In their model, two counter-rotating quasi-streamwise vortices exist in a region of a

strong mean velocity gradient, wherein the quasi-streamwise vortices cause fluid from the viscous layer at the wall to lift away from the wall and form the near-wall low-speed streaks that are commonly observed in the buffer layer. In other words, with this simple model, the low-speed streaks are explained as the viscous, low-speed fluid that is induced to move up from the wall by the quasi-streamwise vortices. Smith and Walker (1997) also proposed a similar scenario of eruption. They believe that the presence of counter-rotating quasi-streamwise vortices guarantees the existence of low-speed zones which are pumped away from the wall, while high-speed fluid is pushed toward the wall by sweep events. These processes transfer the energy to inner layer (production) while energy dissipates in outer layer. In spite of this scenario that two counter-rotating quasi-streamwise vortices are necessary to generate low-speed flows, Robinson (1990) and Robinson (1991) believed that low-speed streaks can be generated by only a single quasi-streamwise vortex. Robinson also concluded that streamwise vortices populate the inner region, transverse vortices populate the outer layer and overlap layer contains a mixture of streamwise and transverse vortices (figure 2.2). Perry and Chong (1982) suggested a model for turbulence structures within the inner layer in which attached eddies are formed in the viscous sublayer. These eddies are stretched and either die from viscous diffusion and vorticity cancellation, or they pair and become a second hierarchy of attached eddies.

Blackwelder and Kaplan (1976) studied wall structure of the turbulent boundary layer using hot-wire rakes. The authors found a broad movement of fluid towards the wall (consistent with sweep) at $y^+ = 15$ and a strong velocity motion of fluid away from the wall at this position. This is associated with a deficit in the streamwise velocity component. Thus the low-speed streamwise momentum is being lifted away from the wall in this region. Furthermore, their results present a maximum Reynolds shear stress at $y^+ = 15$. This is associated with the bursting structure at $y^+ = 15$. In fact, the authors found high content of Reynolds shear stress during the bursting process. Blackwelder and Eckelmann (1979) studied the vortex structures associated with the bursting phenomenon, similar to Blackwelder and Kaplan (1976), using hot-film sensors and flush-mounted wall elements. The authors proposed a model of the wall structure before the arrival of the sweep similar to that proposed by Blackwelder (1978) as shown in figure 2.1. Blackwelder and Eckelmann concluded that fluid is pumped away from the wall to form a low-speed streak between a pair of counter-rotating vortices. The pumping action is interrupted by a sweep imposed by the outer flow field. This high-speed fluid (sweep) flowing over the low-speed streaks destroys the quasi-streamwise vortices and forms a strongly inflexional velocity profile. The authors also indicated that most of the turbulent production occurred by the ejection from the wall of part of the low-speed streak and by its subsequent interaction with the incoming high-speed fluid. Bernard and Wallace (1997) similarly proposed that quasi-streamwise vortices

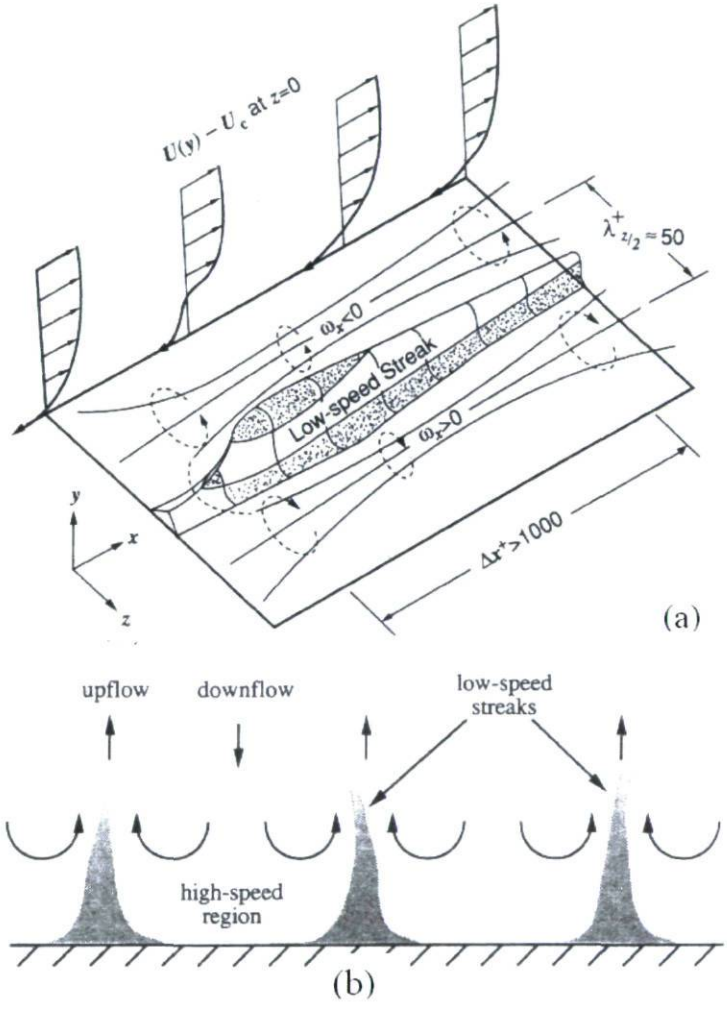

Figure 2.1: (a) Model of near-wall structures in turbulent wall-bounded flows (proposed by Blackwelder 1978). (b) End-view schematic of instantaneous velocity field in the cross-flow plane.

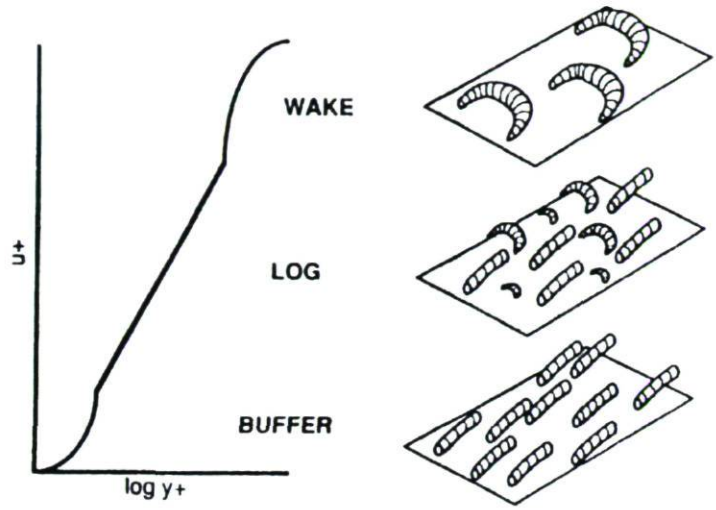

Figure 2.2: Idealized schematic of vortical structure populations in the different regions of the turbulent boundary layer (Robinson 1991).

are responsible for the majority of turbulent momentum and consequently turbulent kinetic energy production in wall-bounded shear flow. The authors also found that these vortices happen singly or less frequently in hairpin loop configurations. Robinson (1991) believed that turbulence production occurs during alternate extreme outward ejection of low speed streaks and during the sweep of high-speed fluid at a shallow angle toward the wall.

Kline et al. (1967) studied the wall turbulent flow using hot-wire anemometry in a fully developed water channel. They believe that burst event plays an important role in determining the structure of the entire turbulent boundary layer. They also proposed that the burst phenomenon dominates the transfer process of turbulent kinetic energy between the inner and outer layers and makes remarkable contributions to turbulence production during bursting occurrence. The authors also found that low-speed streaks are about 80-100 wall units (Δz^+) and can be in the order of 1000 wall units (Δx^+) in length.

Kim et al. (1971) suggested that the bursting process can be described in three stages: i) a turbulent burst begins when a low-speed streak is perturbed and begins to oscillate and the streak gradually lifts up and also moves downstream, ii) when the low-speed streak has reached some critical distance from the wall at which their rate of ejection increases significantly (called low-speed-streak-lifting by the authors), iii) when a low-speed streak lifts, it creates a narrow inflexional zone containing two reversals of slope-gradient and an inflexion point in the instantaneous velocity profile, iv) then

the low-speed streak oscillates and the oscillations increase in magnitude, away from the wall, v) finally the oscillation is terminated and breakup but there is well-defined motion into more random or chaotic motions accompanied by a return to the wall of the low-speed streak, and a more quiescent flow. The authors also mentioned that most of the turbulence production occurs in the buffer layer ($5 \leq y^+ \leq 100$), during bursting, and little or no production occurs on the average during non-bursting times. Smith and Metzler (1983) studied the near-wall structures using a single-sensor hot-film anemometer system. The authors proposed that the bursting process is a primary mechanism for the production of turbulent kinetic energy in the inner region of the boundary layer. It appears as a violent ejection of low-speed fluid from the regions very near to the wall. They also found that the spanwise spacing of low-speed streaks is essentially invariant with Reynolds number ($\lambda^+ \approx 100$).

Hanratty and Papavassiliou (1997) also proposed a conceptual model of turbulence production cycle for the turbulent boundary layer, which involves ring-like vortices that scale on the wall variables, ejections, sweeps, near-wall streamwise vortices, hairpins and streaky structures. When the sizes of vortices grow and their energy increases, then they lift up from the viscous layer and provide energy to the outer layer.

More recent works also proposed similar scenario of streak motion and near-wall quasi-streamwise vortices. Jiménez et al. (2005) introduced a concept of streak motion. They proposed that the streaks grow initially in intensity independent of the vortices strengthening. Then the streaks move away from the wall because of an instability in which vortices are created, and eventually the streaks breakup. Another simplified model is described by Sanghi and Aubry (1993). The authors identify the coherent structures in a random flow using proper orthogonal decomposition. With respect to their results, low-speed streak is generated by a pairs of counter-rotating streamwise vortices in the sublayer. Then the low-speed streak is lifted away from the wall while the streamwise vortices and low-speed streaks propagate downstream. When the low-speed streak has reached some critical distance from the wall, it moves up more sharply (the rate of ejection increases significantly). Then an inflexional velocity profile is formed and an inflexion point arises at the interface between streak and sweep. Finally, the structures experience by a sudden breakup that is like a burst. Moreover, Sanghi and Aubry (1993) found that the structures are convected downstream at the mean velocity value during the burst events. They also proposed that the structures involved in these motions are streamwise rolls, streaks, sweeps, horseshoe vortex lines, and vertical and horizontal shear layers which are consistent with previous studies.

The near wall turbulence structures in a turbulent boundary layer have also been studied by Chernyshenko and Baig (2005) and Toh and Itano (2005) using direct nu-

merical simulations. The authors believe that streaks may be a primary structure appearing directly from an unstructured background. The weak wall streak tends to dissipate due to viscosity or merge into other streaky motions to become a stronger. Then the streaks can produce other structures and each of them repeat the self-sustaining cycle. Finally the last structure in the above-mentioned chain is broken-up into more random or chaotic motions. These motions may be accompanied by a return to the wall of the low-speed streak, and a more quiescent flow. The study of flow structures in a zero pressure gradient turbulent boundary layer over a wide range of Reynolds numbers were done by Osterlund et al. (2003) using a MEMS-type of hot-film. Their results confirmed the existence of low-speed streaks near the wall that lift-up and eject outwards for different Reynolds numbers.

Schoppa and Hussain (2002) presented a new mechanism for near-wall vortices using direct numerical simulations in a turbulent channel flow. They proposed a new streak transient growth mechanism in which generates larger linear amplification of x-dependent disturbances. They show that vortex formation can in fact occur in the absence of a parent vortex, and the dynamics of generation of streamwise vortices are definitely different from those of parent-offspring. The authors show that streamwise vortices are generated from the more numerous normal-mode-stable streaks, via this new streak transient growth mechanism based scenario that transient growth of perturbations leading to formation of a sheet of streamwise vorticity.

With respect to the results of researchers over the several past decades the low-speed streaks and quasi-streamwise vortices occur frequently within the inner layer of wall turbulent flows. Two general ideas were proposed for the near-wall turbulence structures. First, the low-speed streaks are formed by quasi-streamwise vortices and lift up to generate the vortices. In other words, parent of vortices interact with the wall and produce parent-offspring. This is a close cycle regeneration of turbulence structures. In the second category, primary low-speed streaks appear directly from flow disturbances and produces vortices. Then these vortices move up far from the wall and regenerate other vortices.

2.2.2 Outer Layer

The outer layer is commonly known as a layer with $y^+ > 100$ that includes the overlap (log) and wake regions. While the shear decreases from a maximum amount at the wall to zero at the outer edge of the boundary layer, the vortical structures become larger as they move up away from the wall to the outer edge of the boundary layer. In general, although large eddies exist in the outer region, small eddies possibly populate

within this region. Robinson (1990, 1991) reported that the dynamics of the outer layer is controlled by these eddies (low-speed streaks, streamwise vorticity, ejections and sweeps).

Many recent experimental and computational studies support the existence of hairpin structures in the log and wake regions of the canonical turbulent wall flows. Adopting the terminology of Adrian et al. (2000) the term hairpin is used here as a general term to represent cane, hairpin, horseshoe or arch-shaped vortices, or any deformed versions of them.

Theodorsen (1952) proposed the first physical model of coherent structure (called horseshoe vortex) of turbulent boundary layers. He imagined that horseshoe vortices move up away from the wall (figure 2.3). In his conceptual model, since the layer farther from the wall has higher mean flow velocity in comparison to the layer close to the wall, as the structures move downstream, as well as experiencing a high degree of stretching, the head (spanwise part) undergoes a lifting movement from the wall. This motion of the vortex results in the head of the vortex lifting upward toward the free stream allowing higher velocities to carry the head downstream faster than the legs. This action leads to a stretching of the legs as the hairpin vortices are convected downstream. This motion of vortices transports low-speed fluid away from the wall and produces Reynolds stresses. Kovasznay et al. (1970) studied the turbulence structures in the outer region of turbulent wall flow using hot-wire anemometer. The authors confirmed the existence of large scale motions in the outer region. Robinson (1991) studied the coherent structures of turbulent wall flow using the direct numerical simulations of Spalart (1988). He proposed that horseshoe vortex contains three parts; legs, neck and head. This model shown in figure 2.4 is similar to the model of Head and Bandyopadhyay (1981). Recently Hutchins et al. (2005) also detect a similar structure to the model of Head and Bandyopadhyay (1981) using particle image velocimetry. Chong et al. (1998) proposed that wall structures form vortex tube or arch and their results present a strong link between these structures and Reynolds stresses.

Many researchers agree that hairpin vortices naturally occurring in different fully developed wall-bounded turbulent shear flows as well as in transitional flows suggest the existence of a basic mechanism responsible for hairpin regeneration process, under various base flow conditions. Numerical results of Doligalski and Walker (1984) illustrated that convected discrete vortical motions are observed to be an important feature of the outer-layer of turbulent wall flows. The authors found that once detached eddies occur in the boundary-layer flow, intense variations in the velocity field begin to develop near the eddy that the streamlines in the boundary layer near the upstream side of the detached eddies are ultimately deflected in a direction which is almost normal

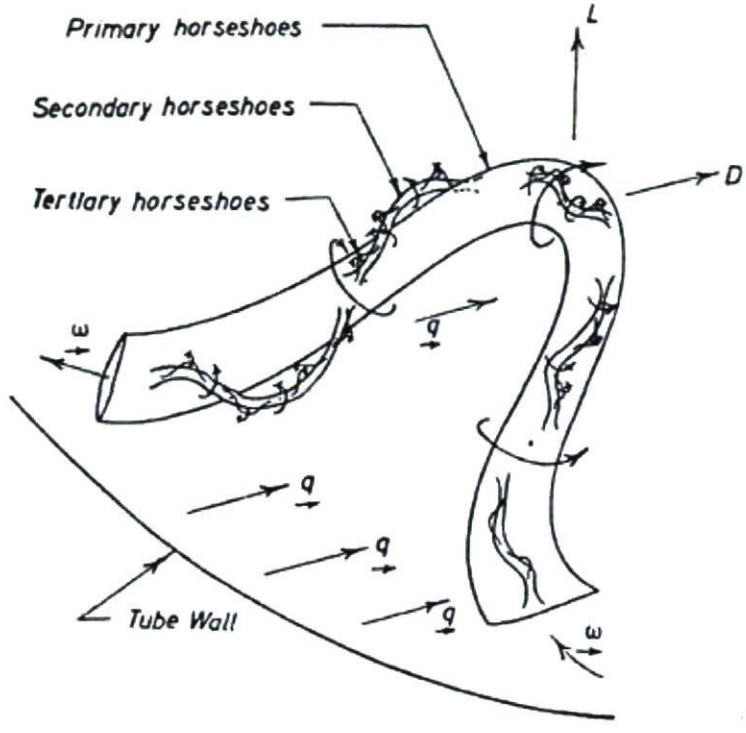

Figure 2.3: Horseshoe (hairpin) concept of Theodorsen (1952).

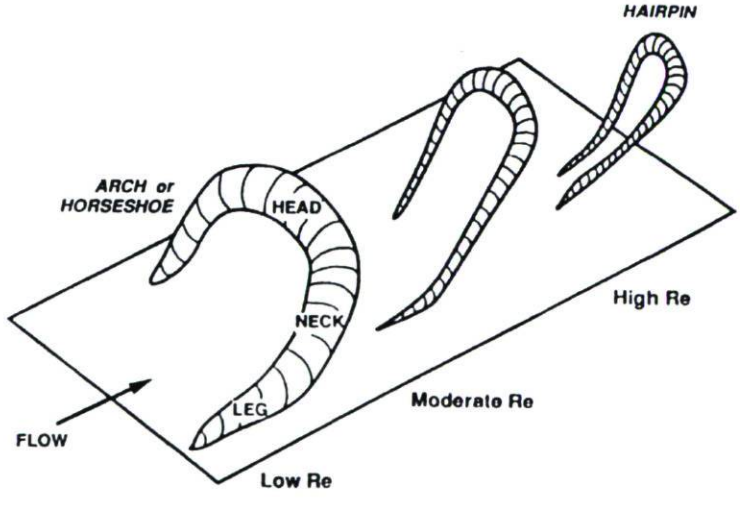

Figure 2.4: Geometry and nomenclature for arch-shaped and hairpin-shaped vortices (Robinson (1991), after Head and Bandyopadhyay (1981)).

to the wall. Doligalski and Walker (1984) also reported that the apparently active vortices near the wall have a typical lengthscale of the order of 100 wall-layer units; these convected vortices are three-dimensional. Smith and Walker (1997) proposed that the legs of hairpin squeeze rapidly together in the spanwise direction in the inner region where shear increases, while the hairpin head expands as it moves up where shear decreases. So the hairpin vortex reforms to an omega shape vortex. The concentration of streamwise vortices increases near the wall, when the legs penetrate into this zone. Hence, new quasi-streamwise vortices appear near the wall. The weak legs dissipate or amalgamate with other legs whereas the strong legs penetrate to the inner layer and generate new vortices. On the other hand, the upper part of hairpin (head) moves up away from the wall and become larger in spanwise scale.

Zhou et al. (1999) tried to reproduce the auto-generation mechanism of the coherent structures in a turbulent channel flow using direct numerical simulations. The base flow consists of the turbulent mean velocity profile free from any fluctuations and at low Reynolds number. A symmetric input disturbance, symmetry hairpin-like vortex, is applied to this turbulent channel flow. They found that this initial structure, symmetry hairpin-like vortex, evolves into a hairpin vortical structure, called primary hairpin vortex shown in figure 2.5. Once the primary hairpin is generated, depending on its strength and distance from the wall, it generates secondary and tertiary hairpin vortices in upstream and possibly a downstream hairpin vortex depending on vortex strength. So the important conclusion of this study is generation and regeneration of single hairpin vortices and creation of a group of hairpins via the auto-generation mechanism via a hairpin-like disturbance. They found that stronger initial vortices participate in the formation of a hairpin packet, while weaker initial hairpin-like vortex structures do not result in the autogeneration of additional hairpins. Additionally, if this aforementioned process is started with an asymmetric initial vortex as an input disturbance, the authors observed that the streamwise spacing between the vortices reduces under asymmetry condition, and the new hairpins form more readily in rapid succession in comparison to the case with a symmetric input disturbance. It is worth noting that their observation under asymmetry condition is in better comparison with the experimental results. Haidari and Smith (1994) generated a single hairpin vortex by an initial impulsive injection of fluid into the flow through a thin slot in the wall. The injection velocity and injection time duration were varied. Below a certain ejection velocity the fluid diffuses without producing a hairpin. For higher level injection of velocity and duration, a single hairpin vortex is formed. For yet higher velocities, the vortex is strong enough to eventually produce three hairpin vortices.

Suponitsky et al. (2005) performed a numerical study to investigate of coherent structures in fully developed turbulent flows, to understand their self-generation ability.

To reproduce the generation mechanism and characteristics of the coherent structures that naturally occur in turbulent bounded shear flows, the authors made an effort to examine the capability of a simple model of interaction, between a localized vortical disturbance and laminar uniform unbounded shear flow. They found that a vortical disturbance with small-amplitude generates a pair of streamwise vortices, whereas a vortical disturbance with large-amplitude produces a hairpin vortex or a packet of hairpin vortices. Kim et al. (2008) have also examined the autogeneration process of hairpin vortices. A new hairpin vortex is created from a sufficiently strong hairpin-like disturbance leading to the formation of a hairpin packet, in a fully turbulent channel flow using direct numerical simulation for both a clean background condition (similar to Zhou et al. (1999) and with background noise. Kim and co-workers studied the effect of background noise on packet formation. They found that the global properties of hairpin and hairpin packets are almost the same for all systems, regardless of the presence of background noise; however, the details of auto-generation of hairpin vortices are sensitive to the initial background noise. The hairpins become asymmetric under the effect of initial noise, and resulting more complicated packet structures in comparison to the symmetric hairpin vortex for the case of clean background. In addition the initial background noise leads to decrease the minimum $Q2$ strength required to trigger auto-generation. In other words, they found that background noise enhances autogeneration, especially in the buffer layer.

Adrian et al. (2000) investigated with PIV measurements the shape and characteristics of single and multiple hairpins in a streamwise-wall-normal plane of the outer region of a zero pressure gradient turbulent boundary layer. They showed that the hairpins generally occur in groups and individual hairpins are aligned upwards in a coherent pattern, hairpin packet, in the streamwise direction at a mean angle of approximately 12^o. They further proposed a conceptual model of nested hairpin packets shown in figure 2.6. In this model, the primary hairpin originates at the wall from a low-speed streak disturbance. Once the primary hairpin is formed, it is stretched and intensified as it moves up away from the wall and propagates downstream. This primary hairpin grows continuously in time and changes from a hairpin-shape to an omega-shape (the same hypothesis of Zhou et al. (1999). A secondary hairpin is generated upstream the primary hairpin if its strength is sufficient. The secondary hairpin also increases in size as time progresses and it moves up and propagates downstream and begins to create a tertiary hairpin. The new hairpin usually participates to autogenerate another hairpin if its strength is sufficient. The formed packets align in the streamwise direction and coherently add together to create large zones of nearly uniform streamwise momentum. Moreover the authors proposed that smaller packets move more slowly because they induce faster upstream propagation. The effect of older, larger packets over-running smaller, younger packets result in multiple zones of uniform momentum

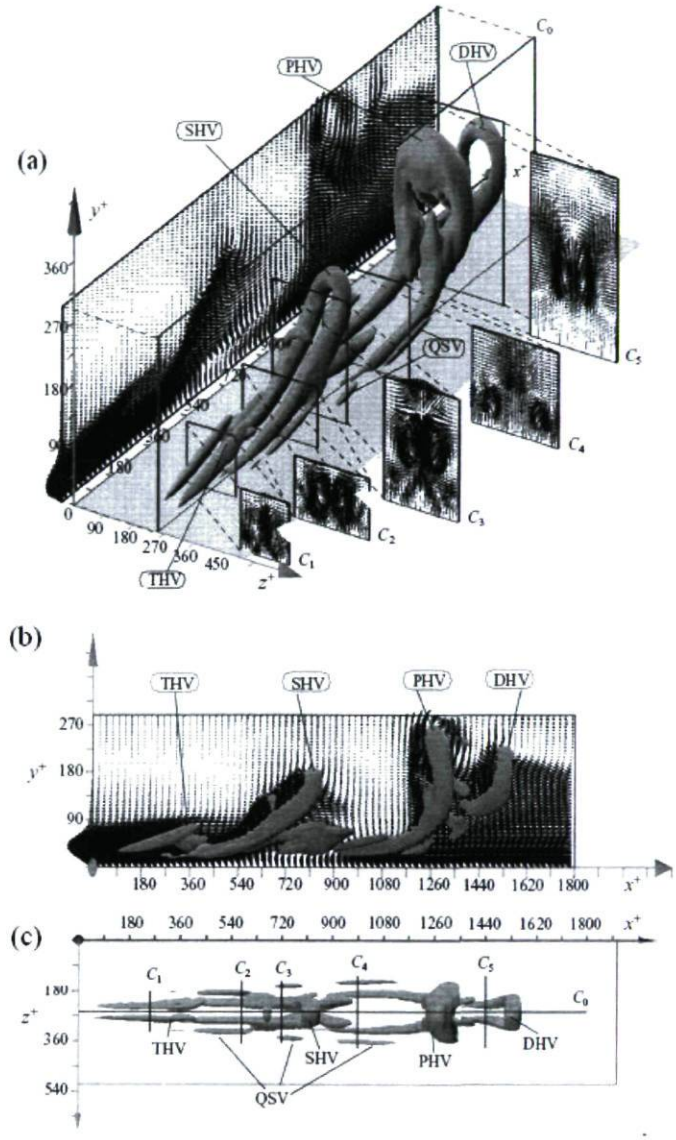

Figure 2.5: The sequence of vortices identifed at $t^+ = 297$ by the iso-surface of λ_{ci}^2 with 2% of its maximum. (a) perspective view; (b) side view; (c) top view. The location of the five (z, y)-cross-sections (C1-C5) at $x^+ = 252,\ 576,\ 720,\ 990$, and 1440, shown in the perspective view (a) are also marked in the top view (c). The (x, y) velocity vector plots shown in (a) and (b) correspond to the spanwise centre of the box and cuts through the hairpin heads. PHV, primary hairpin vortex; SHV, secondary hairpin vortex; THV, tertiary hairpin vortex; DHV, downstream hairpin vortex; QSV, quasi-streamwise vortices (Zhou et al., 1999).

as shown in figure 2.7. The zone I corresponds to the interior of a young packet, while the zone II is associated with the interior of an older packet. This latter result, association of uniform momentum zones and hairpin heads, is consistent with the results of Meinhart and Adrian (1995). The authors reported that the flow is decelerated because of the backflow induced by several hairpins that are aligned in a coherent pattern in the streamwise direction. So, the long region of uniformly retarded flow in each zone is associated with the backflow induced by one or more groups of hairpins. The authors also observed that hairpin vortices combine to create long structures in the streamwise direction. These long structures (hairpin packets) grow in the streamwise direction depending on the coherent alignment of successive hairpins. Tomkins and Adrian (2003) have found that these structures exist even in the buffer layer and that they grow linearly with distance from the wall in the buffer and log layers.

The aforementioned studies of hairpin vortex signature show that this structure is also fully consistent with the existing body of results on the structure of wall turbulence. A stagnation point flow occures when an induced downflow, $Q4$ ($u' > 0$, $v' < 0$), from an upstream vortex head, encounters a low-speed upflow, $Q2$ ($u' < 0$, $v' > 0$), induced by an adjacent downstream vortex. An inclined shear layer is caused by stagnation-point flow resulting from the $Q2/Q4$ interaction. These phenomenon, $Q2/Q4$ interaction and ISL event, are consistent with a VITA event as defiened by Blackwelder and Kaplan (1976). Liu et al. (1991) studied structures of wall turbulence in the streamwise wall-normal plane of a fully developed low-Reynolds-number turbulent channel flow using particle image velocimetry. The authors observed the inclined shear layers similar to those abovementioned, with inclination angle less than 45^o. These ISLs usually terminate in regions of rolled-up spanwise vorticity which probably were interpreted to be a hairpin head.

Christensen and Adrian (2001) studied the turbulence structures in the outer region of a turbulent channel flow using particle image velocimetry. The statistical results using linear stochastic estimation supports that the outer layer of wall turbulence is populated by specially coherent groups of vortices which is similar to the signature of hairpin vortex packet. These results are consistent with previous reported results on hairpin vortices. For instance, these conditional hairpin vortex heads are inclined upwards in the streamwise direction at angle of approximately $12^o - 13^o$ which is close to the results of Adrian et al. (2000).

Ganapathisubramani et al. (2003) measured all three instantaneous velocity components using stereoscopic particle image velocimetry in streamwise-spanwise planes (xz planes). They found both symmetric and asymmetric hairpin vortices. Their results also reveal that hairpin vortices appear with two legs usually. Ganapathisubramani and

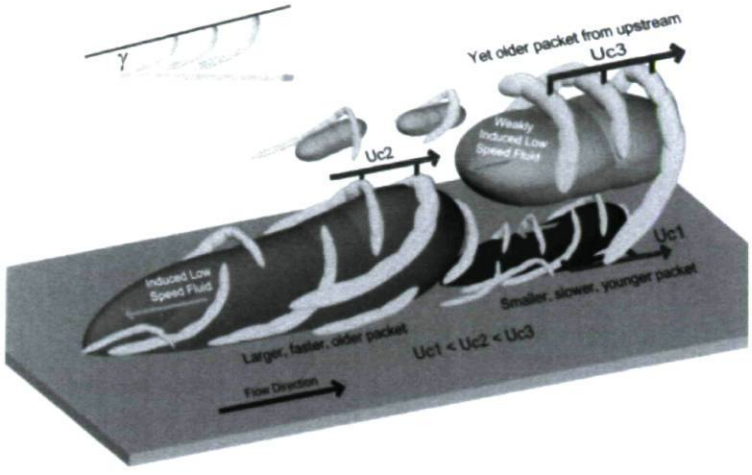

Figure 2.6: Conceptual scenario of nested packets of hairpins or cane-type vortices growing up from the wall. The envelope of the packet is a linearly growing ramp. Smaller packets move more slowly because they induce faster upstream propagation (Adrian et al., 2000).

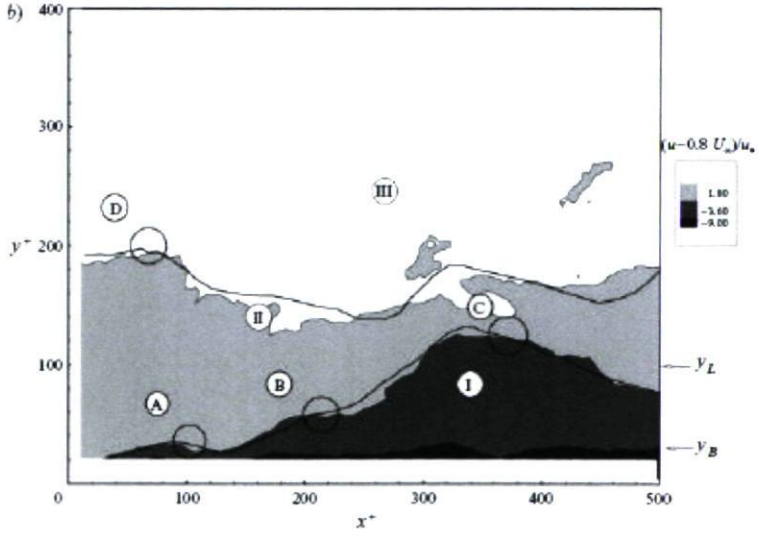

Figure 2.7: Realization of the $Re_\theta = 930$ boundary layer, contours of constant u-momentum (Adrian et al., 2000).

co-workers also investigated the association between Reynolds shear stress and events with large streamwise coherence in the streamwise-spanwise plane. They found that the presence of hairpin structures and packets producing considerable Reynolds shear stress was a common and recurrent feature in the log layer. Similar study of spanwise lengthscales of hairpin vortices was done by Tomkins and Adrian (2003). The instantaneous velocity fields in the streamwise-spanwise plane of a turbulent boundary layer are measured from the buffer layer to the top of the logarithmic region using particle image velocimetry. They studied how the spanwise dimensions of hairpin vortices behave at different wall-normal locations using linear stochastic estimation. Tomkins and Adrian (2003) observed that large scale motions extend 2δ or more in the streamwise direction and $0.1\delta - 0.4\delta$ in spanwise direction, and grow with wall distance from the wall. Two spanwise lengthscales, the mean width of the low speed regions (as estimated by quantitative flow visualization) and the width of the stochastically estimated low-momentum region, increase linearly with distance from the wall (y). Ganapathisubramani et al. (2005) used two-point correlations on stereoscopic particle image velocimetry data to reveal the spanwise width which is consistent with hairpin vortex signature. The authors found that two spanwise lengthscales, the mean width of the low speed regions (as estimated by quantitative flow visualization) and the width of the stochastically estimated low-momentum region, increase with distance from the wall (y). In other words, spanwise width (separation between legs) increased away from the wall and the rate of growth is found to be approximately linear across the boundary layer, and growth rate is higher in the log region than the wake region. In addition, they found that long low-speed zones are statistically more occurred than high-speed zones in the log region. This result is consistent with the idea that the long region of uniformly retarded flow is the backflow induced by several hairpins that are aligned in a coherent pattern in the streamwise direction.

Marušic and Perry (1995) detected the "Λ" or "horseshoe" types of structures in a ZPG TBL which have vortex lines that reach the wall, and produce a finite Reynolds shear stress at the wall (at least outside the viscous zone). Spanwise characteristics of coherent structures were also investigated by Ganapathisubramani et al. (2006). They also proposed a hypothetical "Λ" shape eddy and its projection on the streamwise-spanwise plane. They illustrated that the hairpin vortices are the most frequent structures and these vortices are most frequently inclined downstream at an angle of 45^o with the wall. Hutchins et al. (2005) and Hambleton et al. (2006) have also performed stereoscopic particle image velocimetry, which measurements were taken simultaneously in streamwise-spanwise and streamwise-wall-normal planes in a zero-pressure-gradient turbulent boundary layer, to study the characteristics and dynamics of coherent structures. They used linear stochastic estimation (LSE) based on a condition of positive swirl in the vertical plane, slightly above the log region, and the LSE results reveals an

average three-dimensional structure that is consistent with the hairpin packet model. The acquired result in the vertical plane reveals a strong swirl at the condition point and a packet angle of approximately 13^o with the wall. This result is consistent to those presented by many researchers. A unique feature of this study is to having the simultaneous view of the horizontal and vertical planes. A clear large-scale coherence is noted with the condition event in the vertical plane being accompanied by two pronounced swirling motions that occur just upstream of the condition point. This indicates that the time-averaged conditional event is an inclined hairpin structure, with an inclination angle of close to 45^o. In the horizontal plane, there is a pronounced elongated low-speed region extending some distance up and downstream of the condition point, which is consistent to $Q2$ region between the legs of this conditional eddy. Moreover, in the vertical plane (from the LSE results within a small bounding box), a clockwise spinning swirl event appears above and downstream of the counter-clockwise spinning swirl at the condition point. This pattern is consistent with an omega-shaped vortex or vortex ring structure.Li et al. (2006) studied the turbulence structures in a turbulent channel flow. Asymmetric hairpin vortices were usually found in their results. Moreover, they proposed the formation of low-speed streaks due to hairpin vortex packets. Carlier and Stanislas (2005) also tried to bring some new experimental information using particle image velocimetry (PIV) to characterize and to better understand the near-wall turbulence structures. Their visualization of instantaneous velocity fields shows that counter-rotating adjacent vortices are the most probable configuration in the spanwise direction. Their results also show a larger number of eddy structures with positive vorticity (opposite to mean shear) than other authors. The authors discovered that adjacent vortices with the same sign are extremely rare.

Three-dimensional structures of a low Reynolds number turbulent boundary layer were investigated using a volumetric imaging technique by Delo et al. (2004). They observed groups of large scale structures that were frequently assembled into lumps measuring up to 5δ in length. Moreover, they found that ejections of near wall fluid appeared to be spatially organized and related to the passage of large scale motions. Toh and Itano (2005) also suggested that the large scale structures (two counter-rotating large scale circulations for their study) are linked with near wall structures and sustained by their interactions.

Natrajan et al. (2007) studied spatial signatures of retrograde spanwise vortices in wall turbulence using PIV. Two-point spatial correlations between the swirling strengths of retrograde and prograde vortices are computed to reveal that prograde cores are typically oriented either upstream of and below or downstream of and above the retrograde vortex. In addition, conditionally averaged velocity fields given the presence of a retrograde core were also calculated in a bounding box to further explore its average velocity

signature. The results of these averages are also consistent to the results of two-point spatial correlations. Boundary layer velocity measurements in a water tunnel were performed by Volino et al. (2007) using laser-Doppler velocimeter to study the effect of roughness on coherent structures. The authors found the existence of hairpin vortex packets in the outer region of both smooth-wall and rough-wall turbulent boundary layers. Moreover, an excellent qualitative agreement between the turbulence structures for both rough-wall and smooth-wall boundary layers are observed. This agreement confirmed that structures in the outer region are independent from the wall roughness, whereas the inner region structures can be affected by roughness. Flores et al. (2007) also studied the effect of wall roughness on the turbulence structures in a turbulent channel flow. They also reported that outer layer structures are independent of the wall roughness and near wall details.

Turbulent pipe and channel flows were studied by Monty et al. (2007) using hot-wire. They illustrated that the width of large-scale structures increases away from the wall.

In the two latter sections, sections 2.2.1 and 2.2.2, a brief literature review of turbulent structures in both inner and outer regions is presented. In the inner layer, two main categories are proposed for the self-sustaining mechanism of wall turbulent flows. In the first category parent vortices interact with the wall and produce offspring. In this hypothesis, vortices produce the streaks and streaks generate vortices. In the second category streak velocity profiles are unstable and produce vortices. Many researchers believed that the most frequent structures are low-speed streaks and quasi-streamwise vortices within the inner layer. In the outer layer, many studies support that the hairpin vortex is the most frequent structure that populates the outer layer of canonical turbulent wall flows. In addition, a few researchers also found that hairpin vortices occur in the inner layer. In fact, the legs of hairpin vortices usually attach to the wall as the quasi-streamwise vortices. The flow is retarded by these vortices and low-speed streaks are generated. The legs of hairpin squeeze rapidly together in the spanwise direction in the inner region where shear increases, while the hairpin head expands as it moves up where shear decreases. So the hairpin vortex reforms to an omega shape vortex and new vortices formed beneath the streamwise-elongated vortex legs. Then the legs of the vortex are stretched into a hairpin shape as it traveled downstream. On the other hand, the upper part of hairpin (head) moves up away from the wall and become larger in spanwise scale. In other words, in this autogeneration mechanism, which proposed by some researchers, once the primary hairpin is generated, it generates the secondary hairpin if it has sufficient strength. The secondary hairpin generates the tertiary hairpin and similarly new hairpins are formed. Consequently many researchers believe that, with a few exceptions, the interaction of hairpin vortices and turbulence structures in

the inner region, low-speed streaks and quasi-streamwise vortices, is responsible for the most part of Reynolds stresses and turbulence production.

2.3 Adverse Pressure Gradient TBL

Although our understanding of canonical turbulent wall flows is far from complete, our knowledge of the details of turbulence in these flows has improved steadily over the several past decades. In contrast, not much is known about the characteristics and behaviour of coherent structures in adverse-pressure-gradient turbulent boundary layers. The numerous studies that exist have usually focused on the statistical properties of adverse-pressure-gradient turbulent boundary layers. Recent studies of adverse-pressure-gradient TBL using direct numerical simulations and hot wire anemometry have provided some insight into the turbulent structures found in such flows. It is important to mention that these studies focus only on the near-wall structures at very low Reynolds numbers.

Kline et al. (1967) reported that the bursts appear to play a key role in transporting turbulent kinetic energy to the outer regions of the boundary layer. In addition the authors found that a positive pressure gradient tends to make the bursting more violent and more frequent; on the other hand, negative pressure gradients reduce the rate of bursting. Krogstad and Skare (1995) found that Q2 and Q4 events are equally important near the wall in the ZPG TBL, while APG TBL is strongly dominated by turbulent motions in the fourth quadrant. Moreover, Krogstad and Skare found that observed Q4 motions have higher frequency and last much longer than in the ZPG TBL, while the frequency for Q2 events was reduced, especially for strong events. Skote et al. (1998) performed direct numerical simulations to study turbulent boundary layers in adverse pressure gradients. The authors investigated two cases, where in the first adverse-pressure-gradient case the pressure gradient is close to that for which the corresponding laminar boundary layer would separate and the second case is strong adverse-pressure-gradient. Skote and co-workers proposed that streaks become shorter in the inner layer of adverse-pressure-gradient turbulent boundary layers in comparison to ZPG TBL. Moreover, the streaks become shorter and wider when they move toward the separation point. In such flows, the long streaks occur close to the wall and the shorter streaks appear in the upper part of the inner layer of boundary layer. They also showed that turbulence bursts exist in the near wall region and larger scale vortical structures can be seen in the outer part of the adverse-pressure-gradient turbulent boundary layer but the bursting action seems almost totally suppressed in such flows. Furthermore, Skote et al. (1998) reported that there is only a slight difference

of turbulence structures in inner layer between the ZPG and APG turbulent boundary layers (except near the separation point), whereas in the outer region there is a clear difference. Their results present an outer peak of the production term in the turbulent energy budget for the higher pressure gradient case. The authors believe that this outer peak in the turbulent energy and production might be related to the enhanced streak formation in the outer part of the boundary layer. Similar scenario of low speed streaks was proposed by Skote and Henningson (2002) that near-wall streaks are weakened by the adverse-pressure-gradient, and the spacing increases in viscous units. The authors also found that the low-speed-streaks may reappear in a separated region if the back-flow is strong enough and do not immediately appear after the reattachment but are clearly visible after a certain distance.

Adams and Johnston (1988) found that the bursting rates in the upstream of reattachment region of an adverse-pressure-gradient separated boundary layer (separation bubble) is very close to the bursting rates in a ZPG turbulent boundary layer, whereas the detection rates of bursts in the backflow region (downstream of the reattachment region) are a factor of 4/10 lower than ZPG flow. Simpson et al. (1981) and Pronchick (1983) noted that the lack of ejections in the near-wall region may be the reason for lower detection of bursts in adverse-pressure-gradient boundary layer. Nagano et al. (1998) studied the turbulence structures in an adverse-pressure-gradient turbulent boundary layer using hot wire anemometer. The authors found that the turbulence intensity reduced in the wall region when the pressure gradient increases, but the outer region remains unchanged. Moreover, the occurrence of ejection and sweep become equivalent in an APG turbulent boundary layer whereas the sweep motions follow the ejections phenomenon in zero pressure gradient TBL.

The study of a separated turbulent boundary layer over a flat plate using direct numerical simulation was performed by Na and Moin (1998). The studied flow contains a separation bubble. The authors found that turbulent structures emanate upstream of the separation bubble. Then these structures move upwards into the shear layer in the detachment region and then turn around the bubble. Upstream of the separation bubble, vortical structures are mainly confined to the inner region of the boundary layer, while they are lifted into the shear layer above the bubble. In the detachment region, vorticity appears to be negligible near the wall. Na and Moin (1998) found that most of the vortices which arrive from the upstream boundary layer are weakened in the middle of the detachment region and convect downstream and impinge on the wall in the reattachment region. Furthermore, the maximum Reynolds shear stress occurs close to the wall downstream of the separation bubble, while local Reynolds shear stress maxima are significantly reduced up to the middle of the reattachment region. Since the turbulent structures move up and turn around the bubble, it can be inferred that

the local Reynolds shear stress maximum is in the middle of the shear layer developing around the separation bubble.

It is important to mention that there is not much information about coherent structures in the outer region of adverse-pressure-gradient turbulent boundary layer.

2.3.1 Scaling

Now we turn our attention to the scaling of the mean flow and the turbulent stresses for adverse-pressure-gradient turbulent boundary layers as the modeling of such flows is one of the most challenging of all flow phenomena. The analysis of turbulent boundary layers under adverse pressure gradient has been going on for a long time. Although different velocity scalings have been proposed over the years, an open question still exits for the proper mean velocity scaling of both outer and inner regions in strong adverse pressure gradients and separated turbulent boundary layers. Indeed, despite the large number of attempts, most of these approaches do not seem to be completely satisfactory.

The classical theory of scaling (u_τ) and the inner-outer mixed scaling of u' (a new scaling) of De Graaff and Eaton (2000) appear to only hold in zero pressure gradient flows and as soon as the flow is subjected to even a mild pressure gradient no scaling has been found to collapse the turbulence stress data onto a simple profile.

The fundamental idea of equilibrium was introduced by Rotta (1953). According to Clauser (1956), turbulent boundary layers where the velocity defect normalized with the local friction velocity u_τ is self-similar for $Re \to \infty$ are called equilibrium boundary layers. For such a boundary layer, a pressure gradient parameter, called Rotta-Clauser's pressure gradient parameter, $\beta_T = \frac{\Delta}{u_\tau}\frac{dU_e}{dx} = \frac{\delta^*}{\tau_w}\frac{dp_e}{dx}$ (where Δ is Rotta-Clauser length scale, $\delta^* U_e/u_\tau$) has to be constant. Here, τ_w is the wall shear stress and dp_e/dx is the freestream pressure gradient. The zero-pressure-gradient boundary layer is, therefore, in equilibrium in the sense described by Clauser. Mellor and Gibson (1966) found that the work started by Clauser (1956) was far from complete and did not provide a base from which to construct a more complete theory. They tried to attain a relatively complete and detailed knowledge of the behaviour of equilibrium turbulent boundary layers. The authors used a pressure velocity $u_{press} = \sqrt{\frac{\delta^*}{\rho}\frac{dp}{dx}}$, as the velocity scale for the outer layer, only when $\tau_w \to 0$.

Skote and Henningson (2002) performed a study of turbulent boundary layer flows

subject to a strong adverse pressure gradient where the boundary layer is everywhere attached, and without separation bubble. They found that in the overlap and wake regions the mean velocity profiles could be collapsed using a pressure gradient velocity scale of $u_p = \left(\frac{\nu}{\rho}\frac{dp}{dx}\right)^{1/3}$, while in such flows u_τ is not the relevant velocity scale. Indeed, the velocity scale u_p should be used instead of u_τ close to separation, where $u_\tau << u_p$. The authors developed further the analysis where the local pressure gradient is the key factor. So Skote and Henningson (2002) used u_τ or u_p as the velocity scale for the inner region of attached boundary layers. The authors developed an expression for the shear stress ($\tau^p \equiv \tau/(\rho u_p^2)$) as a function of $y_p \equiv y u_p/\nu$ as follows

$$\tau^p = y^p \left(\frac{u_\tau}{u_p}\right)^2 \tag{2.1}$$

where y_p is y scaled by u_p/ν. Equation 2.1 has the asymptotic form $\tau_p = y_p$ when separation is approached. Thus, in this rescaled form, the singularity (using the traditional scaling) is avoided.

$$u^p = \frac{u}{u_p} = \frac{1}{2}(y^p)^2 + \left(\frac{u_\tau}{u_p}\right)^2 y^p \tag{2.2}$$

where u^p is the velocity scaled by u_p.

For the overlap region, neither u_τ nor u_p as a velocity scale results in a self-similar expression. However, equation 2.1 can be formulated as

$$\tau^* \equiv \frac{1}{u_*^2}\left(\nu\frac{\partial u}{\partial y} - \langle u'v'\rangle\right), \tag{2.3}$$

where u_* is a velocity scale that depends on y and can be expressed in either viscous or pressure gradient units as follow

$$u_*^2 = u_\tau^2 + u_p^2 y^p \tag{2.4}$$

Finnaly, for the separated boundary layer τ_p can be experessed as (or equation 2.1 can can be formulated as)

$$\tau^p = y^p - \left(\frac{u_\tau}{u_p}\right)^2 \tag{2.5}$$

and for the velocity in the viscous sub-layer of the separated boundary layer, the expression becomes

$$u^p = \frac{1}{2}(y^p)^2 - \left(\frac{u_\tau}{u_p}\right)^2 y^p \tag{2.6}$$

A new extended inner scaling is proposed for the wall layer of wall-bounded flows under the influence of streamwise pressure gradient by Manhart et al. (2008). They

demonstrated that the velocity profiles are not linear if the streamwise pressure gradient is much higher than the wall shear stress even in the viscous sublayer. The authors defined the nondimensional velocity U^* and length y^* as follows

$$U^* = \frac{U}{u_{\tau p}} \tag{2.7}$$

$$y^* = \frac{y u_{\tau p}}{\nu} \tag{2.8}$$

where $u_{\tau p} = \sqrt{u_\tau^2 + u_p^2}$ and $u_p = \left(\frac{\nu}{\rho}\frac{dp}{dx}\right)^{1/3}$.

With this scaling, the velocity profile in the viscous region including pressure gradient effects can be written in nondimensional form as a function of only two nondimensional parameters

$$U^* = f(y^*, \alpha)$$

where $\alpha = \frac{u_\tau^2}{u_\tau^2 + u_p^2} = \frac{u_\tau^2}{u_{\tau p}^2}$. The range of validity of y^* strongly depends on how high the Reynolds number and fast the convective terms gain weight in the momentum balance when moving away from the wall. Angele and Muhammad-Klingmann (2006) studied a separating adverse-pressure-gradient turbulent boundary layer at high Reynolds number using PIV. The authors examined different outer scaling for the acquired data. Angele and co-workers found that the mean velocity profiles in the outer part of the boundary layer around the separation bubble are self-similar when using both a velocity scale based on the local pressure gradient, namely $u_p = \sqrt{\frac{\delta^*}{\rho}\frac{dP}{dx}}$, and the scaling suggested by Perry and Schofield (1973). Indeed, these two different scalings are closely comparable.

Indinger et al. (2006) showed that the logarithmic law does not work well for adverse-pressure-gradient turbulent boundary layers using water-tunnel experiments. They analyzed their experimental results for the outer region and also experimental results from several independent research groups using classical scaling for zero-pressure-gradient turbulent boundary layers, the scaling by Castillo and George (2001), and the scaling by Zagarola and Smits (1998) ($U_{zs} = U_e\frac{\delta^*}{\delta}$). Indinger and co-workers found that the outer scaling originally proposed by Zagarola and Smits (1998) is the most suitable for the mean velocity defect profile, even for very strong adverse-pressure-gradients. Buschmann and Gad-el Hak (2005) found that the Zagarola-Smits scaling works well even in the inner region of zero-pressure-gradient turbulent boundary layer, channel and pipe flows. The results show good agreement with the classical scaling (u_τ).

Maciel et al. (2006a) studied a very strong adverse-pressure-gradient turbulent boundary layer leading to separation and suffering from an abrupt transition from strong favourable-pressure-gradient to strong adverse-pressure-gradient using PIV. It is worth

noting that the experimental setup of this latter study is exactly the same experimental setup of the present study, and, the mean flow conditions are also the same in both studies. The authors showed that U_{zs}^2 scales all the Reynolds stresses in the outer region of such flows, while U_e^2 and u_τ^2 were definitely not appropriate outer scales for the Reynolds stresses. Maciel et al. (2006a) also reviewed adverse-pressure-gradient data from several experiments (i.e. Maciel et al. (2006b) and group of Castillo), and they presented that the Zagarola-Smits scaling works well.

Castillo and George (2001) proposed U_e as the outer velocity scale, while Panton (2005) believed that U_e is not a proper scale for turbulent velocity since it does not scale with the Reynolds shear stress. Since the Zagarola-Smits velocity scale is definitely the most pertinent outer velocity scale for the mean flow in general pressure-gradient conditions and the works of Castillo and George (2001), Castillo et al. (2004) and Castillo and Wang (2004) also revealed the potential of U_{zs} as an outer velocity scale and they found that U_{zs} is successful in collapsing the defect profiles for general pressure-gradient conditions, Maciel et al. (2006a) proposed the new pressure gradient parameters Π_{ZS} and β_{ZS} as follows

$$\beta_{zs} = -\frac{\delta}{\gamma_{zs}}\frac{U_e'}{U_e} = -\frac{\delta}{U_{zs}}U_e' \tag{2.9}$$

$$\Pi_{zs} = \frac{\beta_{zs}}{\gamma_{zs}} = -\frac{\delta^3}{\delta^{*2}}\frac{U_e'}{U_e} \tag{2.10}$$

where $\gamma_{zs} = \frac{U_{zs}}{U_e} = \frac{\delta^*}{\delta}$ and $U_e' = \frac{dU_e}{dx}$. These parameters are definitely more apt than β to characterize turbulent boundary layers in general pressure-gradient conditions.

Recently, Lögdberg et al. (2008) focused on the mean velocity distribution of turbulent boundary layers near, at, and after separation. They found that the mean velocity defect profiles are self-similar in the regions between separation and the position of maximum mean reverse flow. The authors also found that the Zagarola-Smits velocity scaling for mean velocity defect profiles is useful not only for the region near separation but also for cases of different adverse-pressure-gradients. With regards to these results, since the Zagarola-Smits scaling can be used in all flow conditions (favourable-pressure-gradient, zero-pressure-gradient, adverse-pressure-gradient, complex-pressure-gradient, rough wall and other conditions) of turbulent wall flows, it appears to be more universal than u_τ. In the present work, we also apply the Zagarola-Smits scaling on the acquired data using PIV. The Zagarola-Smits scaling is used as an outer velocity scale for the Reynolds stresses and as an outer time scale for the swirling strength and swirl intensity.

Chapter 3

Experimental Set-up and Instrumentation

3.1 Introduction

The experiments in this study are performed in an open-circuit suction-type wind tunnel with a modified test section. The wind tunnel is specially designed to facilitate the investigation of an adverse pressure gradient turbulent boundary layer. The wind tunnel is installed in the Laboratoire de mécanique des fluides (LMF), at the Mechanical Engineering Department of Laval University. This chapter presents the experimental facilities and measurement techniques.

3.2 Wind Tunnel

3.2.1 Entrance

The entrance of the wind tunnel is made mainly of two parts, the settling chamber and the convergent section (see figures 3.1 and 3.2). The settling chamber is located upstream of the convergent section and consists of a honeycomb followed by three screens with decreasing mesh size. The entrance of the wind tunnel is 2.29×0.61 m, after which there is a hexagonal honeycomb cell flow straightener. The honeycomb is used to straighten and make more homogeneous the entering flow by breaking the

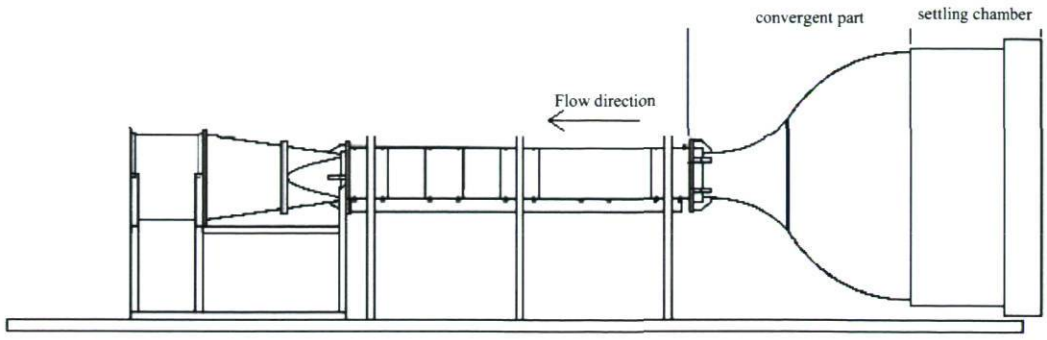

Figure 3.1: Schematic of wind tunnel.

vortical structures which may exist in the flow. After the honeycomb, the flow passes through three screens of decreasing mesh size which are separated by a distance of about 200 mesh sizes. The dimensions of the settling chamber are 2.29 m high, 0.61 m wide, and 0.97 m length.

Figure 3.2: Inlet of wind tunnel.

3.2.2 Test Section

Before proceeding, it should be noted that an airfoil profile model is not used in these experiments. First, in presence of an airfoil the dimension of the test section should

be increased enough to have a potential flow around the airfoil. The presence of large viscous zones in the flow due to the boundary layer separation on the trailing edge introduces important blockage effects. Next the endwall effects can no longer be neglected. The adverse pressure gradient causes the endwall boundary layers to grow rapidly and probably separate too. Their vorticity is also severely skewed by the presence of significant levels of transverse strain rates. Finally the complexity of interaction between the endwall boundary layers and the airfoil is spatially widespread. So, in order to reduce the aforementioned undesired effects, a small airfoil model with a large aspect ratio should be used to achieve an acceptable flow. On the other hand using a small model reduces the achievable Reynolds number, increases the manufacturing tolerances of the model, complicates measurements seriously and reduces their accuracy and scope.

These drawbacks partly explain why the test section is modified instead of using an airfoil model in a regular test section of wind tunnel. As a result, it is not necessary to use a large wind tunnel in order to achieve high Reynolds numbers when the measurements can be done directly on the floor of the wind tunnel. Additionally, the boundary layer is much thicker when it develops on the floor of the test section. A thick boundary layer facilitates measurements and also improves the maximum achievable spatial resolution. Finally, flow measurement and visualization on a flat plate is also easier to perform. Although the flow can be performed at higher equivalent Reynolds numbers, which are closer to reality, and with thicker boundary layers using the wind tunnel floor, the initial conditions are different for the boundary layer in two cases and have different curvature effects.

The strategy adopted is to change the shape of the roof and floor of the test section, in order to produce the desired pressure conditions in a relatively small wind tunnel. Indeed, the rectangular test section was modified to a test section including a convergent part and a divergent part. It is assumed that the mean flow is in the x-direction, y-direction is perpendicular to the floor where the studied boundary layer develops and z is the spanwise direction. The origin of the coordinate system is situated at the entrance of the test section, at the mid-span and on the floor (figure 3.3).

This modified test section, which is shown in figure 3.4, was designed to reproduce external flow conditions corresponding to the suction side of an airfoil in trailing-edge post-stall condition. For such an airfoil separation starts at the trailing edge and gradually moves upstream as the angle of attack is increased (see figure 3.5). Julien (2004) designed the modified test section during his Master's thesis. The desired pressure distribution is achieved by means of a deformed ceiling and a small bump on the floor. This small bump partially reproduces the effect of the leading edge of an airfoil (figure 3.6-b) that the pressure coefficients C_p down to -16 were attained. To design the form

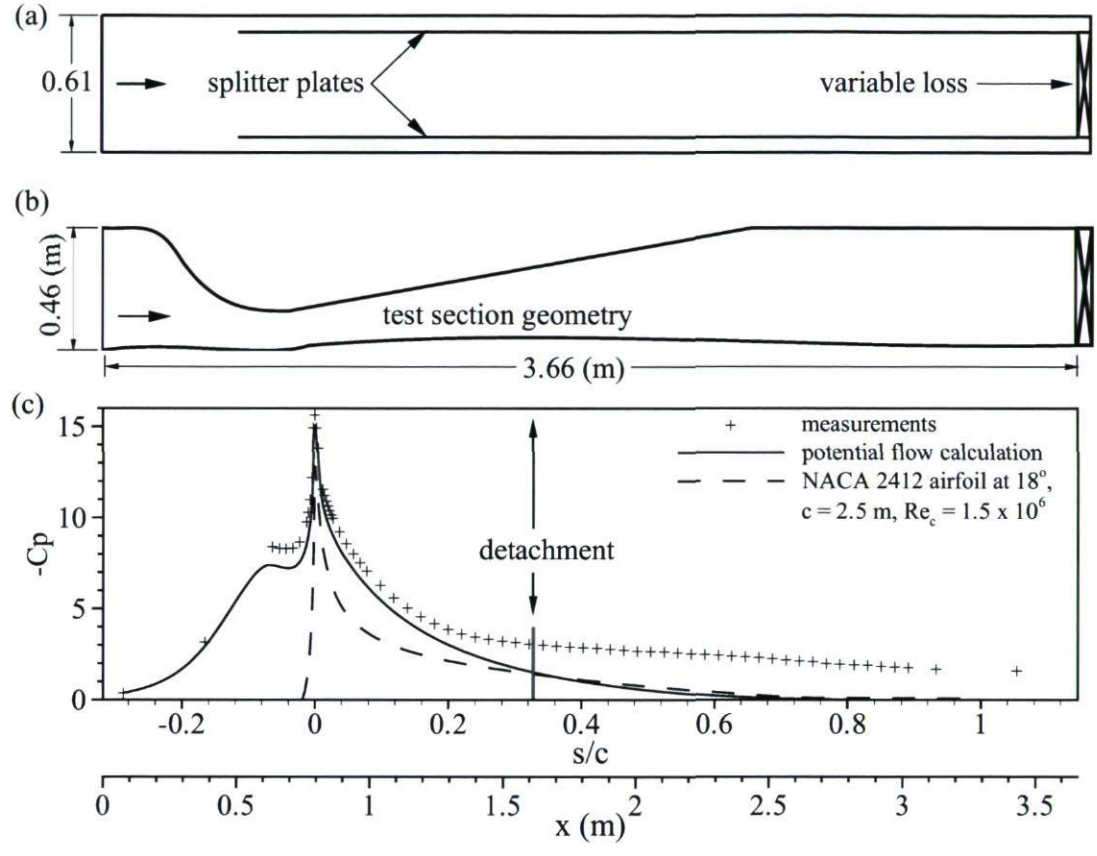

Figure 3.3: a) Top view and b) side view of the modified test section of the boundary-layer wind tunnel, c) Pressure coefficient distribution along the floor of the test section: experimental results (+); potential flow calculation (solid); pressure distribution on the suction side of the NACA 2412 airfoil at 18^o for comparison purposes, chord length of 2.5 m (dashed).

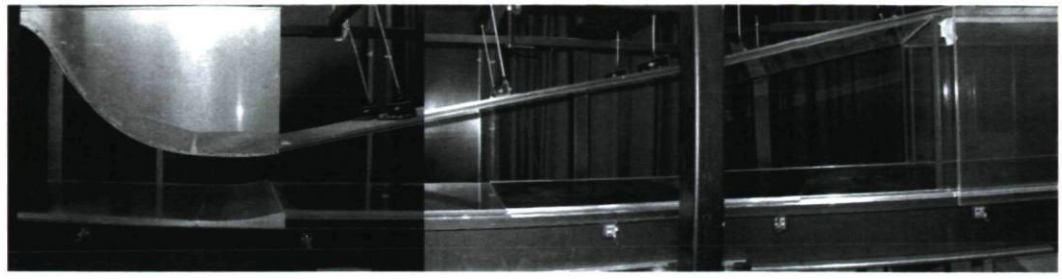

Figure 3.4: Test section of wind tunnel.

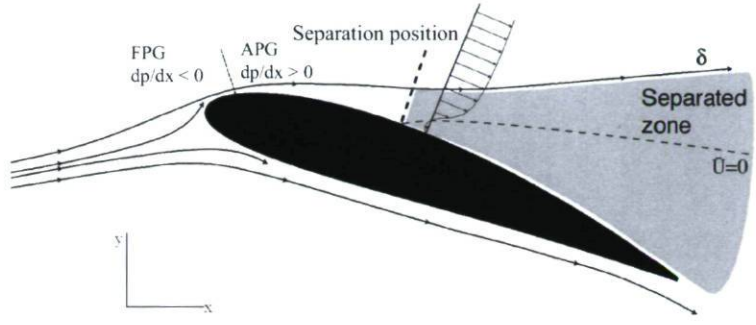

Figure 3.5: Schematic of flow around NACA 2412 airfoil at high angle of attack.

of this small bump, an iterative procedure using a potential flow solver and a boundary layer solver was used. The inviscid and viscous solvers were matched by direct mode via surface transpiration (two dimensional computations only). Combinations of two matched cubic polynomials were used for the geometry of both the converging section at the entrance of the wind tunnel and the small bump on the floor (figure 3.3). The reference pressure distribution used for the design was that of the NACA 2412 airfoil set at an angle of attack of 18^o and at $Re_c = 2.5 \times 10^6$. It is important to note however that the aim was not to reproduce exactly the pressure distribution of the NACA 2412 airfoil but rather to reproduce qualitatively its features. In the present study, Reynolds number Re_c reaches to 1.5×10^6 with an effective chord length of approximately 2.5 meters. As shown in figure 3.3-c, pressure decreases drastically in the convergent section and then it increases in the divergent section, transition strong favorable to strong adverse pressure gradient, within the test section.

The ceiling was designed with special care in order to avoid a separation bubble in the concave part and to minimize the strain rate ($\partial U/\partial y$) at small bump location ($x = 800$ mm) where the pressure peak occurs. Moreover, special care has also been taken to reduce the possibility of re-laminarization in the area of strong favourable pressure gradient. Decreasing the possibility of re-laminarization also leads to reducing the risk of generation of a separation bubble on the bump. The shape of the ceiling of test section is shown in Figure 3.3. Final adjustments of the geometry were done in

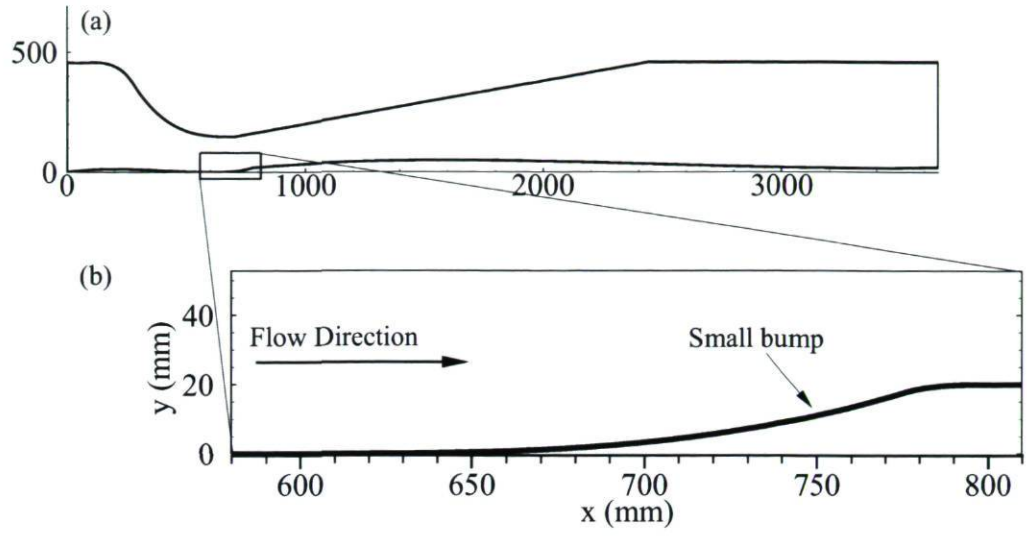

Figure 3.6: a) Schematic of side view of wind tunnel, b) Zoom on small bump at the floor of test section.

the laboratory. Tufts have been used to visualize the flow in order to confirm that the flow remained attached everywhere on the ceiling. Moreover the set-up was designed so that separation occurs after a relatively long length of development in the test section in order to be able to study the boundary layer prior to separation (see figure 3.3). More details on the design and tests of the test section are given in the master's thesis of Julien (2004).

Control and Validation of the Flow

Venisse (2004) developed a control system to reduce the end-wall and corners effects during his Master's thesis. A brief description of his work is presented here.

The boundary layer developes at the lateral walls of the test section. Since the boundary layer coarsens much more rapidly in a strong adverse pressure gradient turbulent boundary layer in comparison to canonical wall-bounded turbulent flows, the development of boundary layer at the lateral walls of test section is much worse for the present flow. Moreover, large vortical structures appear at the corners between floor and the lateral walls of the wind tunnel. These vortices increase the three dimensional effects of the boundary layer and probably interfere with the main flow. A control system was developed to reduce the effects of the lateral wall boundary layers and corner eddies. The control system consists in 19.05 mm thick Plexiglas splitter plates that start at $x = 510$ mm (285 mm before the suction peak, figure 3.3-a). The leading edge

of each splitter plate is a half ellipse with an axis ratio of 2:1. The distance between the splitter plates and lateral walls of wind tunnel is 31.75 mm in order to suction the whole boundary layer. Two adjustable perforated plates are installed at the main channel exit in order to insure proper splitting of the flow between lateral and main channels.

The splitter plates reduce non-uniformities of the flow significantly. Skin friction was measured after the suction peak at $x = 0.86$ m in the spanwise direction. Good uniformity of the spanwise distribution of skin friction was found. The variations were less than 1% in the central 50% of the wind-tunnel span. Additionally, the wall streamlines were found to be parallel and aligned with the streamwise direction using oil film visualization. This is seen everywhere in the test section at least up to $x = 1.2$ m. Since the skin friction is too small to displace the oil film downstream of that position, flow visualization was not possible further downstream. Detailed information can be found in the Master's thesis of Venisse (2004) .

To further validate the flow, extensive PIV measurements were made with horizontal (x, z) planes. These planes covered a large area centered on the midspan ($z = 0$) and located at the start of the separation zone. The detachment point is at $x = 1.615$ m, see figure 3.3-b,c. These measurements were done to characterize the flow further downstream in the detachment zone. It was also found that the mean flow streamlines in the boundary layer remain everywhere parallel and aligned with the streamwise direction except very near the wall just prior to detachment. Moreover, the turbulence was not affected by the three dimensional character of the mean flow close to the wall. A detailed description of these measurements and of the results can be found in Maciel et al. (2006b) and Rossignol (2006).

Optical Access

A modular design was used to construct the test section of the wind tunnel in order to have an adaptable test section. The divergent part of the ceiling and the lateral walls of the test section are made from plexiglass or glass plates that can be fitted together. These glass and plexiglass plates allow an excellent optical access for the laser sheet and the cameras of the PIV system or for flow visualization in the test section. The wind tunnel floor consists in of several 12.52 mm (0.5 in) thick inter-changeable aluminum plates and plexiglass plate. Each aluminum plate can be replaced by a plexiglass plate in order to have optical access at the location of interest. The modular design of the test section also allows easy physical access, for instance to install a probe or to carry out the calibration of a digital camera (in the case of PIV measurements, see section 3.4) within the test section. More details about the design of the test section can be

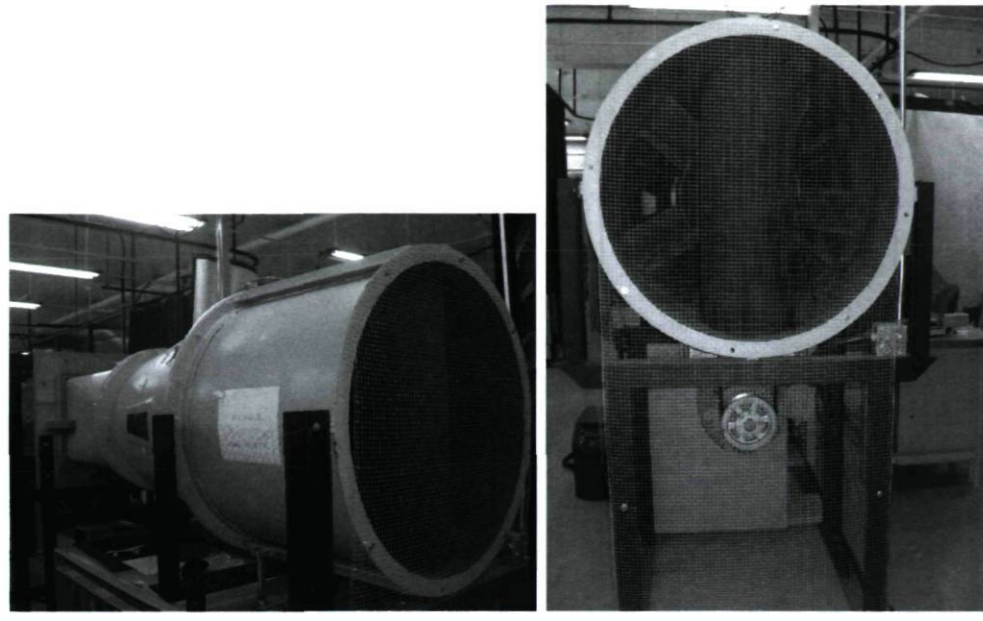

Figure 3.7: Perspective view and front view of the wind tunnel outlet.

found in the Master's thesis of Julien (2004).

3.2.3 Outlet

The air flow exits from the wind tunnel through a diverging section with circular cross-section where the propeller is placed. This circular diverging section is connected to the square test section with a junction mode of foam. The length of the divergent part is 0.91 m. The circular section has a length of 0.79 m. The length of the short adaptor part which makes the transition from the square to circular cross-section is 0.66 m. Figure 3.7 shows pictures of the outlet of the wind tunnel. The divergent cone has a small inclination to avoid the separation of the boundary layer. The propeller is driven by an electric motor of 5.5 kW. The rotation speed can be adjusted with a frequency drive to control the flow velocity in the test section. The frequency drive can be controlled remotely from a computer via serial port.

3.3 Instrumentation

This section of the chapter provides a general description of the instrumentation which was used during the study to characterize the flow. Most of the information is provided

based on the Master's thesis of Venisse (2004) .

3.3.1 Data Acquisition System

A Dell computer with an Intel Pentium IV at 2.4 GHz CPU and 1 GB of RAM is used to acquire the data. Two network cards with 100 Mb/s are installed in order to connecting to the network of Laval University and to controll the SystemHub for PIV measurements. The FlowMap System Hub is a core member of the FlowMap system and like the rest of the system it has a modular structure. This unit provides physical communication links between the Hub and other elements in the system such as illumination devices (laser), digital cameras and PC. The FlowManager software, published by Dantec Dynamics, is used to input the desired delay between the two frames of the double image, and to take the many sets of double frame images are to be taken. When the program is started, FlowManager communicates with the FlowMap System Hub, which then outputs two separate signals - one signal to the laser and another to the camera. These signals are already synchronized when coming out of the hub. With this set-up, one laser pulse occurs in each of the two frames of a double image, resulting in clear, frozen images of droplets. The Flowmap System Hub also stores pairs of images. Afterwards, the acquired images have to be transferred from the Flowmap System Hub to the PC before another set can be taken.

Two HP HEWLETT PACKARD 34401A Multimeters are used to measure the reference velocity and temperature. The signals from a pressure transducer which is connected to two taps at the convergent part are used to measure the static pressure (see section 3.3.2).

The flow velocity in the test section can be controlled by the angular velocity of the fan. The rotating speed of the fan is controlled using a control box. A visual basic program, previously prepared, is used to inputs the desired RPM. Once the desired rotating speed is entered, the PC communicates with the control box via a serial bus and the fan starts rotating. In the present work, the reference velocity is 9 ± 0.01 m/s to have the same flow in all cases. The rotating speed of the fan is about 1300 ± 10 rpm for this reference velocity.

The stands of the cameras are robust displacement systems which have stepper motors. These motors are controlled by a control box. Moreover, this positioning system has a very stable base with four legs as shown in figure 3.8. Similar to the controller of the fan, the user inputs the desired displacement. When the desired displacement is entered, the PC communicates with the control box via a serial bus and the stepper

motor begins to rotate. Each stand has two controllable stepper motors. One motor controls the vertical displacement and the other motor controls the horizontal displacement. The accuracy of displacement is ±0.05 mm using this system. This system allows us to position the cameras with high accuracy. Actually, we need high precision displacement systems for this study as two cameras are used simultaneously in both side of the test section to capture the images. More details are given in section 3.5.

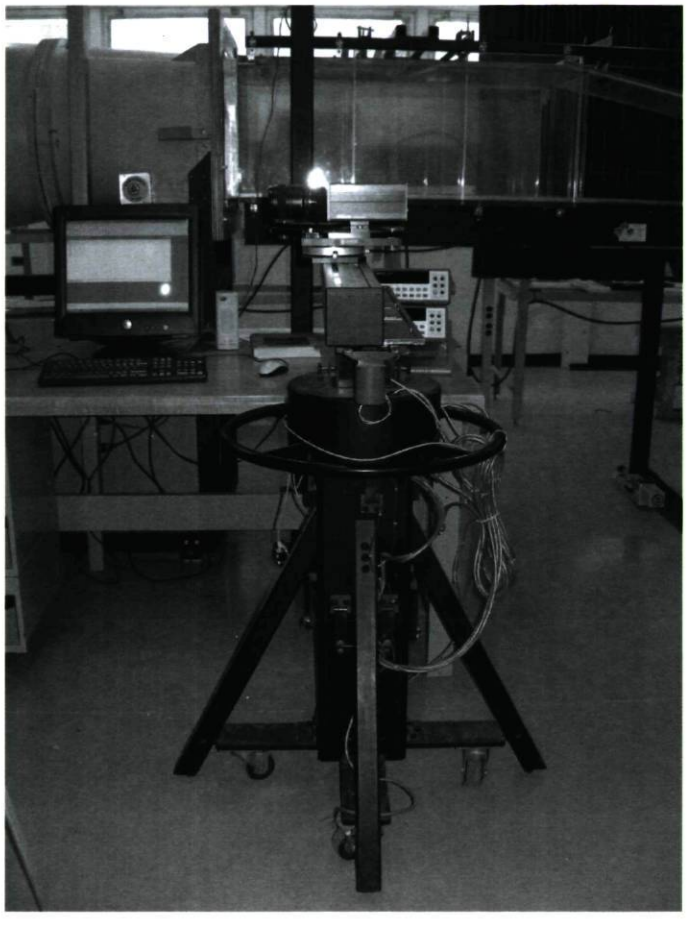

Figure 3.8: Displacement system.

3.3.2 Pressure Measurement

The atmospheric pressure and ambient temperature are measured directly using a mercury barometer of Fortin type and a mercury thermometer. A MKS Baratron 223BD pressure transducer is used to measure the pressure in the wind tunnel. Its range of operation is from −1 to 1 inch of water (−249.1 Pa to 249.1 Pa) for an output signal from −1 to 1 Volt. The measurement accuracy provided by the manufacturer is ±0.5% of the range (±1.25 Pa). The static pressures at the beginning of the convergent sec-

tion, after the settling chamber, and at the end of it are measured by this pressure transducer. To measure the pressures this pressure transducer is connected to two taps which are placed at the beginning and at the end of the convergent part on the lateral wall. The dynamic pressure can be determined using these static pressures. To calculate the dynamic pressure a preliminary calibration is required. This preliminary calibration was done by Vénisse (2004) using a Pitot-static-tube which was placed at the centre of the test section without pressure gradient (no bump at the floor and the ceiling). The Pitot-static-tube is placed 1.35 m downstream of the entrance of test section. The dynamic pressure is measured as follow

$$P_{dynamics} = 1.607 \times \Delta P_{statics} \tag{3.1}$$

where the $\Delta P_{statics}$ is the difference of static pressures at the beginning and the end of convergent part. The $P_{dynamics}$ is used to calculate the reference velocity that is described in the next section.

3.3.3 Measurement of Reference Velocity

The reference velocity (U_{ref}) is determined using the dynamic pressure, $P_{dynamics}$. Once the $P_{dynamics}$ is determined as explained in section 3.3.2, the reference velocity can be calculated as follow

$$U_{ref} = \sqrt{\frac{2 \times P_{dynamics}}{\rho}} \tag{3.2}$$

where ρ is the air density in the test section and equals to $\rho = P_{atm}/(286.9 \times T)$. T is the temprature of air. The calculation of T is explained in the next section.

3.3.4 Temperature Measurement

The temperature in the converging section is measured using a linearized Omega Thermistor Composite 44018. The temperature is determined by the following equation

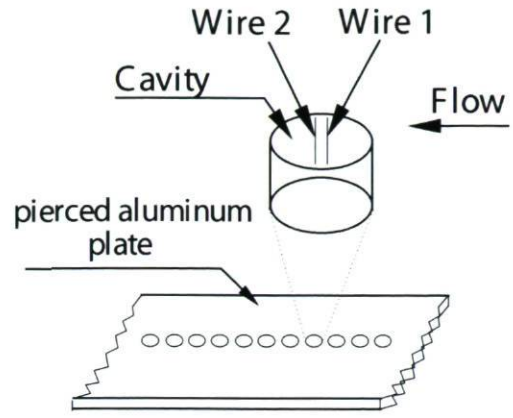

Figure 3.9: Schematic of the two-hot-wires probe.

which is provided by the manufacturer.

$$T = -147.13\frac{E_{out}}{E_{in}} + 95.79 \tag{3.3}$$

where
T is the temperature in degrees Celsius,
E_{in} is the input voltage in volt,
E_{out} is the output voltage in Volts.
The accuracy of measurements is $\pm 0.15^o\ C$ according to the manufacturer report.

3.3.5 Friction Measurement

In order to measure the skin friction, a pierced aluminum plate is placed at the floor of the test section as one of its modules. A probe with two hot wires is located in each holes of the pierced plate. The hot wires are perpendicular to the flow and have the same level of height with the floor (figure 3.9). A calibration channel with a special design is used to calibrate the probe for this technique. The calibration of the probe and the measurements in the wind tunnel were done by Pageau (2004). More detailed can be found in her technical report.

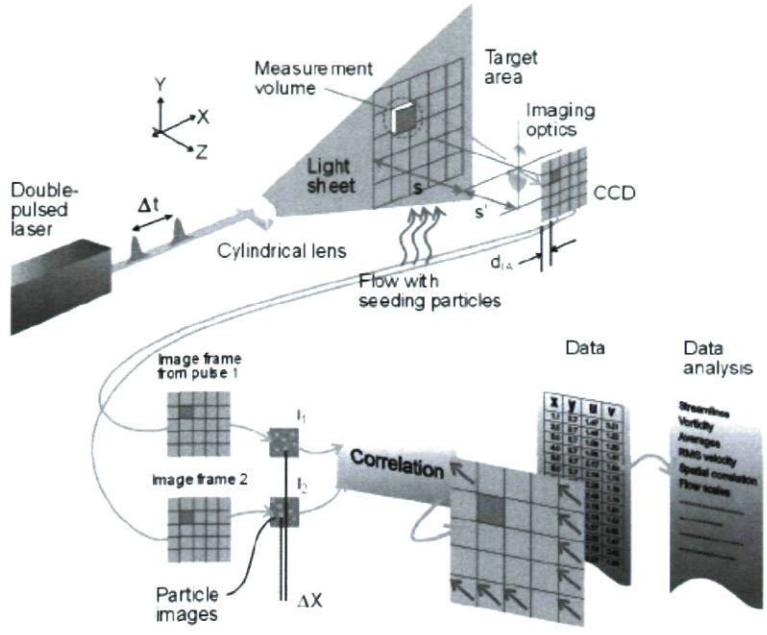

Figure 3.10: Schematic of different elements and working principle of PIV.

3.4 Particle Image Velocimetry System

Particle image velocimetry (PIV) is an optical method used to measure velocities and related properties in fluid flows. The fluid flow is seeded with particles for the purposes of the PIV. These tracer particles are sufficiently small that they faithfully follow the fluid motion and do not alter the fluid properties or flow. It is the motion of these seeding particles that is used to calculate the flow velocity. Typical PIV apparatus consists of one or two digital cameras, a high power double-pulsed laser, an optical arrangement to convert the laser output light to a light sheet (normally using a cylindrical lens). The planar laser light sheet is pulsed twice as a photographic flash for the digital cameras, and the particles in the fluid flow scatter the light. So images of fine particles lying in the light sheet are recorded using digital camera. Once a sequence of two light pulses is recorded, the recorded images are typically processed offline on a digital computer. First, the particle-image patterns are divided in small sub-domains, or interrogation zones. The interrogation zones from each image frame are cross-correlated with each other to provide the displacement of the seeding particles in the interrogation zone resulting a single instantaneous velocity vector. A velocity vector map over the whole target area is obtained by repeating the cross-correlation for each interrogation area over the two image frames captured by the camera. The working principle of PIV is schematically described in figure 3.10. More information on this subject can be found in Raffel et al. (1998).

The velocity measurements of this study were made with PIV (figure 3.10). The laser pulses are generated using a two cavity, frequency doubled 120 mJ New Wave Research Solo PIV Nd:YAG laser. The maximum energy of laser beam is 120 mJ at a wavelength of 532 nm. The pulse width is 3-5 ns and beam diameter is 4.5 mm. The maximum repetition rate of the laser is 15 Hz. The frequency of acquisition rates are however limited to 4 Hz by the framing rate of the cameras. A multi-joint optical arm is used to bring the laser light to the place of interest for measurements. Therefore, it is convenient to install the head of arm accessing all around the test section. A spherical lens is placed at the head of the optical arm. This spherical lens allows to focussing the laser sheet at the place of interest. A cylindrical lense is installed at the end of the arm after the spherical lens. This cylindrical lense converts the circular laser beam into a planar laser sheet with a divergence angle of 30^o. The light sheet thickness was roughly 1 to 2 mm depending on the dimensions of measurement areas. The laser sheet thickness reaches a minimum at the focal length. It is tried to adjust the focal length at the middle of measurement planes in order to have the minimum thickness in the area of interest.

A SAFEX Nebelgerat fog generator is used to seed the flow using SAFEX Inside NebelFluid Normal fog fluid. Special care was made to optimize the seeding so that a homogenous fog enters the wind tunnel with an acceptable density. The produced particles sizes are distributed uniformly and remain sufficiently in the flow to pass the test section before disappearing. They scatter the laser light to illuminate the CCDs of cameras. The fog generator is installed under the converging section of wind tunnel entrance (see figure 3.11). A plate at the front of fog generator inhabits fog to move directly toward the wind tunnel inlet. Two vertical fans are set on both sides of the converging section along with the fog generator. The fans help to push the fog toward the inlet of the wind tunnel in both sides. The fans help to improve mixing of fog clouds around the wind tunnel inlet and allows having a uniform mix of fog cloud and air. The fog generator can control the flow rate of fog, so the seeding density is adjusted with special care before each acquisition in order to obtain the best possible quality of images.

Two HiSense digital cameras equipped with a 1280×1024 pixels CCD array are used to capture the images. Nikkor lenses with focal lengths of 60 mm and 105 mm were used. The cameras are mounted on a displacement system (figure 3.8) which can be easily adjusted. Movement of each displacement system is controlled by computer in both horizontal and vertical directions with an excellent precision (about 0.05 mm displacement) as explained in the section 3.3.1.

The FlowMap System Hub unit provides physical communication links between the

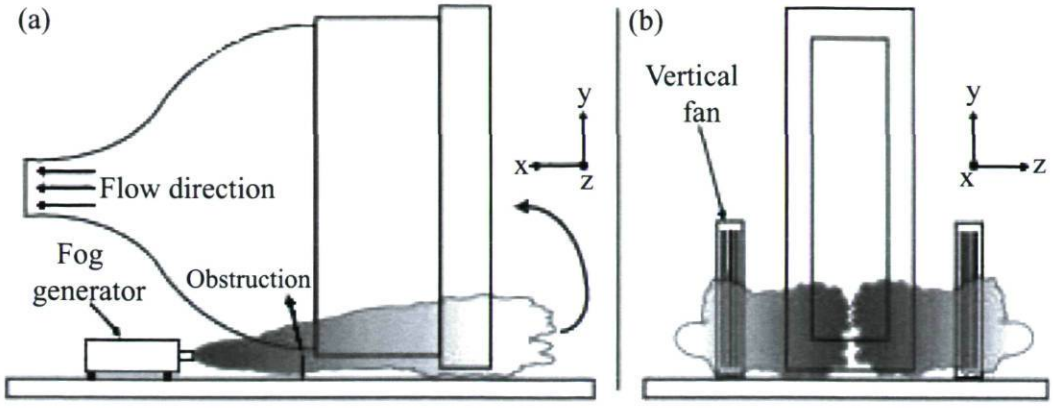

Figure 3.11: Schematic of side view and front view of the wind tunnel inlet and fog cloud.

Hub and other elements in the system such as the Solo Nd:YAG laser, the digital cameras and the computer (see figure 3.12). This unit is controlled by the application PC using Dantec Dynamics FlowManager software. The FlowMap System Hub communicates with the application PC via a 100 Mb/s network card and also with a 1 Gb/s Ethernet. The 100 Mb/s network card is always used for control command between the FlowMap system Hub and the other elements, but data (images) are transferred to the hard disk of application PC through the 1 Gb/s network card. The 1 Gb/s network card transfers data in the range 8 to 20 MByte/s. These rates are average performance for continuous data transfer, meaning that peak performance may be considerably higher.

Figure 3.12 shows a schematic of the FlowMap System Hub. A measurement sequence begins with the synchronisation board, where a sequence of events is loaded from the application PC to the FlowMap System Hub. The synchronisation may for example warm up the laser, before the first camera trigger is sent, ensuring that stable light conditions has been obtained before the image acquisition begins. After receiving a trigger, the cameras transmit the image maps to the System Hub bus, via their frame grabbers, either for storage in the LIFO buffer or for direct uploading to the PC, where application processing takes place.

3.4.1 Software

The acquired images are processed using Dantec Dynamics FlowManager software. Image interrogation was done with the adaptive cross-correlation (using FFT and iterations for offsetting the second interrogation window). The calculation begins with bigger interrogation zones, usually in the range of 64×64 pixels. In this step a velocity

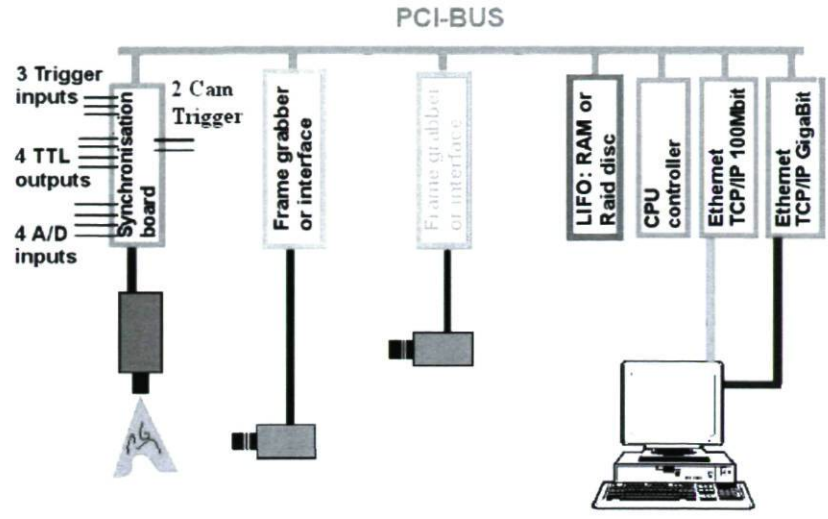

Figure 3.12: Architecture of the FlowMap System Hub with two cameras. The images are routed from the camera via the frame grabber onto the bus in the System Hub. The images then stream into the LIFO buffer or directly onto the 1 Gb/s Ethernet; and ends up in the Application PC. The synchronisation-board directs the events that take place in a timely matter.

vector corresponding to the movment of particles is determined. This vector is then used to shift the second interrogation zone of the second image, when smaller interrogation zone are taken into account in the next step (see figure 3.13). This method is more accurate than simple cross-correlation and achieves a better spatial resolution. In this project, the final size of interrogation zone was 16×16 pixels with 50% overlap of the interrogation zones and the number of refinement steps was fixed as two resulting in interrogation zone of 64×64 pixels, 32×32 pixels and 16×16 pixels. Two iterative steps were also done for each size of interrogation zone, and the 3×3 local median validation and substitution during the adaptive cross-correlation procedure was used.

The same software is used to calculate velocity statistics of the instantaneous velocity fields of measurement (about 1000 fields in each position).

3.5 Measurements

This section describes the methodology used to obtain PIV data to study the turbulence structures in the APG turbulent boundary layer. The proposed approach consists of two overlapping large x-y planes in streamwise dimension (i.e. two cameras, see figure 3.14-a). This method is chosen to increase the spatial resolution and extend the streamwise

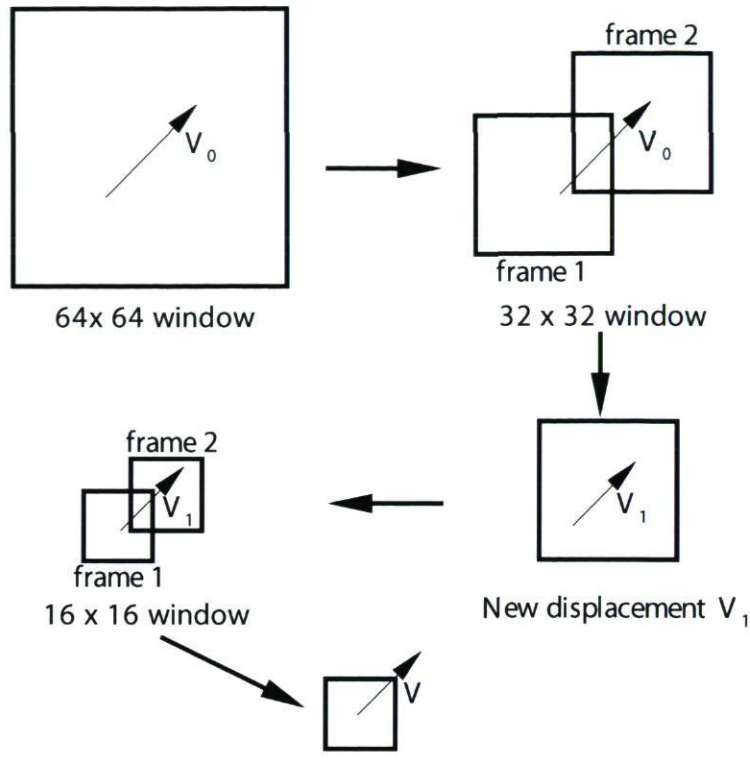

Figure 3.13: Schematic of the adaptive cross-correlation technique.

dimension in order to study the vortex packets. It is explained in more details in section 3.5.1.

In the present experiment, the measurements were made at three streamwise positions covering the adverse pressure gradient region between the suction peak and the detachment point (figure 3.14-b). These positions cover a position near the pressure peak up to the separation point in order to study the evolution of turbulence structures in the adverse pressure gradient zone. Furthermore, these positions are chosen based on the previous study done by Rossignol (2006). The areas cover most of Rossignol's measurements zones in order to validate our results. Table 3.1 and figure 3.15 show different streamwise positions and interrogation zone dimensions (real size in mm and normalized size) for both the present study and Rossignol's study.

3.5.1 Methodology

Each acquired velocity field should cover all the thickness of boundary layer to enable the study of the turbulence structures in all layers. In other words, the PIV plane dimensions should be greater than the boundary layer thickness at each streamwise po-

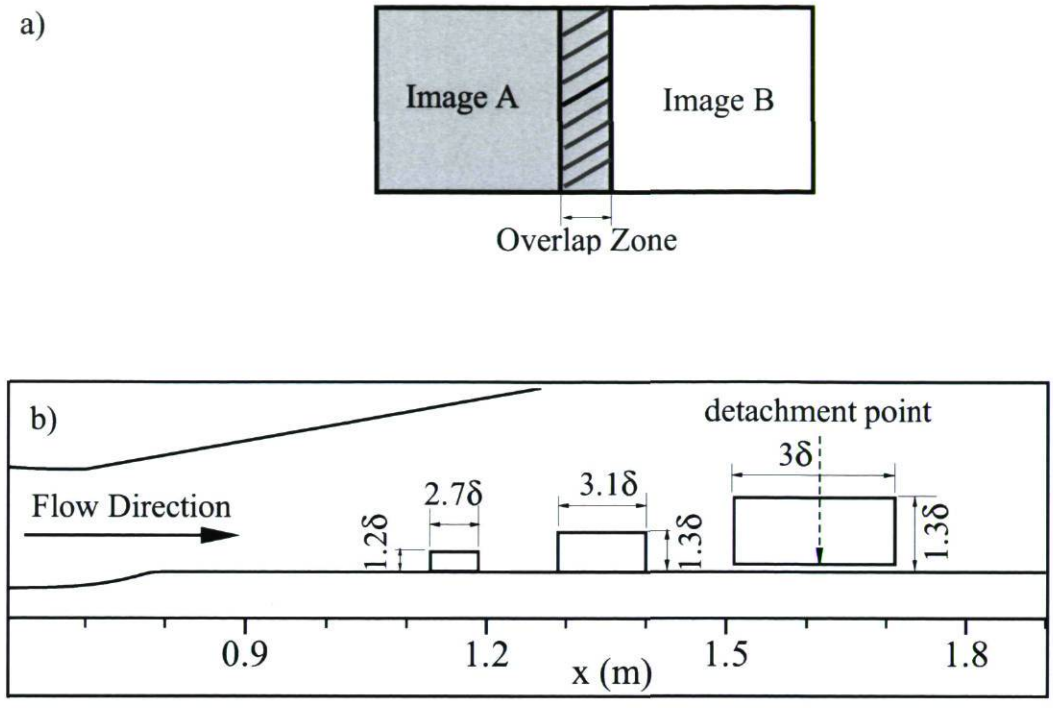

Figure 3.14: Measurement set-up: a) configuration of the two image planes, b) position of measurement planes.

sition. On the other hand, a large streamwise dimension of the PIV measurement plane is necessary to study the hairpin packets characteristics. That is why the dimension of the PIV measurement planes is chosen to be about 3δ in streamwise direction at each streamwise position.

The CCD panel of the digital camera has a resolution of 1280×1024 pixels. So the images are rectangular with the ratio of bigger side to smaller side equal to 1.25. Thus if the interest plane has 3δ in streamwise direction, the other side of planes will be about 2.4δ. The area $y > \delta$ is of no interest. Although the plane with $3\delta \times 2.4\delta$ dimensions covers the entire boundary layer thickness, the spatial resolution is not optimal. High spatial resolution is crucial to resolve the velocity fluctuations and vortices. Consequently, to increase the spatial resolution and to have a large extended dimension in the streamwise direction, measurements were made simultaneously with two overlapping large xy planes (i.e. two cameras, see figure 3.14-a). The combination of the two xy planes results is 3δ in the streamwise direction. Each camera therefore sees a region of about $1.6\delta \times 1.3\delta$ that has an overlap zone in the streamwise direction with other camera. The overlap zone is used to validate the results. So, an extended instantaneous velocity field in streamwise direction is obtained after matching two simultaneously obtained fields with an overlap zone. To cover an area of about $3\delta \times 1.3\delta$, the y dimensions of images are chosen to be about 24 mm at the first position, 48 mm at second position

	x (mm)	Pixel^2	mm^2	$\Delta x/\delta$, $\Delta y/\delta$	Δx^+, Δy^+
Present study	1128-1185	16×16	0.38×0.38	0.014×0.014	13.2×13.2
Rossignol (2006)	1136-1162	32×16	0.029×0.014	0.64×0.32	24×12
Present study	1285-1400	16×16	0.78×0.78	0.016×0.016	15.2×15.2
Rossignol (2006)	1312-1337	32×16	0.64×0.32	0.016×0.008	14×7
Present study	1509-1705	16×16	1.32×1.32	0.014×0.014	-
Rossignol (2006)	1482-1507	32×32	0.64×0.64	0.011×0.011	-
Rossignol (2006)	1601-1627	32×32	0.64×0.64	0.008×0.008	-
Rossignol (2006)	1693-1717	64×64	1.28×1.28	0.014×0.014	-

Table 3.1: Interrogation area dimensions in different streamwise positions in the present study and Rossignol's study. Normalized values of Δx, Δy are taken at $x = 1156$, 1392, 1600 mm, and the center of measurement planes for Rossignol's positions.

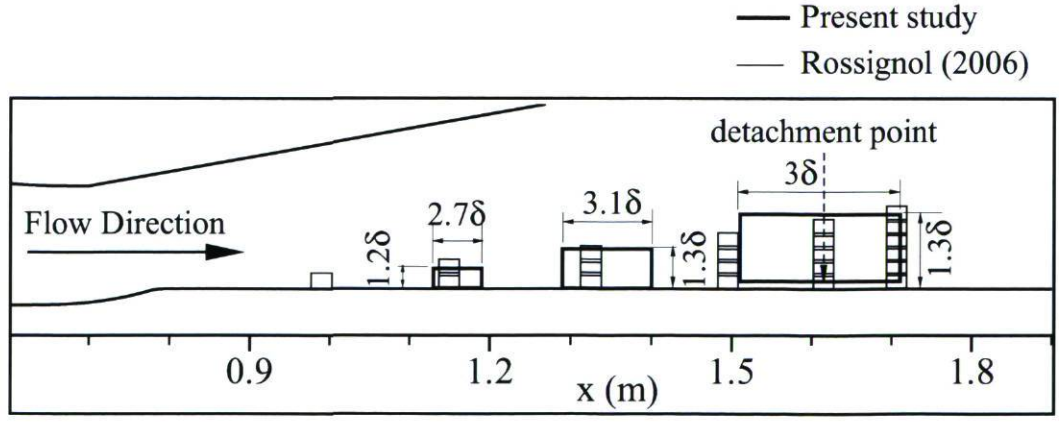

Figure 3.15: PIV measurement planes, the small planes are those of Rossignol's measurements and the big planes are those of the present study.

and 83 mm at the last position. These are the dimensions of the wall-normal direction which is the smaller side of the images.

It is important to mention that the measurement planes are placed about 0.9 mm ($y/\delta = 0.13$ at the middle of measurement plane) above the floor of the test section at the last streamwise position ($x = 1509$ mm), while they are close to the floor for other streamwise positions. It means there is not information for the inferior region ($y/\delta \leq 0.13$) as the acquired PIV images are taken over the $y/\delta > 0.13$. This is because of the image dimensions which should be chosen as small as possible to have a better spatial resolution. Since the spatial resolution is directly dependent to interrogation window width and the resolution of cameras are constant (1280×1024 pixels), the image dimensions should be decreased as much as possible to improve the spatial resolution. On the other hand, the upper region ($y/\delta > 0.2$) which includes the large scale structures is more interesting to study in the present work. This is why the measurements are just done for the $y/\delta > 0.13$ at $x = 1509$ mm.

So the streamwise (x) size of images is 30 mm at first position, 61 mm in the second position and 104 mm at the last position. Figure 3.16 shows the cameras when they are installed in side-by-side configuration. The distance between the center of cameras is 90 mm. So, the acquired images using this set-up can have an overlap zone only when the dimension of the images are more than 90 mm. The overlap dimension can be calculated as follow

$$H = L - d_{AB}$$

where
H is the dimension of overlap zone,
L is the streamwise dimension of image,
d_{AB} is the distance between centers of two cameras.

Consequently, the cameras can be installed side-by-side only when the streamwise dimension of the image is larger than 90 mm. Only the last streamwise position has streamwise dimension greater than 90 mm. Thus, the side-by-side configuration of cameras is used at this position as is shown in figure 3.16. The cameras are next to each other and overlap zone dimension is about 14 mm in this position (10.6 times the interrogation zone width). So the streamwise dimension of the entire image is 194 mm after matching the two images (about 3δ). The side-by-side configuration of cameras can not be used in the other streamwise positions since the streamwise dimensions are less than 90 mm. Therefore, the cameras are installed at both sides of the wind tunnel (figure 3.18) at the first and second positions (figure 3.14-b). In this case, it was

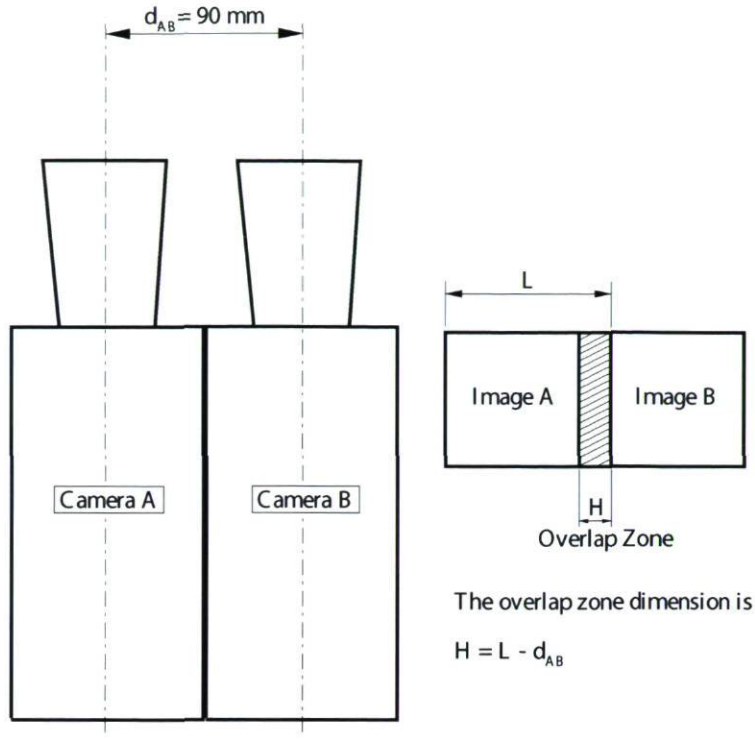

Figure 3.16: Schematic of the cameras in side-by-side configuration (used only at $x = 1509 - 1705$ mm).

tried to locate the cameras at the same height precisely (less than 2 pixels difference). Moreover, the streamwise positioning was done precisely to get predetermined overlap zone dimensions. This is explained rigorously in section 3.5.2.

In conformity with the image dimensions, the biggest lens (105 mm) is used for the first location and the 60 mm lens for the last two positions.

3.5.2 Calibration of Cameras and Laser

It is important that the images of cameras have the same scale factor and coincide in the overlap zone, since their corresponding velocity fields are fused into a single extended field. Adjusting the cameras is easy when they are located side-by-side, whereas special care is needed to adjust them when they are located on both sides of the wind tunnel. Moreover the overlap dimension should be chosen precisely. The supports of the cameras (figure 3.8) let us move the cameras in wall-normal and streamwise directions precisely (± 0.05 mm). The cameras are located in the spanwise direction (z) at the same distance from the center line of test section in order to obtain the same scale factor (figure 3.18).

A transparent ruler is put in the measurement area as a target. Since the letters of the transparent ruler are seen by the both cameras simultaneously, using one point as a reference (figure 3.17) let us adjust the cameras in both of the streamwise and the wall-normal directions in order to have a desired overlap zone width and regulate the height of cameras. Using the streamwise position of the reference point, the overlap width is adjusted. The size of the overlap zone is tried to be a multiple of the final interrogation zone width (16 pixels). This size allows us to have a uniform mesh after deleting some columns from each velocity field in the overlap zone as each column covers 8 pixels (50% overlap of the interrogation zones). The three main goals of having an overlap zone are checking the positioning of the cameras, avoiding the poor quality of correlations which happens at the borders of the images and checking the validity of the velocity results. Since the quality of the correlations is low at the border of the images, some columns are always deleted at the border of each image. The overlapping area includes 19 vector columns. So, the last ten vector columns of image A and the first nine vector columns of image B were deleted.

In these measurements, the optical axes of the cameras are positioned perpendicular to the walls of the wind tunnel (see figure 3.18). The camera aperture is adjusted between f/2.8 and f/5.6 depending on image dimensions. The diaphragm was more opened (smaller f-stop) when the image size was bigger in order to maintain the same depth of field (about 3 mm). Thus special care is taken to have sufficient depth of field covering the entire thickness of the laser sheet. The optimum depth of field is a bit larger than laser sheet thickness because large depth of field increases image noise. Higher intensity of laser light is needed when the diaphragm is less open. In the last streamwise position, because of the image dimensions, the head of optical arm should be located far from the target area in order to have a large laser sheet covering the entire measurement plane. Since the energy of the laser is constant, the light intensity decreases when the size of laser sheet increases leading to need smaller f-stop.

Once the cameras are adjusted using the Plexiglas ruler, the main target is put in the measurement area for final adjustment of cameras and laser light. The target plate is placed on a machined support to be upright and perpendicular to the wind tunnel floor. The cameras and laser light are aligned using the target. The face of the target should be in the middle of depth of field and laser sheet thickness. Aligning the laser is done using a support which holds the head of the optical arm and moves in three directions. When half of the light sheet thickness is blocked by the target and the rest light sheet sweeps its face, the laser light is aligned in spanwise direction. Similarly, when the target is at the middle of the light sheet width and laser sheet focal line at the middle of target, the streamwise alignment is done. The focal lengths of the cameras are changed manually until the target appears to be in the middle of the depth of field.

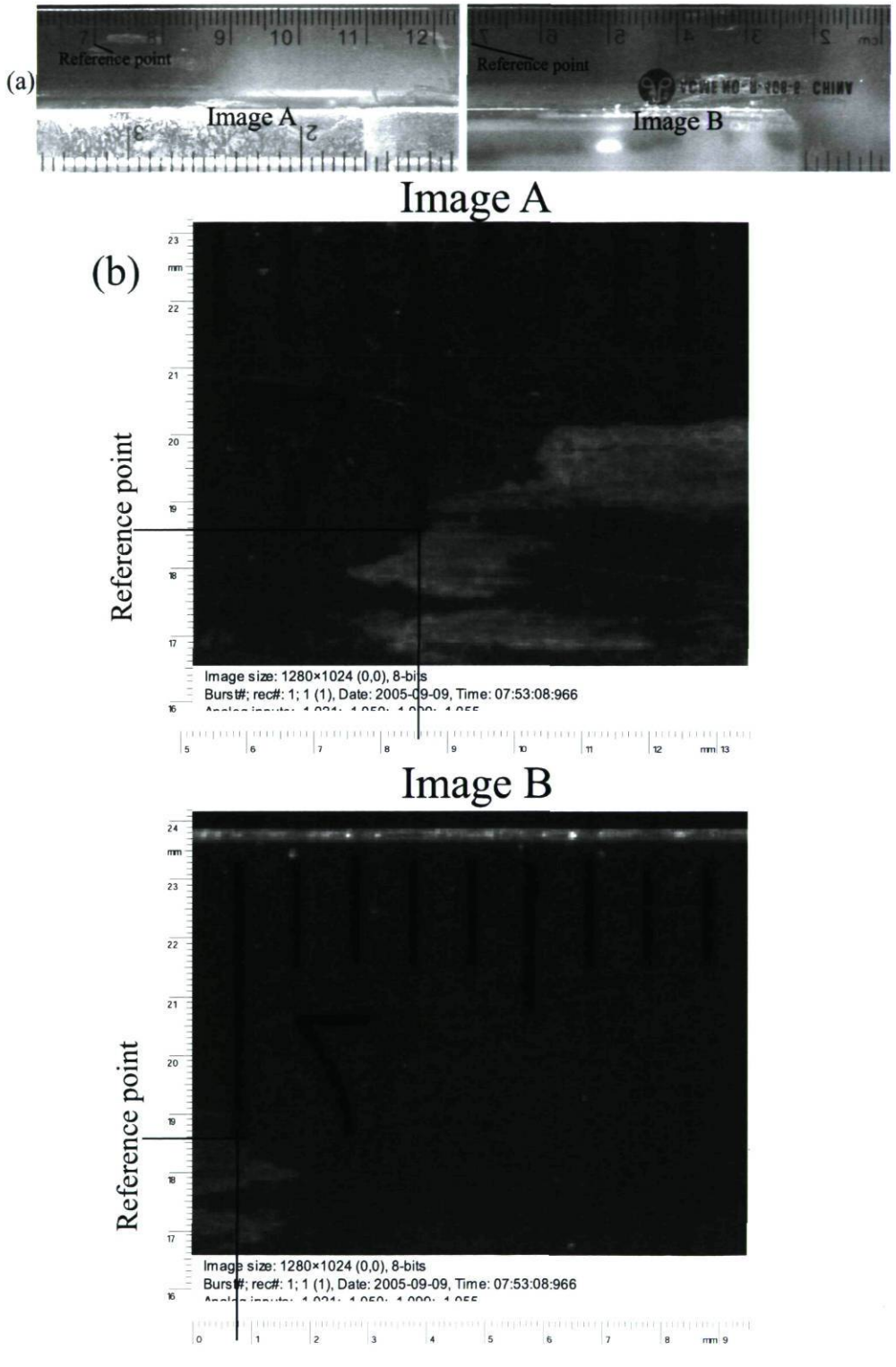

Figure 3.17: Ruler (as a target) images of both cameras: a) ruler picture in image A and B, b) zoom on reference point ($x = 1285 - 1400$ mm).

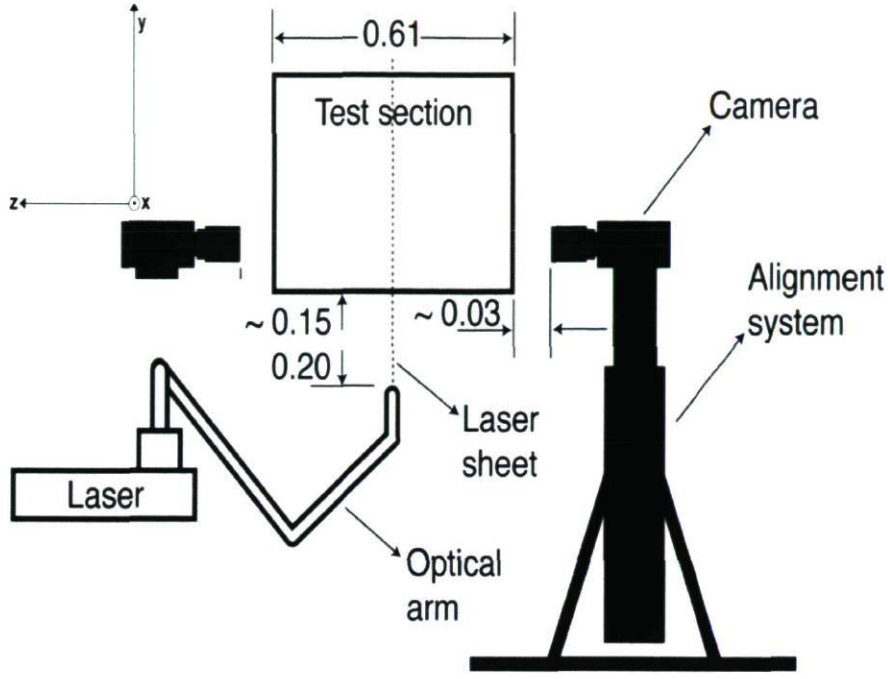

Figure 3.18: Schematic of PIV system set-up (dimensions are in meter).

Figure 3.19 shows the images of the target. It also illustrates the good alignment of cameras since the reference point is at the same height (22.53 mm) in the two images. The horizontal position of the reference point is used to measure the overlap width. Finally the ruler is used once again in order to do a final check of the alignment of the cameras.

3.5.3 Laser and Laser Timing

The laser sheet comes from beneath the floor of the wind tunnel. A Plexiglas plate was designed specially for PIV measurements. This plate allows passing the laser sheet without much loss of intensity or spreading the laser light. The optical arm is placed at a distance of about 20 cm from the floor of the wind tunnel (see figure 3.18) in order to obtain a very thin sheet over the whole boundary layer thickness. The laser sheet thickness is about 1.5 mm at the focal line.

The timing and the pulse separation of the laser pulses and the cameras are controlled using the FlowManager software. The maximum displacement of the particle in the correlation vector map is used as a reference to determine the optimal timing between the laser pulses (Δt). The time delay between the illumination pulses must be long enough to be able to determine the displacement of the tracer particles with

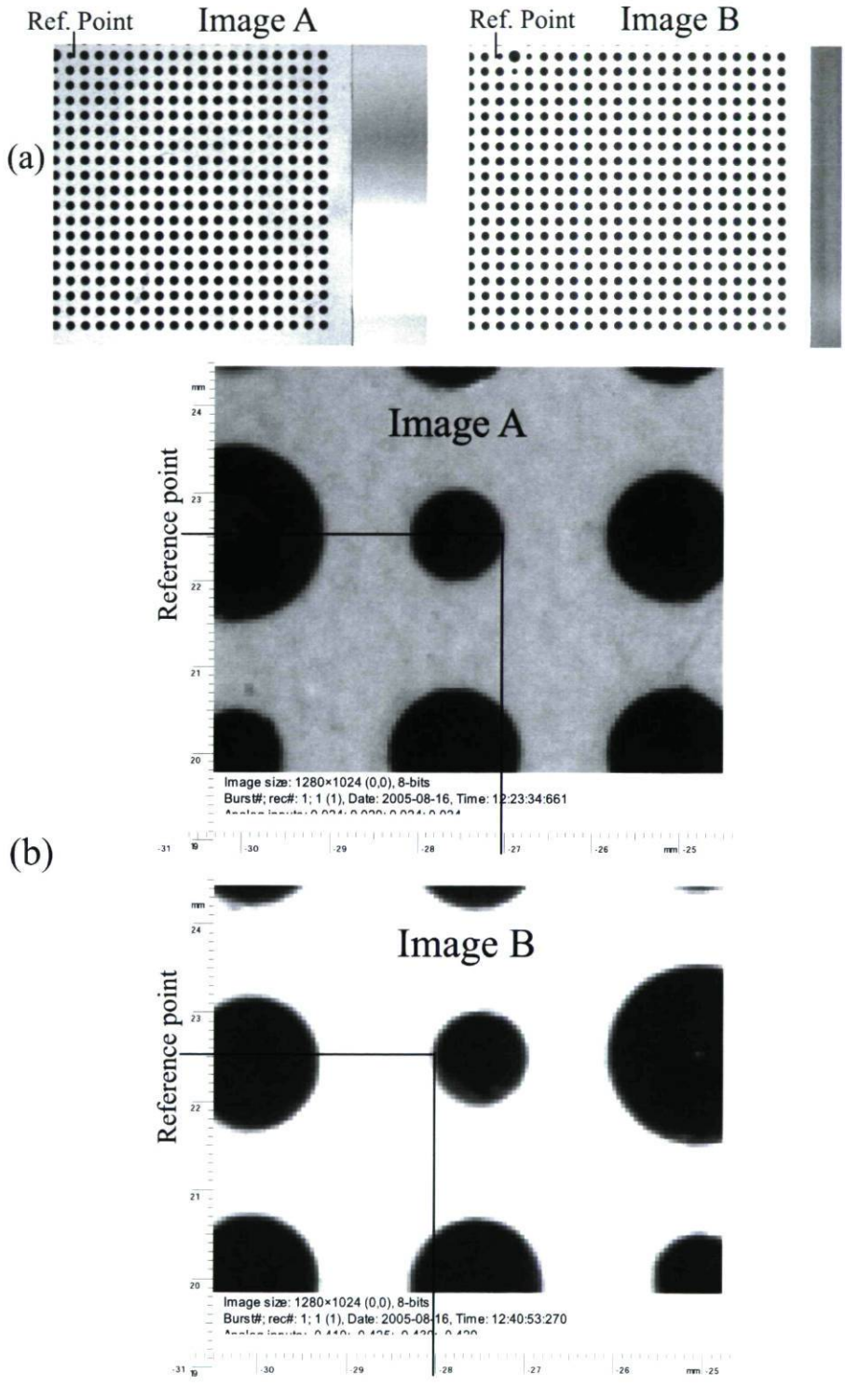

Figure 3.19: Target images of both cameras at $x = 1285 - 1400$ mm: a) whole image, b) zoom on reference point.

sufficient resolution and short enough to avoid particles with an out-of-plane velocity component leaving the light sheet between subsequent illuminations. For this reason, the maximum displacement is usually chosen to be about 10 pixels. So, the optimal time is determined using this reference and a trial and error method. (Δt) is 12 μs, 25 μs and 30 μs at the first, second and last streamwise position respectively.

3.5.4 False Vector Detection and Substitution

The adaptive cross-correlation procedure (16×16 pixels with 50% overlap) yields 20193 vectors per image set. The velocity vector fields are contaminated by spurious vectors as mentioned previously. Effects of background noises, displacement gradient across the interrogation window, out-of-plane motion and poor quality of images cause these vectors because identifying the real correlation peak associated with the movement of particles in an interrogation zone becomes difficult (Westerweel, 1994). The false vectors can be recognized by comparing each vector with its neighbours. Considering a threshold for our comparisons, if any component of the vector of interest is different from its nearest neighbours' median component, the vector would be false. The purpose of the validation is to eliminate all false vectors and replace them with a median value of neighbouring vectors if at least a given number of valid neighbours exist.

Since it is very important to eliminate false vectors form velocity, a validation algorithm has been developed by Rossignol (2006) and modified and improved in the present study. This algorithm, named ValidationLocale.m, is programmed in Matlab. The basic principles used for chosing the validation method comes from the works of Westerweel (1994) and Westerweel and Scarano (2005).

The algorithm works based on the comparison of each vector with its eight neighbours' vectors. Rossignol (2006) used a constant threshold for identification of false vectors. This is justified by the fact that large variations in the flow speed should not happen in a short distance. Obviously, this method is largely dependent on spatial resolution. When the spatial resolution is low and the velocity gradient is high, there is a risk of eliminating good vectors. The investigation of vectors to indentify the false and good vectors is done based on each component of the velocity vector. The equation 3.4 shows how the constant threshold is used in this method.

$$\begin{aligned} |U_{i,j,pixel} - U_{median,pixel}| &< \epsilon_u \\ |V_{i,j,pixel} - V_{median,pixel}| &< \epsilon_v \end{aligned} \tag{3.4}$$

The variables $U_{i,j,pixel}$ and $V_{i,j,pixel}$ identify the components of the displacement vector, in pixels. The vector with indices i and j should be validated. The $U_{median,pixel}$ and $V_{median,pixel}$ are the median components of valid neighbour vectors. An absolute criterion (ϵ_u, ϵ_v) is used to identify the false vectors. The vectors for which one or both of its components exceeds the criterion value when compared to the median value, are eliminated.

The principle and effectiveness of this method was demonstrated for velocity fields with low-gradients of velocity, for which a constant detection threshold can be applied. In contrast, using a fixed criterion of detection reduces the effectiveness of this method when significant velocity gradients exist or in uniform flow region. This means when a fixed detection criterion applied to the entire flow domain, a part of valid vectors may be rejected, while it would not occurr when using a proper criteria. That is why another method is used in the present study. In this new method, which was proposed by Westerweel and Scarano (2005), an adjustable detection threshold is used. The adjustable detection criterion works based on the root-mean-square of velocity fluctuations (σ_u) calculated using its neighbours. It is worth noting that few number of samples is available to estimate σ_u and that the local neighbourhood may contain spurious measurement data too. These effects may make an unreliable estimation of σ_u. Thus, this will make it more difficult to detect the false vectors in the presence of other spurious data.

An adaptation of the original median test which uses a median estimate of σ_u is used in order to reduce the effects of spurious measurement data in the neighbourhood. The 3×3 neighbourhood data of a displacement vector denoted by U_0 called U_1, U_2, ... , U_8. The median of U_1, U_2, ... , U_8 is called U_m. A residual r_i is defined as $r_i = |U_i - U_m|$ (Westerweel and Scarano, 2005). The r_i is determined for each vector U_i where $i = 1, ..., 8$. The median of this residual r_i (r_1, r_2, ... , r_8) is determined and called r_m. The r_m is used to normalize the residual of U_0 as follows

$$r'_{0_u} = \frac{u_0 - U_m}{r_{m_u}}$$
$$r'_{0_v} = \frac{v_0 - V_m}{r_{m_v}} \tag{3.5}$$

where u and v are the velocity components.

This adjustable outlier detection value can be used to process a large variety of data with significant velocity gradients. Westerweel and Scarano (2005) found that the histograms of normalized r'_0 defined in equation 3.5 approximately collapse on a single

curve and become independent of the turbulence level. Moreover, it was found that r'_0 shows elevated values for regions with very low turbulence intensities. In fact, the normalization factor r_m tends to zero when the flow is purely uniform. This can be compensated by assuming a minimum normalization level ϵ, i.e.:

$$\begin{aligned} r^*_{0_u} &= \frac{u_0 - U_m}{r_{m_u} + \epsilon} \\ r^*_{0_v} &= \frac{v_0 - V_m}{r_{m_v} + \epsilon} \end{aligned} \tag{3.6}$$

where ϵ may represent the acceptable fluctuation level due to cross-correlation. It was found that a suitable value for ϵ is about 0.1 pixel, which would correspond to the typical rms noise level of the PIV data (Westerweel, 2000).

The two steps of this method can be summarized as: 1- the r^*_0 are determined for both u and v components of velocity. 2- The calculated residuals are compared with a defined threshold to distinguish the false vectors, i.e.:

$$\begin{aligned} R^*_{0u_{i,j}} &= \left| r^*_{0u_{i,j}} - r_{m_u} \right| \\ R^*_{0v_{i,j}} &= \left| r^*_{0v_{i,j}} - r_{m_v} \right| \\ R^*_{0uv_{i,j}} &= \sqrt{R^{*2}_{0u_{i,j}} + R^{*2}_{0v_{i,j}}} \end{aligned} \tag{3.7}$$

where $r^*_{0u_{i,j}}$ and $r^*_{0v_{i,j}}$ are calculated using equation 3.6. A vector is detected as a false vector if $R^*_{0uv_{i,j}} > Thr$. Where Thr is the threshold which should be determined by user. $Thr = 2.5$ and $\epsilon = 0.1$ in the present work.

The program can be used iteratively (see Rossignol's thesis, 2006). The validation process is based only on the vectors that have not previously been identified as false vectors. Note that there are 3 types of vectors, according to the convention used in the FlowManager software (see Table 3.2).

State	Code
rejected	1
validated	0
substituted	16

Table 3.2: Status code of vectors for the FlowManager and the program ValidationLocale.m.

These status codes are also used in the validation phase. For border points of the velocity field, the validation test is different. In this case, each point has five neighbours instead of eight neighbours. A similar problem also exits at the corners where each point has just three neighbours. Figure 3.20 shows the three possibilities.

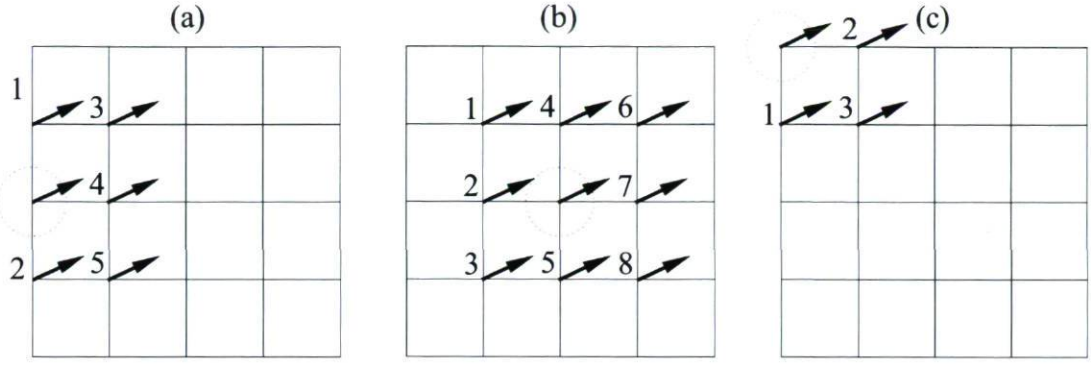

Figure 3.20: Three possibilities of neighbourhood points.

The false velocity vectors have generally non-zero components. It is also possible to observe zero vectors because of significant reflections within the images. These vectors are also false because they have no physical sense, and should be eliminated. Therefore all the velocity vectors which have zero-value components are detected as false vectors by the program.

Once a vector is detected as a false vector, it goes through the validation phase and will be substituted if the user desires. Two conditions are necessary to substitute a false vector. Firstly, the percentage of false vectors in the velocity field must not exceed a certain percentage which is defined by the user. It is usually supposed 40% in this study. The entire velocity vector field is rejected if more than forty percents of its vectors are false. Secondly, in order to obtain a valid outlier threshold a minimum number of valid vectors must be available in the neighbourhood of the vector. This number is proposed five for the internal points, three for the borders points and two for the corners points in the present study. The false vector is rejected if the number of valid vectors is less than the minimum validation criteria.

Several parameters can be adjusted in the program in order to make the method flexible. The first parameter is the number of iterations that the program performs to do validation process specified equal to two in our case. Actually the iteration number helps to eliminate the false vectors as much as possible, but we found that there is no significant improvement when we boost it. The adjustment of the threshold is done by visual observation of validated velocity vector fields. It should eliminate the false vectors as much as possible without elimination of visually correct vectors.

Finally, it is important to note that the program also uses a velocity conversion factor from m/s unit to pixel unit. This step is necessary as the false vectors identification is calculated based on pixel unit. Once the validation is complete, velocity vector units must be converted to m/s to be compatible with FlowManager entries, because any input velocity to FlowManager (i.e. from Matlab) is considered to be in m/s.

3.5.5 Applying the Gaussian Filter

Having excellent spatial resolution is importance to detect and follow the turbulence structures. For that reason the smallest possible interrogation window width within the correlation process is chosen. Since acquiring velocity fields without noises or fewer noises are strongly depended to image quality and interrogation window width, the obtained velocity fields are contaminated with more experimental noises when smaller interrogation window width is chosen. To reduce experimental noise in the velocity field, a two-dimensional homogeneous Gaussian filter is used to smooth the instantaneous PIV velocity fields. The sizes of the spatial filtering window are chosen depending on the analysis performed. The spatial filtering window was set at 0.028δ for the study of the spanwise vortices, the hairpin vortices and packets. More details are given in appendix A.

3.6 Validation of the Velocity Fields

3.6.1 Checking Positioning and Calibration of Cameras

Matching of the instantaneous velocity vectors in the overlap zone was found to be always very good at each streamwise position (figures 3.21-3.23). So this good matching of instantaneous velocity vectors confirms that both cameras look precisely the same points in the overlap zone and the accuracy of the measurement. Therefore, a continuous velocity vector field can be achieved after deleting some columns from each image. It is worth recalling that the cameras are placed side-by-side at the last streamwise position, while they are placed in both sides of the wind tunnel for other ones. So, the streamwise location of one camera relative to other one can not be adjusted precisely like the other positions. So, the overlap zone does not include 10 interrogation zone widths exactly, while this is not the case for the other positions. This is why; the instantaneous vectors are not at the same x in figure fig:InsVelX1509. Furthermore, the points at the border

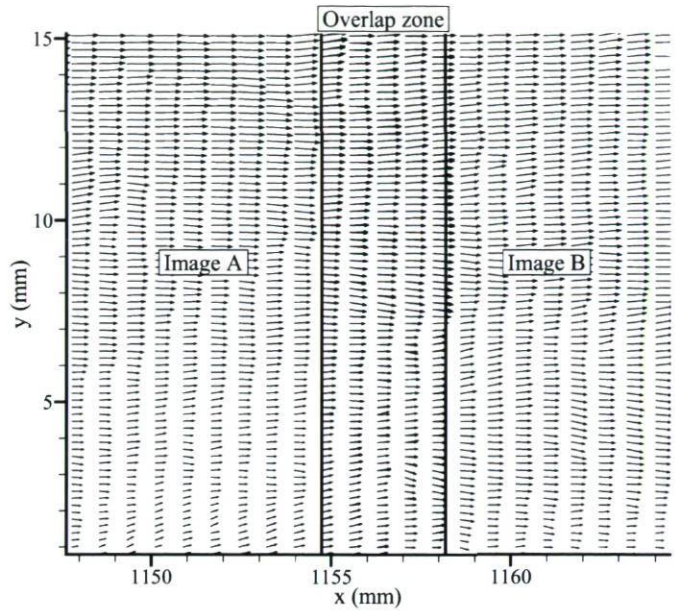

Figure 3.21: Instantaneous velocity vectors fields obtained with both cameras showing good match of vectors in the overlap zone (One vector out of 4 in x-direction for clarity), in region $x = 1128 - 1185$ mm.

of velocity fields are not used in the analysis procedure as these points can not be validated perfectly.

3.6.2 Validation of Mean Flow Results

Since the experiments are performed over a large period of time and several measurements at different streamwise positions are done; it is necessary to use a methodology which can establish a consistent set of conditions for all experiments. For this reason, it is tried to have approximately the same Reynolds number as those studied by Rossignol (2006). Since, the fluid properties do not vary in the laboratory, and the wind tunnel dimensions are also the same for the both studies, fixing the reference velocity (U_{ref}) for all the experiments leads to have approximately the same Reynolds number. In the present study U_{ref} is chosen 9 m/s, ± 0.02 m/s similar to the study of Rossignol.

Before comparing the statistical characteristics of the flow in the present and Rossignol's (2006) studies, an example of the variation of mean streamwise velocity component in the x direction is illustrated in figure 3.24. The different curves show the mean streamwise velocity variation at different heights of the boundary layer. Matching the results in the overlap zone confirms the good positioning and calibration of cameras

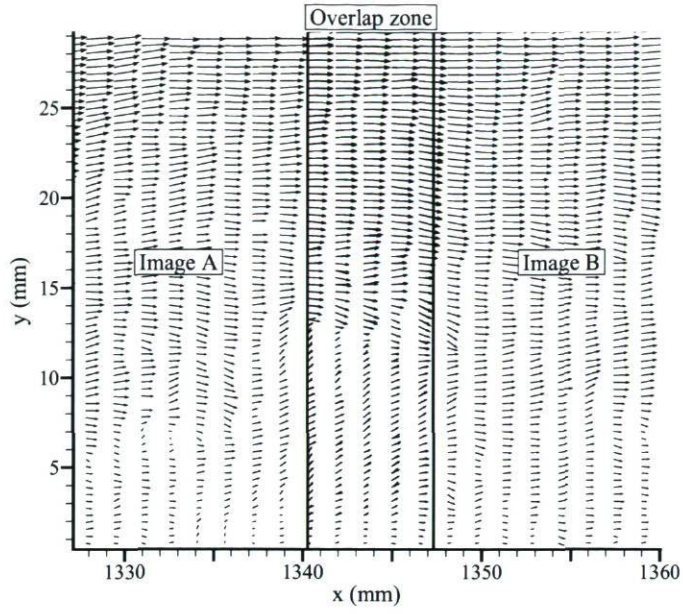

Figure 3.22: Instantaneous velocity vectors fields obtained with both cameras showing good match of vectors in the overlap zone (One vector out of 4 in x-direction for clarity), in region $x = 1285 - 1397$ mm.

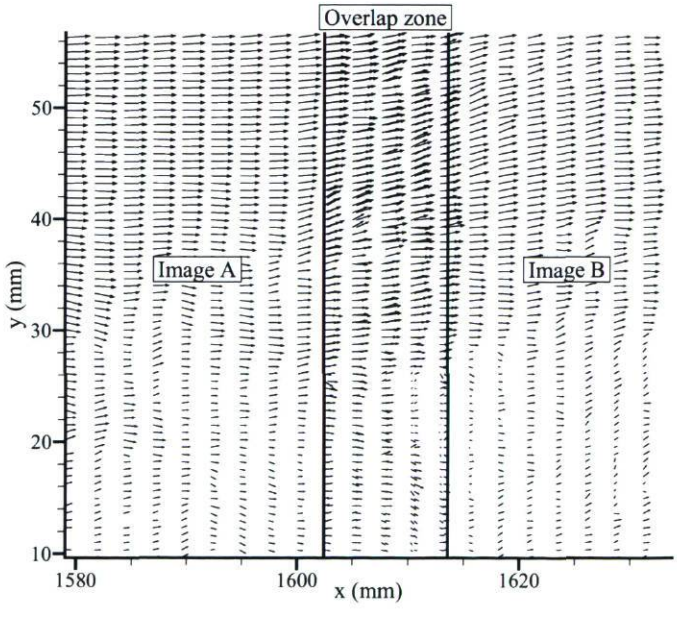

Figure 3.23: Instantaneous velocity vectors fields obtained with both cameras showing good match of vectors in the overlap zone (One vector out of 4 in x-direction for clarity), in region $x = 1509 - 1680$ mm.

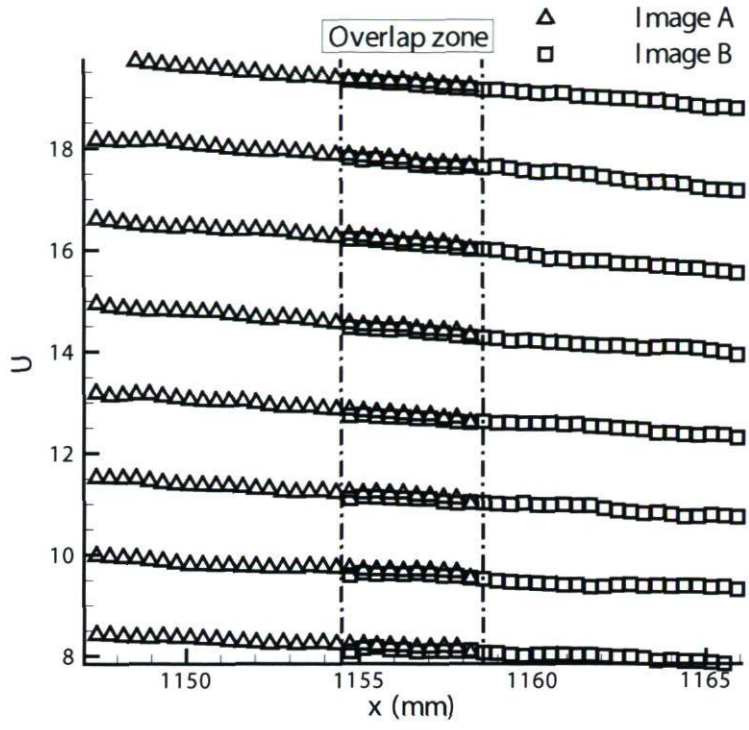

Figure 3.24: Variation of mean streamwise velocity component in x direction (in region $x = 1128 - 1185$ mm) obtained with both cameras. One out of ten curves at constant y are shown and one out of two values in the streamwise direction for clarity.

(the difference of U is about 0.05 m/s). The statistical characteristics of the flow were previously studied by Rossignol (2006). As explained in section 3.5.1, the measurement areas in the present study cover most of the streamwise positions of Rossignol's measurements (2006). As a result, the boundary layer parameters in the present study and Rossignol's study should be approximately the same as the Reynolds numbers are similar in both studies. Figure 3.25 shows δ, δ^* and θ of boundary layer for both cases. Matching of all parameters in both studies is found to be very good except at the second streamwise position ($x \cong 1300$ mm). The streamwise evolutions of all three parameters of our results are more consistent than those of Rossignol's results. Figure 3.26 shows the mean velocity profile in the present study and Rossignol's study, as well as the zero pressure gradient turbulent boundary layer (Oesterlund 2000). It also shows an excellent agreement. Figure 3.27 shows the streamwise Reynolds normal stress normalized by U_e in both present and Rossignol (2006) studies. The results agree very well except at the last streamwise position ($x = 1600$ mm). Since the spatial resolution in this region is higher in the Rossignol's study in comparison to the present study, this exception may be due to the effect of spatial resolution.

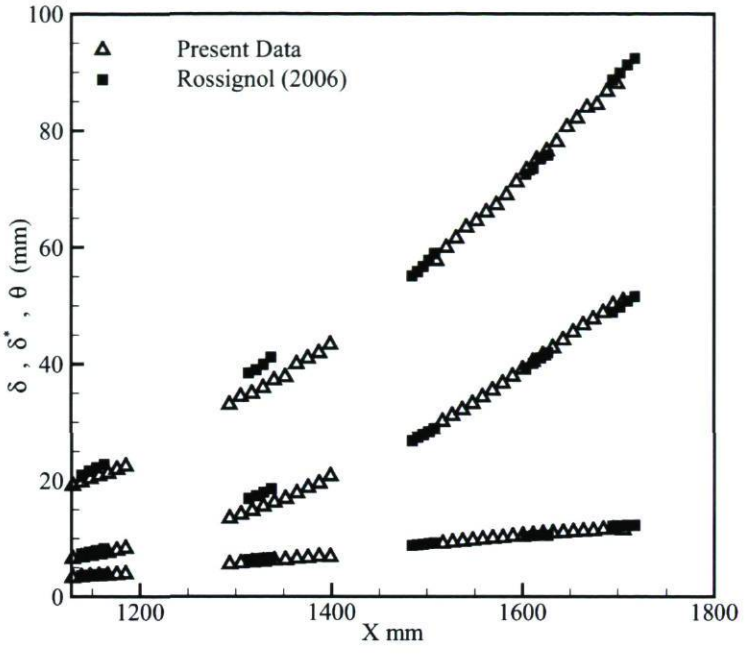

Figure 3.25: Boundary layer thicknesses (δ, δ^*, θ) for the present study and Rossignol (2006). One data point out of 8, 4 and 2 for the first, second and the last streamwise positions respectively for the others for clarity.

3.7 Streamwise Evolution and Global Parameters of Mean Flow

This section is intended to give a brief description of the mean flow characteristics. The evolution of streamwise and wall-normal components of mean velocity scaled by U_e, U/U_e and V/U_e are shown in figures 3.26 and 3.28 respectively. These evolutions show clearly the effect of the pressure gradient on the boundary layer. The pressure gradient decelerates the flow and leads to detachment of the boundary layer. The last U/U_e profile is at the detachment point, $x = 1615$ mm, inflection points appear in the velocity profiles.

The most important parameters of boundary layer are shown in table 3.3. The parameters corresponding to ZPG TBL are taken from Adrian et al. (2000). Fifty instantaneous velocity fields from this reference are also used in the present study for comparison purposes. Since the PIV measurements of Adrian et al. (2000) were also done in xy-plane and at high Reynolds number, this PIV database is actually a good reference for the ZPG TBL. In fact, the PIV data of our study and their study are interpreted in the same manner. In chapters 4 and 5, this enables us to have an

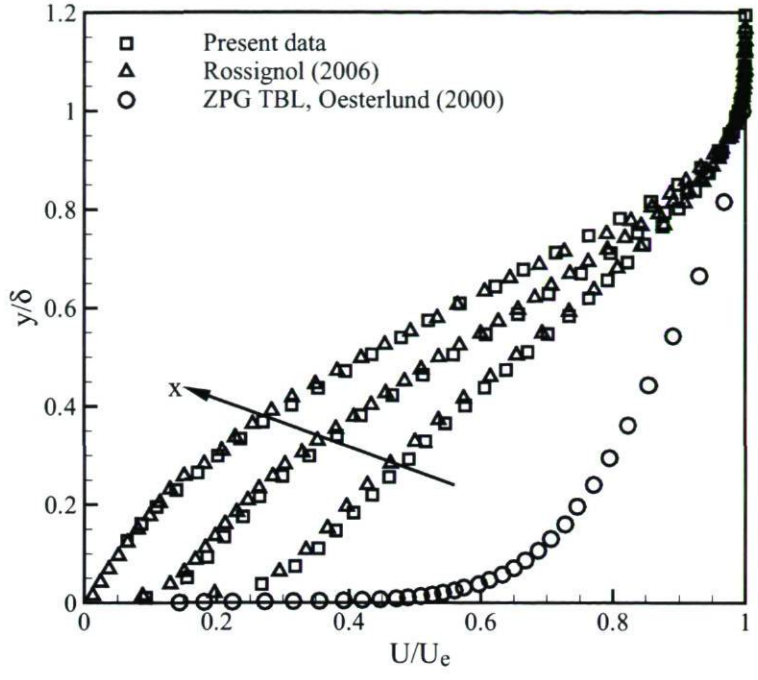

Figure 3.26: Mean streamwise velocity profile for the present and Rossignol (2006) studies at $x = 1156$ mm, $x = 1392$ mm and $x = 1600$ mm. The ZPG profile at $R_\theta = 12633$ of Oesterlund (2000) is also shown. One data point out of 2 for the present study and one data point out of 3 for the others for clarity.

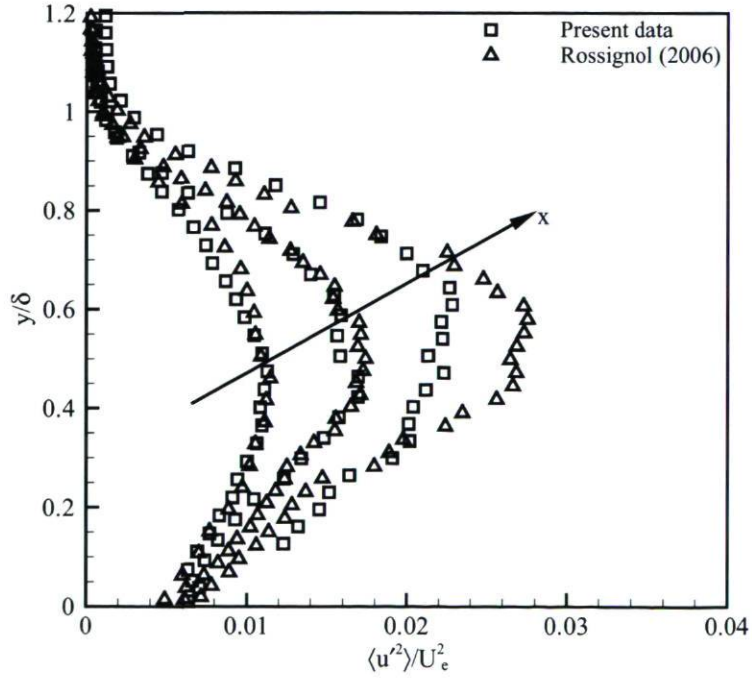

Figure 3.27: Streamwise Reynolds normal stress normalized by U_e, for the present and Rossignol (2006) studies at $x = 1156$ mm, $x = 1392$ mm and $x = 1600$ mm.

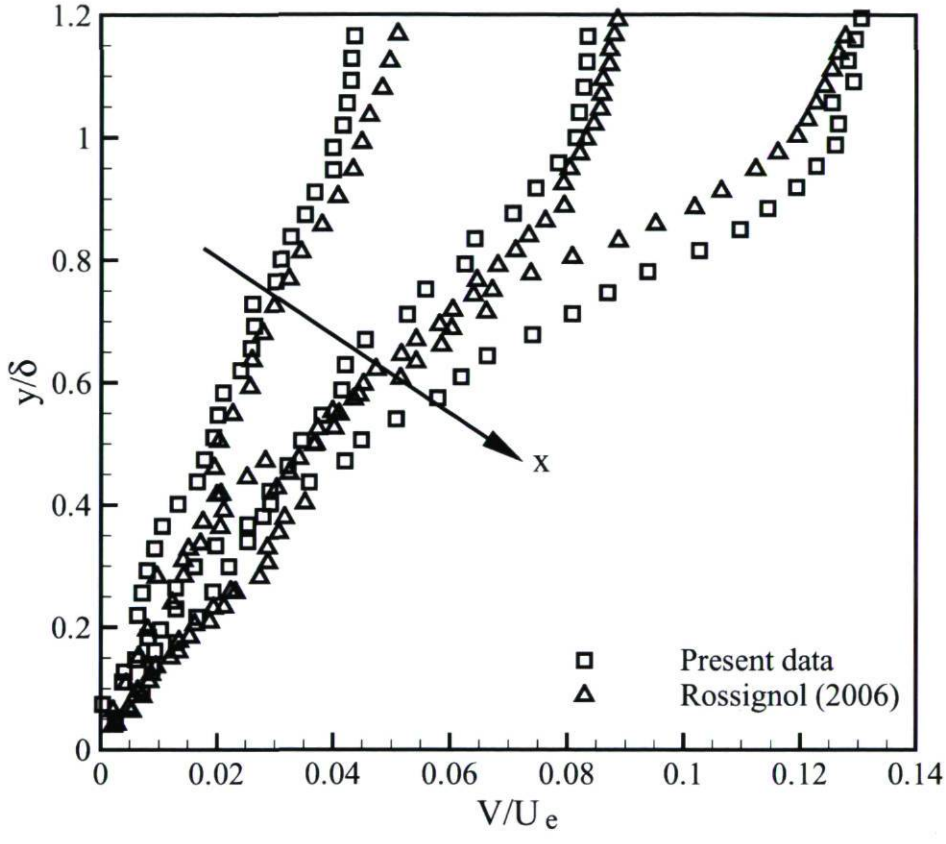

Figure 3.28: Evolution of V/U_e in streamwise direction.

equivalent basis of comparison to compare the different parameters and characteristics in such flows.

x (mm)	ZPG	1156	1392	1600
No. of realizations	-	1688	885	770
Δx, Δy	1.134	0.19	0.39	0.66
$\Delta x/\delta$, $\Delta y/\delta$	0.015	0.009	0.009	0.009
Δx^+, Δy^+	30	6.6	7.6	-
δ^+	2216	765.9	836.7	$\approx= 0$
Re_θ	7705	5329	8638	12095
β	0	8660	32200	∞
β_{ZS}	0	0.048	0.067	0.041
δ	83.1	21.0	42.8	73.7
δ^*	14.40	7.40	19.96	38.94
θ	10.35	4.12	7.50	10.34
H	1.39	2.03	2.86	3.65
U_e	11.4	22.1	19.2	18.2
U_{ZS}	1.97	7.78	8.95	9.63
U_τ	0.41	0.553	0.297	$\approx= 0$
U_τ/U_e	0.0360	0.0251	0.0152	-
U_τ/U_{zs}	0.2081	0.0711	0.0331	-
ν/U_τ	0.0375	0.0276	0.0515	-

Table 3.3: Vector spacings ($\Delta y = \Delta x$) and boundary layer parameters for the reference streamwise positions. Lengths in mm and velocities in ms^{-1}. In both studies vector spacing is half of interrogation window width (50% overlap).

The global parameters of the boundary layer are also affected by the pressure gradient as presented in table 3.3 and figure 3.25. The displacement thickness (δ^*) and momentum thickness (θ) increase significantly in the streamwise direction. These behaviours are similar to those occurring on the suction side of an airfoil with high angle of attack. The streamwise evolutions of Reynolds stresses scaled by U_{zs}^2 are shown in figure 3.29. These results also present strong dependency of Reynolds stresses to pressure gradient especially for $y/\delta \leq 0.6$. Furthermore, it is illustrated that the maximum Reynolds stresses occurs near the wall for ZPG TBL, while in the APG case they have a maximum peak around $y/\delta = 0.6$, and decrease towards the wall.

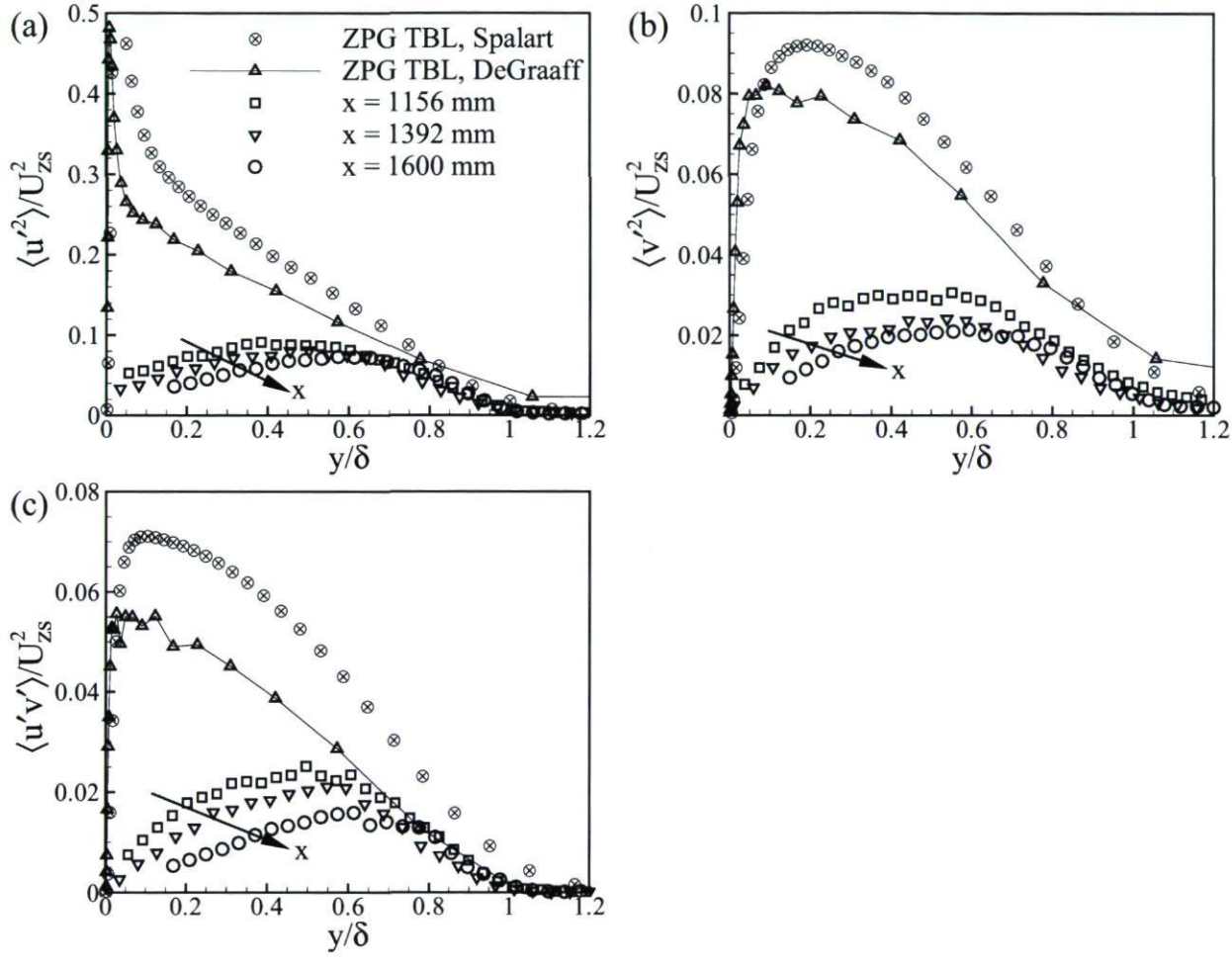

Figure 3.29: Profiles of a) $\langle u'^2\rangle/U_{zs}^2$, b) $\langle v'^2\rangle/U_{zs}^2$, c) $\langle u'v'\rangle/U_{zs}^2$ for all streamwise positions and ZPG TBL. ZPG TBL, Spalart is from Spalart (1988) at $R_\theta = 1410$ and ZPG TBL, DeGraaff is from experiments of De Graaff and Eaton (2000) at $R_\theta = 5160$. One data point out of 2 for clarity except for DeGraaff.

Chapter 4

Spanwise Vortices

4.1 Introduction

Although it is widely accepted that turbulent flows found in nature and in engineering applications are full of vortices, and that these vortices play important roles in these flows, a generally accepted mathematical definition of a vortex and the understanding of vortex dynamics (i.e. generation, evolution, interaction, and decay of vortical structures) are still lacking or incomplete. Indeed, defining a vortex is surprisingly a challenge for fluid dynamicists. A brief survey dealing with vortex identification methods and especially those that are based on λ_{ci} (the phrase "swirling strength" hereon refers to λ_{ci}) are presented. The statistical results of spanwise vortices characterization (i.e. population trends and spatial signatures of spanwise vortices) are also discussed in the present chapter.

4.2 Spatial Resolution

In the present study, since we were considering the outer region, we were careful to adjust the PIV mesh (scale factor) with the outer length scale δ. So we used an outer-scale-consistent grid and it is barely sufficient to resolve all the scales of interest in a fairly uniform manner. Moreover, the PIV grid spacing in outer units is changing rapidly even within a xy-plane. So, each streamwise position will have a different outer-scaled grid spacing, meaning that we are resolving different minimum length scales as we move downstream. This behaviour will have a dramatic effect on counting of vortices because

there would be no consistency in the range of scales resolved at different streamwise locations. The most important thing to consider is the consistency of scales being resolved. In this regard, the only way to quantitatively compare one streamwise position results with another would be to exactly replicate the spatial resolution in outer units as well as the exact methodology used to identify the vortices themselves. This latter point is also extremely important because the absolute number and the size of vortices identified can also be dependent on the method used for identification and any threshold one must set to achieve that identification. With respect to the aforementioned, the various vortex parameters are studied statistically at certain x-positions having the same spatial resolution. In this way, the effect of Gaussian filter bandwidth on the size and swirling strenght of vortices is also the same at these streamwise positions. Table 3.3 shows the boundary layer parameters and number of realizations for these selected streamwise positions.

4.3 Vortex Identification

What is a vortex? A general accepted definition for a vortex is a spinning or any spiral motion with closed streamlines, but the consensus on the generic definition of a vortex does not exist. For a vortex identification, the importance of a rational definition of a vortex can not be overemphasized. Vorticity has traditionally been used to detect vortices, but it has been recently emphasized by many authors (i.e. Jeong and Hussain (1995); Kida and Miura (1998); Cucitore et al. (1999)) that vorticity is not suitable for the identification of a vortex as it cannot distinguish between pure shearing motions and the actual swirling motion of a vortex. This is why an accurate vortex extraction method is required to identify and track the vortical structures. Various tools and algorithms have been developed and proposed by many investigators for the identification of vortices. The traditional technique employs the iso-surface of vorticity magnitude (Kim et al., 1987). Local methods were developed recently where according to a criterion based on the point values, each point can be classified as inside or outside a vortex. The most widely used local methods for vortex identification are based on the kinematics implied by the velocity gradient tensor, $\nabla \boldsymbol{u}$, thereby making them Galilean invariant. Depending on the method, the local criteria is based on the variable λ_2 (Jeong and Hussain, 1995), Δ (Perry et al., 1990), Q (Hunt et al., 1988) and λ_{ci} (Zhou et al., 1999).

Perry et al. (1990) used the regions of complex eigenvalues of the velocity gradient tensor for vortex identification. Zhou et al. (1999) followed the work of Perry et al. (1990) in their general classification of the three-dimensional velocity field around a

critical point. Zhou and co-workers have used the iso-surfaces of the imaginary part of the complex eigenvalue of the local velocity gradient tensor (λ_{ci}) to visualize vortices in a turbulent channel flow. The advantages of vortex identification via λ_{ci} or Q or λ_2 or Δ also are

1. Since the iso-surfaces of the imaginary part of the eigenvalues contain only the local velocity with circular or spiralling streamline, choosing a proper frame of reference for swirling strength is not necessary, while it is necessary for Galilean decomposition. In other words, vortex identification via λ_{ci}, Q, λ_2, Δ is Galilean invariant.
2. These methods automatically eliminates regions having vorticity but no local spiralling motion, such as shear layers, while it is the most important challenge in the traditional technique that employs the iso-surface of vorticity magnitude.

In the present study, we detected and investigated the vortices using the local criteria based on λ_{ci} which was proposed by Zhou et al. (1999). The mathematical and physical meaning of λ_{ci} is presented in appendix B.

Since the swirling strength is defined as the imaginary part of the complex eigenvalue of the local velocity-gradient tensor; it does not indicate the sense of the rotation. So, it is signed here according to the sign of the spanwise vorticity component as follows

$$\lambda_{ci} = \frac{\omega_z}{|\omega_z|}\lambda_{ci} \tag{4.1}$$

where ω_z is the instantaneous fluctuating spanwise vorticity. The λ_{ci} has therefore a negative sign for prograde vortices (spanwise vortices with rotation in the same sense as the mean circulation). The λ_{ci} with positive sign are retrograde vortices (spanwise vortices with rotation in the opposite sense compared to the mean circulation).

The calculated swirling strength is contaminated by noise as it is calculated based on the velocity gradient tensor. To remove noise from the instantaneous swirling strength fields and to identify the boundaries of individual vortices, three thresholds on λ_{ci} were used. These thresholds are defined based on i) the root-mean-square value of the λ_{ci}, ii) maximum value of the $|\lambda_{ci}|$ within each instantaneous field, iii) the number of mesh containing the λ_{ci}.

First, let us introduce the threshold based on the root-mean-square value of the λ_{ci}. This is called the main threshold because most of the noises are eliminated by

applying this threshold. Wu and Christensen (2006) proposed this threshold because they believed that the selection of a universal λ_{ci} threshold would be possible as Q and λ_{ci} yield comparable vortex identification results (Chakraborty et al., 2005). Although, from theoretical grounds, this threshold can be chosen to be zero, the surface with some threshold appears significantly smoother, allowing easy interpretation of vortices. Since the λ_{ci} is non-zero only within vortices and commonly zero elsewhere, the mean λ_{ci} is significantly smaller than its root-mean-square. Wu and Christensen (2006) proposed λ_{rms} as a representative of the characteristic magnitude of λ_{ci} and they concluded that λ_{rms} is a good scale for the magnitude of the swirling strength at a given (x,y) location. Hence they defined a normalized λ_{ci} by λ_{rms} as follows

$$\tilde{\lambda}_{ci} = \frac{\lambda_{ci}}{\lambda_{rms}} \tag{4.2}$$

where λ_{rms} is the local root-mean-square value of λ_{ci} computed from the ensemble of all instantaneous fields (including zero-values).

Since the flow parameters vary considerably in x-direction, λ_{rms} is calculated at each point of the velocity field. Figures 4.1-a, b and c present probability density functions (pdf) of $\tilde{\lambda}_{ci}$, when no threshold is applied, at the three streamwise stations and at several wall-normal locations in the region $0.2 \leq y/\delta \leq 0.8$, while figures 4.1-d, e and f present the same pdfs except the zero probability ($\lambda = 0$ events) is excluded from the samples. The probability of $\lambda_{ci} = 0$ events is extremely high for all positions. Indeed, most of the surface of the flow fields does not contain swirling motions as mentioned before. Similar pdfs of $\tilde{\lambda}_{ci}$ were reported by Wu and Christensen (2006) for turbulent channel flow and ZPG turbulent boundary layer at different Reynolds numbers. Comparing these pdfs with the pdfs of Wu and Christensen (2006), they turn out to be narrower in our case (smaller $\tilde{\lambda}_{ci}$). It may be partly because of the Gaussian filter and spatial resolution. Since smoothing the velocity field is done by applying the Gaussian filter; the swirling strength is also affected by it. Indeed the value of λ_{ci} is underestimated by applying a filter. Moreover the spatial resolution in the study of Wu and Christensen (2006) is higher than the one used in the present study ($\Delta x/\delta$, $\Delta y/\delta = 0.005$ vs. $\Delta x/\delta = 0.009$ for the present study). The $\tilde{\lambda}_{ci}$ is affected by spatial resolution and the $\tilde{\lambda}_{ci}$ increases when width of the interrogation window decreases (see section 1.5). So the $\tilde{\lambda}_{ci}$ is more underestimated for the present study compared to the study of Wu and Christensen (2006), because of the effect of the width of the interrogation window.

Wu and Christensen (2006) proposed that the probability density function of the $\tilde{\lambda}_{ci}$ displays both Reynolds-number and flow insensitivity for canonical flows. Figure 4.2 shows that the pdfs of $\tilde{\lambda}_{ci}$ are almost identical at the three streamwise positions.

The fact that the shape and the probability values of the pdfs remain unchanged is an astonishing result. It means that although the vortices might change in size and swirl intensity, the probability of occurrence of vortices and the distribution of the normalized swirling strength, including the distribution between prograde and retrograde swirl, are unaffected by the varying strong adverse pressure gradient conditions. Moreover, this is the case all the way up to detachment since the last streamwise station is the position of detachment of the boundary layer. The distribution characteristics of the vortices are therefore persistent flow properties in such a flow. Additionally, figure 4.1 illustrates the pdf of $\tilde{\lambda}_{ci}$ at several wall-normal locations in the region $0.2 < y/\delta < 0.8$ and confirms that this pdf does not vary significantly with y. Figure 4.3 presents wall-normal profiles of the ensemble average of $\tilde{\lambda}$ (see equation 4.7 in section 4.4) normalized by λ_{rms}. The ensemble average is carried out separately for the prograde and retrograde vortices, thus the two values we get on figure 4.3. The collapse of the profiles and nearly constant values of $\langle\tilde{\lambda}\rangle/\lambda_{rms}$ in figure 4.3 and the collapse of the pdfs at different wall-normal locations (figure 4.1) confirm that $\tilde{\lambda}_{ci}$ is a good scale for the magnitude of non-zero λ_{ci} (i.e. swirling strength of vortices) at a given x,y location; similar to the conclusion of Wu and Christensen (2006).

With respect to the aforementioned, the threshold value for $|\tilde{\lambda}_{ci}|$ was first chosen the same as that of Wu and Christensen (2006). They found that a threshold of $|\tilde{\lambda}_{ci}| \geq 1.5$ defined well the boundaries of the vortex cores while minimizing experimental noise. To explore the best value for $|\tilde{\lambda}_{ci}|$, the iso-contours of swirling strength and associated Galilean frame of instantaneous velocity field are examined. If the swirling strength patches and velocity signatures in moving frame of reference show acceptable feature the appropriate value of $|\tilde{\lambda}_{ci}|$ is employed, otherwise we settle on a slightly larger or smaller threshold (by about 3%). It means the acquired swirling strength clusters, after applying the thresholds, are superimposed in different Galilean frames. This let us to see both the velocity patterns and the λ_{ci} clusters simultaneously. So, if each detected λ_{ci} patch corresponds to a vortex which can be revealed in moving frame of reference, the $|\tilde{\lambda}_{ci}|$ value is chosen appropriately. The final threshold value for $|\tilde{\lambda}_{ci}|$ is 1.45 for the present study. Figure 4.4 presents pdf of $\tilde{\lambda}_{ci}$, when threshold is applied, at the three streamwise stations and at several wall-normal locations in the region $0.2 \leq y/\delta \leq 0.8$.

$$|\lambda_{ci}(x,y)| \geq 1.45\lambda_{rms}(x,y) \tag{4.3}$$

Investigating many instantaneous fields show that the $\tilde{\lambda}_{ci}$ works very well within the boundary layer, but does not work for the potential flow region. Since, there is no shearing in the potential flow vortices should not also exist in such flow. It means, the swirling strength should be also zero within this region. Appearing the λ_{ci} clusters

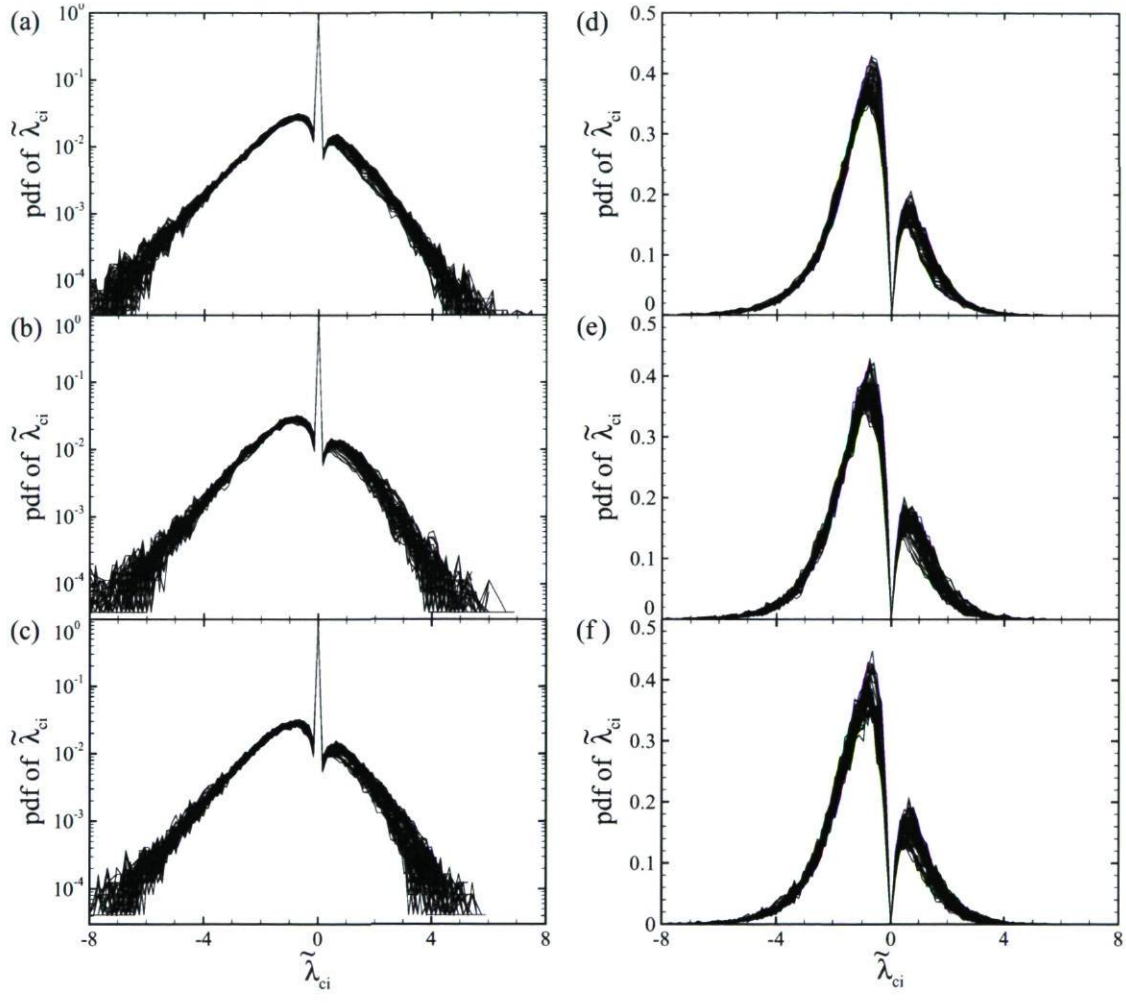

Figure 4.1: Probability density functions of $\tilde{\lambda}_{ci}$ for $0.2 \leq y/\delta \leq 0.8$ in regions a) $1128 - 1185$ mm, b) $x = 1285 - 1397$ mm, c) $x = 1509 - 1680$ mm. (d-f) correspond to a-c in respective order but by excluding the zero values from the samples.

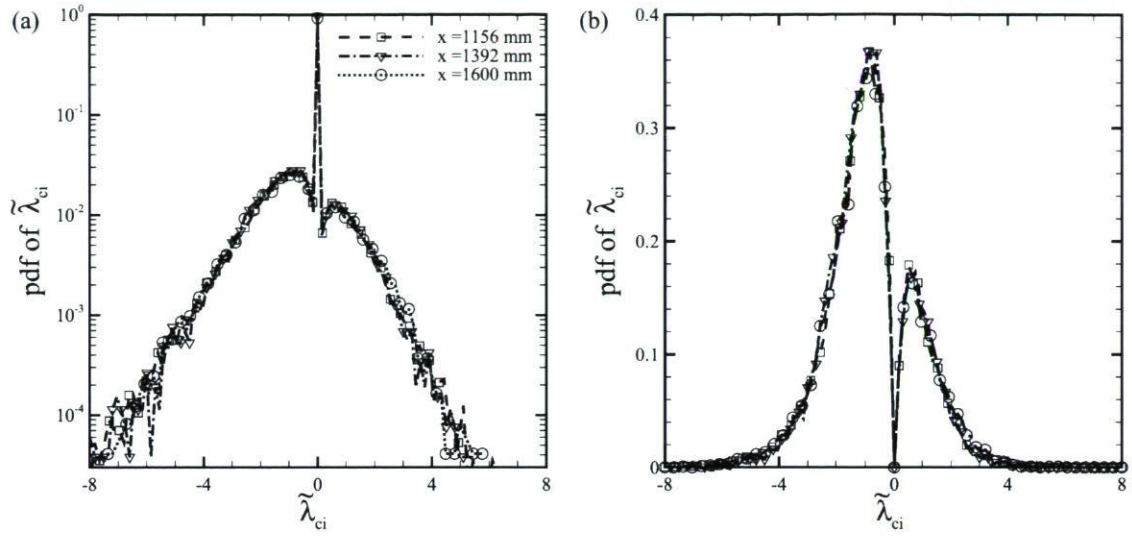

Figure 4.2: Probability density functions of $\tilde{\lambda}_{ci}$ at $y/\delta = 0.5$ for all streamwise positions. a) including the zero values in the samples, b) excluding the zero values from the samples.

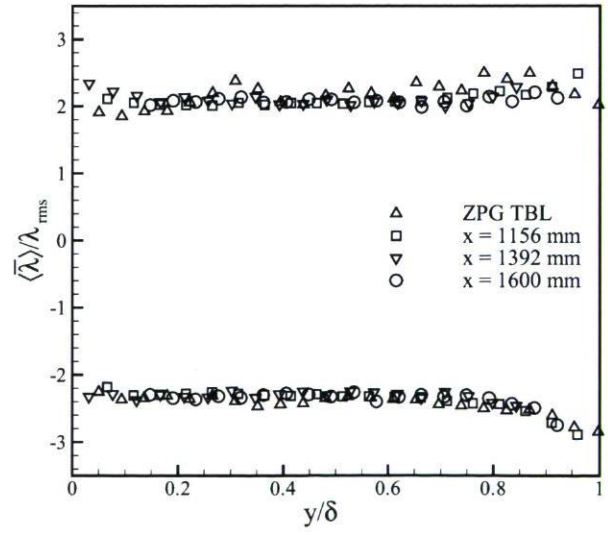

Figure 4.3: Normalized ensemble average of swirl intensity by λ_{rms}, (one data point out of 5 for clarity).

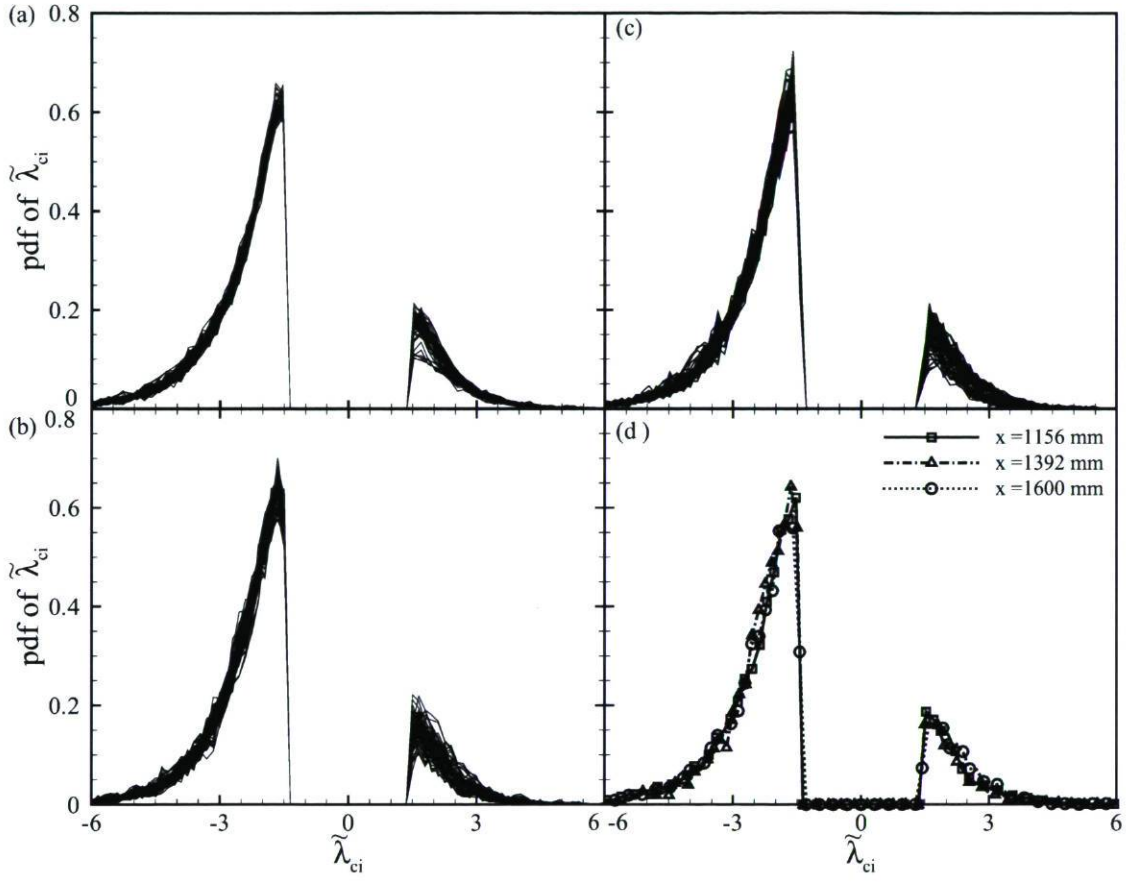

Figure 4.4: Probability density functions of $\tilde{\lambda}_{ci}$ when the thresholds are applied, (a-c) for $0.2 \leq y/\delta \leq 0.8$ at $x = 1156$ mm, $x = 1392$ mm and $x = 1600$ mm respectively, d) at $y/\delta = 0.5$ for the three streamwise positions.

with non-zero values across this region can be caused by the noises in the velocity fields. It is worth noting that these iso-regions of swirling strength have lower intensity compared to the λ_{ci} clusters within the boundary layer, that turbulence activity is high, as expected. Although, the λ_{ci} value is low within the potential flow region, but the $\tilde{\lambda}_{ci}$ value is also low in this region as it is calculated locally. Therefore, the criteria of $\tilde{\lambda}_{ci} \geq 1.45$ does not work properly for the potential flow region. Since it does not work well for this region where vortices occur, the threshold 10% of the maximum value of swirling strength within the instantaneous field is applied as follows

$$\frac{|\lambda_{ci}|}{\Lambda_{max}} \geq 0.1 \tag{4.4}$$

where Λ_{max} is the maximum of $|\lambda_{ci}|$ in the instantaneous field.

The size of the smallest resolvable vortex is inherently limited by the width of the interrogation window of the PIV measurements. Indeed, the grid spacing in the velocity field defines the size of the smallest vortex that one can resolve. As such, the λ_{ci} patches with fewer than two meshes across their span in both x and y (4 grid points of surface) satisfying $\tilde{\lambda}_{ci} \geq 1.45$ are not considered vortices due to insufficient spatial resolution. Hence, if clusters of λ_{ci} contain less than four grid points, they are considered as noise and removed from the field.

The applied thresholds on swirling strength can be summarized by equations 4.5 and 4.6.

$$\lambda^{p}_{ci}(x,y) = \begin{cases} \lambda_{ci}(x,y) & \text{if} \begin{cases} \lambda_{ci}(x,y) \leq -1.45\lambda_{rms}(x,y) & \text{and} \\ \lambda_{ci}(x,y) \leq 0.1\Lambda_{min} & \text{and} \\ N_\lambda \geq 4 \end{cases} \\ 0 & \text{otherwise} \end{cases} \tag{4.5}$$

$$\lambda^{r}_{ci}(x,y) = \begin{cases} \lambda_{ci}(x,y) & \text{if} \begin{cases} \lambda_{ci}(x,y) \geq 1.45\lambda_{rms}(x,y) & \text{and} \\ \lambda_{ci}(x,y) \geq 0.1\Lambda_{max} & \text{and} \\ N_\lambda \geq 4 \end{cases} \\ 0 & \text{otherwise} \end{cases} \tag{4.6}$$

where $\lambda^{p}_{ci}(x,y)$ and $\lambda^{r}_{ci}(x,y)$ represent the prograde ($\lambda_{ci} < 0$) and retrograde ($\lambda_{ci} > 0$) vortices respectively, Λ_{min} and Λ_{max} are the minimum and maximum of λ_{ci} in each instantaneous field and N_λ is the number of grid points for each patch.

Figure 4.5 shows an example of swirling strength detected via the mentioned technique. Figure 4.5-a illustrates the iso-regions of λ_{ci} before applying the thresholds. It can be seen that the λ_{ci} field is contaminated with noise associated with differentiation of the PIV velocity data. This noise is removed from the λ_{ci} field by the thresholds as illustrated in figure 4.5-b.

Figure 4.6 presents an example of vortex identification via swirling strength using an instantaneous velocity field in the xy-plane at the second streamwise position. Instantaneous velocity vectors are viewed in a frame-of-reference convecting at $u_c = 0.5U_e$ and $v_c = 0.6V_e$ in figure 4.6-a. Since a constant convection velocity was used, as opposed to a local one adjusted for each vortex, this Galilean decomposition reveals only those spanwise vortices convecting at this speed. Contours of instantaneous λ_{ci} are also superimposed in the background of figure 4.6-a. When the local velocities at the positions of the local maxima of λ_{ci} are used as the convection velocities, as in figure 4.6-b orbital streamlines become visible over these patches of swirl and the centre of these vortices coincide with the local maxima of the swirling strength. Figure 4.6-b confirms that all regions of non-zero λ_{ci} are associated with circular streamline patterns. Figure 4.6-b also highlights the large populations of prograde and retrograde spanwise vortices that can exist in APG turbulent boundary layer as 20 retrograde and 35 prograde vortices are identified in this realization. In addition, although these cores represent spanwise vortices in the xy-plane, their orientations relative to the measurement plane cannot be determined from the two-dimensional fields. It is worth mentioning that if the inclination of vortices with respect to the xy-plane is small, λ_{ci} does a poor job at identifying them.

4.4 Spanwise Vortex Parameters

Before discussing the various flow parameters, it is useful to explain the different steps used to obtain vortices parameters. Once the spanwise vortices have been detected using the local method based on λ_{ci} value and the thresholds have also been applied, one needs to develop an automated procedure to acquire the different parameters of spanwise vortices. The details of this automated procedure to identify the vortex core characteristics are described below. It is worth mentioning that what are truly measured are not spanwise vortices per say but rather turbulence vortices with a spanwise vorticity component. In other words, the presented spanwise vortices here are the cross sections of three dimensional turbulence structures in streamwise/wall-normal plane.

Step 1: All points from a cluster of swirling strength are marked with the same

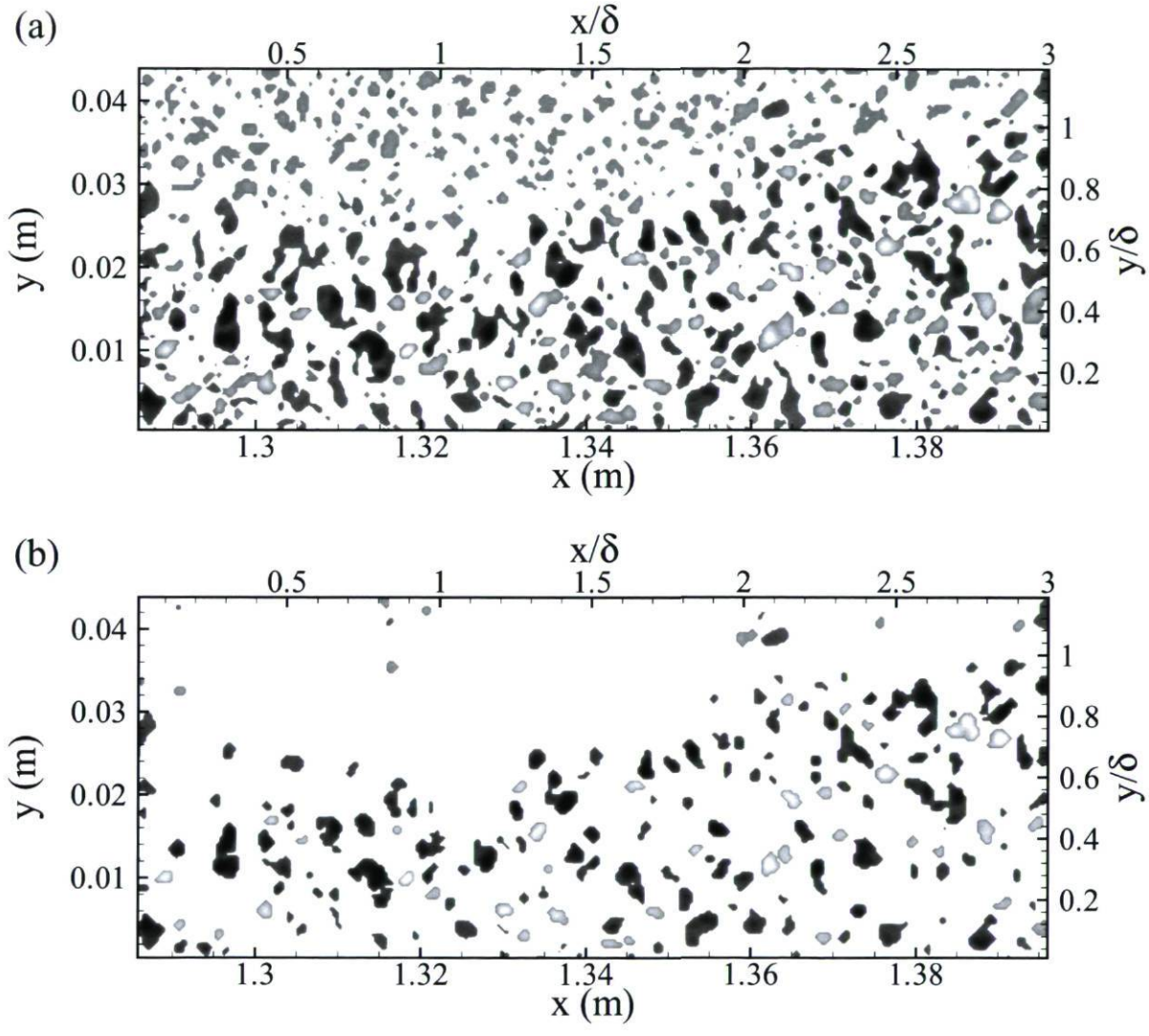

Figure 4.5: Example of swirling strength in an instantaneous, two-dimensional velocity field at second streamwise position ($x = 1285 - 1397$ mm): a) swirling strength iso-regions within the instantaneous field, b) as figure (a), but the thresholds are applied on λ_{ci}. The dark areas represent $\lambda_{ci} < 0$ and the light areas $\lambda_{ci} > 0$.

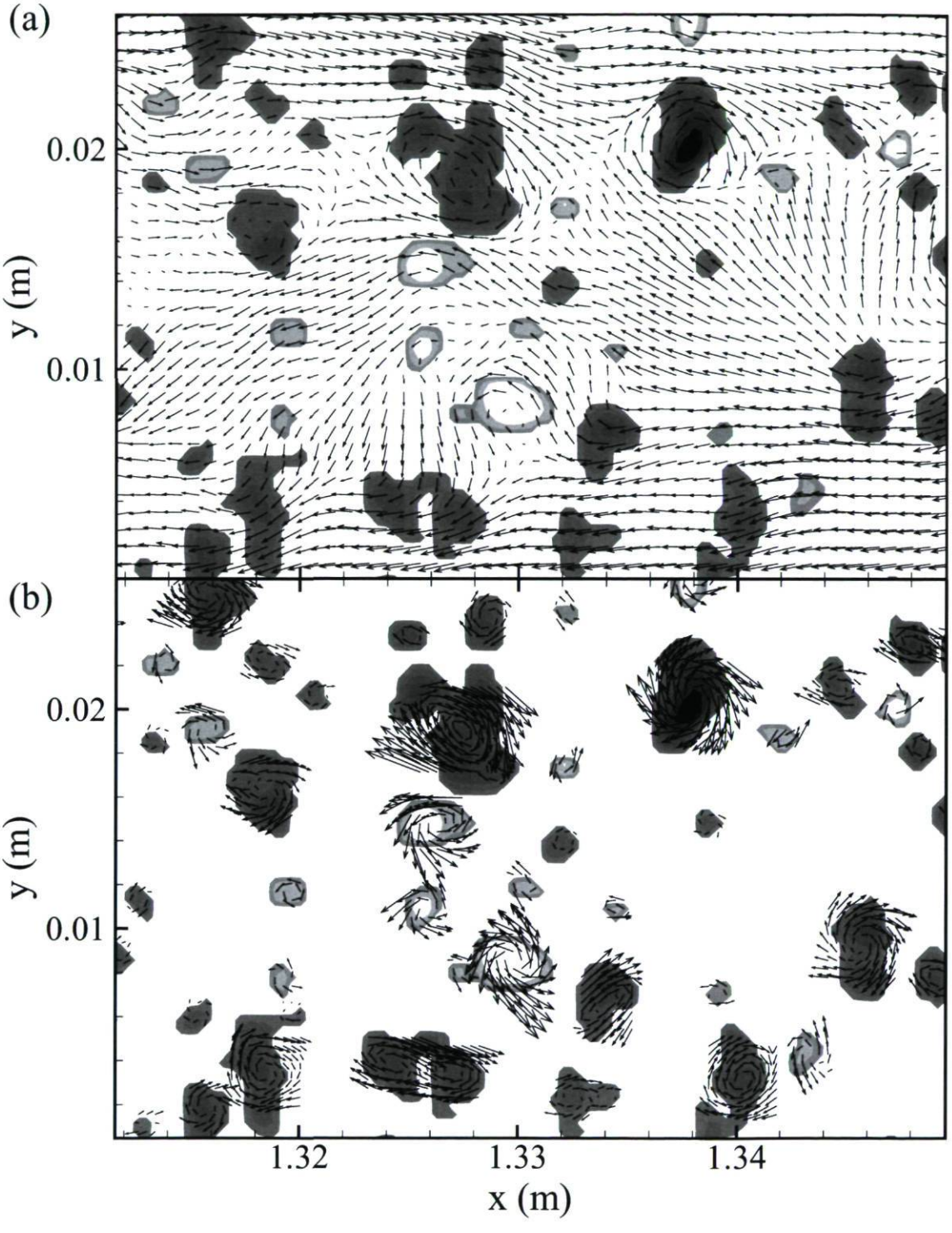

Figure 4.6: Example of vortex identification and extraction in an instantaneous, two-dimensional PIV velocity field in region $x = 1285 - 1397$ mm: (a) Galilean decomposition of the instantaneous velocity field with $u_c = 0.5U_e$ and $v_c = 0.6V_e$ with contours of instantaneous λ_{ci} in the background (one vector out of 4 for clarity); (b) localized Galilean decomposition of vortices identified using λ_{ci}. Retrograde spanwise vortices are presented with light patches and prograde vortices with dark patches.

number. It means all the grid points with non-zero value of λ_{ci} have a unique number associated with a spanwise vortex at that position. Scanning the vortices begins at the left/bottom corner of each instantaneous swirling strength field and continues in x-direction line by line. So, the first number corresponds to a vortex at left/bottom corner of λ_{ci} field. The total number of vortices is known in each instantaneous field as it is the maximum number within the field. The numbered vortices are useful tool to do the statistics on vortices as each vortex can be identified by its corresponding number.

Step 2: The arithmetic average of swirling strength in each vortex ($\bar{\lambda}$, the phrase "swirl intensity" hereon refers to $\bar{\lambda}$) is calculated as follows

$$\bar{\lambda} = \frac{\sum_{j=1}^{N_\lambda} \lambda_{ci,j}}{N_\lambda} \tag{4.7}$$

where $\lambda_{ci,j}$ is the λ_{ci} value at j^{th} point of swirling strength cluster corresponded to a spanwise vortex and N_λ is the number of grid points with non-zero value of λ_{ci} in the spanwise vortex.

Figure 4.7 shows the pdfs of $\bar{\lambda}$ scaled by λ_{rms} for both prograde and retrograde vortices. This figure confirms that $\bar{\lambda}/\lambda_{rms}$ is also insensitive to pressure gradient like the pdfs of $\lambda_{ci}/\lambda_{rms}$. It is worth noting that each vortex is accounted only once in the present pdfs, whilst all the points corresponded to a vortex within the bounded box are accounted in figures 4.1, 4.2 and 4.4. So the pdfs in this latter figure are not affected by the size of vortices, whereas the pdfs shown in figures 4.1, 4.2 and 4.4 are affected by the size of vortices.

Step 3: Calculating the effective diameter of vortices has also been done using the numerated λ_{ci} patches. The effective diameter is the diameter of a circle with an equivalent area corresponding to the λ_{ci} patch (figure 4.8). This calculation is done as follows

$$D = \sqrt{\frac{4N_\lambda dA}{\pi}} \tag{4.8}$$

where D is the effective diameter and dA is the area of a single mesh. Since the mesh width $\Delta x/\delta = 0.009$ for the x-positions is considered and only clusters with at least four continuous points with non-zero λ_{ci} were considered to form a vortex core, this study is restricted to vortical structures with an effective diameter exceeding approximately 0.02δ. It is worth noting that the effective diameter is overestimated because the velocity

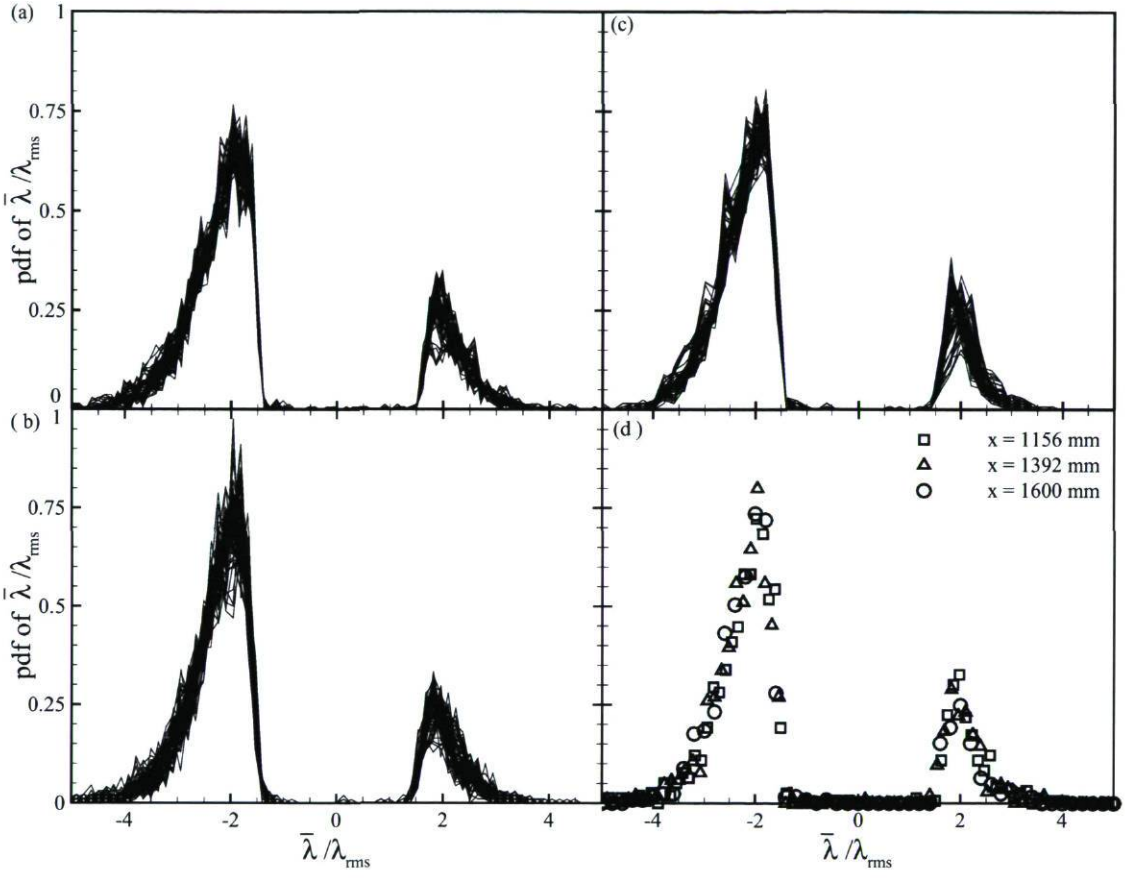

Figure 4.7: Probability density functions of $\bar{\lambda}$ normalized by λ_{rms} when the thresholds are applied, (a-c) for $0.2 \leq y/\delta \leq 0.8$ at $x = 1156$ mm, $x = 1392$ mm and $x = 1600$ mm respectively, d) at $y/\delta = 0.5$ for the three streamwise positions.

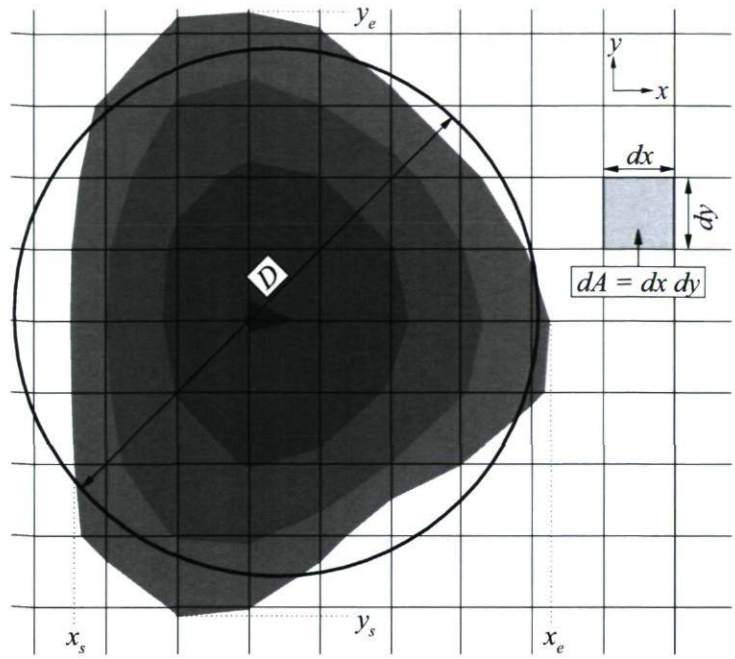

Figure 4.8: Iso-region of λ_{ci} consisting of a single two-dimensional spanwise vortex core.

vector fields are smoothed by Gaussian filter (more details in section 4.5).

Step 4: Next, the centers of vortices are determined. To determine the center positions of spanwise vortices, we refer to the isolated regions with $\lambda_{ci} \neq 0$. The x and y coordinates consistent with the center of a vortex are calculated as follows

$$\begin{aligned} x_c &= \tfrac{x_s+x_e}{2} \\ y_c &= \tfrac{y_s+y_e}{2} \end{aligned} \tag{4.9}$$

where x_c and y_c are the coordinates of vortex center, x_s and x_e are the first and last point of the λ_{ci} patch in x-direction and y_s and y_e are the first and last point of the λ_{ci} patch in y-direction (see figure 4.8). The x_s, x_e, y_s and y_e can be easily obtained using the numerated of isolated regions with $\lambda_{ci} \neq 0$. Once the coordinates of vortex centers are obtained, they are saved in the ASCII files for future applications.

Step 5: The convection velocity of vortex structures (u_c, v_c) is defined as the mean traveling velocity of vortex cores. When a vortex core is viewed in an appropriate moving frame of reference, it appears as a circular streamline pattern. Since the velocity is theoretically zero at the center of the vortex core; it should be also zero at the center of vortex core in the experimental results when viewed in a proper convecting frame. Hence, the convection velocity of individual structures is the instantaneous velocity at

the center position of an isolated region with $\lambda_{ci} \neq 0$ as follows

$$u_c = u(x_c, y_c)$$
$$u_c = v(x_c, y_c) \tag{4.10}$$

where u and v are the streamwise and wall-normal components of the instantaneous velocity. So u_c and v_c are known when x_c and y_c are determined.

Step 6: Probability distributions, fractions of resolved prograde and retrograde spanwise vortices, population densities and ensemble average of different parameters of spanwise vortices are studied using the parameters obtained in steps 1 to 5.

4.5 Effect of Spatial Resolution and Filter on Vortex Parameters

Before discussing and delving into analyzing the vortex parameters like swirl intensity and diameter of vortices, it is useful to present the effect of filter, mesh width and interrogation window width (spatial resolution) on these parameters. It is important to mention that they are the only parameters significantly affected by spatial resolution. In both the present work and the ZPG turbulent boundary layer database of Adrian et al. (2000), the mesh width is half of the interrogation window width since 50% overlap was used within the correlation process.

The effective diameters of vortices are sensitive to **"interrogation window width (PIV resolution)"** , **"mesh width"** and **"size of filter window"**. It means the D could be changed and affected by any small or large variation of PIV resolution and size of filter window. The hypothetical distribution of vortices diameter can be divided schematically in three parts as shown in figure 4.9.

1. The first part scales with η (Kolmogorov length scale) and is sensitive to $\Delta x/\eta$, σ/η, where Δx and σ are the mesh width and standard deviation of Gaussian filter respectively.
2. In the intermediate region the vortices may be scaled with η or δ.
3. The third part scales with probably δ and is sensitive to σ/δ and variation of $\Delta x/\delta$ in each streamwise position.

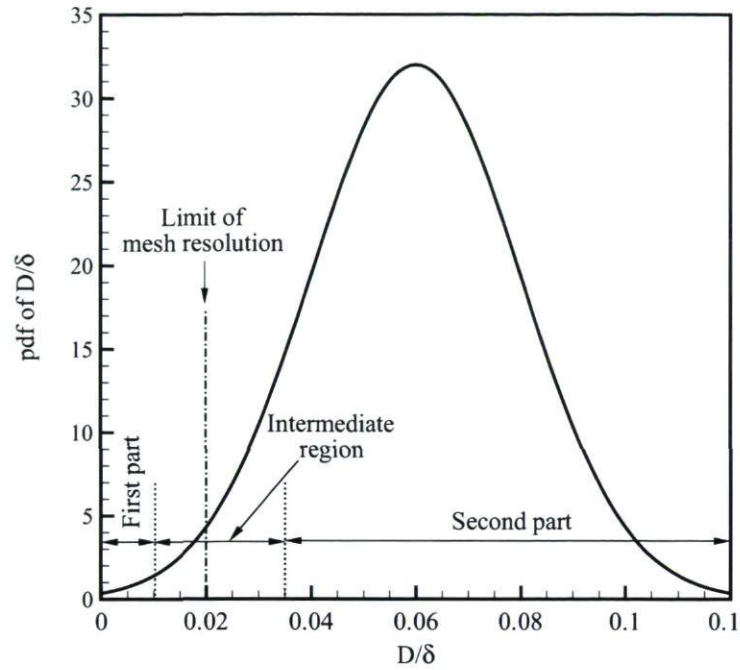

Figure 4.9: Schematic of the probability density function of the vortex diameter.

This sensitivity of D to the mentioned parameters is shown in figure 4.10. Figure 4.10-a illustrates that the diameter of vortices increases when the size of filter window increases. With respect to the definition of swirling strength, the bigger size of filter window causes more smoothing within the velocity fields and therefore causes more grid points to contain non-zero value of λ_{ci} in each patch. On the other hand, the boundary layer coarsens significantly within the adverse pressure gradient, and it is worth noting that the PIV resolution is scaled by δ approximately in the present study and it is not scaled by η. Therefore, the PIV resolution vs. by δ varies about 25% to 30% in each PIV measurement plane. Figure 4.10-b presents the pdf of vortices diameter at the start point ($x = 1515$ mm) and the last point ($x = 1667$ mm) of instantaneous swirling strength field in region $x = 1509 - 1680$ mm, where the $\Delta x/\delta$ decreases by about 30% ($\Delta x/\delta = 0.011$ at $x = 1515$ mm and $\Delta x/\delta = 0.008$ at $x = 1667$). It is because, the mesh grid (PIV resolution) is uniform and the δ increases in x-direction, so the spatial resolution ($\Delta x/\delta$) decreases. The figure 4.10-b shows that D/δ decreases when the $\Delta x/\delta$ decreases. In this case, the cut-off of the vortices by the λ_{ci} threshold does not have the same minimum limit value, and this minimum limit value decreases when the $\Delta x/\delta$ decreases (see figure 4.10-b). Indeed, the smaller vortices can be detected by better spatial resolution which is the case at the last part of instantaneous swirling strength field. Based on these aforementioned, comparing the D/δ should be done with the same conditions (the same filter size and the same spatial resolution).

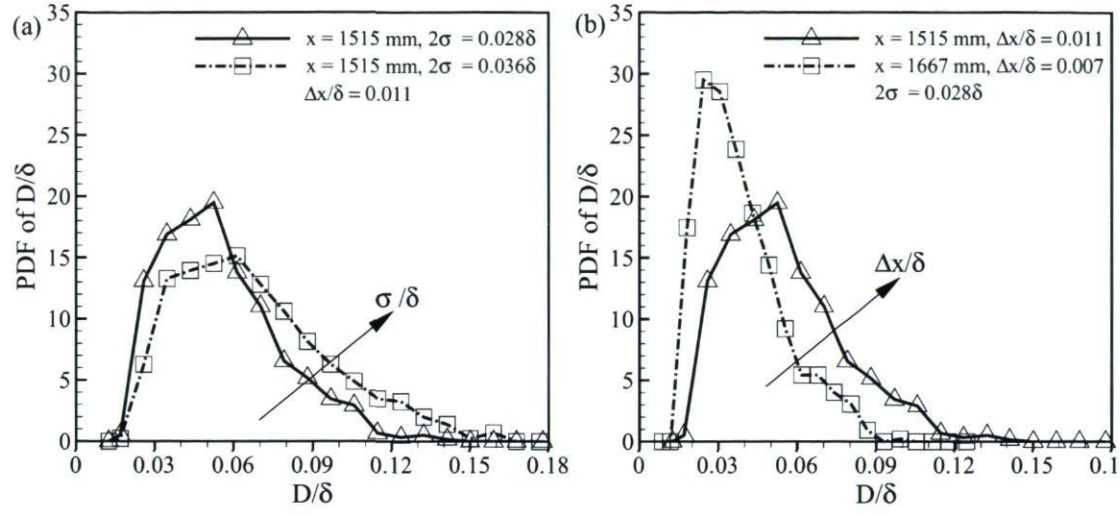

Figure 4.10: Probability density functions of D/δ for spanwise vortices at $y/\delta = 0.5$ in region $x = 1509 - 1680$ mm: a) at the same streamwise position (same spatial resolution) and different size of filter window (2σ), b) the same size of filter window and different streamwise positions for which the spatial resolution changes by about 30%.

Since the λ_{ci} is calculated based on the velocity gradient tensor, it is affected by changing the velocity gradients. The velocity fields are smoothed with a Gaussian filter as previously mentioned, and therefore the velocity gradients decrease. In this case, the λ_{ci} also decreases when the velocity gradients decrease. Indeed, the λ_{ci} is affected by filter and it is underestimated when a filter is applied on the velocity fields. The deviation of the acquired λ_{ci} value from its real value increases, as the filter bandwidth increases.

To provide a better idea about the effect of **"interrogation window width (PIV resolution)"** , and **"mesh width"** on the vortices diameter and λ_{ci}, the ensemble average of these parameters are presented as a function of **"interrogation window width"** , and **"mesh width"** (see figures 4.11 and 4.12). First, it is useful to explain the method used for studying the effect of spatial resolution on the vortices diameter and swirling strength. In order to study the effect of mesh width and interrogation window width, each velocity field is divided into many subregions (14 subregions in the case of spanwise vortices and 6 subregions in the case of hairpin vortices, the detection of hairpin vortices is discussed in section 5.2.1) in the streamwise direction. Although the ideal case is to calculate the ensemble average of D/δ and of $\bar{\lambda}$ at each x position as the spatial resolution is constant at each point in streamwise direction, but we have to include some x positions in each subregion to increase the accounted samples. Indeed, the lack of samples at each x position leads us to chose an interval with many

x positions. Since the sample numbers is high in the case of spanwise vortices, the width of subregions can be chosen small enough, whereas the subregions have to be wider for the hairpin case. The spanwise vortices with effective diameters greater than 4% of boundary layer thickness ($D/\delta \geq 0.04$) are compiled to study the effect of both mesh width and interrogation window width on the diameter and swirling strength. It is important to mention that a similar study (studying the effect of both mesh width and interrogation window width on $\bar{\lambda}$ and D/δ) was not done for the hairpin heads as there is not information for $\bar{\lambda}$ and D/δ based on both mesh width and interrogation window width in the acquired database of hairpins. Additionally, a large number of samples resulted in a well converged statistical result for the case of spanwise vortices. The number of spanwise vortices is about 70000 (in 1000 fields) while it is only 600 for the hairpin heads (in 50 fields). These typical numbers indicate that around 17% of spanwise vortices with $D/\delta \geq 0.04$ are hairpins inside hairpin packets. The rest of spanwise vortices could be interpreted as other structures or individual hairpin vortices.

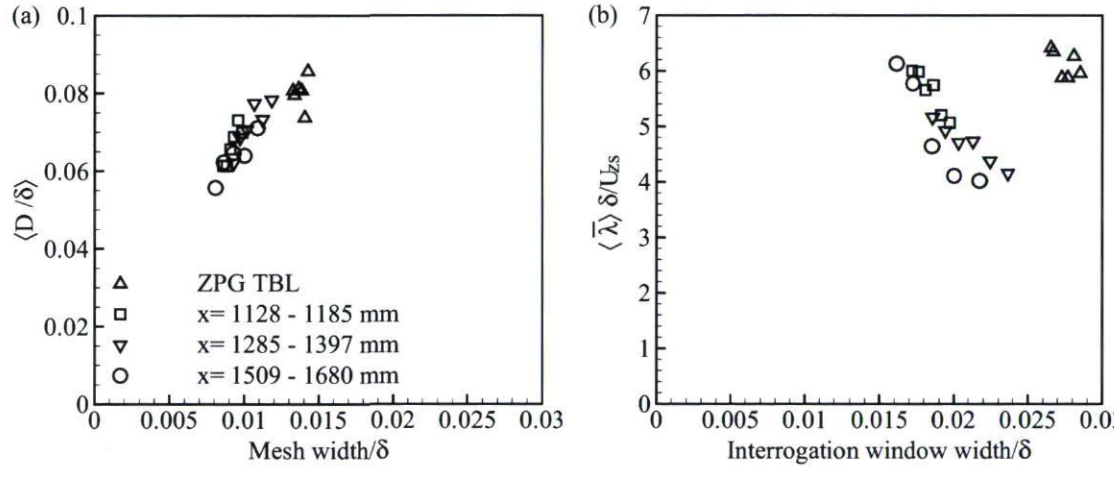

Figure 4.11: Ensemble average of hairpin head parameters in outer units for $y/\delta > 0.2$: a) average effective diameter as a function of mesh width. b) average of $\bar{\lambda}$ as a function of interrogation window width.

The ensemble average of vortices diameter and of $\bar{\lambda}$ are calculated in each subregion. The spatial resolution is roughly the same in these subregions, while it varies by about 30% from the first subregion to the last subregion in one plane as previously mentioned. Since the spatial resolution varies in different subregions, the effect of spatial resolution on the ensemble average of vortices diameter and of $\bar{\lambda}$ should be seen.

Figure 4.11-a presents the ensemble average of diameter of hairpin heads in outer unit as a function of mesh width. Each symbol represents $\langle D/\delta \rangle$ in one subregion.

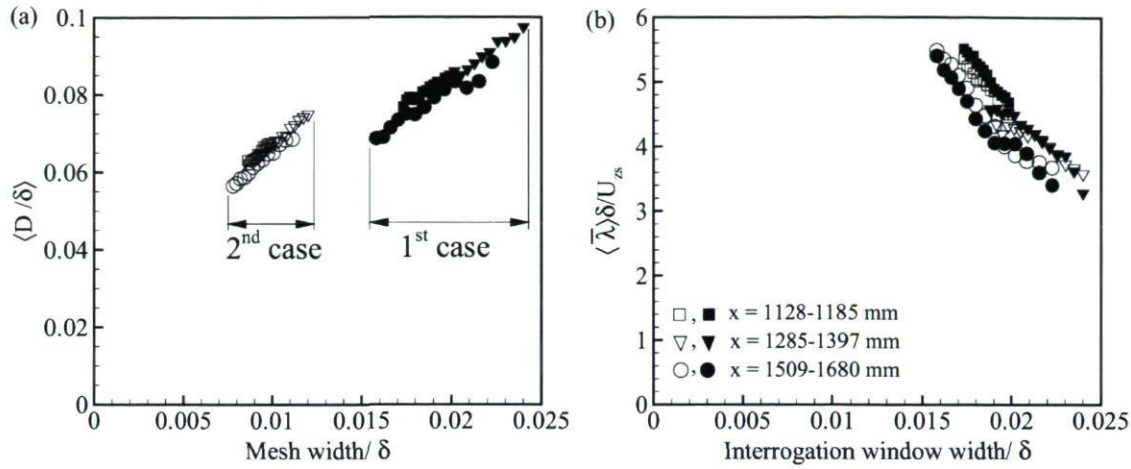

Figure 4.12: Ensemble average of spanwise prograde cores (with effective diameter greater than 0.04δ) parameters in outer units: a) average effective diameter as a function of mesh width. b) average of $\bar{\lambda}$ as a function of interrogation window width. Empty symbols correspond to the results obtained using a mesh width half the interrogation window width (50% overlap), and filled symbols correspond to the results obtained using mesh width and interrogation window width of same size (no overlap). One data point out of 2 for clarity.

This figure illustrates that the effective diameter of hairpin heads is a function of mesh width. Figure 4.12-a presents the ensemble average diameter of spanwise vortices with $D > 0.04\delta$ in outer unit as a function of mesh width. The diameter of vortices is calculated based on two different mesh widths while the interrogation window width is the same in both cases. In the first case there is no overlap zone during the adaptive correlation of PIV images, while 50% of overlap is applied in the second case. This figure illustrates that the effective diameter of vortices is affected by both the mesh width, the interrogation window width and the filter bandwidth. The variation of ensemble average of diameter in figures 4.11-a and 4.12-a within different subregions, at each streamwise position, is only because of the effect of mesh width and of interrogation window width. The second principle contribution is to interpret the effect of mesh width and of interrogation window width on D/δ separately. Is the vortex diameter a function of mesh width, of interrogation window width or both of them? To answer this question, figure 4.12-a provides a clear idea to interpret the effect of these widths. If we suppose that the presented curve for the first case decreases linearly, then this curve passes under the curve for the second case when the mesh width is 50% smaller. It means smaller diameters are obtained when D/δ is calculated based on interrogation window width variations compared to the acquired results using mesh width variations. So, it seems that the effective diameter of vortices is a function of both mesh width and of interrogation window width.

Since $\langle D/\delta \rangle$ decreases when the mesh width decreases, the diameter of vortices is overestimated for both the present study and ZPG TBL. The effective diameter of hairpin heads are less overestimated in the present study compared to ZPG TBL. It is hard to estimate the deviation of calculated $\langle D/\delta \rangle$ from the real diameter via the present results as we do not know the tendency when the mesh width tends to zero. It is worth recalling that the vortices decrease slightly in size, with respect to δ, between the first streamwise position and the last one (see section 4.6.3). In other words, the effective diameter of vortices in streamwise direction does not follow the boundary layer thickness coarsening in the adverse pressure gradient region and the increasing of vortex diameter is slower than boundary layer thickness. This effect is also seen in figures 4.11-a and 4.12-a. $\langle D/\delta \rangle$ for the last streamwise position is slightly lower comparing to other positions.

The swirl intensity for hairpin heads is presented as a function of interrogation window width in figure 4.11-b. $\langle \bar{\lambda} \rangle$ for spanwise vortices with $D > 0.04\delta$ is illustrated as a function of interrogation window width in figure 4.12-b. In this latter $\langle \bar{\lambda} \rangle$ is calculated using two different mesh sizes. In the first case there is no overlap for the interrogation zone during the correlations while 50% overlap for the interrogation zone is used during the correlations for the first case. Collapse of the symbols for both cases confirms that the swirl intensity is only a function of interrogation window width and $\langle \bar{\lambda} \rangle$ is independent of the mesh width. It is worth recalling that the swirling strength is calculated based on the velocity gradient tensor (see section 4.3). Since the velocity gradients can be changed by interrogation window width, $\langle \bar{\lambda} \rangle$ is also changed by interrogation window width. Figures 4.11-b and 4.12-b illustrate $\langle \bar{\lambda} \rangle$ increases when interrogation window width decreases. So $\langle \bar{\lambda} \rangle$ is underestimated for both the present study and ZPG TBL, because of the effect of the interrogation window width. $\langle \bar{\lambda} \rangle$ is more underestimated in the ZPG TBL compared to the present study since the spatial resolution is higher in the present study than the ZPG TBL. Once again, it is hard to estimate the deviation of the calculated $\langle \bar{\lambda} \rangle$ from the real swirl intensity via the present results as we do not know the tendency as the interrogation window width tends to zero.

Finally the effect of **"interrogation window width"** , **"mesh width"** and **"size of filter window"**on the vortices diameter and swirling strength can be summarized as follow.

- The $\langle D/\delta \rangle$ decreases when the interrogation window width and the mesh width decreases.
- The $\langle D/\delta \rangle$ increases when the filter bandwidth increases.
- The $\langle \bar{\lambda} \rangle$ increases as interrogation window width decreases and it is independent

to the mesh width.

- The $\langle\bar{\lambda}\rangle$ decreases as the filter bandwidth increases.

4.6 Statistical Analysis of Spanwise Vortices Data

At the onset of this study, the state of knowledge suggested that APG turbulent boundary layers contained many spanwise vortices. Several of prograde spanwise vortices are forward-leaning hairpin-shaped vortices and various mechanisms have been proposed for their formation and existence (see sections 2.2.2, and 5.2). In this study, λ_{ci} is used to identify vortex cores as previously discussed. The swirling strength isolates regions that have swirling motion about an axis aligned normal to the plane of measurements. Therefore, we are looking at vortices with a spanwise component of vorticity.

4.6.1 Probability Trend

Vortex Probability and Characteristics of Vortices

The characteristics and probability trends of the spanwise vortices are now investigated in a manner similar to the study done by Wu and Christensen (2006) in ZPG TBLs and channel flows. It is worth noting that Wu and Christensen (2006) calculated the population surface density, while the probability of occurrence of vortices at a given x, y location is acquired in the present study. In fact, the population density in the present flow is not appropriate because of the issue of strong streamwise dependency of the trends (see appendix C). This is why we use a pointwise definition instead of a vortex population surface density. The probability trends of prograde (retrograde) vortices, $\Pi_{p(r)}(y/\delta)$, are defined herein as the ensemble averaged number of prograde (retrograde) spanwise vortices as follows

$$\Pi_{p(r)}(y/\delta) = \frac{N_{p(r)}}{N_s} \tag{4.11}$$

where $\Pi_p(y/\delta)$ and $\Pi_r(y/\delta)$ are the probability of occurrence of prograde and retrograde vortices respectively, $N_{p(r)}$ is the number of prograde (retrograde) spanwise vortices and N_s is the total number of samples.

Figure 4.13 illustrates the probabilities of occurrence of prograde and retrograde vortices, Π_p and Π_r, as a function of y/δ at the three different streamwise stations and for ZPG TBL. The ZPG TBL data is taken from the database of Adrian et al. (2000). These wall-normal trends reveal that the largest populations of prograde vortices occur near the wall (for the first two stations and ZPG TBL where measurements exist in that region) with a sharp decrease as we move away from the wall. In addition, near the wall, this probability has higher values in the ZPG TBL compared to the present flow, and it also decreases in the streamwise direction of the present flow. The minimum available y/δ for such PIV plane begins around $y/\delta = 0.04$, 0.02 and 0.13 for the first, second and for the last streamwise positions respectively (see section 3.5.1). In the upper region, $y/\delta \leq 0.1$, Π_p continues to decrease monotonically in ZPG TBL, but at a much slower rate than near the wall. This is also the case for the first streamwise position, $x = 1156$ mm, of the present flow, but at a slower rate than the ZPG TBL, while this trend changes for the other two locations. The probability of occurrence of prograde vortices slightly increases in the upper region, with a maximum around $y/\delta = 0.6$ in the last two streamwise locations. Furthermore, contrary to the near wall trend, this probability increases slightly in the streamwise direction within the upper region of the present flow. As a result, Π_p is therefore affected by the pressure gradient. The maximum population of these vortices shifts from near the wall to the outer region when the boundary layer is subjected to an adverse pressure gradient. Shifting the maximum population of prograde spanwise vortices to the upper region in the adverse pressure gradient zone, as separation is approached, is consistent with the results of Chong et al. (1998). Chong and co-workers have suggested that detached eddies are more frequently encountered near the detachment point.

We turn now our attention to the population trends of retrograde vortices. Figure 4.13-b presents the population densities of retrograde spanwise vortices, Π_r, as a function of y/δ for all streamwise stations and ZPG TBL. The profiles of Π_r are also found to be remarkably similar for the three streamwise stations. In all streamwise positions and ZPG TBL, in contrast to Π_p, the population of retrograde spanwise vortices grows away from the wall up to $y/\delta = 0.25$ and then gradually decreases. Furthermore, the probability of occurrence of retrograde vortices is small and very similar for both flows, while it is not the case for the probability of occurrence of prograde vortices.

At this point, a qualitative comparison can be made with the profiles of vortex population densities obtained by Wu and Christensen (2006) in their ZPG TBL experiments. Note that a quantitative comparison cannot be done because of the different parameters used in both studies: pointwise probability in our case, surface density for Wu and Christensen (2006). The near-wall behaviour of Π_p is found to be qualitatively similar to that of the prograde vortex population densities obtained by

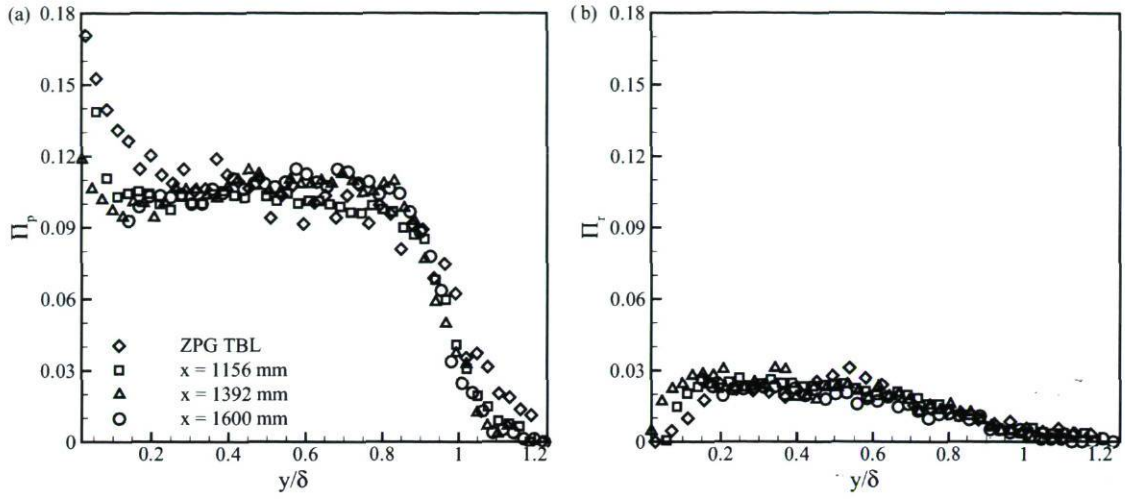

Figure 4.13: Probability of occurrence of prograde and retrograde vortices.

Wu and Christensen (2006) in their ZPG TBL experiments. Similar to the profile of Π_p for ZPG TBL shown in figure 4.13-a, the population densities continue to decrease monotonically for $y/\delta > 0.1$, but at a much slower rate than near the wall.

According to Wu and Christensen (2006), these wall-normal trends can be explained by two possible scenarios. First, the average streamwise spacing between prograde vortices seems to increase as these vortices grow away from the wall and advect. This scenario is supported by Christensen et al. (2004) and also figure 4.15-a and b. This latter figure presents the pdf of streamwise spacing of all prograde vortices at different wall-normal positions. It exhibits results similar to Christensen et al. (2004) who found that the average streamwise spacing of vortices within outer-layer increases with y. In the second scenario, the monotonic decrease of population density with y would be due to the vortex merging mechanism which would predominantly take place in the outer region. A vortex merging mechanism has been proposed in the attached-eddy model of Perry and Chong (1982), Perry and Marušic (1995) and in the study of hairpin structures by Tomkins and Adrian (2003). We may also offer a complementary explanation that in canonical turbulent wall flows, a large portion of the prograde vortices are generated near the wall and that a fraction of them do not evolve away from it.

Turning now our attention to the population trends of prograde vortices, Π_P, for the present study. In the wall proximity, Π_p is higher in ZPG TBL compared to the APG TBL an also Π_p is higher in the first streamwise position compared to the second station. This tendency is expected as $\partial U/\partial y$ also decreases in the streamwise direction.

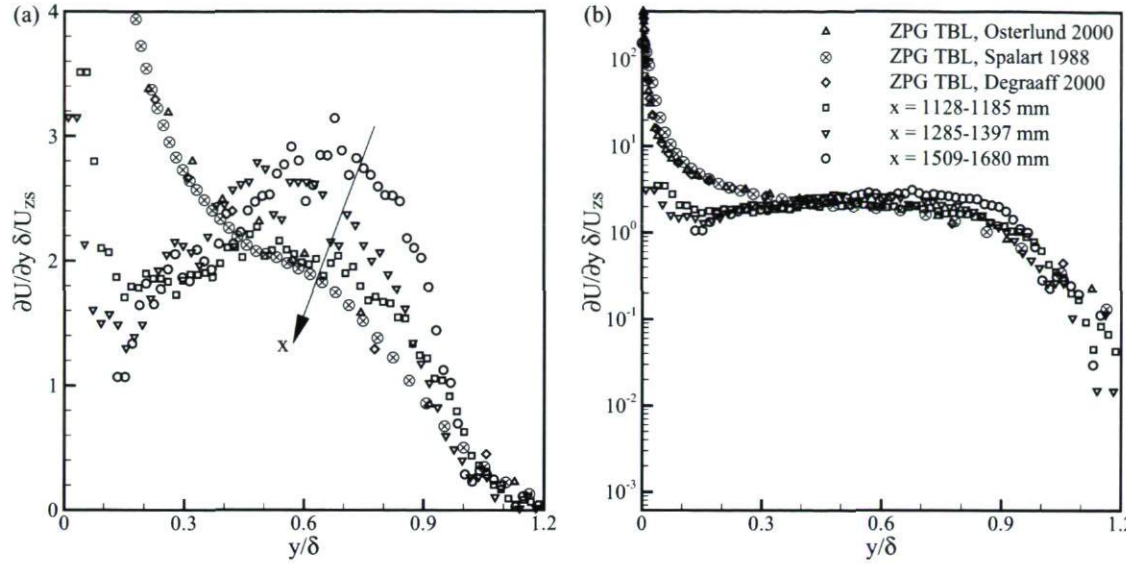

Figure 4.14: Variation of $\partial U/\partial y$ normalized by U_{zs}/δ at different streamwise positions, a)use linear scale for y axis to show the tendency of $\partial U/\partial y$ in outer region, b) use log scale for y axis to present the significant difference of $\partial U/\partial y$ between the ZPG TBL and the present flow near the wall. One symbol out of 2 for clarity except for ZPG TBL profile.

Figure 4.14 shows that $\partial U/\partial y$ is much higher within the inner region of the ZPG TBL while it decreases when moving downstream in the adverse pressure zone. Thus it is expected to have higher probability occurrence of vortices close to the wall when $\partial U/\partial y$ is high because of shearing effect. Next, as mentioned previously, a clear difference exists between the outer regions of this APG TBL and the ZPG TBL. In this APG TBL, the population of prograde vortices remains fairly constant in the region $0.1 < y/\delta < 0.8$ while it monotonically decreases in the ZPG TBL cases. One possible explanation for this difference lies in the fact that the prograde vortices are advected away from the wall faster in a strong APG TBL because wall-normal component of convection velocity (v_c) is more important in the outer region of a strongly decelerated flow than in that of a ZPG TBL. The fact that the hairpin vortices were found to be more inclined in APG TBL compared to the ZPG TBL supports this explanation (see section 5.3.2 and 5.3.3). Furthermore, to verify the first scenario mentioned by Wu and Christensen (2006) (streamwise spacing of prograde vortices) the pdfs of scaled streamwise spacing of prograde vortices by δ are presented in 4.15. The collapse of the pdfs (except for $y/\delta > 0.8$) illustrates that the average streamwise spacing within the outer-layer is roughly constant in the wall-normal direction for $0.1 \leq y/\delta \leq 0.8$. The $\Delta x/\delta$ increases near the boundary layer edge. As a result, the previously mentioned scenarios of streamwise dispersion of the vortices may be less important in a strong APG TBL than in a ZPG TBL.

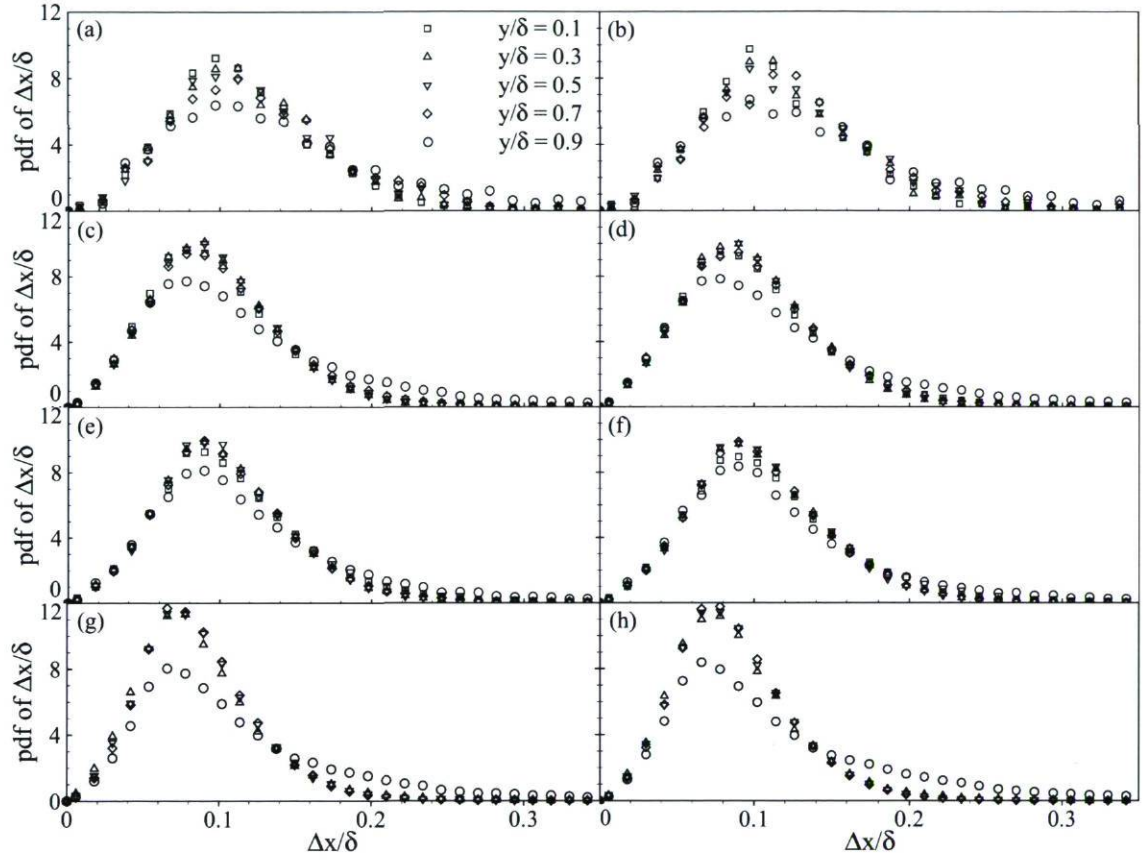

Figure 4.15: Probability density functions of $\Delta x/\delta$ of prograde vortices at different y/δ for all streamwise positions and ZPG TBL (a, c, e and g) $\Delta x/\delta$ for the vortices at upstream of the event location, (b, d, f and h) $\Delta x/\delta$ for the vortices at downstream of the reference point, (a,b) for the ZPG TBL, (c,d) at $x = 1156$ mm, (e,f) at $x = 1392$ mm, (g,h) $x = 1600$ mm. Each y/δ represents a band of $\Delta y/\delta = 0.2$, for instance $y/\delta = 0.1$ is for $0 < y/\delta \leq 0.2$, $y/\delta = 0.3$ is for $0.2 < y/\delta \leq 0.4$ and so on.

Vortex Probability Fractions

The proportion of the probability trends of the prograde and retrograde spanwise vortices as a function of y can now be determined as follows

$$\Psi_{p(r)}(y/\delta) = \frac{\Pi_{p(r)}(y/\delta)}{\Pi_p(y/\delta) + \Pi_r(y/\delta)} \tag{4.12}$$

where $\Psi_{p(r)}$ is the fraction of prograde(retrograde) spanwise vortices as a function of wall-normal direction.

The profiles of Ψ_r are presented in figure 4.16 (Ψ_p is not shown since $\Psi_p = 1 - \Psi_r$). As expected from the trends of Π_p and of Π_r shown in figure 4.13, the profiles of Ψ_r collapse for the three streamwise stations in the outer region. Figure 4.16 shows that Ψ_r increases with y in the inferior region where $y/\delta < 0.25$, but Ψ_r decreases slowly in the region $0.25 < y/\delta < 0.75$ of the boundary layer for all streamwise positions. Moreover, this is the case all the way up to detachment since the last streamwise station is the position of detachment of the boundary layer. At $y/\delta = 0.2$, 20% of the spanwise vortices are retrograde and this proportion drops to 10% near the edge of the boundary layer. A similar behaviour is seen for Π_r in the ZPG TBL below $y/\delta = 0.25$, but Π_r is fairly constant at 20-25% for $y/\delta \geq 0.25$ (see figure 4.13). Similarly, in the ZPG TBL experiments of Wu and Christensen (2006) data, the proportion of retrograde vortices was fairly constant at 25-30% for $y/\delta > 0.2$. Retrograde vortices seem therefore to be less prevalent near the edge of the boundary layer in a strong APG TBL. Contrary of the upper region, retrograde vortices seem to be less prevalent within the inner region of the boundary layer in a ZPG TBL compared to APG TBL as shown in figure 4.16.

It is possible that hairpin vortices are more stretched near the wall and less omega-shaped hairpin vortices therefore occur in this region. Natrajan et al. (2007) presented evidence that a portion of retrograde vortices have a well-defined spatial relationship with neighbouring prograde vortices in canonical wall-bounded turbulent flows. Like Hambleton et al. (2006), they found that the preferred orientation is a prograde spanwise vortex positioned downstream and above the retrograde core. They conjectured this pattern to be on occasion the imprint of an omega-shaped hairpin structure. In the strong APG TBL studied here, the hairpin vortices seem to be more stretched (see section 5.3.2) and move away faster from the wall. Omega-shaped hairpin structures are therefore less likely to occur. By studying conditional averages of the local velocity field around detected retrograde vortices, we have not clearly found evidence of a preferred orientation between prograde and retrograde vortices, while Natrajan et al.

(2007) found clear evidence for ZPG TBL. The reduced presence of omega-shaped hairpin structures may partly explain why the proportion of retrograde spanwise vortices is less in a strong APG TBL. Alternatively, as mentioned previously the merging of hairpin structures may be less frequent in a strong APG TBL. This would also translate into less retrograde spanwise vortices since vortex merging can generate isolated retrograde structures (Adrian et al. (2001), Tomkins and Adrian (2003)).

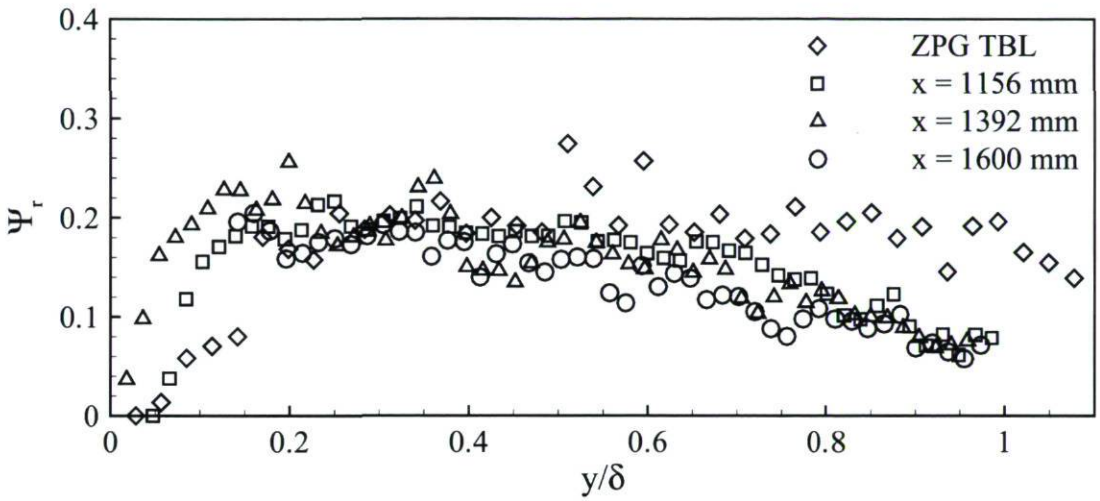

Figure 4.16: Fraction of retrograde spanwise vortices (Ψ_r) at the three streamwise positions and ZPG TBL. One data point out of 2 for clarity.

4.6.2 Ensemble-Averaged Swirling Strength per Vortex

Figure 4.17 shows probability density functions (pdf) of the swirl intensity per vortex ($\bar{\lambda}$) normalized by U_{zs}/δ. The latter can be considered to be the inverse of the outer time scale for the mean flow and the large-scale scale turbulent structures. Since the pdfs at the three different streamwise positions shown in figure 4.17 cover similar ranges of $\bar{\lambda}$-values (figure 4.17-d), U_{zs}/δ is indeed a good scale for $\bar{\lambda}$ (see also figure 4.18). Similar to pdfs of $\tilde{\lambda}_{ci}$ (before and after applying the thresholds) and $\bar{\lambda}/\lambda_{rms}$ shown in figures 4.2, 4.4 and 4.7 respectively, this figure also shows that the pdf of $\bar{\lambda}\delta/U_{zs}$ is qualitatively similar at the three streamwise positions. Contrary to $\tilde{\lambda}_{ci}$ and $\bar{\lambda}/\lambda_{rms}$, the $\bar{\lambda}\delta/U_{zs}$ is affected by varying strong adverse pressure gradient. The pdfs are broader at first streamwise position compared to second and third locations. In fact, the pdfs become narrower in streamwise direction, where the pressure gradient increases. To provide a better idea, the average and standard deviation of $\bar{\lambda}/\lambda_{rms}$ and $\bar{\lambda}\delta/U_{zs}$ are presented in table 4.1 for prograde and retrograde vortices. The mean value of $\bar{\lambda}\delta/U_{zs}$

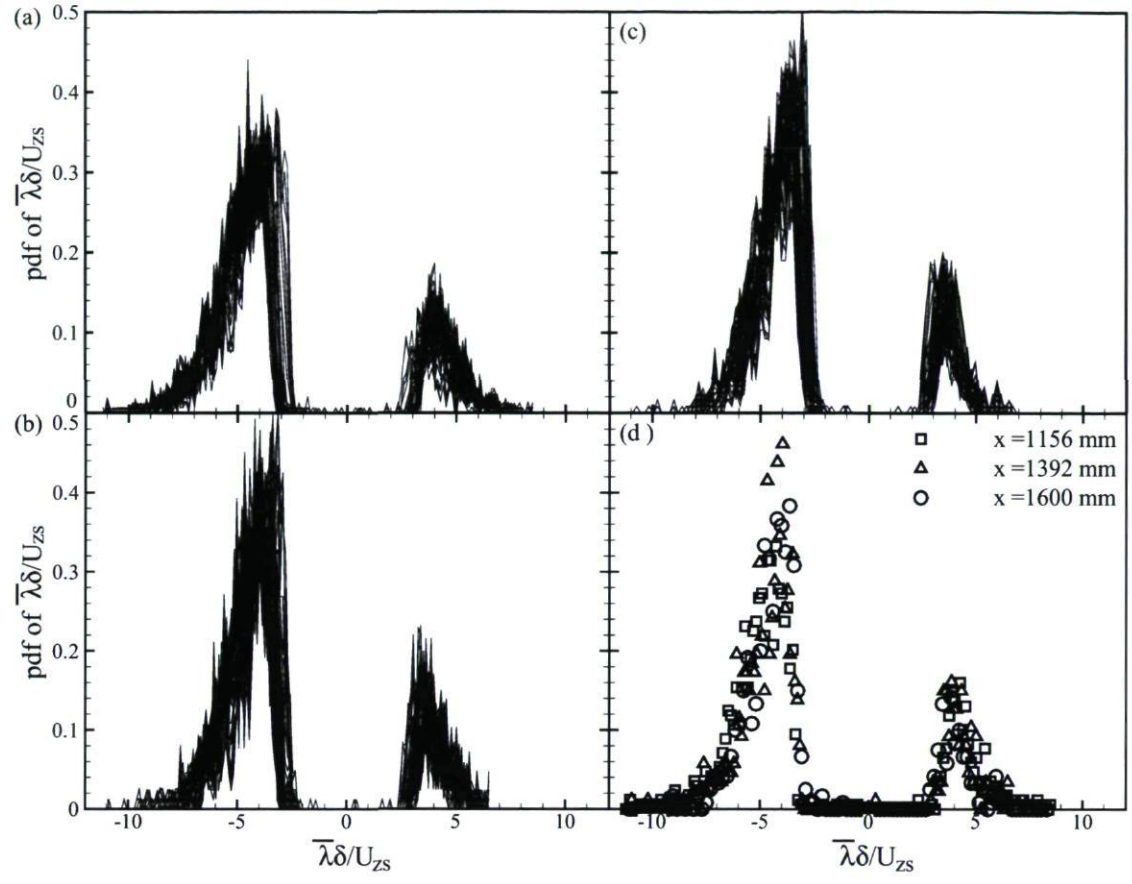

Figure 4.17: Probability density functions of $\bar{\lambda}$ normalized by U_{zs}/δ for $y/\delta = 0.2 - 0.8$ in the insets a-c and at $y/\delta = 0.5$ in the inset d. a) $x = 1156$ mm, b) $x = 1392$ mm, c) $x = 1600$ mm, d) for all streamwise positions (One data point out of 3 for clarity).

decreases in streamwise direction (specially in the inner region), while it is constant for the $\bar{\lambda}/\lambda_{rms}$. In addition, the value of $\langle\bar{\lambda}\rangle\,\delta/U_{zs}$ also decreases in x-direction, whereas it remains unchanged for the $\bar{\lambda}/\lambda_{rms}$. Furthermore, the pdfs of $\bar{\lambda}/\lambda_{rms}$ do not to vary significantly with respect to y in the range 0.2-0.8, while the pdfs of $\bar{\lambda}\delta/U_{zs}$ vary in y-direction.

To provide a better idea about the variation of $\bar{\lambda}\delta/U_{zs}$ in y-direction, the normalized $\bar{\lambda}$ by δ/U_{zs} is now determined as a function of y/δ. Figure 4.18 presents wall-normal profiles of the ensemble average of $\bar{\lambda}$ normalized by U_{zs}/δ. This figure shows that the prograde and retrograde spanwise vortices have approximately the same swirl intensity as the mean values also present in table 4.1. It is also seen that the level of swirl, normalized by U_{zs}/δ, decreases in the streamwise direction in the region below $y/\delta \leq 0.6$ while it remains approximately constant above that region. It is worth recalling that

		$x = 1156$ mm		$x = 1392$ mm		$x = 1600$ mm
		$y/\delta \leq 0.2$	$y/\delta > 0.2$	$y/\delta \leq 0.2$	$y/\delta > 0.2$	$y/\delta > 0.2$
$\langle\bar{\lambda}\rangle\,\delta/U_{zs}$	Prog	-4.3	-4.1	-3.0	-3.6	-3.8
	σ_λ	1.15	1.41	0.87	1.15	1.25
	Retrog	4.0	3.7	2.9	3.2	3.4
	σ_λ	0.81	1.19	0.63	0.94	1.02
$\langle\bar{\lambda}/\lambda_{rms}\rangle$	Prog	-2.1	-2.3	-2.1	-2.2	-2.2
	σ_λ	0.57	0.69	0.57	0.67	0.67
	Retrog	2.0	2.1	2.0	2.1	2.0
	σ_λ	0.40	0.54	0.40	0.49	0.41

Table 4.1: Ensemble average of normalized $\bar{\lambda}$ by U_{zs}/δ and by λ_{rms} at different streamwise positions. σ_λ is the standard deviation of normalized $\bar{\lambda}$ distribution in figures 4.17 and 4.1.

contrary $\bar{\lambda}$ scaled by U_{zs}/δ the values of $\bar{\lambda}/\lambda_{rms}$ are approximately the same within the entire boundary layer as seen in figure 4.3. Such a behaviour of $\bar{\lambda}\delta/U_{zs}$ in y-direction is consistent with that of the Reynolds stresses already reported by Maciel et al. (2006b). To illustrate this, figure 3.29 presents the profiles of $\langle u'\rangle$, $\langle v'\rangle$ and $\langle u'v'\rangle$ normalized by U_{zs}/δ at roughly the same streamwise positions. Streamwise evolutions of the profiles similar to that of the profiles of $\bar{\lambda}\delta/U_{zs}$ are observed. This suggests the strong link between the vortices and the Reynolds stresses, although the Reynolds stresses are second-order moments which are not solely the result of spanwise vortices.

4.6.3 Effective Diameter of Vortices

Probability density functions of the effective diameter of prograde and retrograde vortices scaled by δ are shown in figure 4.19 for the three streamwise positions. Table 4.2 presents the ensemble average and standard deviation of D/δ for prograde and retrograde vortices. The collapse of pdfs of diameter is seen within the outer region of boundary layer, $0.2 \leq y/\delta \leq 0.8$, for all streamwise positions. The fact that the shape and the probability values of the pdfs remain roughly unchanged wrt y/δ in the range 0.2-0.8 at each streamwise position is an astonishing result. In other words, it is found that the size of the vortices scales well with δ. A trend can nonetheless be seen from the pdfs. To illustrate this, figure 4.20 presents the ensemble average of diameter normalized by δ, $\langle D/\delta\rangle$, as a function of y/δ for all streamwise positions and ZPG TBL.

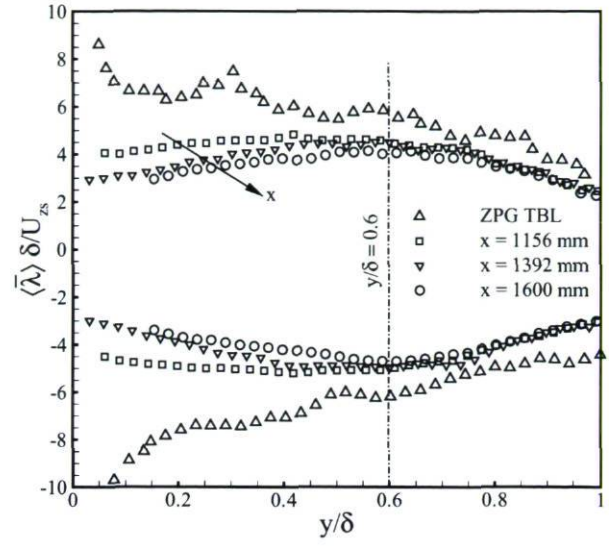

Figure 4.18: Normalized ensemble average of $\bar{\lambda}$ by U_{zs}/δ, (One data point out of 3 for clarity).

		$x = 1156$ mm		$x = 1392$ mm		$x = 1600$ mm
		$y/\delta \leq 0.2$	$y/\delta > 0.2$	$y/\delta \leq 0.2$	$y/\delta > 0.2$	$y/\delta > 0.2$
$\langle D/\delta \rangle$	Prog	0.040	0.044	0.045	0.049	0.041
	σ_D	0.017	0.020	0.019	0.021	0.018
	Retrog	0.034	0.034	0.038	0.037	0.031
	σ_D	0.011	0.012	0.012	0.013	0.011

Table 4.2: Ensemble average of diameter of prograde and retrograde vortices at different streamwise positions. σ_D is the standard deviation of D/δ distribution in figure 4.19.

This figure shows that the $\langle D/\delta \rangle$ is approximately constant in y-direction within the outer region. The effective diameter decreases significantly close to wall.

Now we turn our attention to the evolution of $\langle D/\delta \rangle$ in streamwise direction. The vortices decrease slightly in size, with respect to δ, between the first streamwise position and the last one as shown in figure 4.20 and table 4.2. Furthermore, $\langle D/\delta \rangle$ is higher in the ZPG TBL compared to the results of present study for the first streamwise position (0.06 vs 0.045). Since the mesh width is also bigger in the ZPG TBL, $\langle D/\delta \rangle$ is affected by mesh width and interrogation window width as explained in section 4.5. So, the higher value of $\langle D/\delta \rangle$ in the ZPG TBL compared to the APG TBL could be caused by the effects of both mesh width and interrogation window width. The mean flow evolves rapidly in this strong APG TBL. It is therefore possible that the turbulent structures respond with a certain delay to the changes of the mean flow.

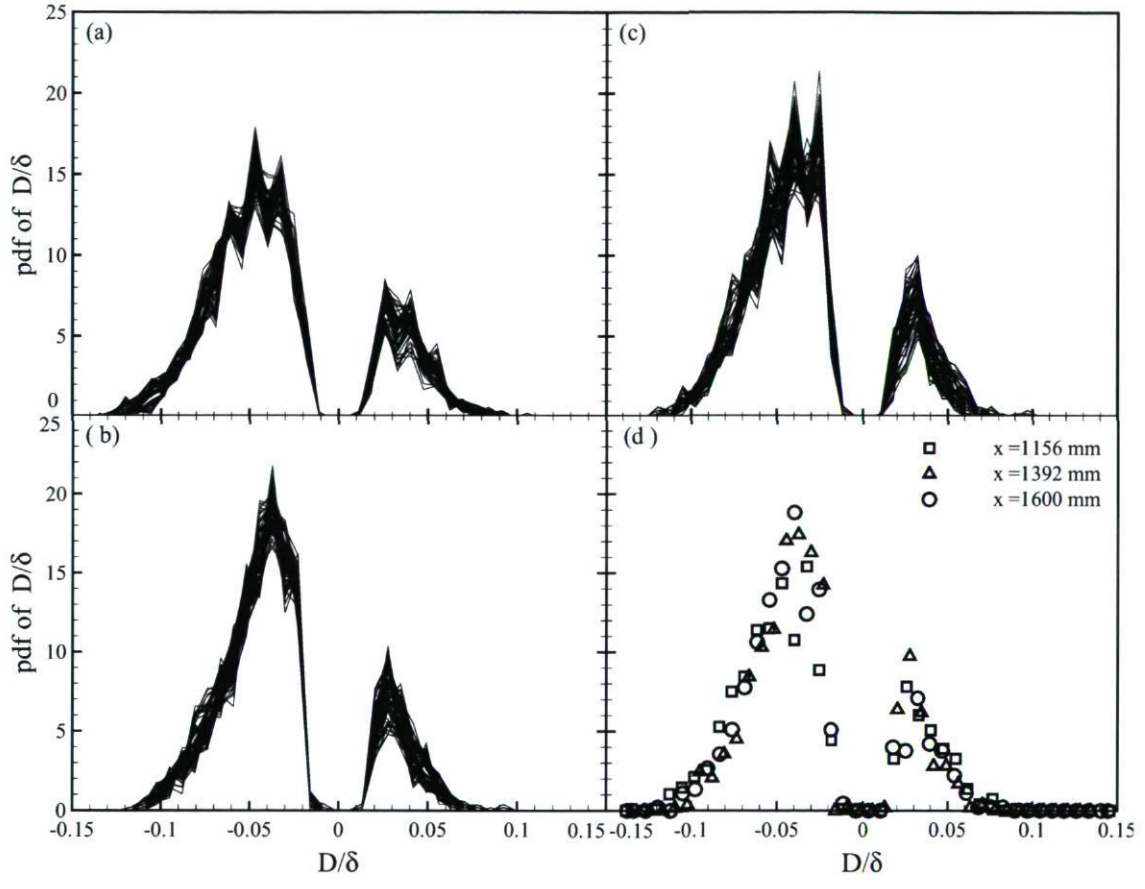

Figure 4.19: Probability density functions of D normalized by δ for $y/\delta = 0.2 - 0.8$ in the subfigures a-c and at $y/\delta = 0.5$ in the subfigure d. a) $x = 1156$ mm, b) $x = 1392$ mm, c) $x = 1600$ mm, d) for all streamwise positions (One data point out of 3 for clarity).

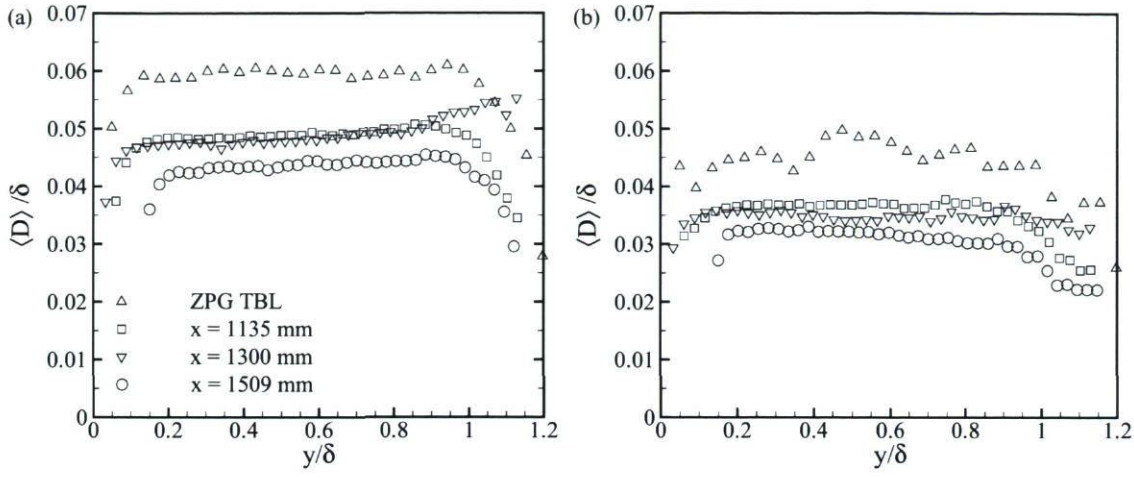

Figure 4.20: Ensemble average of diameter scaled by δ as a function of y/δ: a) progarde vortices, b) retrograde vortices (One data point out of 3 for clarity).

It means the size of vortices in streamwise direction does not follow the boundary layer thicknesses coarsening in the adverse pressure gradient region. In other words, increasing the size of vortices is slower than boundary layer coarsening, as the boundary layer coarsens abruptly across the adverse pressure gradient region (specially near the separation point). It is worth recalling that the spatial resolution relative to δ is the same for three streamwise positions of the present study as mentioned in section 4.2 in order to eliminate the effects of spatial resolution and filter band size.

Finally, it is found that the retrograde spanwise vortices are generally smaller than the prograde vortices. As seen in figure 4.19 the maximum size of prograde vortices is about 0.12δ, while it is about 0.08δ for the retrograde vortices. The maximum probability of D/δ of prograde spanwise vortices is around 0.04δ, while it is 0.03δ for the retrograde vortices.

4.6.4 Convection Velocities

The statistical results of convection velocities for prograde and retrograde vortices are presented in this section. Figure 4.21 presents the mean streamwise convection velocities, u_c, of both prograde and retrograde spanwise vortices as a function of y/δ for the three streamwise positions. It is found that both prograde and retrograde spanwise vortices are convected with velocities close to the mean streamwise velocity at all streamwise positions. Similar behaviours were reported by Wu and Christensen (2006)

and Carlier and Stanislas (2005) for ZPG TBL and channel flow.

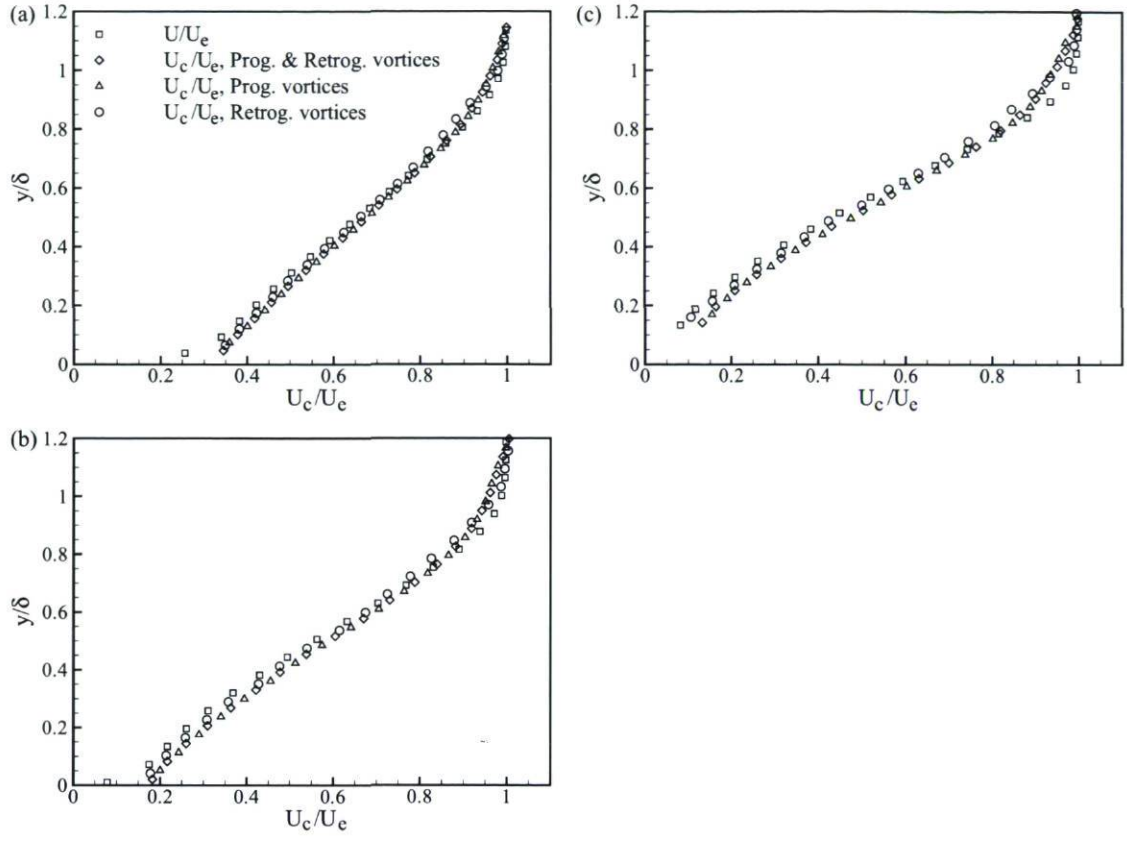

Figure 4.21: Mean advection velocities of prograde and retrograde spanwise vortices versus y/δ in a) $x = 1156$ mm, b) $x = 1392$ mm, c) $x = 1600$ mm (one data point out of 6 for clarity).

Probability density functions of the prograde and retrograde convection velocities, u_c and v_c at five different wall-normal locations, are presented in figures 4.22 and 4.23 (for brevity, only the pdfs for the first streamwise position are presented as the other streamwise positions exhibit similar trends). The distributions of convection velocities present strong wall-normal dependence, while the mean convection velocities of these vortices are close to the local streamwise mean (figure 4.21). The widths of pdfs decrease significantly with increasing y. In fact, the pdfs have broad widths in the inner region and narrow widths within the upper region. Comparing the pdfs of convection velocities of the present study with those of ZPG TBL (Wu and Christensen, 2006) indicates more variation of u_c in the APG TBL. With respect to these results, the distribution of convection velocities are greatly dependent to distance from the wall in the APG TBL whereas it is less dependent to wall-normal distance in ZPG TBL as the velocity gradient is also low within the upper region of ZPG TBL. This is much important especially for

the wall-normal component of convection velocity, v_c. In fact v_c is negligible in the ZPG TBL, while the wall-normal component of convection velocity has important values in the APG TBL.

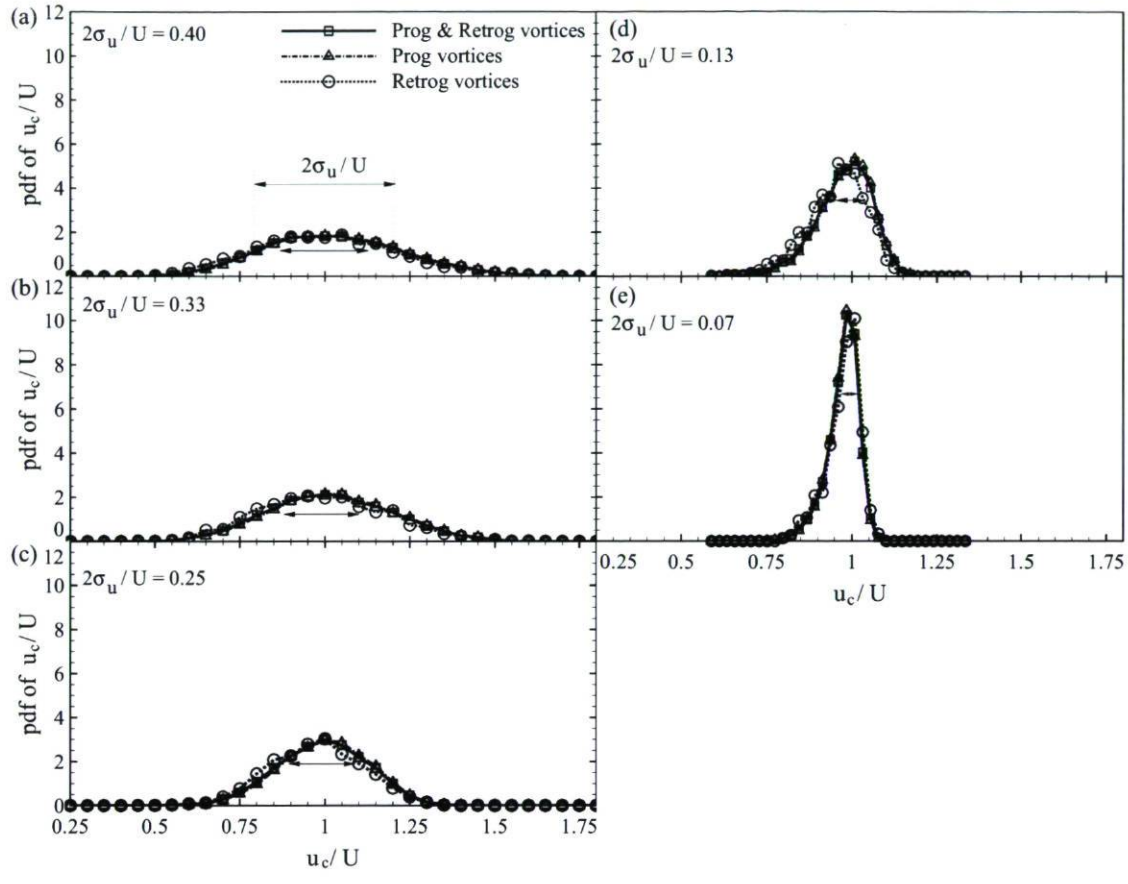

Figure 4.22: pdfs of prograde and retrograde vortex convection velocities (streamwise component u_c/U) at a) $y/\delta = 0.1$, b) $y/\delta = 0.25$, c) $y/\delta = 0.5$, d) $y/\delta = 0.75$, e) $y/\delta = 0.95$.

4.7 Conclusion

PIV measurements are employed to examine the structure of the spanwise vortices in the adverse pressure gradient zone of a turbulent boundary layer. The dimensions of planes were chosen carefully to adjust the PIV mesh with the outer length scale δ. The iso-contours of λ_{ci} are employed to detect vortices.

The presented results show that prograde and retrograde spanwise vortices occur

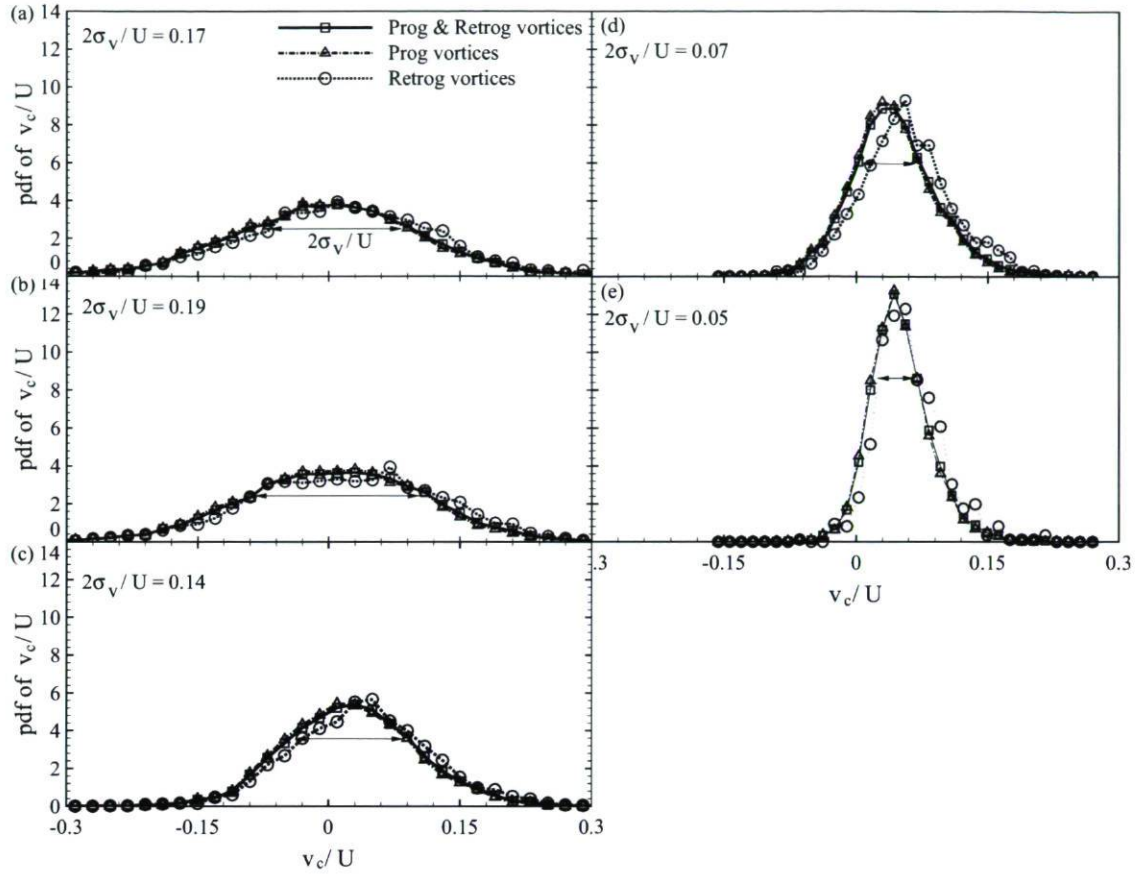

Figure 4.23: pdfs of prograde and retrograde vortex convection velocities (wall-normal component v_c/U) at a) $y/\delta = 0.1$, b) $y/\delta = 0.25$, c) $y/\delta = 0.5$, d) $y/\delta = 0.75$, e) $y/\delta = 0.95$.

frequently throughout the entire of boundary layer. Despite the presence of a very different pressure environment in this flow in comparison to the ZPG TBL, the gross features of the spanwise vortices remain essentially the same, even as separation is approached. The fact that the pdfs of $\tilde{\lambda}_{ci}$ at the different streamwise locations remains fairly similar is an astonishing result. It means that although the vortices might change in size and swirl intensity in absolute terms, the probability of occurrence of vortices and the distribution of the normalized swirling strength, including the distribution between prograde and retrograde swirl, are almost unaffected by the varying strong adverse pressure gradient conditions. Moreover, this is the case all the way up to detachment since the last streamwise station is very close to the position of detachment of the boundary layer ($x = 1615$ mm). The population trends and distribution characteristics of the vortices are therefore persistent flow properties in such a flow.

Additionally, the wall-normal trends reveal that the largest populations of prograde vortices occur near the wall with a sharp decrease as we move away from the wall. This near wall trend decreases in amplitude from ZPG TBL to APG TBL and in the streamwise direction in the present study. Indeed, Π_p is higher in the ZPG TBL compared to the first streamwise position of the present work, and further decreases at the second streamwise location. This would be because of the mean shearing effect within the near wall region that is high in ZPG TBL and decreases within the adverse pressure gradient zone of APG TBL. The sharp decrease in Π_p stops around $y/\delta = 0.1$ in the APG TBL while continues to decrease monotonically for $y/\delta > 0.1$ in ZPG TBL, but at a much slower rate than near the wall. This is also the case for the first streamwise position of the present flow but at a slower rate than the ZPG TBL. On the other hand, contrarily to the situation in the ZPG TBL and the first streamwise position, the population of prograde vortices increases slightly with increasing wall-normal distance in region $0.1 \leq y/\delta \leq 0.8$ in other locations. Finally, instead of the near wall trend, the probability of occurrence of prograde vortices increases slightly in the streamwise direction within the upper region of the present flow.

The proportion of retrograde vortices with respect to prograde vortices is also less in a strong APG TBL and the prograde vortices are more frequent than retrograde vortices. In particular, the fraction of retrograde vortices decrease with wall-normal position for $y/\delta \geq 0.25$ in the present study while it remains roughly constant in the ZPG TBL. Tentative explanations for these various dissimilarities were given resting on the fact that the mean strain rates are more important in a strong APG flow.

The pdfs of $\bar{\lambda}$ scaled by U_{zs}/δ at the three different streamwise positions presents that it is affected by varying strong adverse pressure gradient. The pdfs of $\bar{\lambda}\delta/U_{zs}$ are broader at first streamwise position compared to second and third locations. In fact, the pdfs become narrower in streamwise direction, where the pressure gradient increases. Furthermore, the pdfs of $\bar{\lambda}\delta/U_{zs}$ vary in y-direction. $\bar{\lambda}\delta/U_{zs}$ is shown as a function of y/δ to provide a clear idea about the variation of $\bar{\lambda}\delta/U_{zs}$ in y-direction. The wall-normal profiles of the ensemble average of $\bar{\lambda}$ normalized by U_{zs}/δ shows that the prograde and retrograde spanwise vortices have approximately the same swirl intensity. It is also seen that the level of swirl, normalized by U_{zs}/δ, decreases in the streamwise direction in the region below $y/\delta \leq 0.6$ while it remains approximately constant above that region. For the ZPG TBL, the $\langle\bar{\lambda}\rangle\,\delta/U_{zs}$ is maximum near the wall and monotonically decreases in y direction. It is seen that the $\langle\bar{\lambda}\rangle\,\delta/U_{zs}$ is higher for the ZPG TBL compare to the present study for $y/\delta \leq 0.6$. Such behaviour is consistent with that of the Reynolds stresses. This suggests the strong link between the vortices and the Reynolds stresses, although the Reynolds stresses are second-order moments which are not solely the result of spanwise vortices.

It was also found that the size of the vortices scales well with δ in y direction and a trend can nonetheless be seen from the profile of $\langle D/\delta \rangle$ in y-direction within the outer region, $0.2 \leq y/\delta \leq 0.8$, of both APG and ZPG TBLs. The diameter of vortices are much smaller close to the wall, $y/\delta \leq 0.1$. Furthermore, the D/δ decreases from ZPG TBL to APG TBL and in the streamwise direction in the present study. Since the D/δ is affected by spatial resolution, the higher value of $\langle D/\delta \rangle$ in the ZPG TBL compared to the APG TBL would probably be because of the effects of both mesh width and interrogation window width. In the APG TBL case, since the mean flow evolves rapidly, it is therefore possible that the turbulent structures respond with a certain delay to the changes of the mean flow. It means the size of vortices in streamwise direction does not follow completely the boundary layer thicknesses coarsening in the adverse pressure gradient region. It is important to recall that the spatial resolution relative to δ is the same for the three streamwise positions of the present study in order to eliminate the effects of spatial resolution and filter bandwidth size.

Finally, it was found that prograde and retrograde vortices travel, on average, with a velocity close to the local mean velocity, while the distribution of their instantaneous convection velocities significantly changes in the y-direction. Moreover, the distribution of convection velocities in APG TBL are more dependent to y-direction compare to ZPG TBL. This dependency would be related to the gradient of velocities, $\partial U/\partial y$ and $\partial V/\partial y$. The $\partial U/\partial y$ is higher in the ZPG TBL compare to the present study, especially for $y/\delta \leq 0.6$, whilst the $\partial V/\partial y$ is much lower in the ZPG TBL.

Chapter 5

Hairpin Vortices and Packets

5.1 Introduction

As mentioned previously, the instantaneous velocity fields are obtained using PIV in streamwise/wall-normal (xy) planes at three streamwise positions in the adverse pressure gradient region between the peak of pressure and the separation point. Investigation of the instantaneous velocity fields show that the boundary layer is densely populated with velocity signatures associated with hairpin vortices. The term hairpin vortex, introduced in section 2.2.2 is here taken to represent horseshoe, cane, hairpin, or omega-shaped vortices. A cross-section of three dimensional structures can be viewed via planar PIV data if the laser sheet cuts the mid-plane of the structures.

Before analyzing the statistical behaviours and various parameters of hairpin vortices, it is useful to study the instantaneous velocity vector fields, in order to describe qualitatively the instantaneous structures. A technique similar to that of Adrian et al. (2000) is used to identify the presence of hairpins and hairpin packets in the present study. The hairpins are then characterized qualitatively by analyzing the associated instantaneous velocity vector patterns. Finally the statistical parameters of these structures like neck inclination, inclined shear layer (ISL), diameter of hairpin heads, streamwise spacing and swirling strength are determined and analyzed.

5.2 Instantaneous Results

The geometric structure of typical vortices in a turbulent boundary layer is much debated. There are various viewpoints on the shapes and sizes of vortices that may be present. However, there is significant evidence that in the logarithmic region and beyond, the ZPG turbulent boundary layer contains many hairpin-shaped vortices (with one or two legs). A simple coherent structure which was described as a hairpin vortex was previously presented by many researchers (see section 2.2.2).

This section describes the individual and group of hairpin vortices which are detected in the instantaneous velocity fields. It explains how the various parameters of a 3D vortex called hairpin and of packets of hairpins are obtained through a 2D instantaneous velocity signature.

5.2.1 Individual Hairpin Vortex Signature

The hairpin properties which have been found experimentally in the present work are qualitatively comparable with those found in the works presented in section 2.2.2. Many of these 3D structures, which are randomly located in the boundary layer, cross the laser sheet of the PIV system which was set in a streamwise/wall-normal (xy) orientation. These structures leave signatures in the measured instantaneous velocity fields. It is important to mention that based on this planar information, we can not distinguish between symmetric or asymmetric hairpin vortices, nor can we distinguish between omega shape vortices, cane shape vortices, horseshoe vortices and hairpins. So in this study, a hairpin vortex can be symmetric or asymmetric and narrow or wide.

It is necessary to determine how three dimensional coherent structures can be recognized from two dimensional experimental results acquired via PIV measurements. Adrian et al. (2000) presented an idealized model of a hairpin vortex which is shown in figure 5.1. In planar PIV, identification of these vortices typically requires identification of hairpin vortex signatures: in the case of xy plane data, the 2-D velocity vector pattern created when the measurement volume slices between vortex legs. The qualitative signature of the instantaneous velocity field induced by a hairpin vortex which crosses a streamwise/wall-normal plane is also shown in figure 5.1 and figure 5.2 using our PIV data. So the instantaneous velocity pattern in a streamwise/wall-normal cross-section of the hairpin, and in a frame moving with the hairpin, contains the following features:

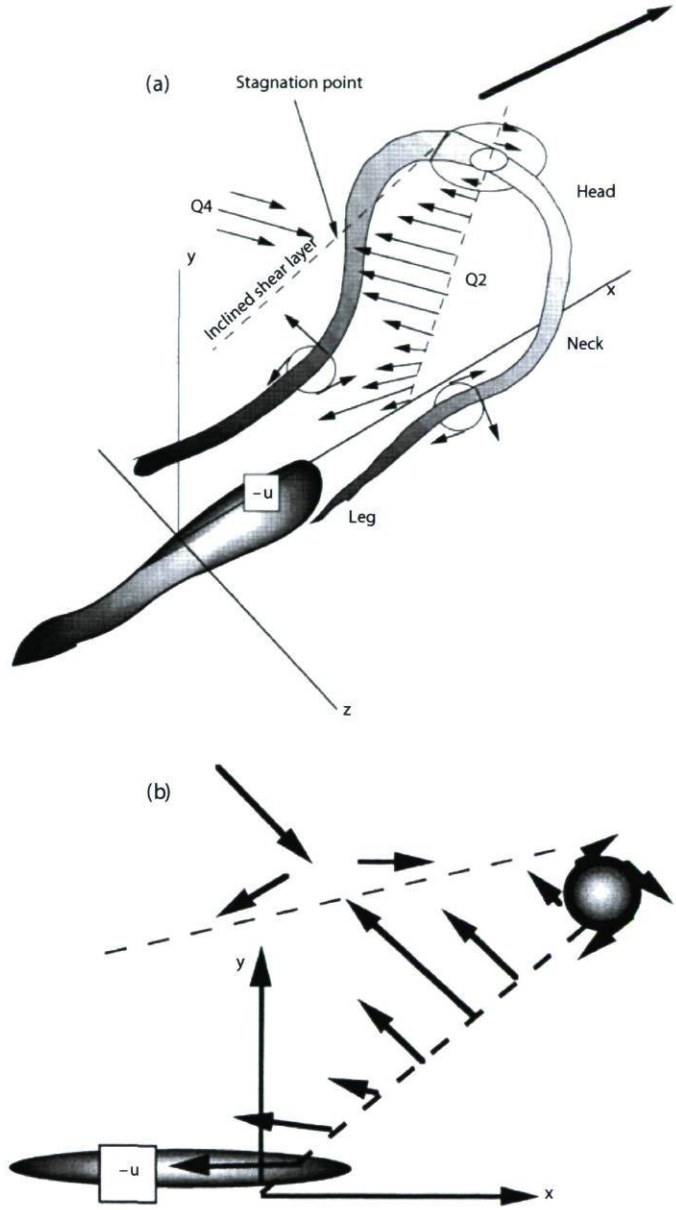

Figure 5.1: (a)Schematic of a hairpin vortex attached to the wall and the induced motion. (b) Signature of the hairpin vortex in the streamwise-wall-normal plane. The signature is insensitive to the spanwise location of the plane and independent of symmetric or asymmetric the real hairpin vortex, until it intersects the concentrated core forming either side of the hairpin (proposed by Adrian et al. (2000)).

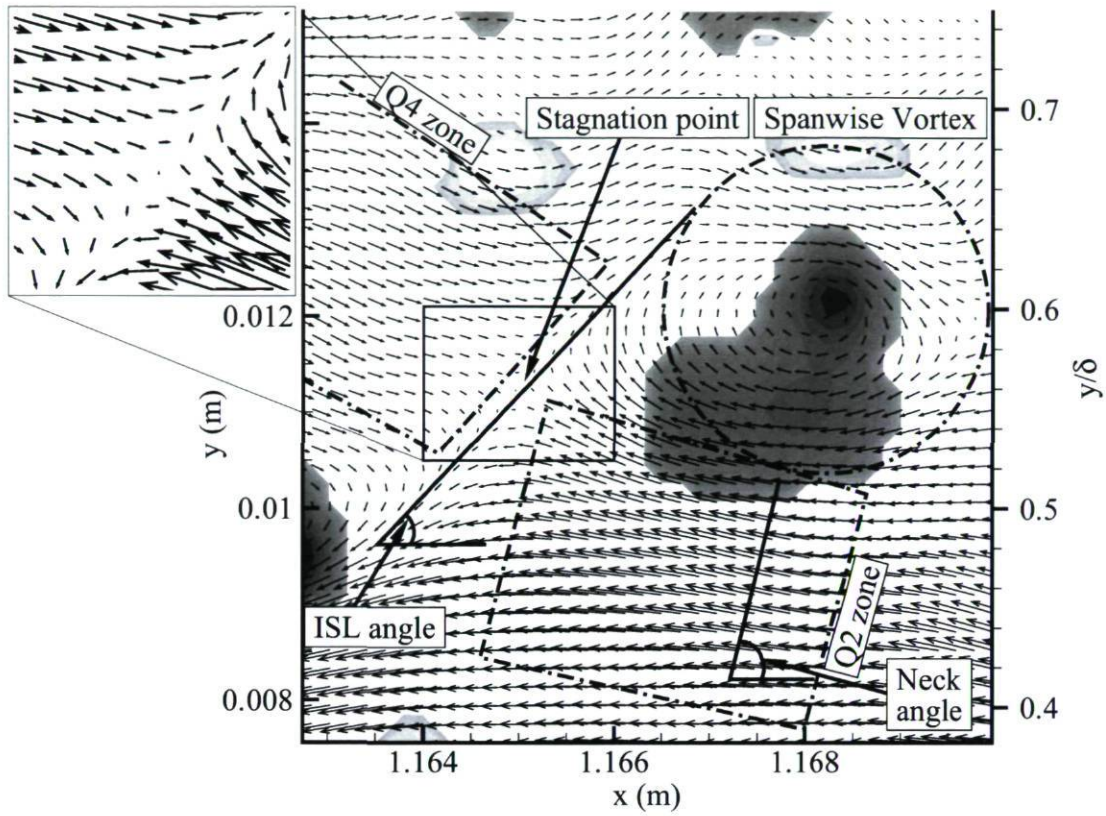

Figure 5.2: Single hairpin vortex signature (iso-regions of swirling strength are superimposed).

1. a spanwise vortex core rotating in the same direction as the mean velocity circulation which is the head of the hairpin;

2. a region of low-speed fluid (second-quadrant ejections: $u - u_c < 0$, $v - v_c > 0$) which is located below and upstream of the vortex head. This low-speed fluid is caused by vortex induction from the legs and the head of the hairpin. The spatial extent of the region of second-quadrant vectors is approximately the same as the diameter of the region of circular streamlines;

3. an inclination of this region occurs on a locus inclined at $35^o - 90^o$ with respect to the x-direction;

4. A fourth-quadrant region ($u - u_c > 0$, $v - v_c < 0$) is habitually found to face the second-quadrant event from upstream, as can be seen in figure 5.2. The sharp frontier between the $Q2$ and $Q4$ events consists of a stagnation point that resembles a saddle point and an inclined shear layer.

The second-quadrant vectors fall along regions inclined at about 60 degrees to the x-

direction. Adrian (2007) proposed that each $Q2$ event has a local maximum of the flow speed (see figure 5.1). The observed local maximum of $Q2$ event can not be produced by a straight spanwise vortex, but an arch shaped vortex can generate it. Additionally, $Q2$ events are usually stronger (greater speed) than the $Q4$ events due also to the existing curvature of the head and neck of the hairpin which focuses induction in the inboard region and defocuses it in the outboard region.

The aforementioned velocity signature associated with a hairpin vortex was also observed by Zhou et al. (1999) via a DNS study (see figure 2.5). This latter figure exhibits the correspondence between a three dimensional hairpin vortex and its signature in the xy plane. The similarities between our results and the hairpin signatures of Zhou and co-workers also provide a strong basis for associating the two-dimensional velocity patterns with three-dimensional hairpin vortex signature.

5.2.2 Hairpin Detection Method

A hairpin vortex identification technique similar to that of Adrian et al. (2000) is used to detect the presence of hairpins and hairpin packets in the present study. This technique can be summarized as follows.

First, all prograde spanwise vortices are identified using the calculated swirling strength (section 4.3). The prograde vortices are found everywhere and some of them are hairpin heads. Then it must be determined which identified vortices are hairpin vortices.

Since only hairpin packets are studied in the present study and isolated hairpin vortices are not considered, we consider only series of three or more prograde vortices in close spatial proximity to each other in the streamwise direction (see figure 5.3). A series of three or more prograde spanwise vortices in close spatial proximity to each other are potential to be considered a hairpin packet. Although a series of two hairpins could probably form a hairpin packet, hairpin packets with three or more hairpins propose more systematical characterization avoiding random positioning and undesired parameter determination. This fact motivates us to pick hairpin packets with three or more hairpins in this study.

Finally, the selected prograde vortices are analyzed to determine if they are part of a velocity signature typical of a hairpin. The simplest possible approach for the present xy plane PIV data is to perform Galilean decomposition of the instantaneous velocity vector fields using a constant advection velocity vector (u_c, v_c). This is used

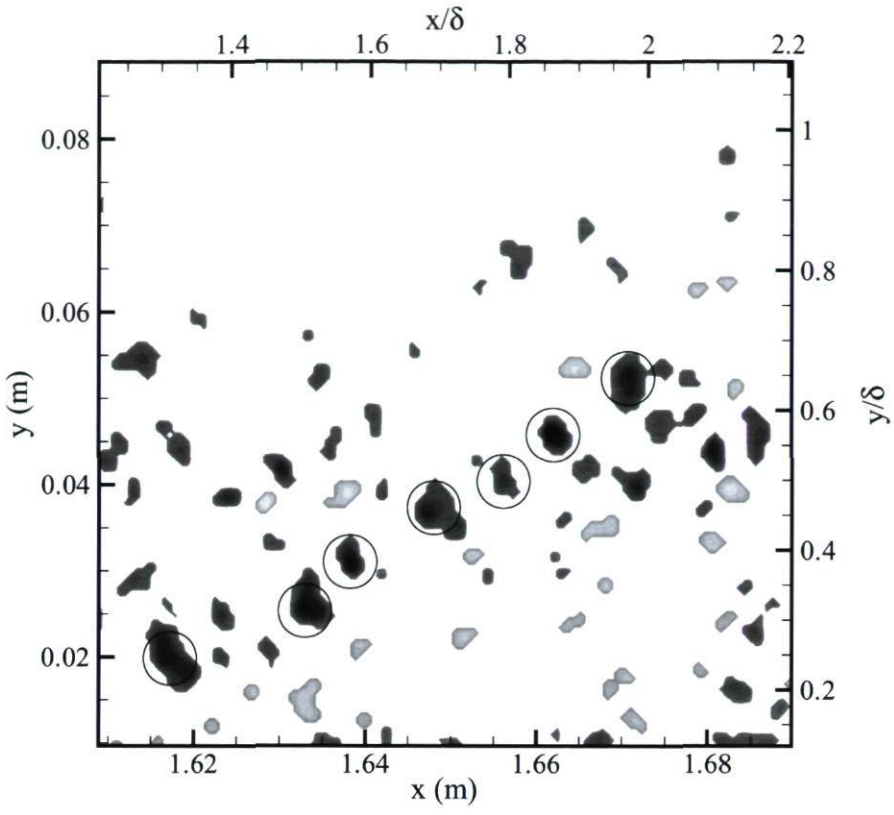

Figure 5.3: Circled iso-regions of swirling strength in close spatial proximity to each other in the streamwise direction can correspond to hairpin vortex signatures within a packet. Dark areas correspond to prograde vortices ($\lambda_{ci} < 0$) and light clusters correspond to retrograde vortices ($\lambda_{ci} > 0$). Region $x = 1509 - 1680$ mm.

to decompose the instantaneous velocity field into a convection velocity and the deviations therefrom. The reference frame moving at the convection velocity illustrates the deviation vectors. Figure 5.2 shows an example of a hairpin signature revealed by this procedure when the convection velocity matches that of the vortex head. If the decomposed velocity vector field contains the hairpin vortex components mentioned above, this signature is probably that of a hairpin vortex.

Adrian et al. (2000) used the coincidence between the concentrated vorticity iso-regions and the boundaries between the zones of uniform momentum to detect hairpin packets, while we used the local maximum of swirling strength clusters within a series of three or more prograde vortices in close spatial proximity to each other in the streamwise direction. Depending on the number of hairpins within the field, different frames are used in our case to truly see the hairpin signatures and for different packets. The convection velocities are obtained directly with the probe tool of Tecplot by clicking on the local maxima of swirling strength patches (see section 4.4). Indeed, it is supposed

that the convection velocities are the instantaneous velocities at the local maxima of swirling strength iso-regions.

A vortex core appears to be a circular streamline pattern when the velocity vector fields are viewed from the viewpoint of a moving reference frame with the appropriate convection velocity. Figure 5.4 illustrates an isolated turbulent eddy and the superimposed swirling strength iso-regions. The velocity vector field is viewed in different Galilean frames in this figure to illustrate the effect of convection velocity on the instantaneous velocity signature when it varies by about 15% of U_e. The velocity-vector map is viewed in a proper convective frame of reference in figure 5.4-b, whereas instantaneous velocity vectors are viewed in frame of references moving with convection velocities about 15% lower and higher than the proper convection velocity in figures 5.4-a and 5.4-c respectively. Although the vortex core apears as circular streamlines in all cases when u_c varies by about 15% of U_e, the local maximum of swirling strength and the vortex core are at the same point in figure 5.4-b, and the center of the vortex is under or over the local maximum of λ_{ci} in figures 5.4-a and 5.4-c respectively. The vortex core does not appear to be a circular streamline pattern when the convection velocity varies by more than 20% of U_e from the appropriate u_c. It is important to mention that other components of hairpin vortex signature ($Q2$, $Q4$ and ISL) are sensitive to convection velocity as shown in figure 5.5. Having the appropriate convection velocity is necessary to determine the proper parameters of the hairpin vortices.

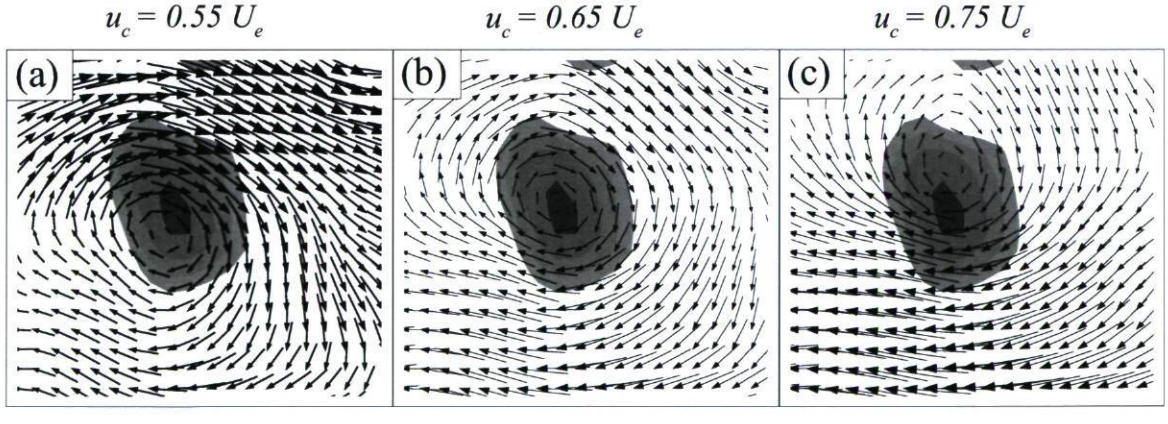

Figure 5.4: Variation of moving frame velocity (about 15%) for an individual spanwise vortex. Velocity field obtained by subtracting the prescribed u_c.

Using the aforementioned technique, we find that there are many hairpin vortices in all the acquired velocity vector fields at all streamwise positions. The detected hairpin vortices qualitatively agree well with available results for canonical flows (Chong et al. (1998), Zhou et al. (1999) and Adrian et al. (2000)). It is important to note that the

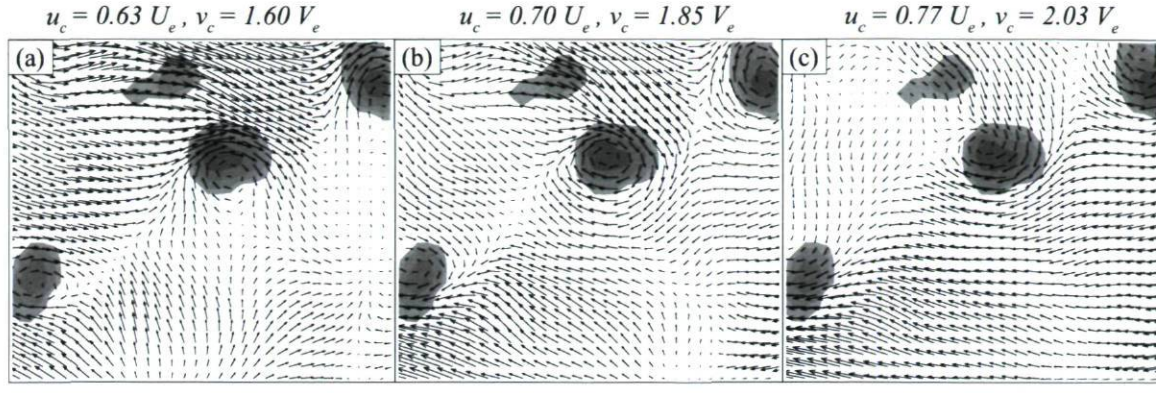

Figure 5.5: Effect of varying the moving frame velocity (by about 10%) on the hairpin components. Velocity-vector map is viewed in a proper convective frame of reference in b, while the convection velocities are about 10% lower or higher than the appropriate convection velocity in a and c respectively.

depiction of a vector field for a given value of convection velocity does not clearly show all of the hairpin vortices as the convection velocity varies from one packet to another packet and sometimes from one hairpin to another hairpin in one packet because of dispersion. Figure 5.6 shows this point clearly in which there are many regions of concentrated vorticity. The circled swirling strength regions (shown in figure 5.6-a) correspond to hairpin vortex signatures but they can only be clearly identified if the convection velocity is properly chosen.

Our strategy of detecting hairpins is illustrated and explained using the data in figures 5.7 and 5.8 for a single realization of the PIV data in region $x = 1128 - 1185$ mm. The circled swirling strength patches in figure 5.7 correspond to vortex heads of hairpin signatures. They form streamwise away inclined with respect to the wall. These away associated with hairpin packets (see section 5.2.4). To detect the hairpin vortex signatures, the velocity field corresponding to figure 5.7 is viewed in different Galilean frames (figure 5.8). It can be clearly seen that the velocity vector patterns appear to be circular streamlines pattern if the convection velocity matches the velocity at the centre of the vortex as mentioned before. The swirling strength iso-regions are also superimposed in this figure to illustrate that the vortex cores and the local maxima of λ_{ci} match. The heads of the hairpin vortices are labeled A-R and the reader can see by inspection where the other elements of the hairpin vortex signature occur. The convection velocities are $u_c = 0.4U_e$, $v_c = 0.4V_e$ for figure 5.8-a and $u_c = 0.7U_e$, $v_c = 1.1V_e$ for figure 5.8-b and $u_c = 0.9U_e$, $v_c = 1.7V_e$ for the inset of figure 5.8-b. The vortices A-G are visualized in figure 5.8-a and vortices I-M and R can be seen in the large graph of figure 5.8-b and N-P in the inset of figure 5.8-b. Non-circular streamlines

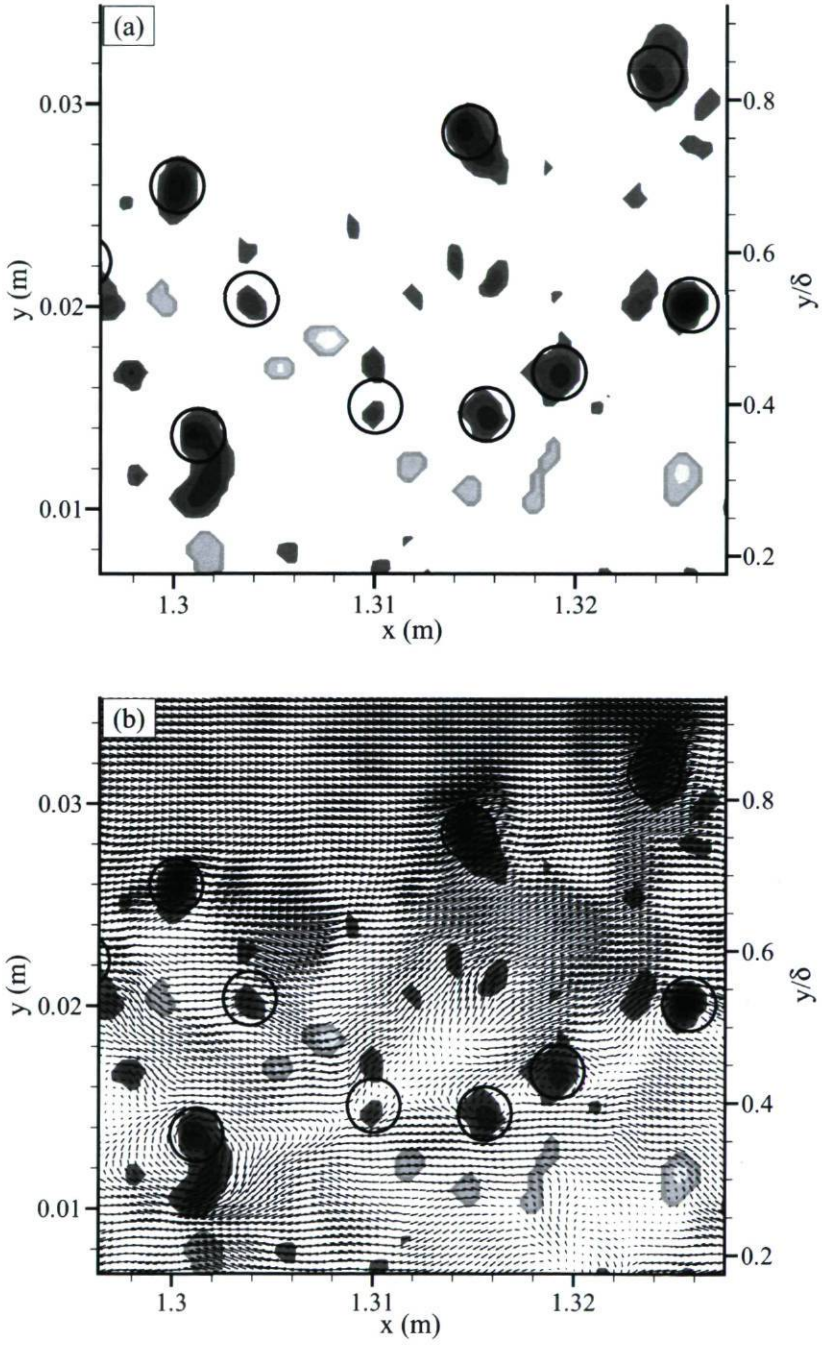

Figure 5.6: Instantaneous field in region $x = 1285 - 1397$ mm: a) iso-regions of swirling strength show spanwise vortices, b) velocity vector field shown using Galilean decomposition (vectors viewed in a frame-of-reference convecting at $u_c = 0.5U_e$, $v_c = 0.45V_e$).

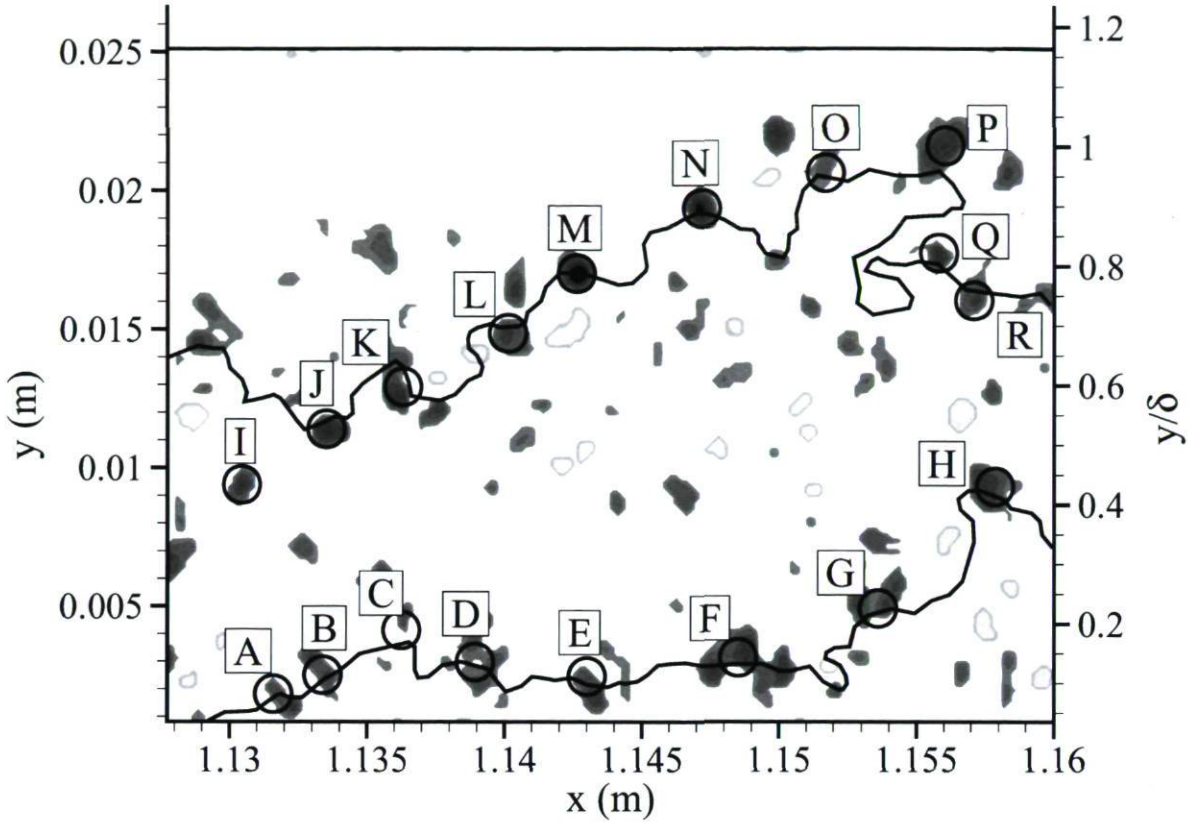

Figure 5.7: Circled iso-regions of swirling strength corresponding to hairpin vortex signatures in region $x = 1128 - 1185$ mm. Dark contours surfaces : $\lambda_{ci} < 0$ (prograde), light contours surfaces : $\lambda_{ci} > 0$ (retrograde). The solid lines are contours of constant streamwise velocity.

(i.e. H in figure 5.8-a and N-P in figure 5.8-b) can be observed if the advection velocity differs from U_e by about 10-20%.

Reynolds decomposition is the traditional technique for decomposing turbulent velocity fields. In this method the decomposed vector patterns are obtained by subtracting the long-time-averaged velocity field from the instantaneous velocity field. The instantaneous structures are however often distorted when the vector patterns are viewed using Reynolds decomposition (Adrian et al., 2000). It is because the Navier-Stokes equations are not Reynolds invariant and all the vortices do not convect with long-time-averaged mean velocity. These distortions may actually mislead the analysis of the structures. Figure 5.9 shows the velocity vector field corresponding to figure 5.7 in Reynolds decomposition frame. In order to see the mentioned events more clearly, close zooms of figures 5.8-b and 5.9 are presented in figures 5.10-a and 5.10-b respectively. It can be seen that certain features in figure 5.10-a can also be observed in figure 5.10-b, but many of the structural elements are distorted. If the vortices (corresponding to

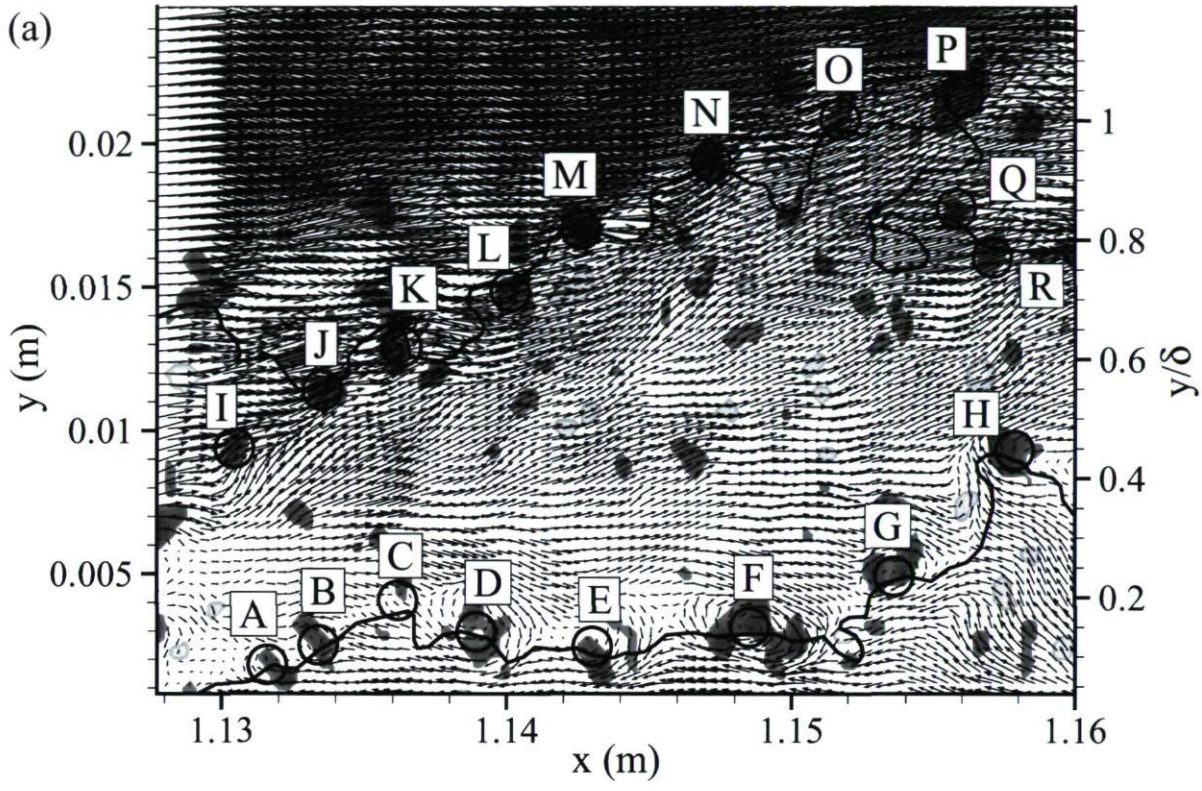

Figure 5.8 (a), for caption see next page.

hairpin heads) would travel with the long-time-averaged mean velocity, the vortices would be visualized clearly by Reynolds decomposition. The head of hairpin vortex J is clearly revealed in figure 5.10-b, whilst the $Q4$ events and inclined shear layers (in the range $0.45 < y/\delta < 0.65$) do not appear. It is because of the variation of convection velocity in Reynolds decomposition (U) at each point, while u_c is constant in Galilean frame.

As explained by Adrian et al. (2000), the decomposed instantaneous velocity fields via Galilean decomposition have additional properties that are useful for interpretation. First of all, the vectors have small magnitude in the regions where velocities are nearly equal to the convection velocity. So these regions contain vectors that appear light to the eye usually. Whereas the regions where the instantaneous velocities differ greatly from the convection velocity appear dark to the eye. Additionally, the Navier-Stokes equations are invariant with respect to Galilean decomposition as mentioned, and the shear zones adjacent to vortex structures are preserved in all Galilean frames.

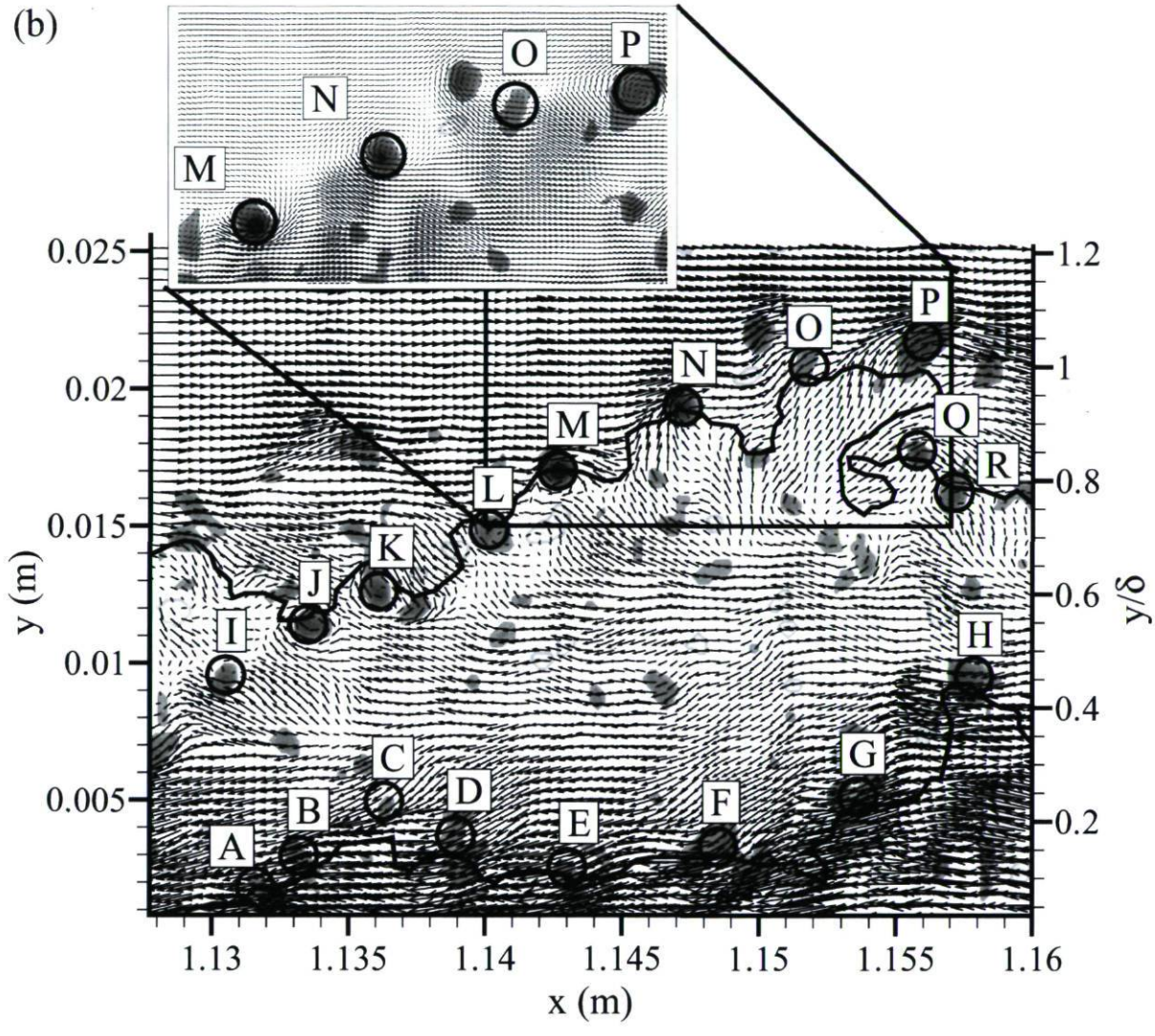

Figure 5.8: Velocity vector field corresponding to figure 5.7, shown using several different Galilean decompositions (one vector out of 4 in large plots for clarity). Vectors viewed in frames of reference convecting at: a) $u_c = 0.4U_e$, $v_c = 0.4V_e$, b) $u_c = 0.7U_e$, $v_c = 1.1V_e$ and $u_c = 0.9U_e$, $v_c = 1.7V_e$ for the inset (contours of swirling strength are superimposed).

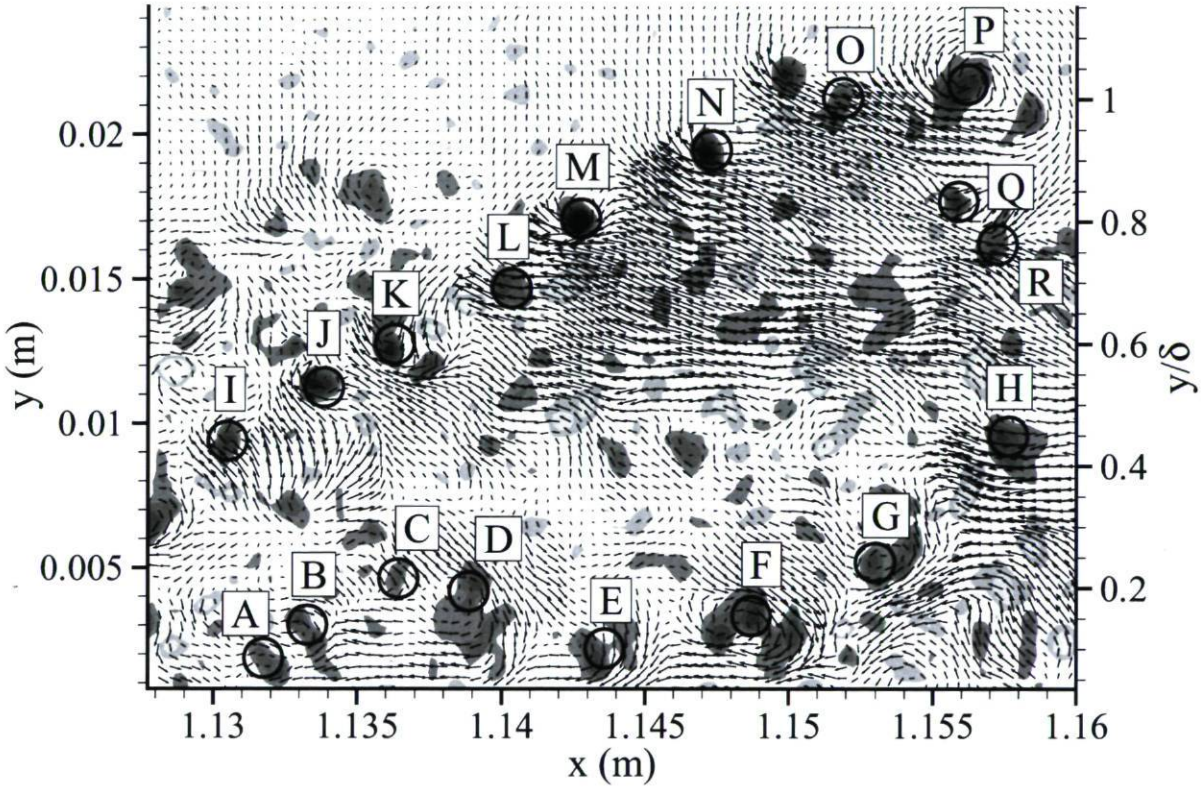

Figure 5.9: Reynolds decomposed fluctuating velocity field corresponding to figure 5.7. One vector out of 4 for clarity and iso-regions of swirling strength are superimposed.

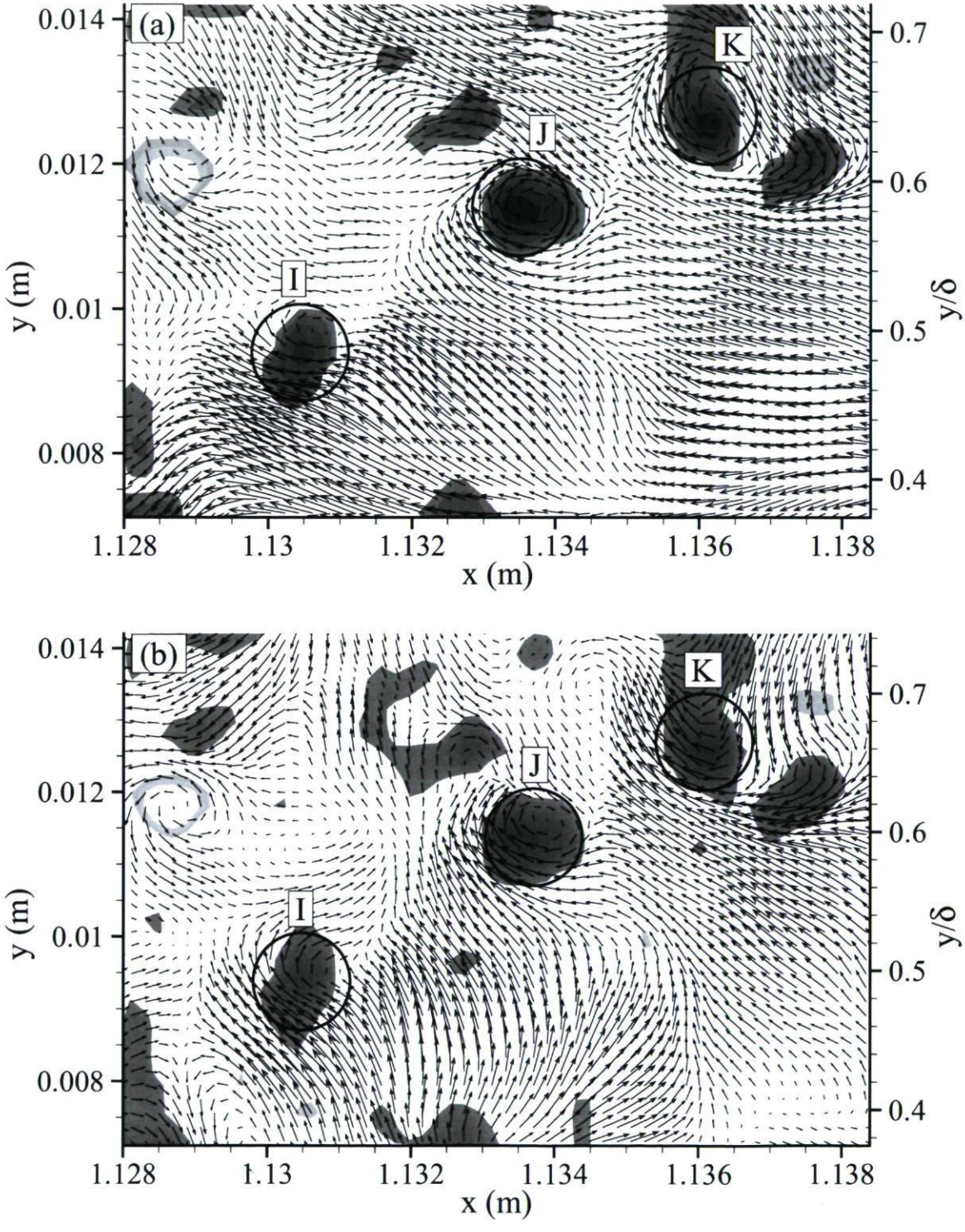

Figure 5.10: a) Close zoom corresponding to figure 5.8-b, b) Close zoom corresponding to figure 5.9.

5.2.3 Qualitative Features of Hairpins

Fifty instantaneous velocity fields at each streamwise position were treated via the aforementioned hairpin identification technique (section 5.2.2). The parameters of hairpin vortex signature ($Q2$ angle, neck angle, ISL angle, diameter of spanwise vortex associated with hairpin head, swirl intensity of the spanwise vortex) and the parameters of hairpin packets (growth angle, streamwise spacing between the hairpin vortices, position of hairpin vortices in the boundary layer) are determined accurately as much as possible in this step. Moreover, 50 instantaneous velocity fields from the data base of Adrian et al. (2000) were inspected with the same method in order to compare the results of APG and ZPG turbulent boundary layers.

Like for the zero pressure gradient TBL (Adrian et al., 2000), hairpin vortex signatures are revealed in all the velocity vector fields and all streamwise positions in the present flow. They can also be found throughout the boundary layer from the wall to the edge of the boundary layer.

The angle at which the plane formed by the head and neck of the hairpin is inclined to the wall can be estimated with the angle of the locus of the $Q2$ region beneath the head (see figure 5.2). This angle cannot however be determined with accuracy from the hairpin signatures. The values given here are therefore only rough estimates. In the present flow, the neck angle is found to vary between 25^o and 90^o ($\pm 5^o$) for all streamwise positions. The same values are found in the zero pressure gradient turbulent boundary layer. The $Q2$ events are always obvious and easy to see in the appropriate Galilean frame of reference, whereas the $Q4$ events are not always seen in the frame moving with the centre of the vortex. So the stagnation point and ISL events are not present in these cases. The calculation techniques for the parameters of hairpin and hairpin packet are described with more details in section 5.3.1.

Zhou et al. (1996, 1999) using computation methods, reported that the hairpin vortices which appear close to the wall have long legs that are consistent with the quasi-streamwise wall vortices. These quasi-streamwise vortices are associated with the low-speed streaks in the buffer layer. Kim (1987) and Kim (1989) also found a similar behaviour using direct numerical simulations. Since it is impossible to detect the hairpin legs and low-speed-streaks with the present two dimensional PIV data in xy plane, we do not know if they exist in the present flow. On the other hand, maximum turbulence production happens around $y/\delta = 0.6$ in the present flow as is shown in figure 5.11, whereas the maximum turbulence production take places close to the wall in ZPG turbulent boundary layers. There exists an unanswered question of knowing what is the turbulence production mechanism in APG turbulent boundary layers? Is

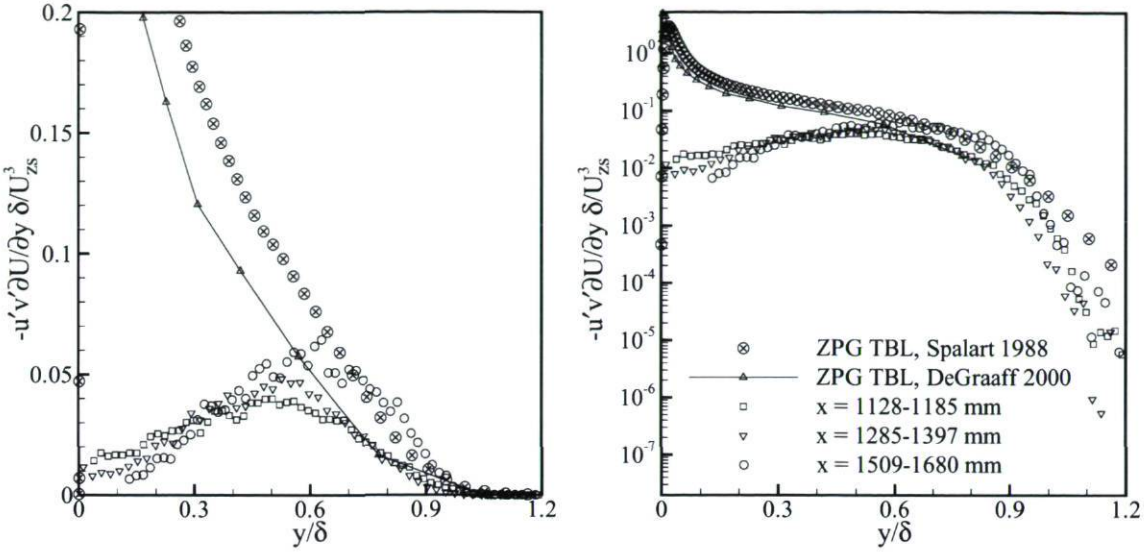

Figure 5.11: Turbulence production as a function of wall-normal distance at all streamwise positions showing that the maximum occurs around $y/\delta = 0.6$.

the turbulence production mechanism similar to those proposed in the ZPG turbulent boundary layer? We can only suppose that hairpin packets are probably involved in turbulence production with the acquired PIV data in the present flow. The strong $Q2$ events associated with the hairpins support that hypothesis. Three dimensional information acquired using DNS or equivalent methods is necessary to study the production mechanisms in adverse pressure gradient TBL.

5.2.4 Hairpin Packets

We almost always found that hairpin vortices occur in streamwise-aligned packets in the outer layer like in the ZPG case. Individual hairpins within one group travel at nearly the same streamwise velocity. In other words, the hairpin vortices within the hairpin packets propagate with small velocity dispersion. Hairpin packets are also found throughout the outer layer for all streamwise locations. The patterns that are identified as the signatures of hairpin packets are qualitatively very similar to the packets created via the auto-generation mechanism (Zhou et al. (1996) and Zhou et al. (1999), see figure 2.5) and also very similar to the PIV results of Adrian et al. (2000).

The present two-dimensional PIV data is compared with the xy plane patterns of Zhou et al. (1999) for channel flow. Zhou et al. (1999) studied the auto-generation mechanism of hairpin packets in a channel flow using DNS. Based on their results a primary hairpin with a certain strength and height can give birth to a packet. Kim et al.

(2008) have also found similar results in a turbulent channel flow using DNS with both clean background and background noise (see section 2.2.2 for more details). If a xy plane (i.e. laser sheet of PIV) passes through the middle of a hairpin packet, the instantaneous velocity vector field would possess velocity signatures similar to those found in the xy plane patterns of Zhou et al. (1999) shown in figure 2.5. The similarities seen between the present PIV results and the results of Zhou and co-workers provide a strong basis for associating the observed two-dimensional patterns with three-dimensional hairpin packets. For instance, the point-by-point similarity between our PIV results and Zhou et al. (1999) results (spanwise vortex, $Q2$, $Q4$ and ISL) are clearly shown when comparing figures 5.12-a and b with figure 2.5. The primary hairpin vortex would be the biggest one, similar the Zhou et al. (1999) results, that spawns the secondary hairpin vortex.

We found at least one hairpin vortex packet in 98% of all examined PIV data. Figure 5.13 illustrates examples of hairpin packets at three streamwise positions (solid lines are associated with the frontier of uniform momentum zones). It is worth recalling that a minimum of three hairpin vortex signatures in close spatial proximity to each other is necessary for us to define it as a packet. Moreover, the hairpin packets are the most commonly observed structure in our PIV data. So the APG turbulent boundary layer is densely populated with hairpin vortex signatures similar to what was described for canonical turbulent wall flows by many researchers (see section 2.2.2). The convection velocity can vary from packet-to-packet at different given y-locations like the individual vortices. Figures 5.14-a and b show two examples of hairpin packets which occur respectively close to that wall and at the edge of the boundary layer. The hairpin heads within the packet 1 occur between $y/\delta = 0.07$ and 0.16 in figure 5.14-a, whereas the hairpin packet in figure 5.14-b goes up to $y/\delta = 1$.

The convection velocities in figures 5.13-a, b and c vary in the range $u_c = 0.56 - 0.67U_e$ and $v_c = 0 - 0.46V_e$. Since the convection velocities may vary from one hairpin to another within a packet because of dispersion, some hairpins within a packet may not be revealed within moving frame of reference because they would convect with a different convection velocity (for instance hairpins N, O and P in figure 5.8-b). There exist cases where some hairpin heads may not be clearly seen even with different Galilean frames. Figure 5.15 presents an example of a hairpin packet in which hairpin vortex signature labeled A is not circular in the presented Galilean frame in large graph. It is tried to have the best possible moving frame of reference in the inset, but hairpin vortex labeled A is only barely seen. Moreover, the associated swirling strength patch is smaller in size and strength than other iso-regions of swirling strength. These features indicate that it can probably be a case of a twisted hairpin packet. The hairpins within a packet are not perfectly aligned in the streamwise direction. Zhou et al. (1999) believed that an asymmetric hairpin leads to twist the hairpin packet and Kim et al. (2008) reported

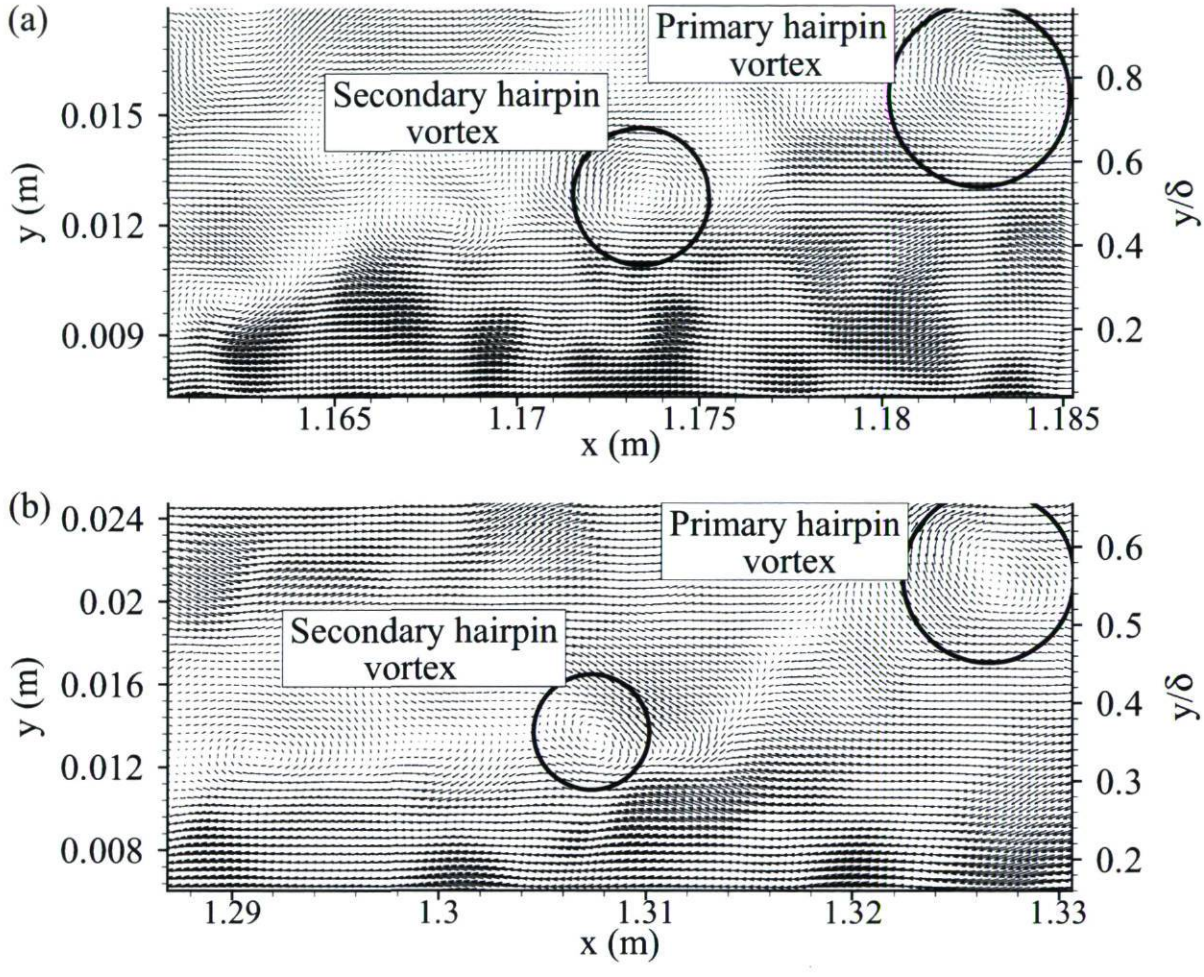

Figure 5.12: Streamwise/wall-normal velocity vector fields shown using Galilean decomposition (the point-by-point similarity with the results of Zhou et al. (1999) in figure 2.5 is illustrated), vectors viewed in frames-of-reference convecting at: a) $u_c = 0.79U_e$, $v_c = 0.5V_e$ in region $x = 1128 - 1185$ mm, b) $u_c = 0.67U_e$, $v_c = 0$ in region $x = 1285 - 1397$ mm.

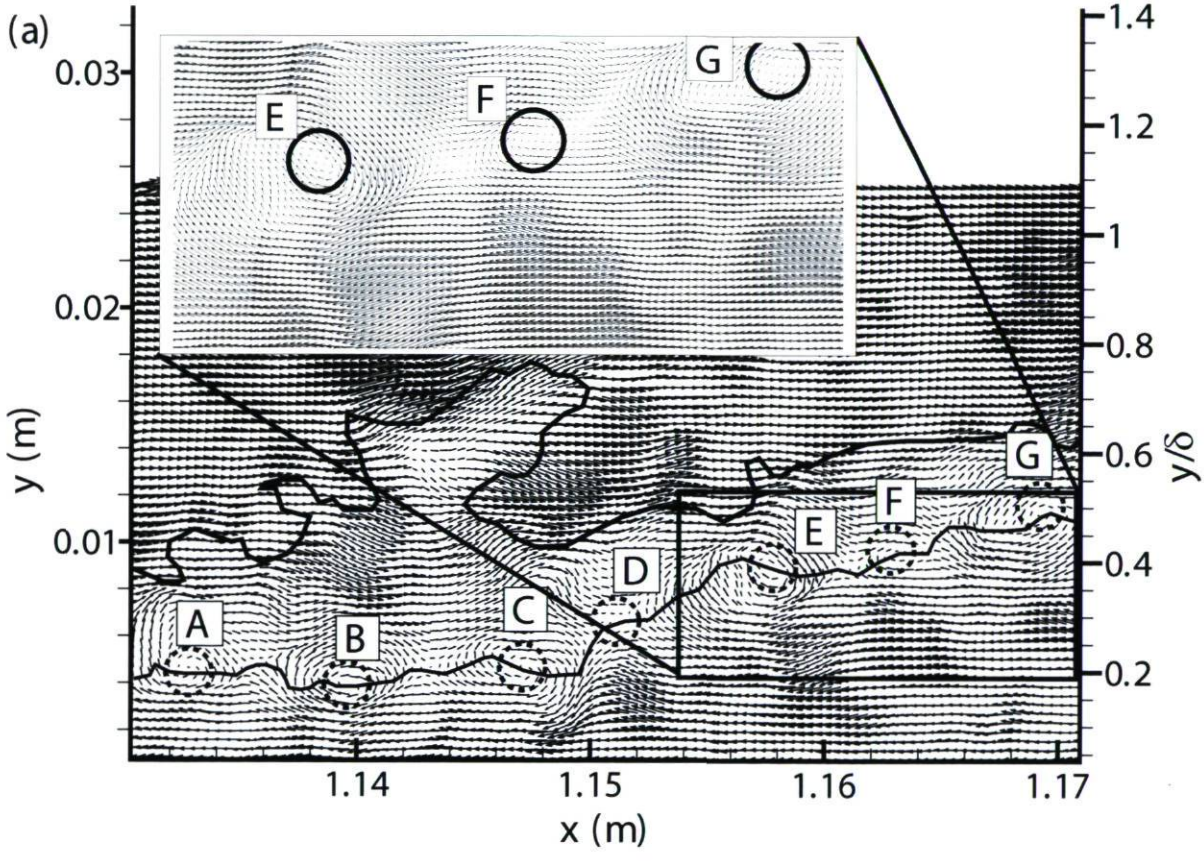

Figure 5.13 (a), for caption see next page.

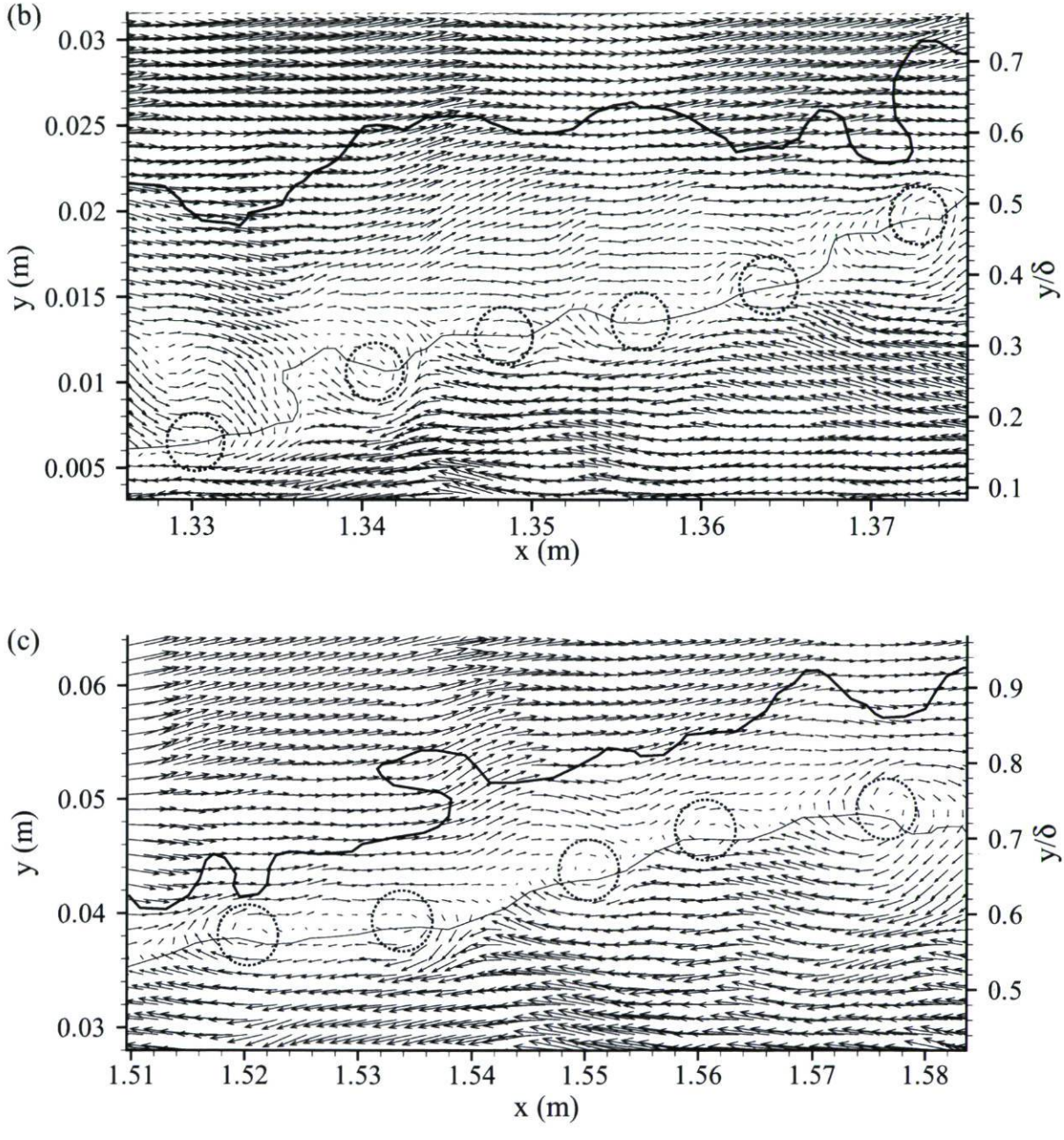

Figure 5.13: Streamwise/wall-normal velocity vector fields shown using Galilean decomposition (one vector out of 4 in large plots for clarity). Vectors viewed in frames-of-reference convecting at: a) $u_c = 0.56U_e$, $v_c = 0$ in region $x = 1128 - 1185$ mm b) $u_c = 0.56U_e$, $v_c = 0$ in region $x = 1285 - 1397$ mm, c) $u_c = 0.67U_e$, $v_c = 0.46V_e$ in region $x = 1509 - 1680$ mm. The solid lines are contours of constant streamwise momentum.

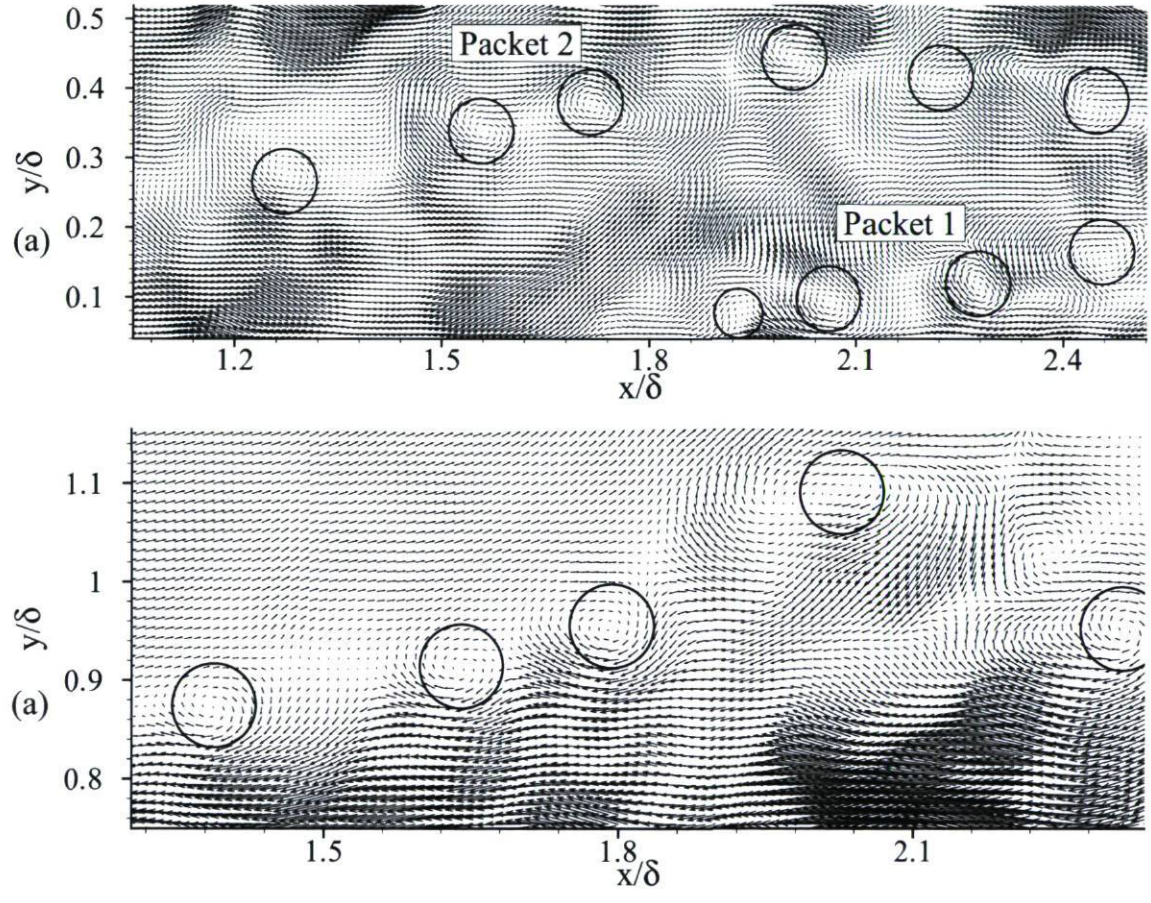

Figure 5.14: Streamwise/wall-normal velocity vector fields shown using Galilean decomposition as vectors viewed in frames-of-reference convecting at: a) $u_c = 0.55U_e$, $v_c = 0$ in region $x = 1128 - 1185$ mm, b) $u_c = 0.89U_e$, $v_c = 0.75V_e$ in region $x = 1509 - 1680$ mm.

that background noises cause the hairpin packets to become complicate. Since in the case of a twisted hairpin packet, the xy plane would not be exactly at the mid-plane of some hairpins, the head of these hairpins can not be clearly revealed in the associated Galilean frames, while the $Q2$ events associated with the hairpin would be seen. So hairpin A in figure 5.15 may not be centered on the xy plane.

To provide a better idea of the spanwise characteristics of hairpin packets, a new series of measurements in an inclined streamwise/spanwise plane were done. These measurements were done by the present worker, Saeed Rahgozar (new PhD student) and Diego Lopez (an undergraduate student). The same reference velocity and the same streamwise position (the first one) were used in order to have the same flow. Figure 5.16 illustrates the side-view of the test section and the positions of the inclined planes for different streamwise positions. The direction of 160^o with respect to the flow direction (x-direction) is chosen based on the upper neck angle of hairpin vortex signatures discovered in the xy plane. The statistical results of neck angle are presented in section 5.3.2. The results show that the neck angle varies between 25^o and 90^o with a maximum peak of occurrence around 70^o to the x-direction (the average neck angle is about 69^o). So the chosen inclined plane with 160^o is approximately perpendicular to the plane of the hairpin arch ($70^o + 90^o = 160^o$).

The component of velocity fluctuation in the x_{160}-direction within the inclined 160^o-plane is hereafter referred to as u'_{160}. Figure 5.17-a shows the uniform regions of u'_{160} in the inclined plane (in region $x = 1128 - 1185$ mm). The dark regions are low-speed regions ($u'_{160} < 0$) and the white regions are the high-speed regions ($u'_{160} > 0$). The vortices associated with hairpin necks usually surround the low-momentum regions. The necks of hairpins within a hairpin packet are indeed expected to cause a strong retarded streamwise momentum in the inboard regions (between the necks of hairpins), while they cause accelerated streamwise momentum in the outboard regions (see figure 5.18). Hence, a high velocity gradient exists between the inboard and the outboard regions. A similar behaviour in xy plane is also seen at the heads of hairpin vortices where significant $\partial u/\partial y$ exists as illustrated in figure 5.20.

Two hairpin packets are detected in figure 5.17-b. With regard to hairpin geometry which could be one-sided or two-sided, strong $u'_{160} < 0$ can be generated in two manners: i) beside the one-sided prograde or retrograde vortices (for example D_{2p} in figure 5.17-b), ii) between the necks of a two-sided hairpin (for example J_{2p} and J_{2r} in figure 5.17-b). If a group of vortices (with appropriate signs) in close spatial proximity to each other are aligned in the x_{160}-direction and surround the low-momentum regions, they are potential candidates to form a hairpin packet. It is clearly seen that hairpin packets are not perfectly aligned in the streamwise direction. If the xy plane crosses

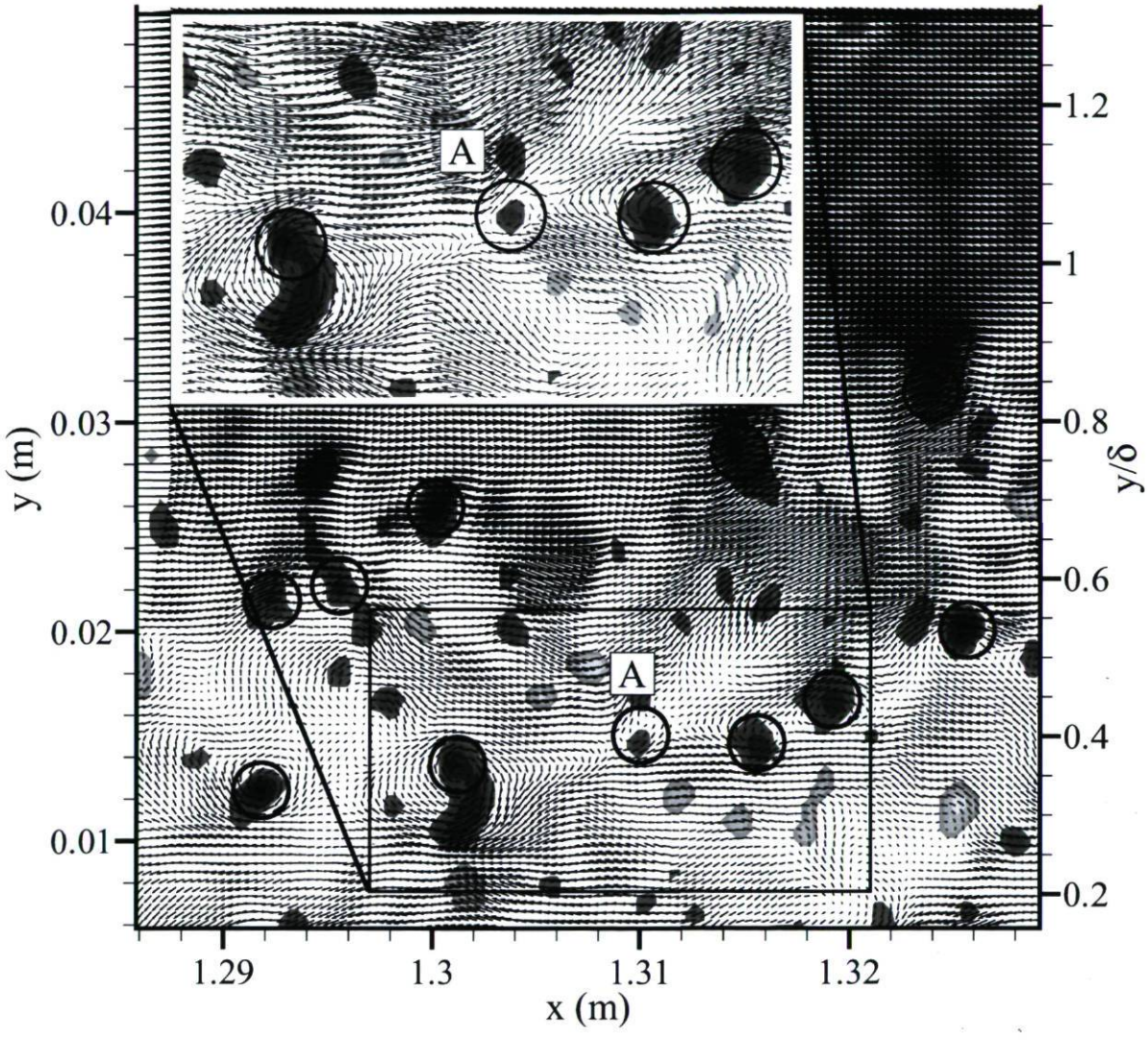

Figure 5.15: Streamwise/wall-normal velocity vector field shown using Galilean decomposition in region $x = 1128 - 1185$ mm and vectors viewed in a frame-of-reference convecting at $u_c = 0.51U_e$, $v_c = 0.43V_e$ in large graph and $u_c = 0.46U_e$, $v_c = 0.13V_e$ in the inset (iso-regions of swirling strength are superimposed).

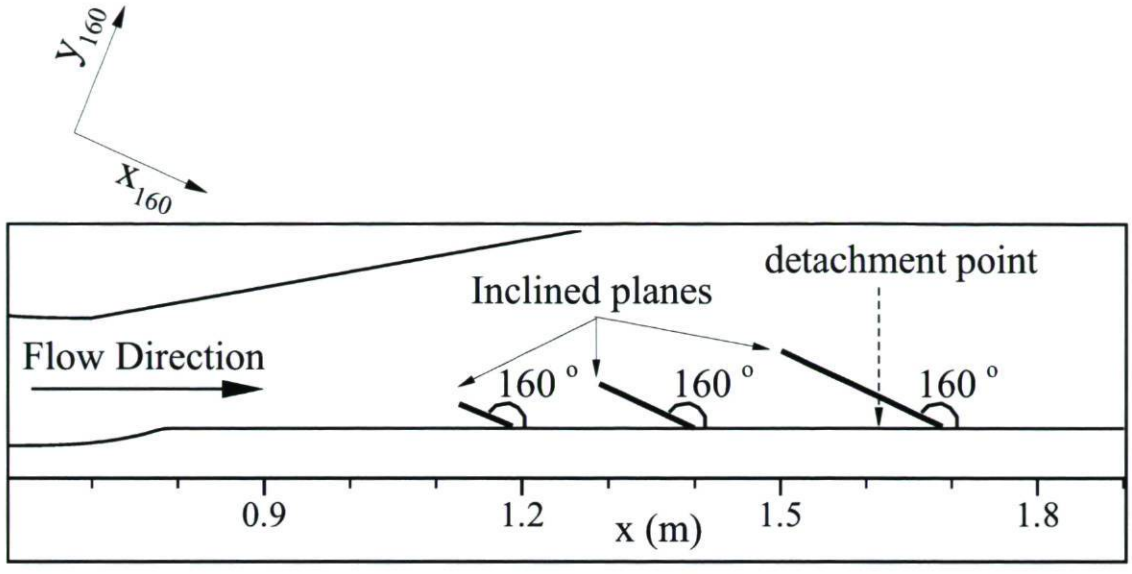

Figure 5.16: Side view of test section showing the inclined planes.

the first packet (labeled packet 1, xy plane 1), we would see only the hairpin vortex labeled C1. So the other vortices of this packet can not be detected in this xy plane since the packet is twisted. If the second proposed xy plane crosses another hairpin packet (labeled packet 2, xy plane 2), it is possible to detect two separate groups of hairpin vortices as two hairpin packets. The first group includes A2 to D2 vortices and the second group contains G2 to L2 vortices. If the hairpin vortex has a strong and wide $Q2$ event, it is possible that the $Q2$ event is seen in the xy plane whilst the head of related vortex can not be detected.

Based on these descriptions we can conclude that the number of hairpin vortices per packet is often underestimated in the xy planes. Additionally, a single packet is sometimes interpreted as two or probably more than two hairpin packets.

5.2.5 Hairpin Packets and Uniform Momentum Zones

Meinhart and Adrian (1995) reported that large regions of the flow in the turbulent boundary layer, which have relatively uniform values of the streamwise momentum, are separated by thin zones with significant velocity gradient ($\partial u/\partial y$). Analysis of our PIV results shows that almost always the instantaneous velocity fields contain zones having these properties too. Figures 5.19-a to c illustrate the uniform momentum zones corresponding to figures 5.13-a to c respectively. The uniform momentum zones have been separated by contour lines of constant u and the dashed circles are the positions

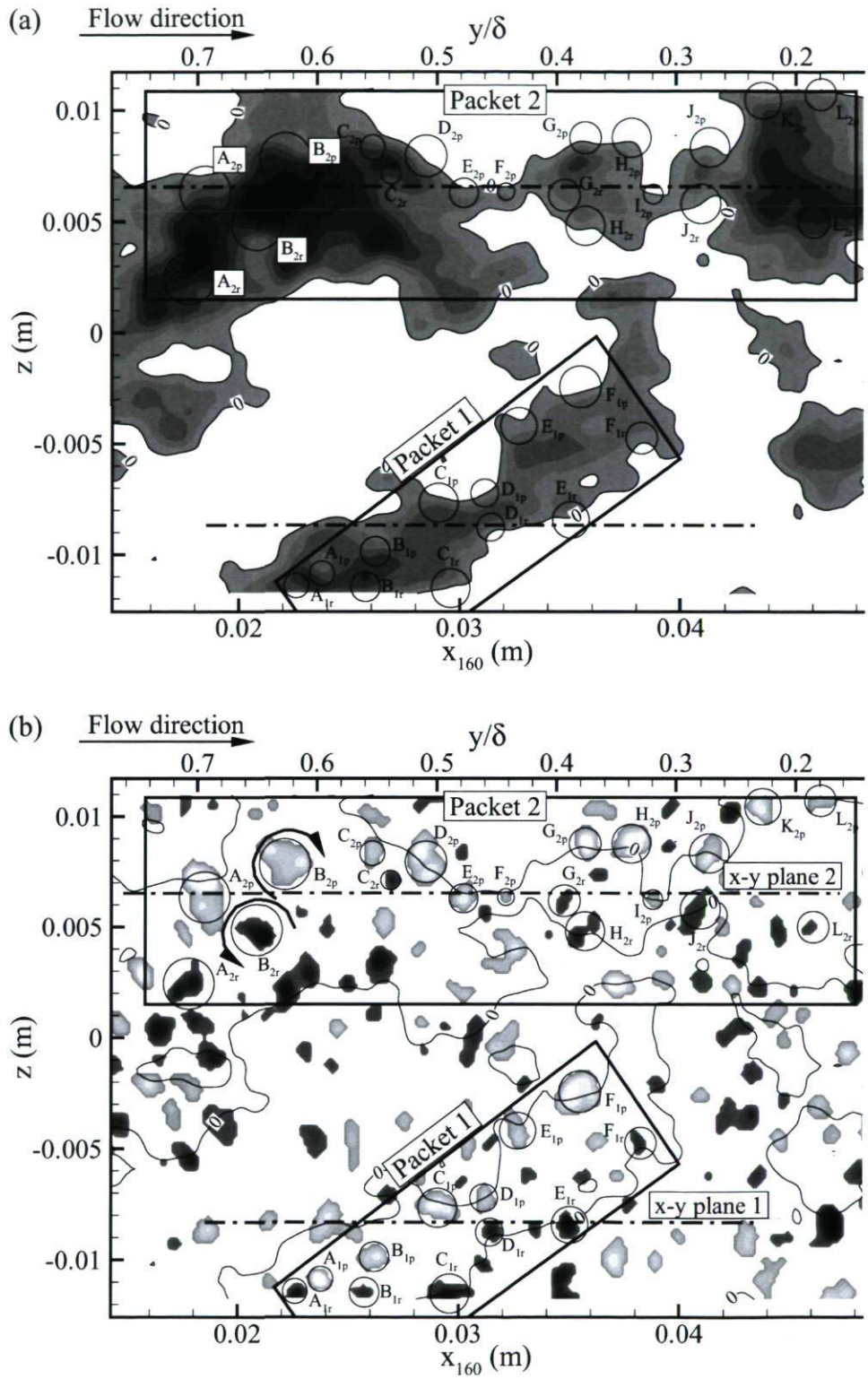

Figure 5.17: Hairpin packets identified using the iso-regions of out-of-plane swirling strength in spatial proximity to each other which have roughly the same convection velocity in 160^o inclined plane; a) regions of $u'_{160} < 0$, b) concentrated regions of swirling strength associated with hairpin necks or legs.

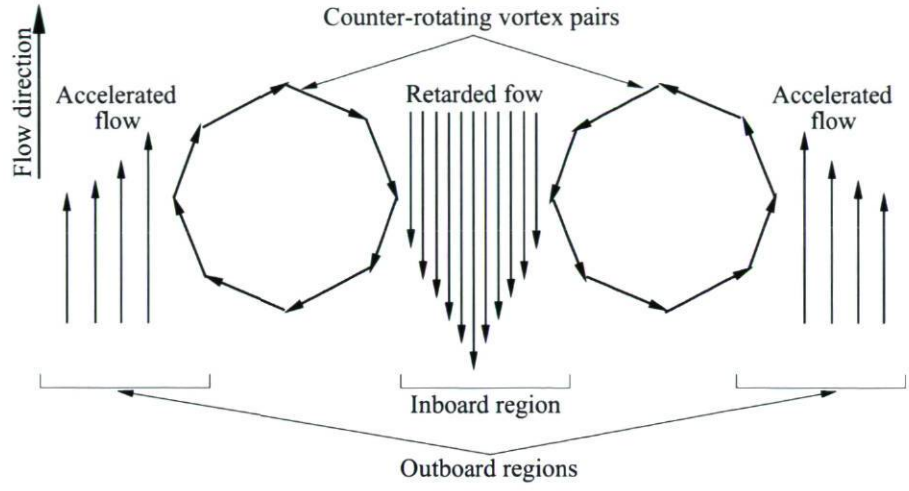

Figure 5.18: Idealized hairpin vortex signature in 160^o inclined plane (the idea of this schematic was taken from Tomkins and Adrian (2003)).

of hairpin heads. The lines pass commonly through the centres of the hairpin heads as seen in figures 5.8 and 5.13.

The coincidence between uniform momentum boundaries and the hairpin heads clearly demonstrates an association between hairpin packets and uniform momentum zones as reported by Adrian et al. (2000). This association is further substantiated by the data in figures 5.20-a and b. In these figures vertical profiles of streamwise velocity component are superimposed on the λ_{ci} iso-regions. The circled λ_{ci} are associated with the heads of hairpin vortices. The hairpin heads create regions of significant $\partial u/\partial y$ along the boundaries between uniform momentum zones. In other words, the u-component changes significantly at the boundaries of uniform momentum zones, whereas it remains roughly constant within the zones. It is important to note that packets of vortices may also align with other packets to create even longer zones. Therefore, a single zone of uniform momentum may be related to more than one packet.

Since, often three and sometimes more than three hairpin packets are present in one vector field at different heights above the wall, the relation between uniform momentum zones and hairpin packets can be summarized as follows. Meinhart and Adrian (1995) and Adrian et al. (2000) suggested that the zones of uniformly retarded flow are the backflow induced by hairpin packets which are aligned in the streamwise direction. Indeed, the induced flow from each hairpin vortex adds coherently with the flows from following vortices in a packet to create a low momentum region. Therefore, the generated low momentum region of flow within a packet is significantly longer than the low-momentum region induced by any single hairpin.

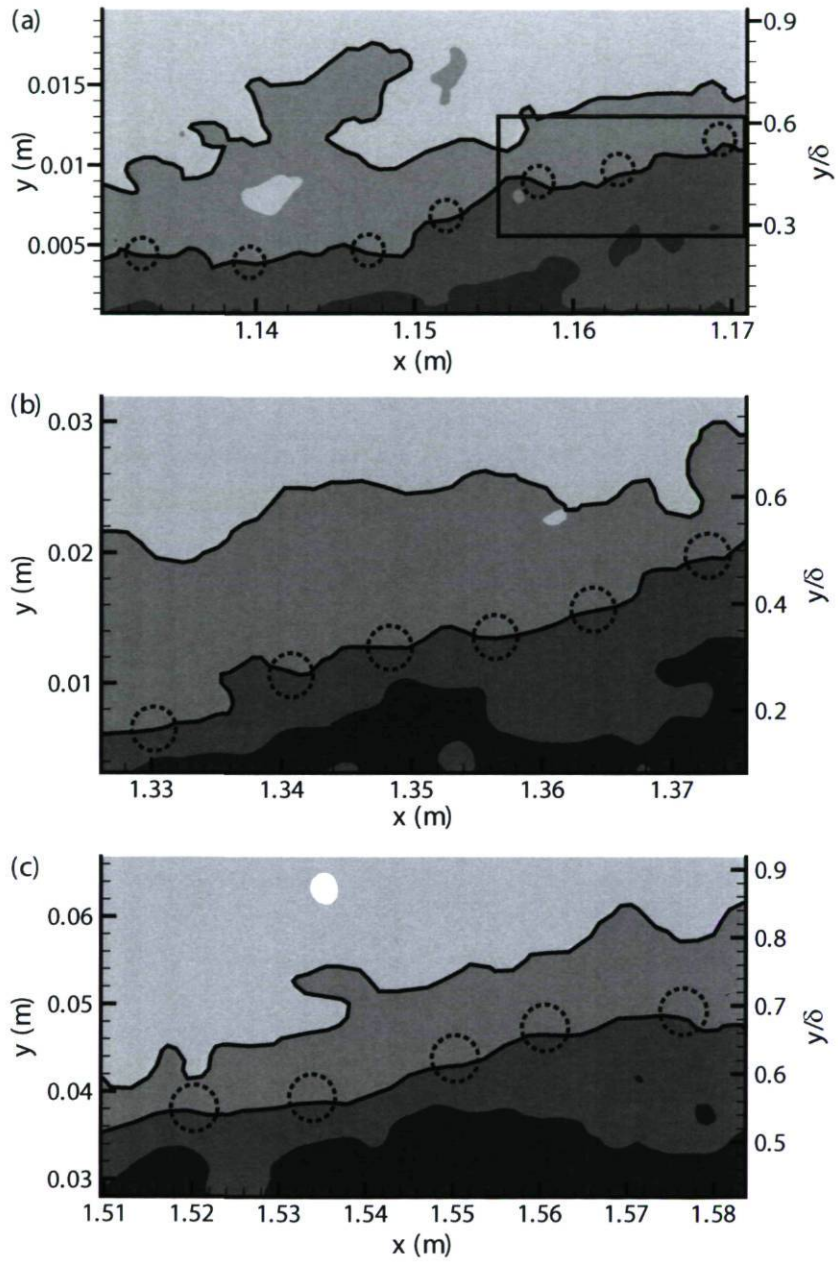

Figure 5.19: Contours of constant u and hairpin vortex heads (circles) along the boundaries separating regions of uniform-momentum fluid (corresponding to figure 5.13). The black lines separate the flow field into zones, in which the streamwise momentum is approximately uniform in regions: a) $x = 1128 - 1185$ mm, b) $x = 1285 - 1397$ mm, c) $x = 1509 - 1680$ mm.

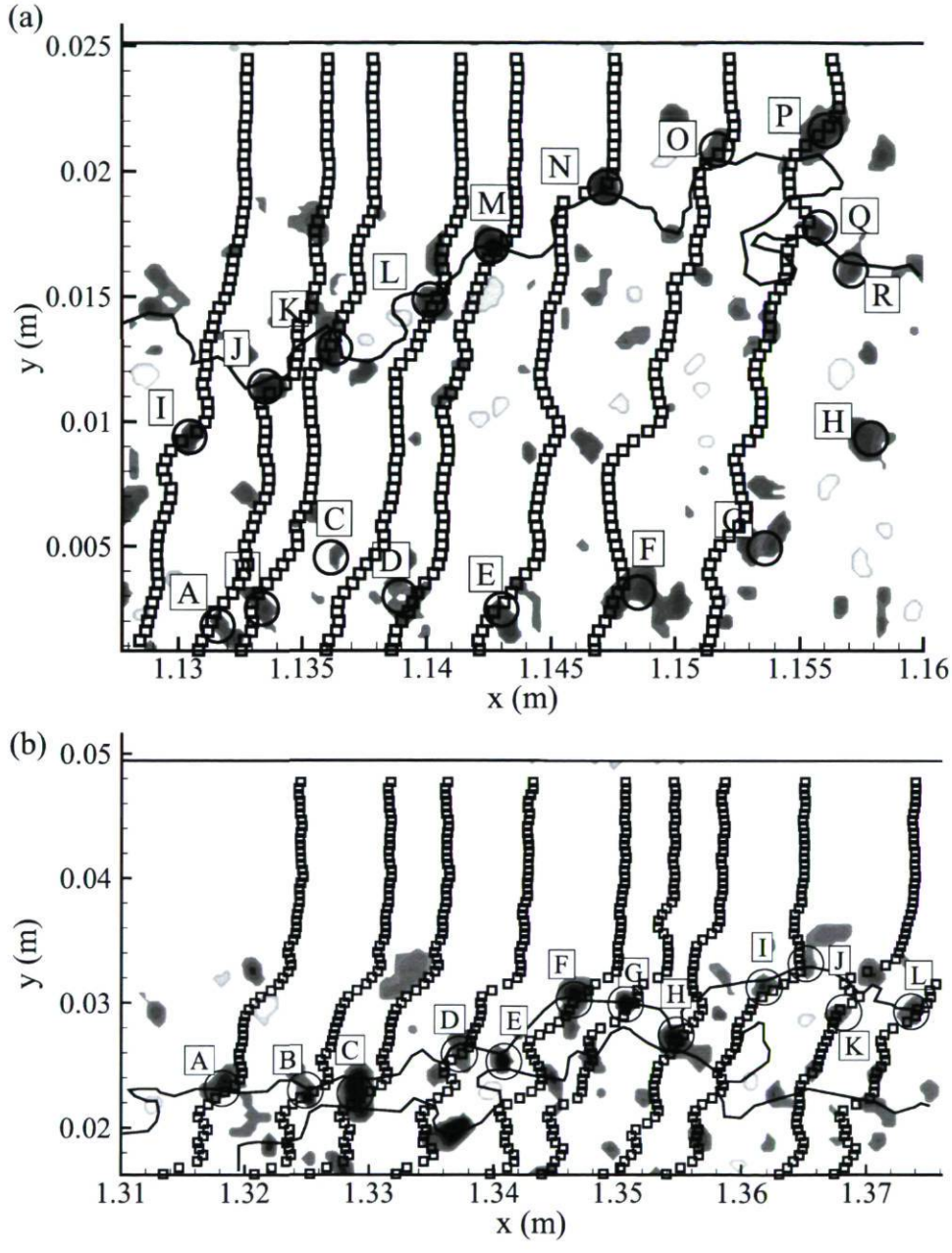

Figure 5.20: Circled iso-contours of λ_{ci} associated with the heads of the hairpin vortices and super-imposed profiles of streamwise velocity showing the u-component changes largely at hairpin heads in regions: a) $x = 1128 - 1185$ mm corresponding to figure 5.8, b) $x = 1285 - 1397$ mm. Profiles correspond to the x-positions of vortices I-P for a, and A-L for b.

5.2.6 Relation to $u'v'$

Figure 5.21 presents the streamwise histories of streamwise fluctuations, wall-normal fluctuations and $-u'v'$ of the upper hairpin packet shown in figure 5.8. These histories are given at three different heights ($y/\delta = 0.61$, 0.89 and 0.98). The characteristic features of the hairpin vortex signatures in figure 5.8 create clear imprints in the streamwise variation. For instance, figure 5.21-a exhibits six peaks of high Reynolds stresses between $x = 1.135$-1.16 m, each of which corresponds to fluid directly underneath the heads of hairpins K-R. This fluid has low momentum because it is being ejected away from the wall by the hairpins as the v'-component is positive. The u' and v' components change signs at $x = 1.1327$ m and $x = 1.1346$ m. These points correspond to the stagnation points on the inclined shear layers associated with the hairpins labeled J and K. The maximum values of $-u'v'$ occur fore and aft of the stagnation points. Streamwise histories of streamwise fluctuations, wall-normal fluctuations and $-u'v'$ at $y/\delta = 0.89$ is shown in figure 5.21-b. The zone of low momentum and of high $-u'v'$ between $x = 1.145$-1.155 m corresponds to fluid directly underneath the heads of hairpins N-P. The maximum of $-u'v'$ occurs at $x = 1.147$ m which corresponds to the head of hairpin N. The streamwise histories of u', v' and of $-u'v'$ at $y/\delta = 0.98$ are given in figure 5.21-c. Similarly, local maxima of u', v' and of $-u'v'$ corresponding to the heads of hairpins O and P occur at $x = 1.151$ m and $x = 1.154$ m. These results show that the presence of hairpin packets producing considerable Reynolds shear stress is a common and recurrent feature in the outer layer.

These results are consistent with results that were reported by Ganapathisubramani (2004) for ZPG TBL. He found hairpin structures and packets producing considerable Reynolds shear stress as a common and recurrent feature in the log layer. So, it can be proposed that turbulence production is inseparable from the dynamics of hairpin vortices in wall-bounded turbulent flows and it would be the case for the present flow. It can even be conjectured that the hairpin vortices would be responsible for the main part of turbulence production in APG turbulent boundary layers. As was pointed out by Adrian et al. (2000), Bogard and Tiederman (1986) and Luchik and Tiederman (1987) observed that several $Q2$ events often occur in temporal series of measurements. These researchers believe a turbulent burst consists of several $Q2$ events. Their idea can be discussed by the concept of hairpin vortex packet. Each $Q2$ event is associated with a hairpin vortex. So a series of Q2 events corresponds to the hairpin vortices occurring in a hairpin packet. Consequently, the temporal histories on which Bogard and Tiederman (1986) and Luchik and Tiederman (1987) based their work are similar to the streamwise histories shown in figure 5.21.

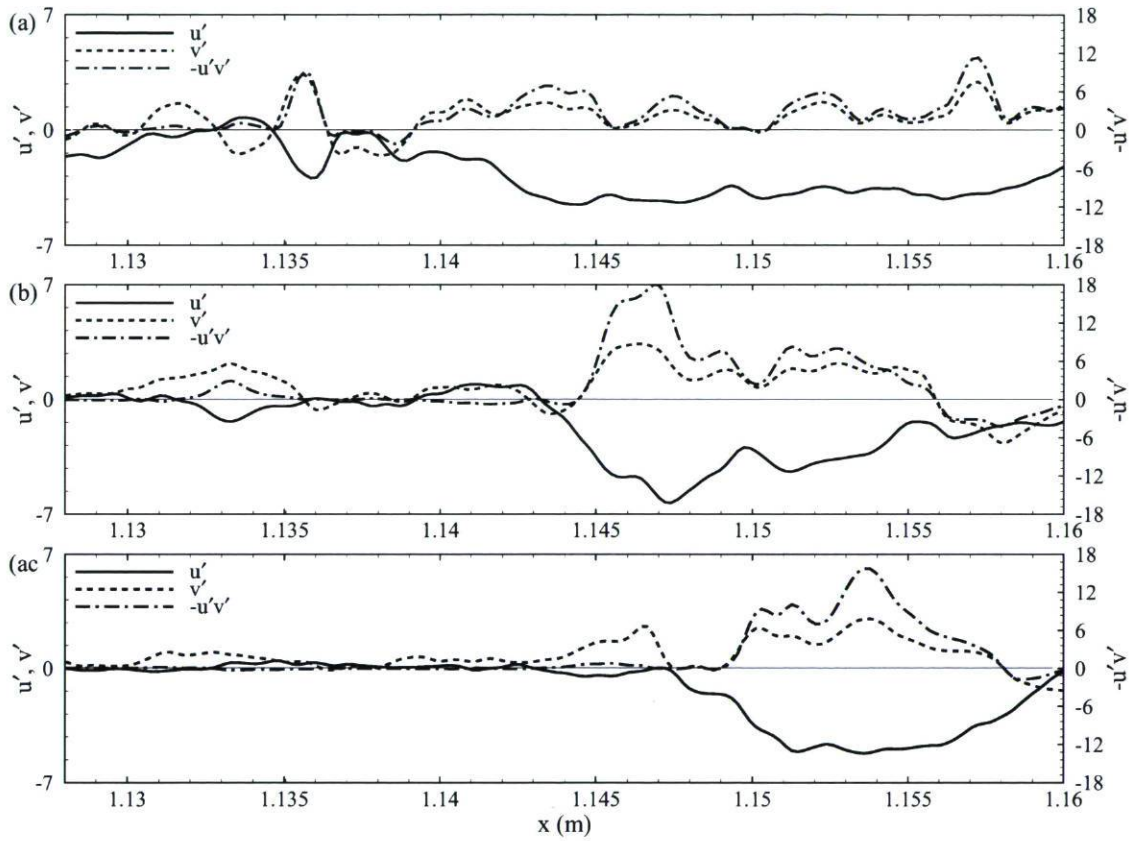

Figure 5.21: Traces of the instantaneous u', v' and $u'v'$ through the vector field in figure 5.8 show that the form of the variation of $u'v'$ is associated with the hairpin vortex signature; a) $y/\delta = 0.61$, b) $y/\delta = 0.89$, c) $y/\delta = 0.98$.

5.3 Statistical Results

Although the vast majority of instantaneous realizations illustrate that hairpin vortex organization is a common feature of the upper region, the parameters of these patterns must be investigated statistically. Statistical results from the two-dimensional PIV datasets in xy planes are presented in this section. Various statistical quantities were computed at different streamwise positions and are compared. Theses parameters are employed to study the evolution of the hairpins and hairpin packets parameters within the adverse pressure gradient zone between the pressure peak and separation point. Indeed, the ensemble average and other statistics are obtained to represent the properties of interest. Moreover the obtained hairpin characteristics for the present study and ZPG TBL are also compared.

5.3.1 Definition of Parameters and Computation Procedure

The parameters of hairpins and hairpin packets are computed with the help of intermediate data files of the instantaneous fields. These files are the same ones that were used to identify the hairpins and the packets as explained in section 5.2.2. They contain coordinates (x and y), x and y scaled by boundary layer thickness (x/δ and y/δ), instantaneous velocity components (u and v), swirling strength (λ_{ci}), swirl intensity for each vortex ($\bar{\lambda}$) and scaled diameter of vortices (D/δ). The calculation methods of $\bar{\lambda}$ and D/δ are explained in sections 4.4.

Once two-dimensional instantaneous velocity fields and swirling strength patches are visualized in Tecplot, the hairpins parameters are determined with the help of the probe tool of Tecplot. Clicking on the local maxima of λ_{ci} patches using the probe tool of Tecplot directly gives $\bar{\lambda}$, D/δ, x/δ, y/δ, u_c and v_c for each vortex core considered to be a hairpin head. x/δ is used to calculate the streamwise spacing between the hairpin vortices. Subtracting the x/δ values of two neighbour hairpin heads gives the streamwise spacing ($\Delta x/\delta$) for these vortex cores. Since the boundary layer thickness varies by about 30% along a field, the scaled coordinates and diameters are calculated with local boundary layer thickness instead of an average δ.

The neck angle and ISL angle can be determined when the velocity field is decomposed in a proper Galilean frame using u_c and v_c. The angle at which the plane formed by the head and neck of the hairpin is inclined to the wall α can be estimated with the angle of the locus of the Q2 region beneath the head (see figure 5.2). A linear curve is matched on the ISL to determine the angle of ISL event β. The angle of this line

x/δ	y/δ	D/δ	$\bar{\lambda}$ (s^{-1})	α $(^o)$	β $(^o)$	$\Delta x/\delta$	γ $(^o)$	No of hairpin	u_c/U_e	v_c/V_e
0.71	0.13	0.05	-1503.8	60	45	0.09	17	6	0.39	0.87
0.80	0.17	0.07	-2989.9	70	-	0.12			0.48	-1.3
0.92	0.19	0.07	-2185.3	78	50	0.07			0.54	-1.1
0.99	0.24	0.06	-1838.4	90	60	0.15			0.62	-1.6
1.13	0.24	0.08	-2047.9	65	45	0.19			0.61	-0.12
1.13	0.28	0.06	-2996.9	73	40				0.62	-1.4

Table 5.1: Example of written hairpin vortices parameters in region $x = 1128 - 1185$ mm

and streamwise direction is the ISL angle as is shown in figure 5.2. These angles are determined using a virtual protractor. Since the virtual protractor has subdivisions of 10^o, the measured angles have an estimated uncertainty of $\pm 5^o$. This virtual protractor is superimposed on the $Q2$ region to determine the neck angle. Similarly it is also superimposed on the ISL line to determine β. The growth angle γ is determined by fitting a linear curve passing through the hairpin heads (figure 5.43). So, once the straight line is drawn, the virtual protractor is superimposed on this line to measure the growth angle. Table 5.1 illustrates a sample of parameters related to a hairpin packet registered in the database.

This database compiles the results of fifty investigated instantaneous velocity fields at each streamwise position for the present study and also fifty instantaneous fields for ZPG TBL from the database of Adrian et al. (2000). The total number of detected hairpin vortices within the fifty fields is 615, 609 and 551 for the first, second and third streamwise positions respectively and 463 hairpins for the ZPG TBL. Table 5.2 presents the ensemble average number of packets per field and number of hairpin vortices per packet. It is worth mentioning once again that the number of hairpins per packet is underestimated because some hairpins are missed when investigating xy-planes (see section 5.2.4). Figures 5.22 and 5.23 show the distribution of population of hairpin vortices and hairpin packets as a function of y/δ. In the subplots a of these figures, each point is computed on an interval of 0.24 of y/δ in region $y/\delta = 0.04 - 1.00$, while in subplots b each point is computed on an interval of 0.2 of y/δ in region $y/\delta = 0.2 - 1.0$. The points are at the center of each interval. In figure 5.22, if the core of a hairpin head is within an interval, i.e. $0.04 \leq y/\delta < 0.28$, this hairpin is accounted in this interval. Similar computation is done for the figure 5.23, but the last hairpin in the streamwise direction which is usually the oldest one in a hairpin packet is accounted for each group of hairpins. In the ZPG case, the maximum of hairpin population is

	No. of hairpins per packet	No. of packets per field
ZPG TBL	3.9	2.4
$x = 1128$ mm	4.0	3.1
$x = 1285$ mm	3.8	3.2
$x = 1509$ mm	3.7	3.0

Table 5.2: Ensemble average of number of hairpins per packet and number of packets per instantaneous field for the different streamwise positions and for the ZPG TBL.

near the wall, and decreases in wall-normal direction. In the present flow, although the figures 5.22 and 5.23 indicate that the hairpin population decreases near the wall in streamwise direction, but the distribution of hairpin population for the first streamwise position is roughly similar to the ZPG TBL. Contrarily to the first streamwise position, the population of hairpins and hairpin packets increase with wall-normal distance in other locations and have a maximum value in the upper region. The hairpin population has a maximum around $y/\delta = 0.4$ for the second streamwise position (figures 5.22-a and 5.23-a) and around $y/\delta = 0.7$ for the last streamwise position (figures 5.22-b and 5.23-b). It is worth noting that the points of $y/\delta = 0.4$ and $y/\delta = 0.7$ are related to the interval of $0.28 \leq y/\delta < 0.52$ and $0.6 \leq y/\delta < 0.8$ respectively. Based on these results, first streamwise position is similar to ZPG TBL and the second location is in between the first and last streamwise positions. It is clear that the hairpin population is affected by pressure gradient. Furthermore, similar trend, but weaker, is also found for the prograde spanwise vortices as shown in figure 4.13. Shifting the maximum population of spanwise vortices, hairpins and hairpin packets to the upper region in the adverse pressure gradient zone, as separation is approached, is consistent with the results of Chong et al. (1998). Chong and co-workers have suggested that detached eddies are more frequently encountered near the detachment point.

5.3.2 Hairpin Vortex Parameters

Before presenting and discussing the statistical characteristics and behaviours of hairpin vortices, it is important to mention that all statistical results associated with the parameters of hairpins and of hairpin packets are obtained using the aforementioned

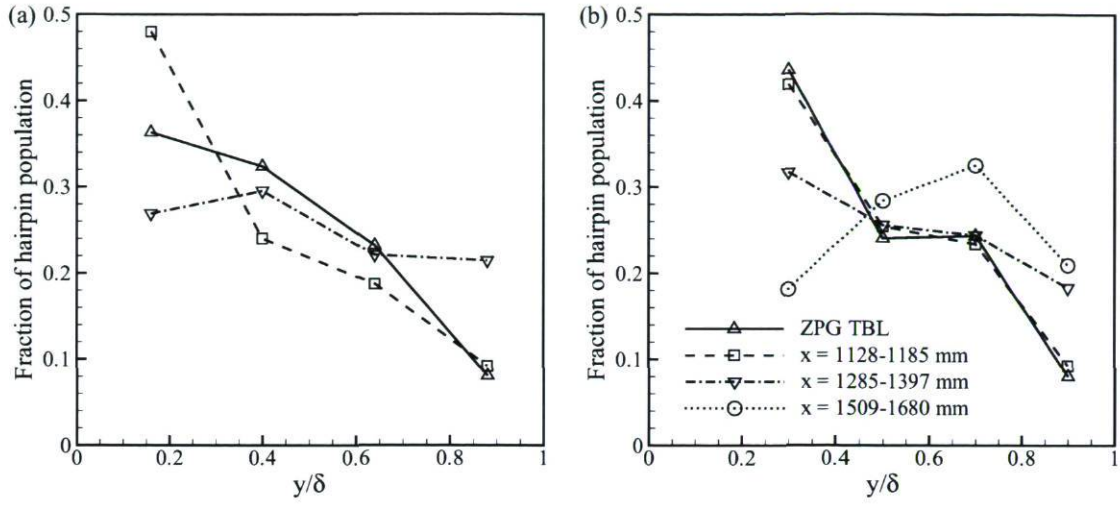

Figure 5.22: Histogram of hairpin population as a function of y/δ: a) for region from $y/\delta = 0.04$-1.00, b) for region from $y/\delta = 0.2$-1.0. Each point is computed on an interval of 0.24 of y/δ for a and 0.2 of y/δ for b. The points are at the center of each interval.

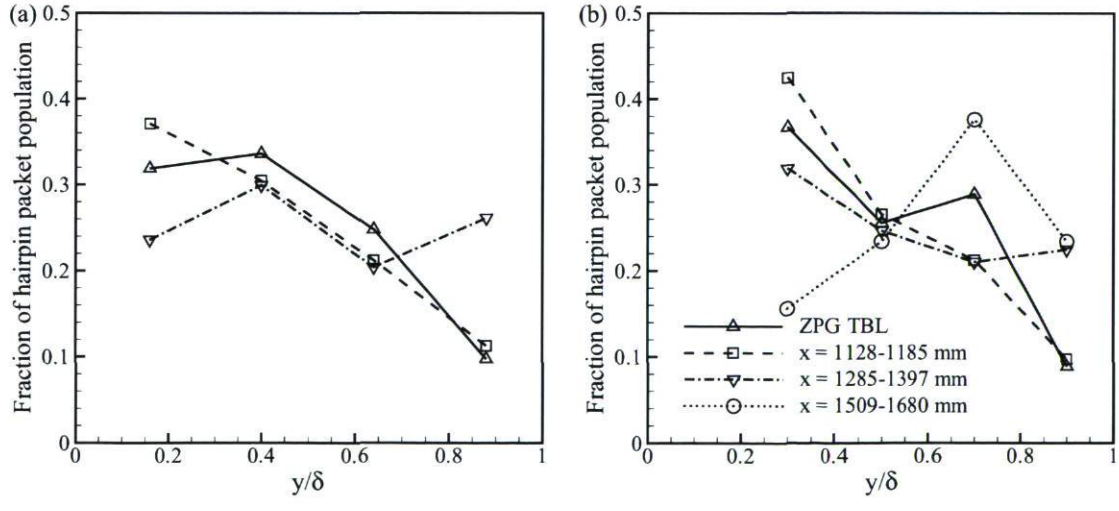

Figure 5.23: Histogram of hairpin packet population as a function of y/δ: a) for region from $y/\delta = 0.04$-1.00, b) for region from $y/\delta = 0.2$-1.0. Each point is computed on an interval of 0.24 of y/δ for a and 0.2 of y/δ for b. The points are at the center of each interval.

database in section 5.3.1 except for mentioned cases. Moreover, it is worth recalling that there is no information for $y/\delta \leq 0.2$ at the last streamwise position for the present study (see section 3.5.1). Probability density functions (pdf) are computed for various parameters of individual hairpin vortex signature and presented in this section. The proposed layers for ZPG TBL (viscous sublayer, buffer layer, logarithmic sublayer and the wake layer) are presented in sections 2.2.1 and 2.2.2. Since these subdivisions do not apply in the case of strong APG TBL, two regions are proposed for APG TBL in the present study. The region close to the wall that is called inner region ($y/\delta \leq 0.2$) where the viscosity and wall can have considerable effect and the upper region ($y/\delta > 0.2$) where the effect of viscosity is less important. These divisions are chosen to study the variation of various parameters in y-direction. It is worth noting that these devisions have no theoritical foundation. In fact, the initial idea to define the inner and upper regions of strong APG TBL and their limits is taken from the reported results for ZPG TBL. The pdfs of hairpin parameters in each region are acquired separately providing an idea of variation of hairpin characteristics in the wall-normal direction. The hairpin packet parameters are presented in the next section. Moreover the parameters of hairpins and of packets are studied before and after detachment for the last streamwise position ($x = 1509 - 1680$ mm).

Before analyzing the swirling strength and the diameter of vortices, it is worth recalling that these parameters are affected by the filter bandwidth, mesh width and interrogation window width. It is important to mention that they are the only parameters significantly affected by these effects. Since 50% overlap zone was used within the correlation process in both the present work and the ZPG turbulent boundary layer database of Adrian et al. (2000), the mesh width is half of the interrogation window width.

Swirling Strength

The probability density function of $\bar{\lambda}$ of hairpin heads scaled by U_{zs}/δ is shown in figure 5.24 for three streamwise positions of the present study and ZPG TBL. Table 5.3 presents the ensemble average of non-normalized swirl intensity and $\bar{\lambda}$ scaled by U_{zs}/δ, u_τ/δ and also $\bar{\lambda}^+$ ($\bar{\lambda}^+ = \bar{\lambda}\nu/u_\tau^2$). It is worth mentionning that hereafter, the computations of random uncertainty for different parameters of hairpin vortices and of hairpin packets, which is due to number of samples, is done based on 95% confidence (more details are presented in Appendix D).

Before presenting and analysing the swirl intensity using the pdf of $\bar{\lambda}\delta/U_{zs}$, we turn our attention first to the effect of spatial resolution on the swirl intensity. As explained

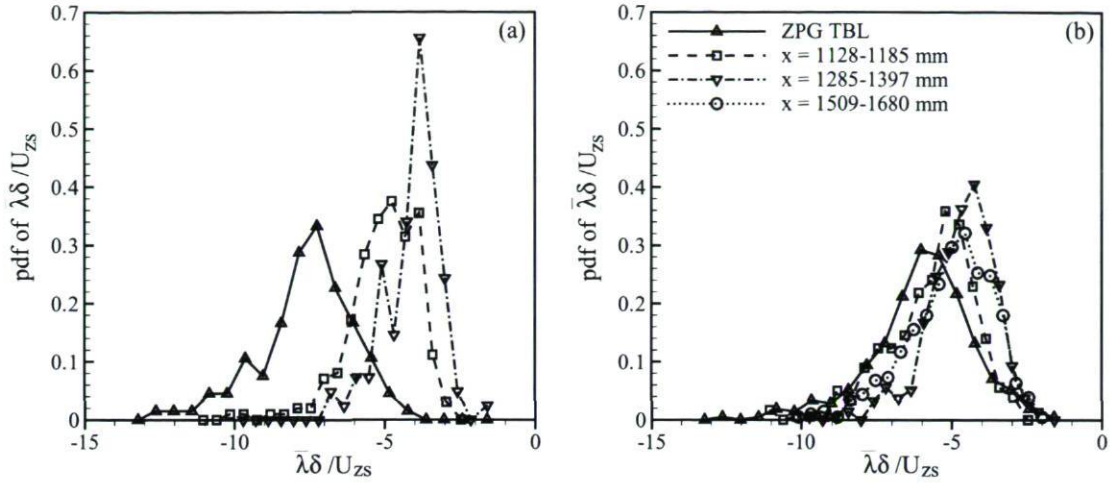

Figure 5.24: Probability density functions of $\bar{\lambda}$ associated with hairpin heads for all streamwise positions and ZPG TBL: a) lower region where $y/\delta \leq 0.2$, b) upper region where $y/\delta > 0.2$.

in section 4.5 the swirling strength is significantly affected by spatial resolution. The value of $\bar{\lambda}$ is underestimated when spatial resolution decreases as shown in figures 4.11-b and 4.12-b. In addition, it is shown in this figure that swirl intensity is much higher in the ZPG TBL in comparison to the present study. So, to interpret the results presented here, the effect of spatial resolution should also be considered. The maximum probability of $\bar{\lambda}$ scaled by U_{zs}/δ within the inner region of the ZPG TBL occurs at higher values in comparison to the present flow as shown in figure 5.24-a. Moreover, the values of $\langle\bar{\lambda}\rangle\,\delta/U_{zs}$ presented in table 5.3 is also show this tendency. Combining the results of the pdfs of $\bar{\lambda}\delta/U_{zs}$, the value of $\langle\bar{\lambda}\rangle\,\delta/U_{zs}$ and the profile of $\langle\bar{\lambda}\rangle\,\delta/U_{zs}$ in y-direction (see figure 5.25) within the inner region, it is found that in the ZPG TBL the swirl intensity is higher in comparison to the present flow. It is worth recalling that the swirling strength is more underestimated in the ZPG TBL because of the effect of spatial resolution, so the pdfs shown should be also shifted to higher negative value of $\langle\bar{\lambda}\rangle$. We can suppose that the swirl intensity is clearly affected by the pressure gradient but can not know the real differences between values of $\bar{\lambda}\delta/U_{zs}$ in such flows. In addition, the form of pdfs are changed in different cases and the width of the pdf distribution decreases as standard deviation is 1.57, 1.14 and 0.99 for the ZPG TBL, first and second streamwise positions for the present study respectively.

In the upper region ($y/\delta > 0.2$), since the PIV data now also exist for the last streamwise position, it is possible to interpret the results up to the point of detachment of the flow. Turning back now our attention once again to figures 4.11-b and 4.12-b,

		$\langle\bar{\lambda}\rangle$ (s^{-1})	$\langle\bar{\lambda}\rangle\,\delta/U_{zs}$	σ_λ	$\langle\bar{\lambda}\rangle\,\delta/u_\tau$	$\langle\bar{\lambda}^+\rangle$
ZPG TBL	$y/\delta \leq 0.2$	-186	-7.91 ± 0.30	1.57	-37.2	-0.018
	$y/\delta > 0.2$	-146	-6.28 ± 0.18	1.67	-29.25	-0.014
$x = 1128$ mm	$y/\delta \leq 0.2$	-1847	-4.89 ± 0.15	1.14	-66.3	-0.082
	$y/\delta > 0.2$	-2071	-5.51 ± 0.14	1.35	-74.4	-0.092
$x = 1285$ mm	$y/\delta \leq 0.2$	-983	-4.20 ± 0.19	0.99	-212.6	-0.127
	$y/\delta > 0.2$	-1107	-4.82 ± 0.10	1.14	-239.3	-0.143
$x = 1509$ mm	$y/\delta \leq 0.2$	-	-	-	-	-
	$y/\delta > 0.2$	-683	-5.09 ± 0.12	1.37	-	-

Table 5.3: Ensemble average of $\bar{\lambda}$ associated with hairpin heads at different streamwise positions and ZPG TBL. σ_λ is the standard deviation of $\bar{\lambda}\delta/U_{zs}$ distribution in figure 5.24.

it is seen that $\bar{\lambda}\delta/U_{zs}$ is slightly lower for the last streamwise position of the present study compared to the other ones. Based on these results, it seems that $\bar{\lambda}$ is slightly affected by pressure gradient (at least near the separation point). The absolute values of $\langle\bar{\lambda}\rangle\,\delta/U_{zs}$ in upper region are 6.28, 5.51, 4.82 and 5.09 for the ZPG TBL, first, second and third streamwise positions respectively (table 5.3). It is worth mentioning that the variation range of spatial resolution in various streamwise positions is $\Delta x/\delta = 0.020 - 0.016$, $\Delta x/\delta = 0.024 - 0.018$ and $\Delta x/\delta = 0.022 - 0.014$ for the first, second and last streamwise positions respectively. In fact, the interrogation window widths are equal at the middle of fields for the first and last streamwise positions ($\Delta x/\delta = 0.018$) whilst it is slightly higher in the second streamwise position ($\Delta x/\delta = 0.021$). Hence, $\bar{\lambda}$ is more underestimated in the second streamwise position compared to the other ones. This might explain, at least partially, why $\bar{\lambda}$ is slightly lower at the second streamwise position in comparison to the other ones, while it is expected to be comparable to the first station (see figure 4.11-b). The pdfs of $\bar{\lambda}\delta/U_{zs}$ for upper region (figure 5.24-b) also present that $\bar{\lambda}\delta/U_{zs}$ has higher absolute value for first streamwise position compared to the last one. Since the spatial resolution is approximately the same in the first and last stations, the results presented in figures 5.24-b and 4.11-b indicate that the swirl intensity is slightly affected by pressure gradient, at least near the separation point.

To provide a better idea of the variation of swirl intensity in y-direction and also in streamwise direction, the wall-normal profiles of the ensemble average of $\bar{\lambda}$ normalized by U_{zs}/δ are presented in figure 5.25. The error bars indicate the random uncertainty which is calculated based on the number of realizations in each interval. It is worth

recalling that the probability event of hairpin vortices is not constant in y-direction as illustrated in figure 5.22. Each point in figure 5.25 is computed on an interval of 0.096 of y/δ, i.e. 0.088 is related to $0.04 \leq y/\delta \leq 0.136$, in region $y/\delta = 0.04 - 1.00$. The ensemble average of $\bar{\lambda}\delta/U_{zs}$ is calculated in each interval to acquire one point in this latter figure. First, figure 5.25 confirms that $\bar{\lambda}\delta/U_{zs}$ is affected by pressure gradient. It is shown that $\langle\bar{\lambda}\rangle\,\delta/U_{zs}$ decreases in the streamwise direction for $y/\delta \leq 0.5$ except for the second streamwise position which has roughly the same value as for the last station (taking into account the underestimation effect of spatial resolution and the random uncertainty).

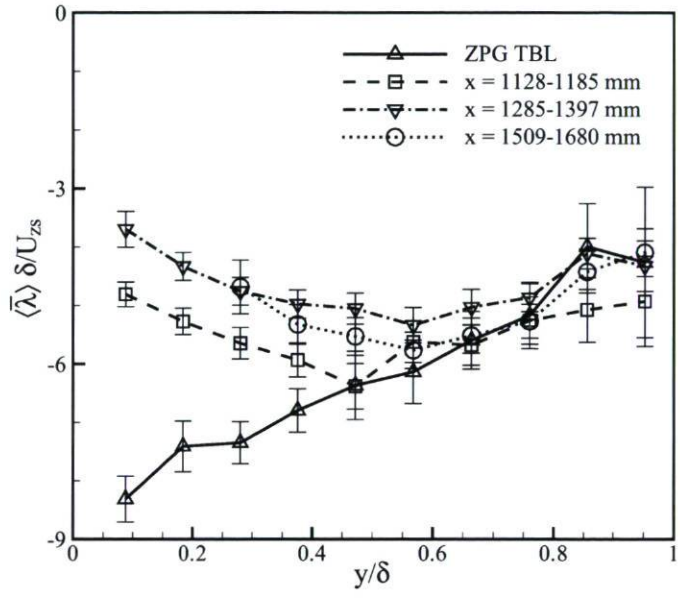

Figure 5.25: Ensemble average of $\bar{\lambda}$ scaled by δ/U_{zs} and associated with hairpin heads for different streamwise positions and ZPG TBL. Each point is an average over an interval of 0.096 of y/δ from $y/\delta = 0.04$ to 1.00. The points are at the center of the intervals. The error bars indicate the random uncertainty which is calculated based on the number of realizations in each interval.

Another feature shown in figure 5.25 is the variation of $\langle\bar{\lambda}\rangle\,\delta/U_{zs}$ in y-direction. It is important to recall that the swirl intensity is significantly affected by spatial resolution (figure 4.11). Indeed, the related curve to ZPG TBL should be shifted to higher negative value of swirl intensity (shifted down) if it is calculated with the same spatial resolution as the present study. In the ZPG TBL case, the absolute value of $\langle\bar{\lambda}\rangle\,\delta/U_{zs}$ increases monotonically toward the wall, while it has a maximum value around $y/\delta = 0.4 - 0.6$ and decreases near the wall in the present flow. Similar behaviours are also obtained for the spanwise vortices (for both prograde and retrograde vortices) as shown in figure 4.18. As explained in section 4.6.2, such a behaviour in the APG case is consistent with

that of the Reynolds stresses reported by Maciel et al. (2006b). To provide a better view of the Reynolds stresses variation in streamwise direction of the present study and also ZPG TBL, a similar analysis is redone here for both the ZPG and APG turbulent boundary layers (figure 3.29). In the case of ZPG TBL, the maximum Reynolds stresses occur close to the wall ($y/\delta \leq 0.1$) and decrease monotonically in y-direction, whilst the Reynolds stresses are maximum around $y/\delta = 0.6$ and decrease near the wall for APG TBL. In the ZPG TBL, the Reynolds stresses normalized by U_{zs}^2 are significantly higher than in the present flow. Furthermore, the Reynolds stresses decrease in the streamwise direction for the present flow. These results show that the turbulence activity decreases near the wall in the adverse pressure gradient region while approaching the separation point. Such behaviours are also found for the ensemble average of $\bar{\lambda}$ scaled by U_{zs}/δ of all spanwise vortices as shown in figure 4.18. As a result, it can be supposed that there is an association between the swirl intensity (vortices) and turbulence activity. It is important to mention that the differences of the Reynolds stresses (figure 3.29) are slightly higher than the differences of the swirl intensity (figure 5.25). This can be because of the Reynolds stresses are second-order moments which are not solely the result of vortices. Moreover, the variation of turbulence production in y-direction is also calculated at each streamwise position and also for ZPG TBL (figure 5.11). The turbulence production also presents similar trends to swirl intensity. This comparison will be further discussed in section 5.4.

Comparisons of the probability density functions of swirl intensity scaled by U_{zs}/δ for the prograde spanwise vortices and hairpin heads are presented in figure 5.26. The maximum probability occurs at higher values of $\bar{\lambda}\delta/U_{zs}$ for the hairpin vortices than the spanwise vortices. It means that the head of hairpin vortices have generally higher swirl intensity than all spanwise prograde vortices. It is important to mention that the hairpin heads are also accounted for in the pdfs and profiles of spanwise vortices. Figure 5.27 presents the wall-normal profiles of the ensemble average of $\bar{\lambda}$ normalized by U_{zs}/δ for both hairpin heads and spanwise vortices. These profiles also show lower swirl intensity for the spanwise vortices compared with the hairpin heads for all streamwise positions. Haidari and Smith (1994) and Zhou et al. (1999), see section 2.2.2, believed that an initial hairpin vortex can participate in the auto-generation mechanism to form a hairpin packet when it has sufficient strength. So, higher swirl intensity for the hairpin heads associated with the hairpin packets in the present study is consistent with this idea.

Turning now our attention to the different scalings used here to scale $\bar{\lambda}$. As mentioned in section 2.3, the traditional inner and outer time scales, ν/u_τ^2 and δ/u_τ, are not valid in strong adverse-pressure-gradient TBLs. Furthermore, the Zagarola-Smits velocity scale has been found to be a useful turbulent outer velocity scale for general

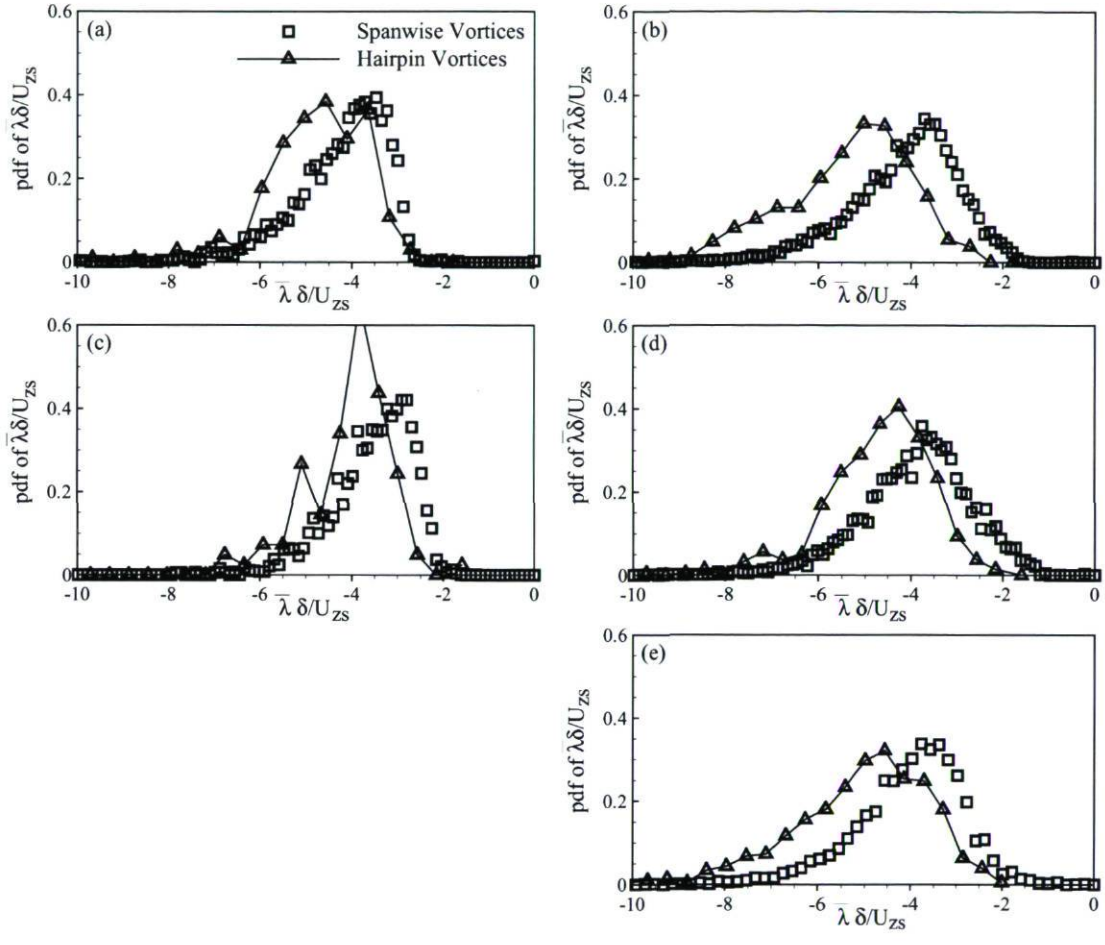

Figure 5.26: Probability density functions of $\bar{\lambda}$ for prograde spanwise and hairpin vortices at all streamwise positions: a) in region $x = 1128 - 1185$ mm for $y/\delta \leq 0.2$, b) in region $x = 1128 - 1185$ mm for $y/\delta > 0.2$, c) in region $x = 1285 - 1397$ mm for $y/\delta \leq 0.2$, d) in region $x = 1285 - 1397$ mm for $y/\delta > 0.2$, e) in region $x = 1509 - 1680$ mm for $y/\delta > 0.2$.

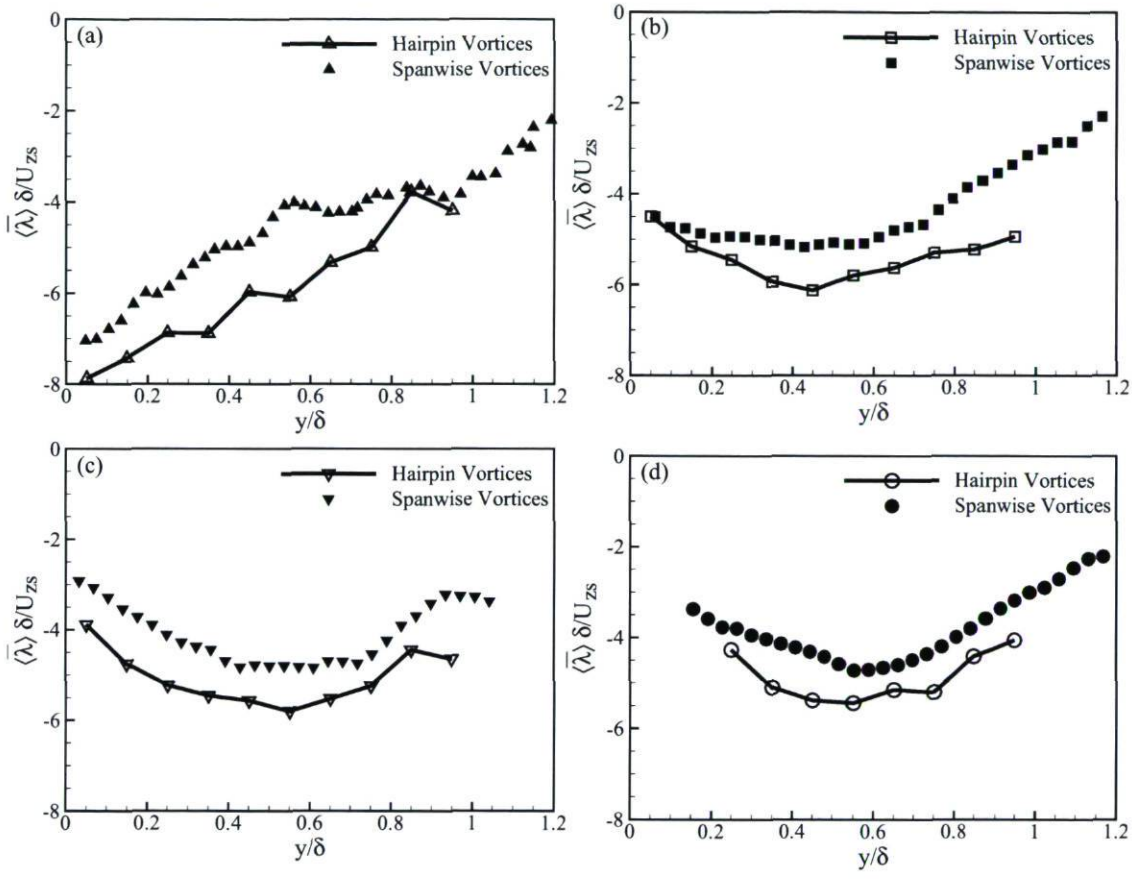

Figure 5.27: Ensemble average of $\bar{\lambda}$ scaled by δ/U_{zs} for prograde cores and hairpin heads in regions: a) ZPG TBL, b) $x = 1128 - 1185$ mm, c) $x = 1285 - 1397$ mm, d) $x = 1509 - 1680$ mm. For hairpin vortices, each point is an average over an interval of 0.096 of y/δ in region $y/\delta = 0.04 - 1.00$. The points are at the center of the intervals.

pressure-gradient turbulent boundary layers. Indeed, the Zagarola-Smits scaling works well not only for the region near separation but also for cases of different adverse-pressure-gradients. The results presented in table 5.3 confirm that the traditional inner and outer time scales are not appropriate scales for $\bar{\lambda}$.

Diameter of Hairpin Heads

It is shown in section 4.5 that the vortices diameter is significantly affected by mesh width and interrogation window width. Figure 4.11-a illustrates that the effective diameter of hairpin heads is a function of mesh width. Figure 4.12-a also shows that the effective diameter of vortices is a function of both mesh width and of interrogation window width. These results reveal that $\langle D/\delta \rangle$ decreases when the mesh width decreases. It means diameter of vortices is overestimated for both the present study and ZPG TBL. Since the mesh width is lower for the present study in comparison to Adrian et al. (2000) ZPG TBL database, the effective diameter of hairpin heads are also less overestimated in the present study compared to ZPG TBL. Because of these effects it is hard to interpret the presented differences between D/δ in figure 5.28 and table 5.4. The pdfs and the ensemble average of D/δ in the lower region ($y/\delta \leq 0.2$), shown in figure 5.28-a and table 5.4, illustrate that the effective diameter is lower for the present flow compared to the ZPG TBL (0.058 vs. 0.073). These differences could be due to the effect of mesh width on the diameter of vortices. So, it is hard to tell if the diameter of vortices is higher in the ZPG TBL compared to the present flow or D/δ are approximately the same in both flows.

In the upper region, figures 4.11-a and 4.12-a show that the vortices decrease slightly in size, with respect to δ, between the first streamwise position and the last one. The related pdf of D/δ at the last streamwise position is shifted to lower values of D/δ compared to the pdf of D/δ for the first streamwise position. The $\langle D/\delta \rangle$ is also higher at the first streamwise position compared to last one (0.068 vs. 0.062). It means that the pdfs of D/δ and the ensemble average of diameter also illustrate the same tendency except at the second streamwise position (5.28-b and table 5.4). So, it seems that D/δ is affected by pressure gradient, at least near the separation point but only slightly. It is worth recalling that although these results show higher diameter of vortices for the ZPG TBL in comparison to the first and second streamwise positions of the present flow, these differences can be due to the effect of mesh width on the size of vortices as mentioned before.

Since the size of the spanwise vortices varies with y near the wall (figure 4.20), we are also interested to have knowledge of the variation of hairpin heads in size in

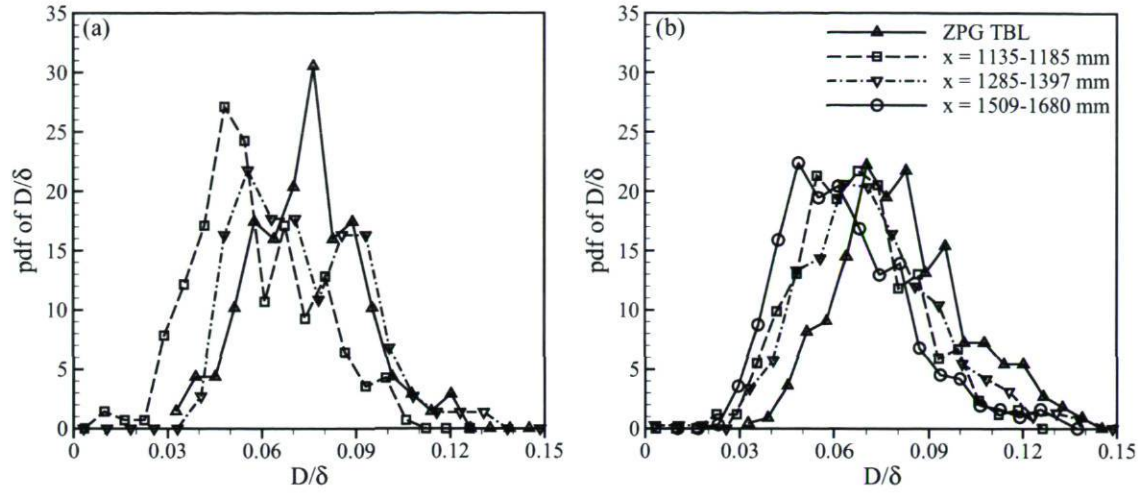

Figure 5.28: Probability density functions of diameter for hairpin vortices within the hairpin packets at all streamwise positions and ZPG TBL: a) lower region where $y/\delta \leq 0.2$, b) upper region where $y/\delta > 0.2$.

		$\langle D/\delta \rangle \pm P_x$	σ_D	$\langle D^+ \rangle$
ZPG TBL	$y/\delta \leq 0.2$	0.073 ± 0.003	0.017	146
	$y/\delta > 0.2$	0.082 ± 0.002	0.021	160
$x = 1128$ mm	$y/\delta \leq 0.2$	0.058 ± 0.002	0.019	49
	$y/\delta > 0.2$	0.068 ± 0.002	0.019	56
$x = 1285$ mm	$y/\delta \leq 0.2$	0.072 ± 0.004	0.019	64
	$y/\delta > 0.2$	0.072 ± 0.002	0.021	64
$x = 1509$ mm	$y/\delta \leq 0.2$	-	-	-
	$y/\delta > 0.2$	0.062 ± 0.002	0.020	-

Table 5.4: Ensemble average of diameter of hairpin vortices associated with hairpin packets at different streamwise positions and ZPG TBL. σ_D is the standard deviation of D/δ distribution in figure 5.28.

y-direction. To provide this knowledge, the ensemble average of hairpin heads diameter normalized by δ, $\langle D/\delta \rangle$, are calculated as a function of y/δ for all streamwise positions and ZPG TBL as shown in figure 5.29. It is important to mention that the probability event of hairpin vortices is not constant in wall-normal direction as shown in figure 5.22. Each point in figure 5.29 is computed on an interval of 0.096 of y/δ in region $y/\delta = 0.04 - 1.00$, i.e. 0.088 is related to $0.04 < y/\delta \leq 0.136$. The ensemble average of $\bar{\lambda}\delta/U_{zs}$ is calculated in each interval to acquire one point in this latter figure. The points are at the center of intervals. The error bars indicate the random uncertainty which is calculated based on the number of realizations in each interval. Figure 5.29 shows that $\langle D/\delta \rangle$ is approximately constant in y-direction within the outer region ($0.2 < y/\delta < 0.8$). Additionally, this latter figure also presents that D/δ decreases slightly in size between the first streamwise position and the last one. Another feature in this figure is the variation of D/δ near the wall. Figure 5.29 indicates that D/δ decreases near the wall.

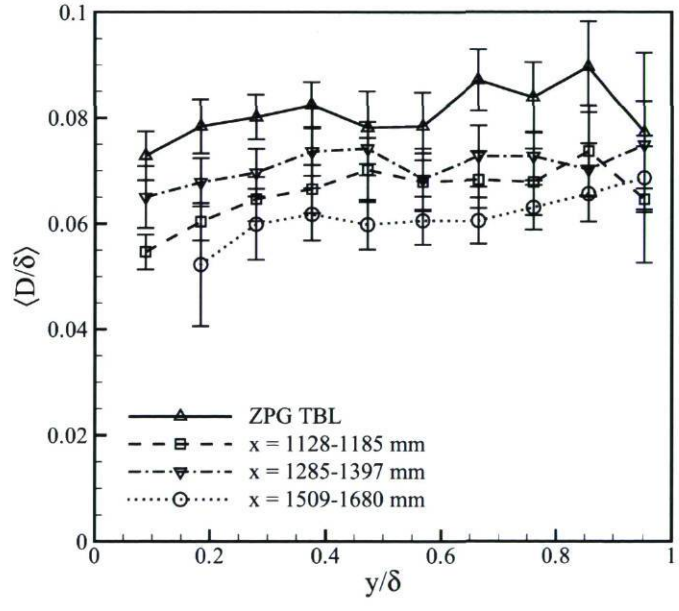

Figure 5.29: Ensemble average of D scaled by δ for hairpin heads associated with hairpin packets for different streamwise positions and ZPG TBL. Each point is an average over an interval of 0.096 of y/δ in region $y/\delta = 0.04 - 1.00$. The points are at the center of the intervals. The error bars indicate the random uncertainty which is calculated based on the number of realizations in each interval.

The higher value of diameter normalized by δ at the first streamwise position compared to the last one would be because of the effect of pressure gradient. In fact, the adverse pressure gradient causes that the mean flow evolves rapidly in this strong APG

experiment especially near the separation point. It is therefore possible that the turbulent structures respond with a certain delay to the changes of the mean flow. As a result, the increase of vortices diameter is slower than boundary layer coarsening (at least near the separation point).

A comparison of the probability density function of effective diameter scaled by δ for all the prograde vortices and for hairpin heads are presented in figure 5.30. This figure shows that spanwise vortices have generally smaller diameter compared to the head of hairpin vortices. It is worth noting that the hairpin heads are also accounted for in the pdfs of prograde spanwise vortices. Figure 5.30 shows that the peak of distribution of D/δ is around 0.03δ for the spanwise vortices, whilst this peak is around 0.07δ for the hairpin heads. As mentioned in section 4.5, around 17% of the prograde spanwise vortices with $D/\delta \geq 0.04$ are hairpin heads within packets. Since, the presented pdfs in figure 5.30 include all sizes of spanwise vortices, less than 17% of the prograde cores would be related to the hairpin heads. With regards to these aforementioned, it seems that the most probable size of spanwise prograde vortices is not related to hairpin vortices (associated with hairpin packets). On the other hand, the spanwise vortices have generally lower swirling rate compared with the hairpin heads as illustrated in figures 5.26 and 5.27. These results confirm that hairpin vortices have in general higher swirl intensity and are larger than most other vortices.

Convection Velocity

In turbulent shear flows, coherent structures are convected downstream once they are generated. In the present study, once the vortices are identified, the instantaneous components of convection velocities of the vortices are determined as explained in section 4.4. The mean streamwise component of convection velocities, U_c, of both prograde and retrograde spanwise vortices as a function of wall-normal position were previously presented for three streamwise positions (see section 4.6.4). It is found that, on average, both prograde and retrograde spanwise vortices travel with the mean streamwise velocity for all streamwise positions.

The results for the hairpin heads show a similar behaviour to that found for the spanwise vortices. The mean convection velocities of the hairpin heads almost collapse on the local streamwise mean velocity as illustrated in figure 5.31. These results are consistent with the observations of Adrian et al. (2000) for the ZPG TBL. In the APG TBL case, the turbulence structures are decelerated while the flow is also decelerated. However, while the mean convection velocities of these vortices collapse on the local streamwise mean, the distributions of convection velocities about the mean exhibit

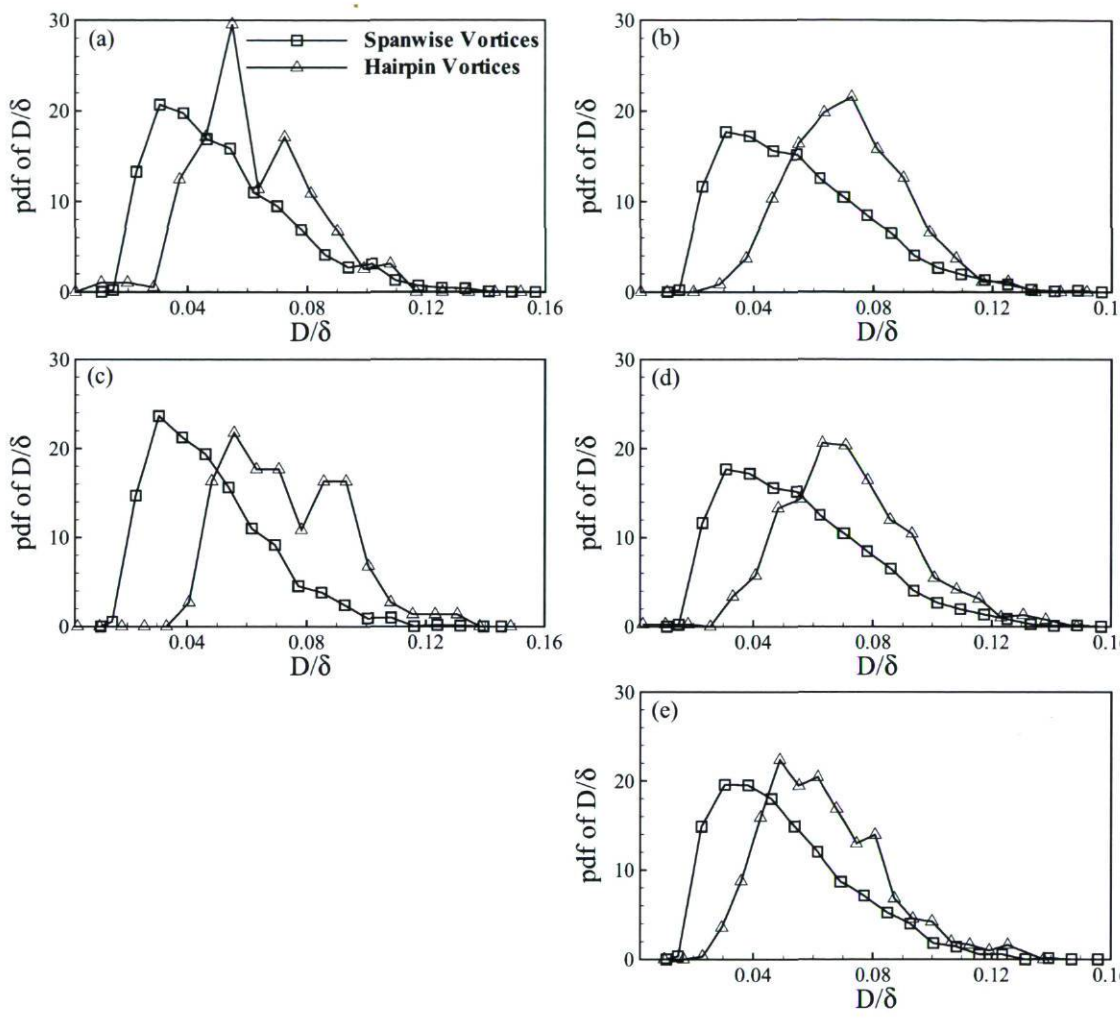

Figure 5.30: Probability density functions of D/δ for prograde spanwise vortices and hairpin vortices at all streamwise positions: a) in region $x = 1128 - 1185$ mm for $y/\delta \leq 0.2$, b) in region $x = 1128 - 1185$ mm for $y/\delta > 0.2$, c) in region $x = 1285 - 1397$ mm for $y/\delta \leq 0.2$, d) in region $x = 1285 - 1397$ mm for $y/\delta > 0.2$, e) in region $x = 1509 - 1680$ mm for $y/\delta > 0.2$.

strong wall-normal dependence. This dependency is more important in the present flow in comparison to ZPG TBL.

It is found that the most probable value of v_c/U_e is about 0 (figure 5.32) for the ZPG TBL as expected. In the APG TBL case, contrarily to the ZPG TBL, v_c/U_e has important values. It was mentioned previously in section 4.6.4 that wall-normal component of convection velocity of vortices is negligible in the ZPG TBL while it is important in the present study. This idea is confirmed here by the results in figure 5.32.

Neck Inclination

The neck angle measurement technique was explained in section 5.3.1. Based on this technique, the α values given here (figure 5.34) are measured with a random uncertainty of about $\pm 6^o$. The neck angle of the hairpin vortex is determined using the angle of the locus of the $Q2$ region as shown in figure 5.33-b (see also section 5.3.1). It is worth noting that these values present the average upper neck angle of hairpin vortex signatures, but the neck angle of the hairpin vortex is not constant since the vortex is not straight. The hairpin neck is less inclined near the legs, whereas it takes a near vertical orientation close to the head of the hairpins as shown in figure 5.33-b. The probability density functions and ensemble averages of α indicate that the neck angle is approximately the same in the lower and upper regions for the present flow (figure 5.34, table 5.5), whereas $\langle\alpha\rangle$ is higher in the inner region compared to the upper region for the ZPG TBL (66^o vs. 60^o). In the lower region, the neck angle is roughly equal for both the present flow and the ZPG TBL as the pdfs of α are superimposed (figure 5.34-a) and the mean values of α are also approximately the same (table 5.5). Contrarily in the upper region, α is smaller in the ZPG TBL since the pdf of ZPG TBL is shifted slightly to lower values of α (figure 5.34-b) and the mean values of α are also higher for the present flow (67^o vs. 60^o).

To provide a better idea of the variation of the neck angle in y-direction, the profile of α in wall-normal direction is shown in figure 5.35. It is important to recall that the population of hairpin vortices is not constant in y-direction as presented in figure 5.22. Figure 5.35 shows that the neck angle is approximately constant in wall-normal direction for the present work, whereas it decreases slightly in y-direction for the ZPG turbulent boundary layer. In the ZPG TBL, the present results contradict the results of Adrian et al. (2000) that showed that the neck angle increases with increasing distance from the wall. They reported that the head takes a near vertical orientation in the upper region of the boundary layer, while near the wall it takes a more conventional angle, whereas the present investigation shows that this angle decreases monotonically

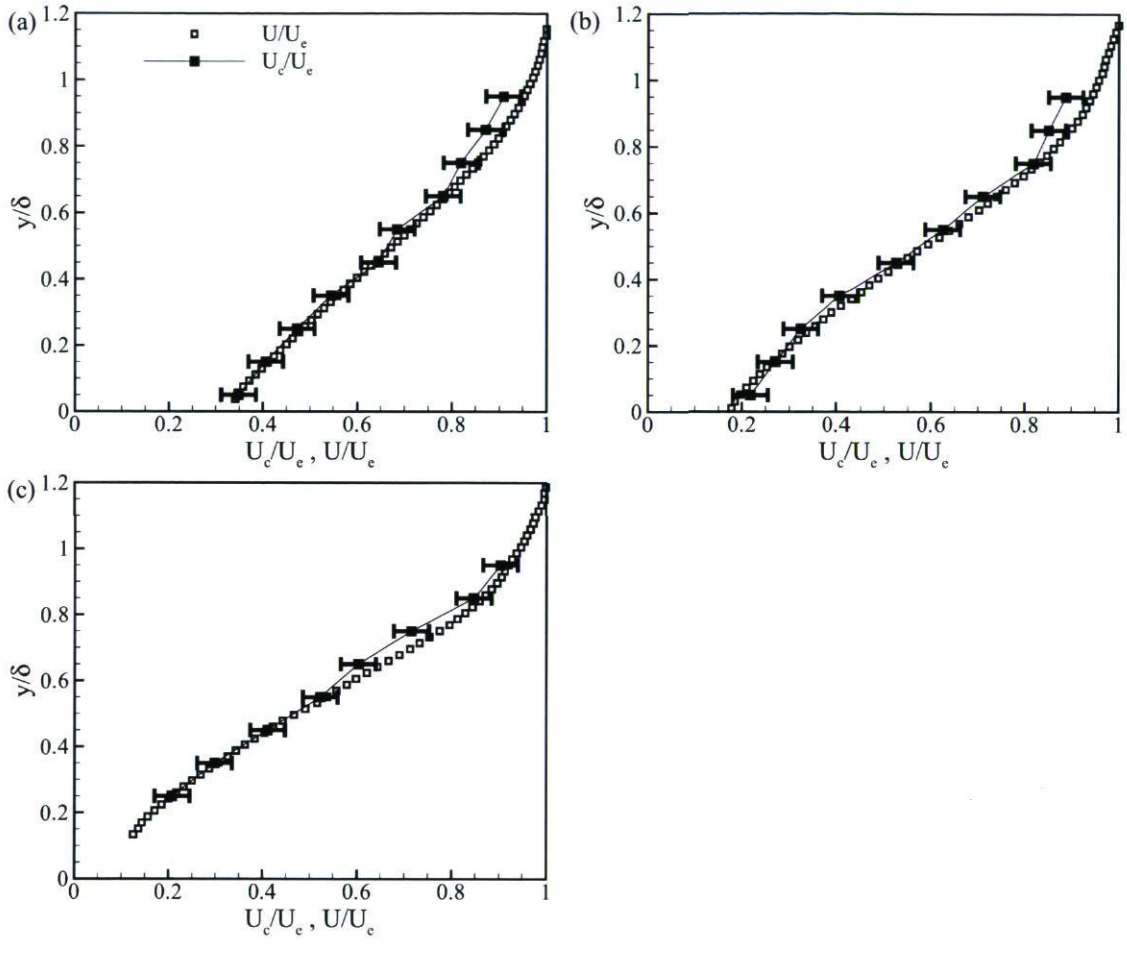

Figure 5.31: The profiles of U_c/U_e and U/U_e for different streamwise positions: a) in region $x = 1128 - 1185$ mm, b) in region $x = 1285 - 1397$ mm, c) in region $x = 1509 - 1680$ mm. Each point is an average over an interval of 0.1 of y/δ in region $y/\delta = 0.0 - 1.0$. The points are at the center of the intervals. The error bars indicate the random uncertainty which is calculated based on the number of realizations in each interval.

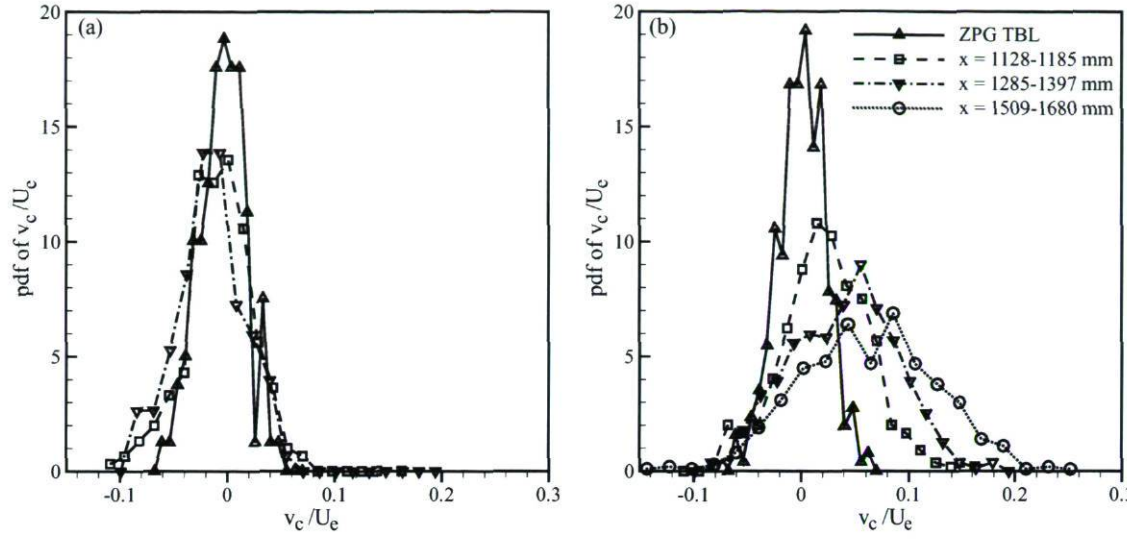

Figure 5.32: Probability density functions of wall-normal component of convection velocity for hairpin vortices within the hairpin packets at all streamwise positions and ZPG TBL: a) lower region where $y/\delta \leq 0.2$, b) upper region where $y/\delta > 0.2$.

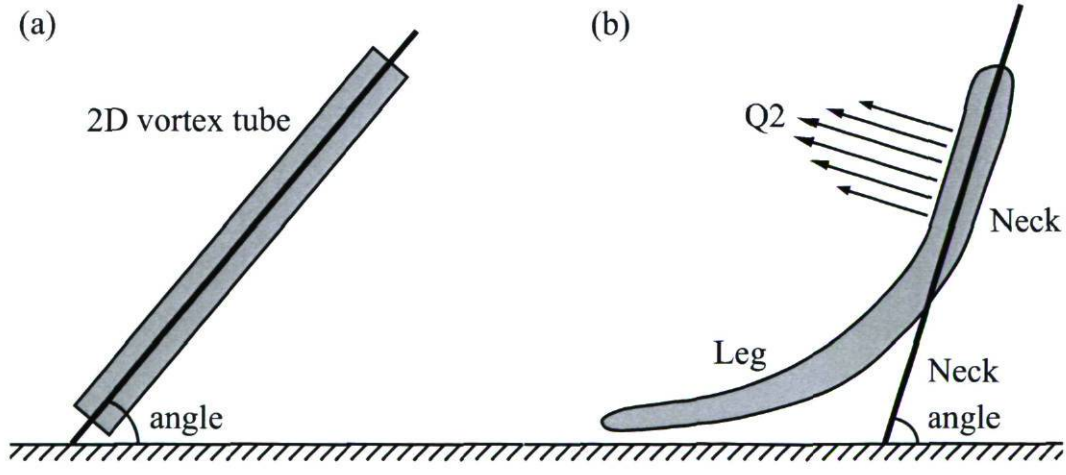

Figure 5.33: a) Schematic of a two-dimensional vortex tube. b) Side view of the schematic model of a hairpin vortex attached to the wall and the induced Q2 event.

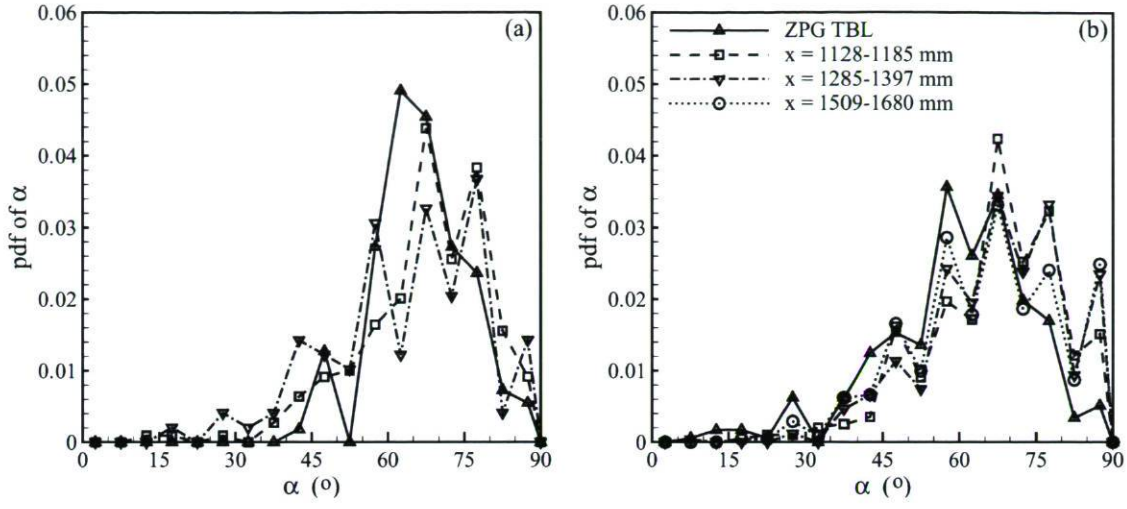

Figure 5.34: Probability density functions of neck angle for hairpin vortices within the hairpin packets at all streamwise positions and ZPG TBL: a) lower region where $y/\delta \leq 0.2$, b) upper region where $y/\delta > 0.2$.

		$\langle\alpha\rangle \pm P_x$	σ_α
ZPG TBL	$y/\delta \leq 0.2$	66 ± 1.8	9.2
	$y/\delta > 0.2$	60 ± 1.5	14.5
$x = 1128$ mm	$y/\delta \leq 0.2$	67 ± 1.7	12.8
	$y/\delta > 0.2$	67 ± 1.3	13.3
$x = 1285$ mm	$y/\delta \leq 0.2$	64 ± 3.0	15.1
	$y/\delta > 0.2$	68 ± 1.2	13.5
$x = 1509$ mm	$y/\delta \leq 0.2$	-	-
	$y/\delta > 0.2$	65 ± 1.2	14.7

Table 5.5: Ensemble average of neck angle of hairpin vortices associated with hairpin packets at different streamwise positions and ZPG TBL. σ_α is the standard deviation of α distribution in figure 5.34.

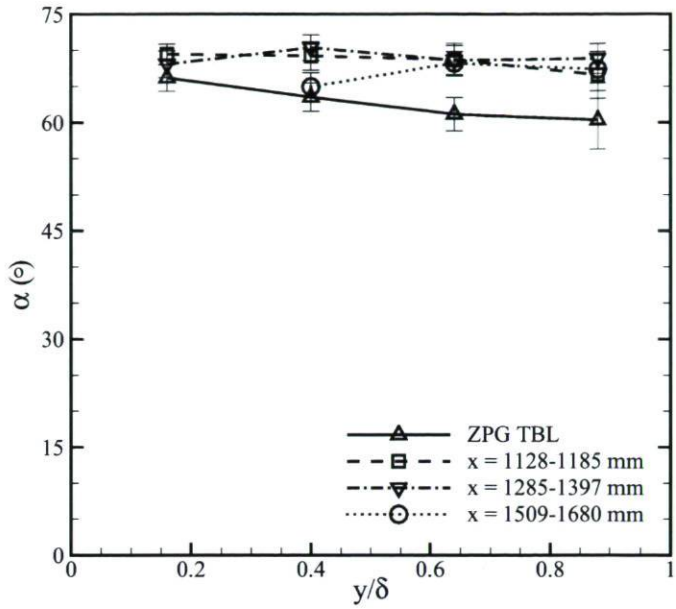

Figure 5.35: Variation of neck angle in wall-normal direction at different streamwise positions and ZPG TBL. Each point is an average over an interval of 0.24 of y/δ in region $y/\delta = 0.04 - 1.00$. The points are at the center of the intervals. The error bars indicate the random uncertainty which is calculated based on the number of realizations in each interval.

from about 67^o near the wall to 58^o at the edge of the boundary layer. It is worth noting that Adrian and co-workers determined the neck angle using the angle of inclined shear layer which is different from the method used in the present analysis.

The aforementioned differences between the upper regions of ZPG TBL and of the present flow can probably be explained by the fact that the mean strain rates are different in those flows. The mean velocity gradients, $\partial U/\partial x$ and $\partial V/\partial y$, are more important in the upper region of a strongly decelerated flow (i.e. present flow) than in the upper region of a ZPG TBL (see figure 5.36). It is worth mentioning that the profiles of $\partial U/\partial x$ and $\partial V/\partial y$ are not shown for the ZPG TBL in this figure, as the values of $\partial U/\partial x$ and $\partial V/\partial y$ are negligible in the ZPG TBL in comparison to the present flow. To illustrate the role of the mean strain rates on the vortex inclination, a simplified inviscid analysis is presented here. The mean strain rate tensor may be expressed as follows

$$S_{ij} = \frac{1}{2}\left[\partial U_i/\partial x_j + \partial U_j/\partial x_i\right] \tag{5.1}$$

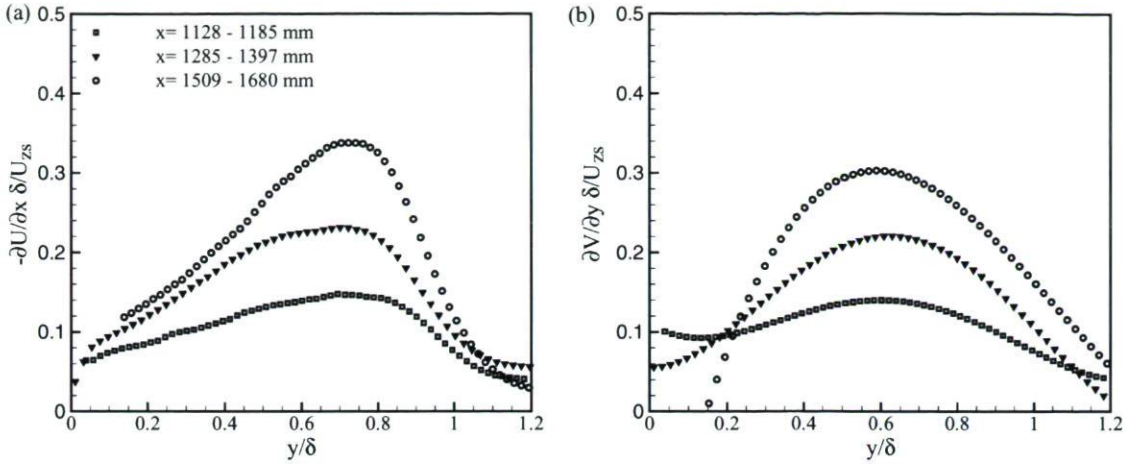

Figure 5.36: Variation of velocity gradients through the boundary layer at different streamwise positions: a) mean streamwise contraction rate, $\partial U/\partial x$ scaled by U_{zs}/δ, b) mean wall-normal extension rate, $\partial V/\partial y$ scaled by U_{zs}/δ (One symbol out of 2 for clarity).

If for a two-dimensional flow $\partial V/\partial x$ is neglected, equation 5.1 becomes

$$S_{ij} = \begin{vmatrix} \partial U/\partial x & \frac{1}{2}\partial U/\partial y \\ \frac{1}{2}\partial U/\partial y & \partial V/\partial y \end{vmatrix} = \frac{1}{2}\partial U/\partial y \begin{vmatrix} a & 1 \\ 1 & b \end{vmatrix} \tag{5.2}$$

where

$$a = \frac{\partial U/\partial x}{\frac{1}{2}\partial U/\partial y} \quad \text{and} \quad b = \frac{\partial V/\partial y}{\frac{1}{2}\partial U/\partial y}$$

Now, the vorticity equation can be expressed as

$$\frac{D\omega_i}{Dt} = \omega_j s_{ij} + \nu \frac{\omega_i}{\partial x_j \partial x_j} \tag{5.3}$$

Some simplifications are now made. First, viscous diffusion is neglected. Second, only the mean values of the strain rate component (equation 5.2) are considered. Third, $\partial V/\partial x$ is assumed negligible as mentioned before. Finally the analysis is restricted to a vortex tube with only two components of vorticity: ω_x and ω_y. Based on these assumptions equation 5.3 can be expressed as follows

$$\frac{D\omega_x}{Dt} = \omega_x \frac{\partial U}{\partial x} + \omega_y (\frac{1}{2}\frac{\partial U}{\partial y})$$
$$\frac{D\omega_y}{Dt} = \omega_x (\frac{1}{2}\frac{\partial U}{\partial y}) + \omega_y \frac{\partial V}{\partial y} \tag{5.4}$$

or

$$\frac{D\omega_x}{Dt} = [a\omega_x + \omega_y]\frac{1}{2}\frac{\partial U}{\partial y}$$
$$\frac{D\omega_y}{Dt} = [\omega_x + b\omega_y]\frac{1}{2}\frac{\partial U}{\partial y} \tag{5.5}$$

This ordinary differential equation system has a solution in the form

$$\boldsymbol{\omega} = c_1 \mathbf{x_1} e^{\lambda_1 t} + c_2 \mathbf{x_2} e^{\lambda_2 t} \tag{5.6}$$

where λ_1 and λ_2 are the eigenvalues of the mean strain rate tensor and $\mathbf{x_1}$ and $\mathbf{x_2}$ are eigenvectors corresponding to λ_1 and λ_2 respectively.

Figure 5.37 shows the variations of a, the ratio of the mean streamwise contraction rate and the mean shear rate, and b, the ratio of the mean wall-normal extension rate and the mean shear rate, in the y-direction. a and b are roughly constant with respect to y/δ in the range 0.2-1 as shown in this latter figure. The values presented in table 5.6 are the average values of a and b in the range 0.2 to 1 of y/δ. If a and b are zero or equal (same sign and value), then the vortex tube is inclined at 45^o. In the present flow, a and b have approximately the same absolute values but different signs as presented in table 5.6. Positive $\partial V/\partial y$ tends to stretch the structures in the wall-normal direction and negative $\partial U/\partial x$ decelerates the structures and compresses them in the streamwise direction. So, more inclined hairpin vortices are expected when the values of a and b increase. The vortex tube angles obtained with this simplified inviscid analysis are 49.0^o, 51.6^o and 53.9^o for the first, second and third streamwise positions respectively in comparison to about 45^o for the canonical flows. Since the velocity gradients ($\partial U/\partial x$ and $\partial V/\partial y$) are negligible within the upper region of ZPG TBL, the values of a and b are also negligible compared to their values in the APG TBL. So, hairpin vortices are therefore expected to be more inclined in the APG TBL in comparison to the upper region of ZPG TBL. In other words, tilting and wall-normal stretching of the legs and necks of the hairpins is more important in APG TBL, leading to more inclined hairpins.

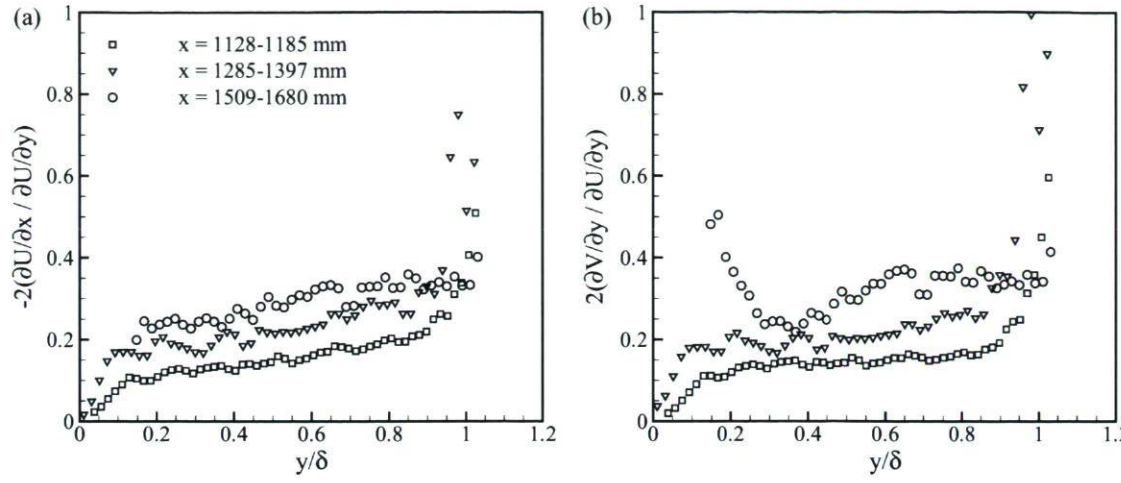

Figure 5.37: Variation of a and b parameters in wall-normal direction at different streamwise positions (one symbol out of 2 for clarity).

	a	b	α
$x = 1128$ mm	-0.145	0.139	49.0
$x = 1285$ mm	-0.227	0.231	51.6
$x = 1509$ mm	-0.285	0.304	53.9

Table 5.6: The average values of the mean strain rate ratios a and b and the vortex tube angle calculated via the simplified two-dimensional inviscid analysis.

Since the most downstream hairpins in a hairpin packet are also normally the older ones, the increased titling and stretching may also imply that the growth angle of the packet should be larger. This latter effect is explained in section 5.3.3.

Although, from the inviscid analysis, it is expected that the neck angle of hairpin vortices increases slightly in the streamwise direction of APG TBL, the experimental results show roughly the same values of ensemble average of α for all streamwise positions (table 5.5). Moreover, the average hairpin neck angles obtained from the PIV database are much higher than the vortex tube angles calculated via the inviscid analysis (67^o vs. 50^o). This significant difference between the results shows that the hairpin inclinations can be caused by the shape of real hairpins as the upper neck part inclination is only measured in the present study. It is worth recalling that regarding the form of real hairpins, the neck takes a near vertical orientation near the head while the legs take a more conventional angle. Second, the dynamic complexity of hairpin vortices changes

the form and orientations of hairpins. Finally, the instantaneous flow and complexity of turbulence also affects the turbulence structures.

Angle of Inclined Shear Layer

It is worth recalling that a stagnation point flow occurs when a second-quadrant ejections ($Q2$, $u' < 0$, $v' > 0$) encounters a fourth-quadrant sweep ($Q4$, $u' > 0$, $v' < 0$) of higher-speed fluid moving toward the back of the hairpin (see figures 5.1 and 5.2). Based on the measurement technique of ISL mentioned in section 5.3.1, the ISL angle, β, (figure 5.38) is measured with a random uncertainty of about $\pm 6^o$.

The probability density function and the ensemble average of ISL angle, β, are shown in figure 5.38 and table 5.7 respectively. For both flows (ZPG TBL and APG TBL), the range of ISL angles vary from 0^o to 90^o with a mean of about 40^o for the lower region and 0^o to 90^o with a mean of about 40^o-50^o for the upper region. Figure 5.39 shows the ensemble average of β as a function of wall-normal distance (y/δ). It is worth mentioning that the population of hairpin vortices is not constant in wall-normal direction as shown in figure 5.22. Although it is hard to interpret the differences of β in this latter figure as the differences of β at different heights are not large when compared to the intervals of random uncertainty, it seems that the ISL angle increases slightly with increasing distance from the wall in all cases. If this is the case, then this difference can probably be explained by the nature of the fourth-quadrant ($Q4$) in different regions. Since the inclination of $Q2$ events ($\alpha + 90^o$) remains constant in the present flow and even slightly decreases with wall distance in the ZPG TBL case, it can be supposed that the high-speed regions are more inclined near the wall, resulting in less inclined ISL, and more horizontal far from the wall, resulting in more inclined ISL. On the other hand, despite differences of the neck angle between the APG and ZPG turbulent boundary layers in the upper region, the ISL has roughly the same inclination in both APG and ZPG turbulent boundary layers. This is the case in both lower and upper regions of these flows.

Adrian and co-workers proposed that the neck of hairpin vortex signatures is usually more inclined than ISL. This scenario has been substantiated by the direct experimental observations of Adrian et al. (2000). This scenario is also confirmed by our results. In the upper region, the ensemble average of α and β show that the neck is inclined about 20^o more than the ISL in the APG TBL and around 14^o more in the ZPG TBL. The higher difference of value between the neck and ISL angles for the APG TBL (20^o vs. 14^o) is because of the higher value of α for the present study compare to ZPG TBL (67^o vs. 60^o), while the ISL angle is approximately the same in both flows as previously

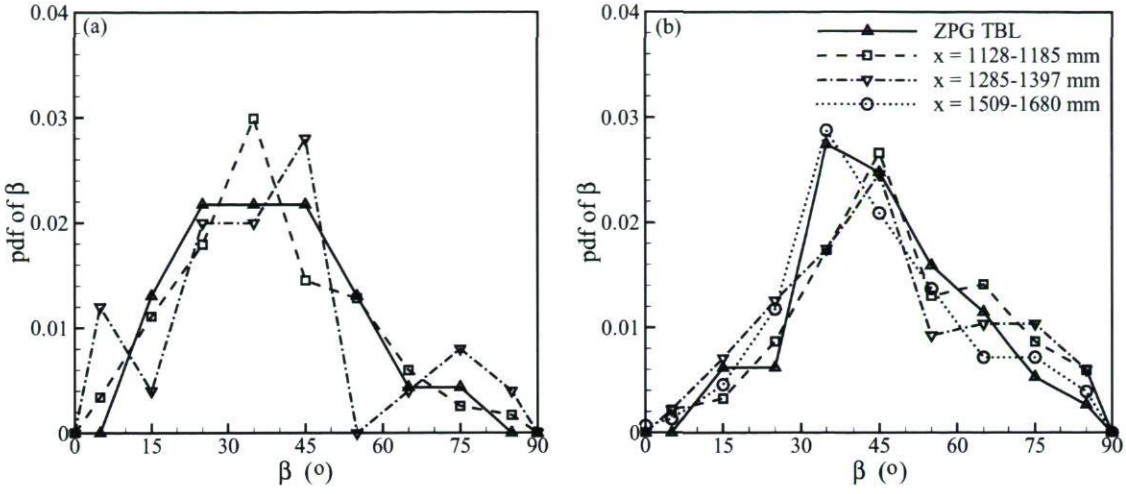

Figure 5.38: Probability density functions of average of ISL angle for hairpin vortices within the hairpin packets at all streamwise positions and ZPG TBL: a) lower region where $y/\delta \leq 0.2$, b) upper region where $y/\delta > 0.2$.

		$\langle\beta\rangle \pm P_x$	σ_β
ZPG TBL	$y/\delta \leq 0.2$	38 ± 3.2	16.1
	$y/\delta > 0.2$	46 ± 1.7	16.2
$x = 1128$ mm	$y/\delta \leq 0.2$	38 ± 2.3	17.1
	$y/\delta > 0.2$	49 ± 1.90	18.6
$x = 1285$ mm	$y/\delta \leq 0.2$	38 ± 4.2	21.1
	$y/\delta > 0.2$	46 ± 1.8	20.2
$x = 1509$ mm	$y/\delta \leq 0.2$	-	-
	$y/\delta > 0.2$	44 ± 1.5	18.0

Table 5.7: Ensemble average of ISL angle of hairpin vortices associated with hairpin packets at different streamwise positions and ZPG TBL. σ_β is the standard deviation of ISL angle distribution in figure 5.38.

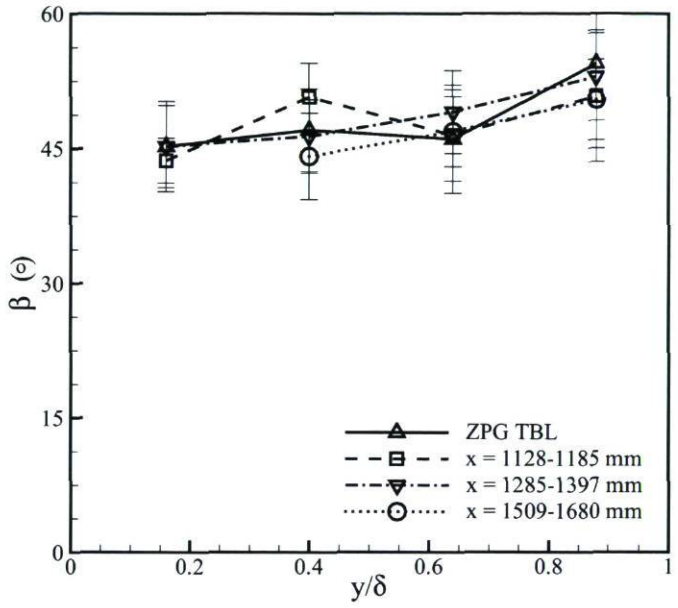

Figure 5.39: Ensemble average of ISL angle β as a function of y/δ for hairpin vortices within the hairpin packets at all streamwise positions and ZPG TBL. The bars represent random uncertainty. Each point is an average over an interval of 0.24 of y/δ in region $y/\delta = 0.04 - 1.00$. The points are at the center of the intervals. The error bars indicate the random uncertainty which is calculated based on the number of realizations in each interval.

mentioned.

5.3.3 Hairpin Packet Parameters

The parameters associated with hairpin packets are presented in this section. These parameters are streamwise spacing and growth angle. It is important to recall that there is no information for the inferior region ($y/\delta \leq 0.2$) at the last streamwise position ($x = 1509$ mm) as mentioned in section 3.5.1.

Streamwise Spacing

Figure 5.40 shows the probability density function of streamwise spacing ($\Delta x/\delta$) for the identified hairpin vortex signatures, and table 5.8 presents the ensemble average and the standard deviation associated with theses pdfs. The streamwise spacing is the streamwise distance between the cores of two neighbour hairpin vortices (see figure 5.43).

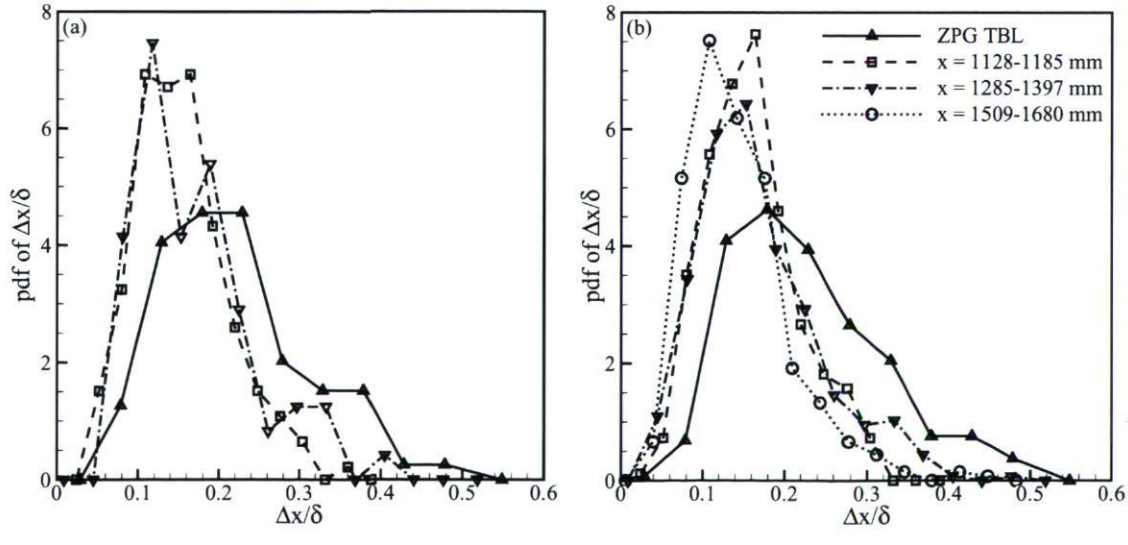

Figure 5.40: Probability density functions of streamwise spacing for all streamwise positions and ZPG TBL: a) lower region where $y/\delta \leq 0.2$, b) upper region where $y/\delta > 0.2$.

The presented pdfs are similar in both lower and upper regions for the APG turbu-

		$\langle \Delta x/\delta \rangle \pm P_x$	$\sigma_{\Delta x}$	$\langle \Delta x^+ \rangle$
ZPG TBL	$y/\delta \leq 0.2$	0.190 ± 0.017	0.092	380
	$y/\delta > 0.2$	0.204 ± 0.010	0.090	408
$x = 1128$ mm	$y/\delta \leq 0.2$	0.138 ± 0.008	0.057	117
	$y/\delta > 0.2$	0.145 ± 0.006	0.055	122
$x = 1285$ mm	$y/\delta \leq 0.2$	0.145 ± 0.015	0.074	128
	$y/\delta > 0.2$	0.150 ± 0.007	0.074	133
$x = 1509$ mm	$y/\delta \leq 0.2$	-	-	-
	$y/\delta > 0.2$	0.126 ± 0.005	0.064	-

Table 5.8: Ensemble average of streamwise spacing of hairpin vortices in different streamwise positions and ZPG TBL. $\sigma_{\Delta x}$ is the standard deviation of $\Delta x/\delta$ distribution in figure 5.40.

lent boundary layer. This is also the case for the ZPG TBL. The calculated ensemble average of streamwise spacing, $\langle \Delta x/\delta \rangle$, is roughly the same in the lower region and the upper region for those flows (see table 5.8). We turn now our attention to the differences in the pdfs between the two flows. First, the pdfs of $\Delta x/\delta$ for the ZPG case are shifted towards slightly higher values of $\Delta x/\delta$ when compared to the pdfs for the present flow. Table 5.8 also provides a clear view that $\langle \Delta x/\delta \rangle$ is larger for the ZPG TBL compared to the present flow (0.2 vs. 0.145). Furthermore, the forms of pdfs are not exactly the same in these flows. In the ZPG case, the pdf of $\Delta x/\delta$ is slightly wider, higher standard deviation, in comparison to the present flow. These results also present that the pdf at the last streamwise position is shifted towards lower $\Delta x/\delta$ values when compared to the other streamwise positions. Table 5.8 shows that $\langle \Delta x/\delta \rangle$ is indeed lower at the last streamwise position compared to the other ones (0.126 vs. 0.145). Finally, there is a bump in the pdfs of $\Delta x/\delta$ at $\Delta x/\delta \approx 0.25$ for both the ZPG and APG cases. Since the hairpin packets are not perfectly aligned in the streamwise direction, as explained previously in section 5.2.2, some hairpins may be missed in xy plane measurements. This can explain why there is an artificial probability increase at a value of $\Delta x/\delta$ which is the double of the most probable spacing. As a result, the average streamwise spacing is slightly over-estimated.

The ensemble average of $\Delta x/\delta$ as a function of y/δ is shown in figure 5.41. It is important to recall that the population of hairpin vortices is not constant in y-direction as shown in figure 5.22. The streamwise spacing slightly increases in wall-normal direction for both the ZPG case and the present flow. It is worth mentioning

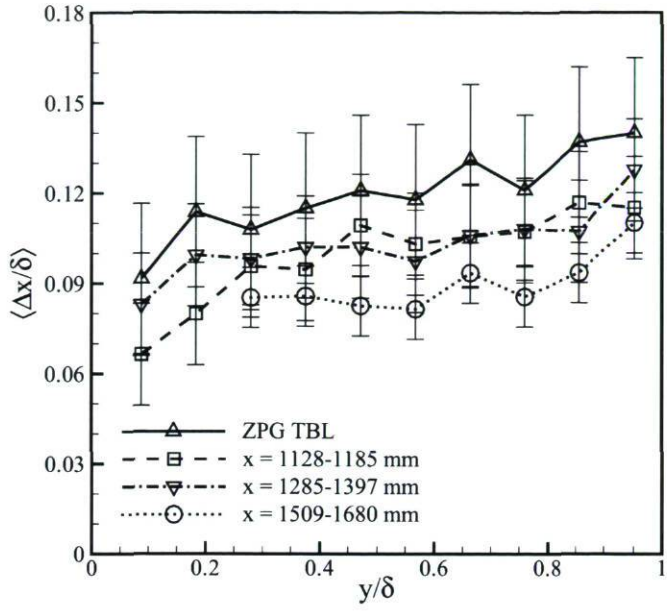

Figure 5.41: Ensemble average of streamwise spacing scaled by δ and associated with hairpin heads for different streamwise positions and ZPG TBL. Each point is an average over an interval of 0.096 of y/δ in region $y/\delta = 0.04 - 1.00$. The points are at the center of the intervals. The error bars indicate the random uncertainty which is calculated based on the number of realizations in each interval.

that this tendency should be interpreted with caution as the differences are within the intervals of random uncertainty. Nonetheless, the trend is similar for all profiles. So, it could be supposed that the streamwise spacing steadily increases in y-direction. In other words, the distance of hairpin vortices in streamwise direction increases as they move up from the wall. Since the hairpin vortices within a hairpin packet are expected to grow upwards in the streamwise direction, it is possible that the older hairpins travel slightly faster than the younger ones and that the spacing between hairpins increases as these hairpins age. Next, the profile of $\langle \Delta x/\delta \rangle$ for ZPG TBL shows higher values of $\Delta x/\delta$ compared to the present flow. Moreover, $\langle \Delta x/\delta \rangle$ decreases in the streamwise direction in the present flow. It is worth noting that these differences of $\langle \Delta x/\delta \rangle$ are within the intervals of random uncertainty. They are however confirmed by the averages of table 5.8. $\Delta x/\delta$ is therefore affected by pressure gradient. The increase in hairpin spacing does therefore not follow the boundary layer coarsening in the adverse pressure gradient region.

The aforementioned differences between streamwise spacing can be caused by different parameters of flow and of vortices (i.e. strain rates, hairpin generation and mutual repulsion mechanisms and population of symmetric or asymmetric hairpin vortices). First, the effects of mean strain rates are described. The gradient of the mean stream-

wise velocity component in x-direction ($\partial U/\partial x$) increases in absolute value within the adverse pressure gradient region as shown in figure 5.36. Moreover, this gradient is much lower for the ZPG TBL because of the nature of this flow. The streamwise spacing of hairpin vortices within a packet is probably reduced by streamwise deceleration $\partial U/\partial x$ during the generation of the hairpins and during their life once they are generated.

Furthermore, the effect of swirling strength on the streamwise spacing can also be discussed here. Zhou et al. (1999) believed that stronger hairpins generate newer ones sooner than weaker hairpins. Moreover, once a hairpin vortex is generated by a stronger hairpin, it is pushed far from the parent hairpin, and the streamwise spacing would also be increased when the swirling strength increases. In other words, the rate of separation between two sequential hairpin vortices could be changed based on $Q2$ intensity. So, it is expected that higher strength of $Q2$ leads to increased streamwise spacing when other parameters are the same. Hence, $\Delta x/\delta$ is expected to decrease in the streamwise direction, since the swirling strength also decreases in the streamwise direction for the present flow albeit only slightly (see figure 4.11). Finally, the evolutions of both symmetric and asymmetric structures were investigated by Zhou et al. (1999) in a channel flow. They found that in the asymmetric case the streamwise distance between the heads of hairpins are smaller than the streamwise spacing in the symmetric case. In the present study, we are not able to distinguish between the symmetric and asymmetric hairpins as mentioned before, but it may be possible that asymmetric hairpins are densely populated in the present flow.

Figures 5.42-a to 5.42-e show the pdfs of streamwise spacing for the hairpin vortices and all prograde spanwise cores. The pdfs of the prograde spanwise vortices indicate smaller streamwise spacings than the pdfs for hairpins only. In other words, hairpin vortices tend to be further apart from each other than other types of spanwise vortices.

Growth Angle

Before discussing and presenting our results of growth angle, it is useful to present the method used by Adrian et al. (2000) to measure the growth angle in order to clarify the comparison of the results. Adrian and co-workers determined the growth angle by fitting a linear curve to the edge of a low momentum zone wherever one occurred, independent of the distance from the wall, whereas growth angle corresponds to the angle between a line passing through the hairpin heads and the wall as shown in figure 5.43 in the present study. Since the hairpin heads are usually aligned at the edge of low momentum zones as explained in section 5.2.5, the results acquired using both methods should be similar. In addition, the statistical information was gathered based on just

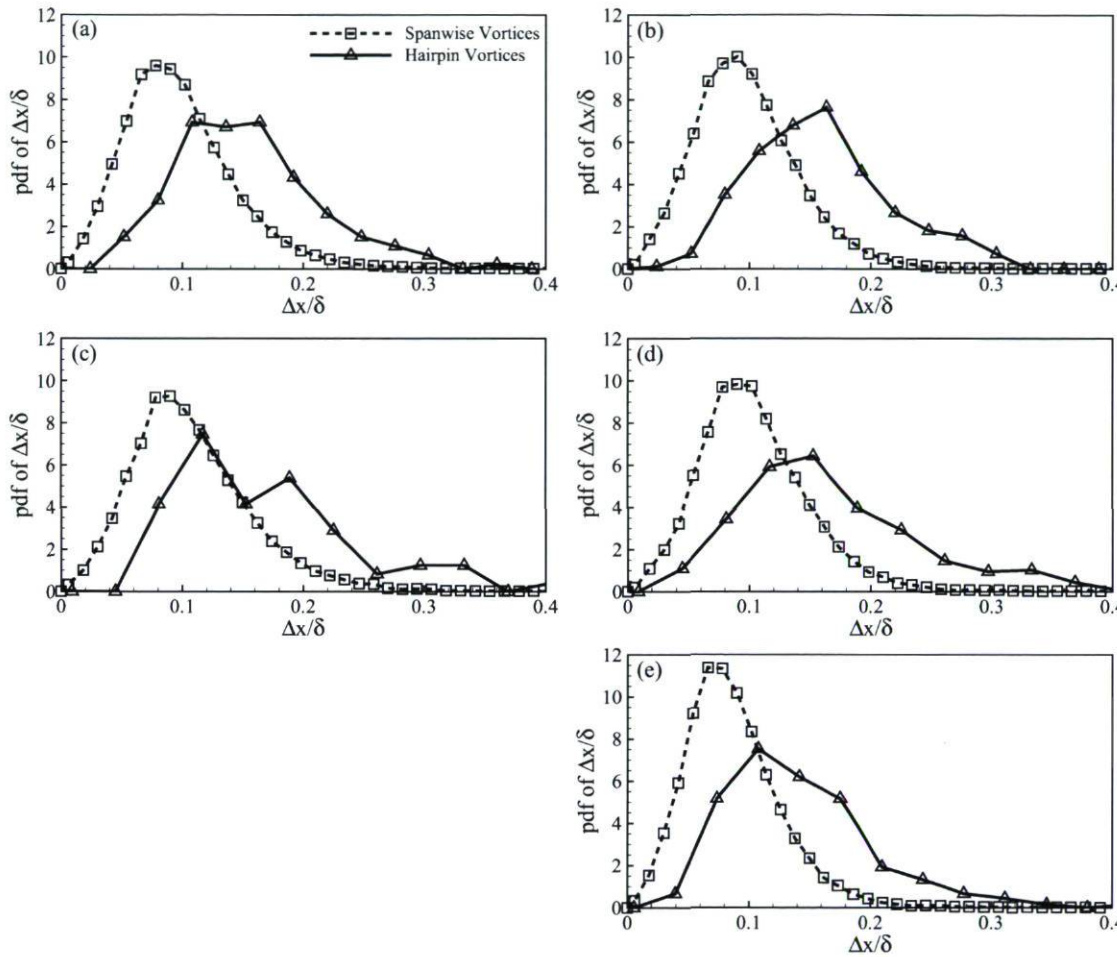

Figure 5.42: Probability density functions of streamwise spacing for spanwise and hairpin vortices at all streamwise positions: a) in region $x = 1128 - 1185$ mm for $y/\delta \leq 0.2$, b) in region $x = 1128 - 1185$ mm for $y/\delta > 0.2$, c) in region $x = 1285 - 1397$ mm for $y/\delta \leq 0.2$, d) in region $x = 1285 - 1397$ mm for $y/\delta > 0.2$, e) in region $x = 1509 - 1680$ mm for $y/\delta > 0.2$.

positive ramp angle in their work, while the ensembles of the present study contain both positive and negative ramp angles (figures 5.43 and 5.44). The ZPG results of Adrian et al. (2000) are that the mean value of growth angle is 10.5^o with the angles ranging from 3^o to 35^o, whereas our results obtained using their database for ZPG TBL show that the mean value of growth angle is about 5^o (table 5.9) with the angles ranging from -45^o to 50^o. The fact that Adrian and co-workers did not account for the negative ramp angles while they are accounted for in the present effort is probably the reason for these differences. They also proposed 12^o as the mean angle instead of 10.5^o, which agrees well with the simulations of Zhou et al. (1999).

The regions of linear growth are a notably frequent feature, while the details of the flow patterns are not the same from realization to realization. It is important to mention that although simple linear ramp structures were found, various other complex growth of hairpin packets have also been observed (figure 5.8). For instance, the hairpin packet far from the wall grows upward roughly linearly for hairpins I to P in the streamwise direction, whereas the hairpin packet close to the wall has a more complex growth. The pdfs of growth angle for APG and ZPG turbulent boundary layers are shown in figure 5.45 and the ensemble average and standard deviation of the ensembles are presented in table 5.9. In the ZPG turbulent boundary layer, it was found that the hairpin packets grow upwards in the streamwise direction at a mean angle of about 5^o, with the angles ranging from -45^o to 50^o with a probability peak around 5^o to 10^o. In the APG turbulent boundary layer, individual packets grow upwards in the streamwise direction at a mean angle of approximately 11^o with the angles ranging from -25^o to 55^o with a probability peak around 10^o-15^o. It is worth noting that lower angles are usually found near the wall. The comparison of the pdfs of growth angle shows that the range of variation of growth angle is more important in the present flow compared to the ZPG TBL. Since the growth angle is affected by the mean strain rates and the latter are more dependent on wall-normal direction in the present flow compared to the ZPG TBL, the narrower pdf of growth angle in the ZPG TBL may be related to the effect of the mean strain rates.

Indeed, higher growth angles in the APG turbulent boundary layer are probably due, at least partly, to the different mean strain rate environment. The individual hairpins are stretched in the wall-normal direction by $\partial V/\partial y$, so the wall-normal distance between the head of two neighbour hairpins would also be increased in y-direction. Indeed, older hairpins would be stretched more than younger hairpin vortices. In addition, $\partial U/\partial x$ causes the vortices to decelerate, so the streamwise spacing would be decreased as explained before. As a result, since $\partial V/\partial y$ and $\partial U/\partial x$ in the present flow are much more important than in the ZPG TBL as discussed before, higher values of γ are also expected in the present flow.

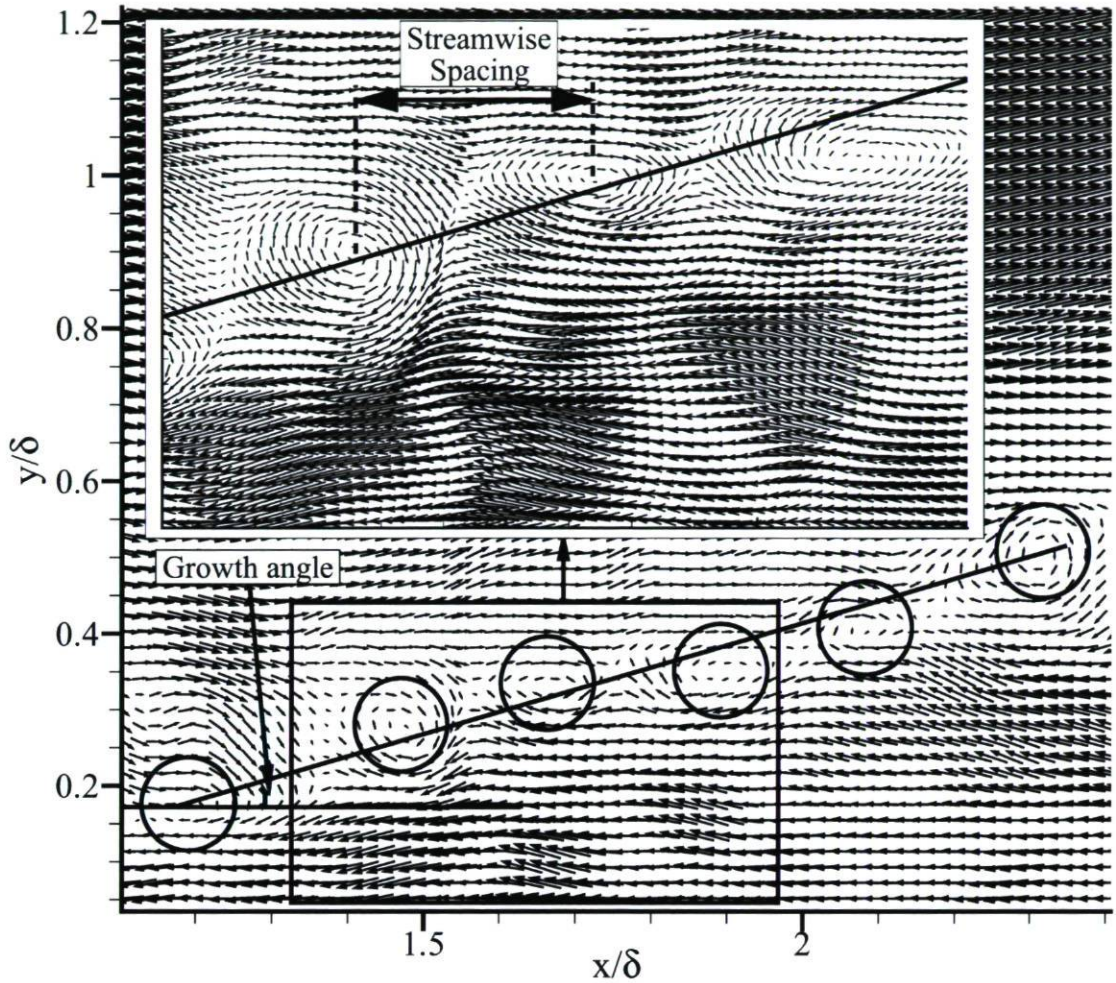

Figure 5.43: Streamwise wall-normal instantaneous field in region $x = 1285 - 1397$ mm, velocity vector field shown using Galilean decomposition as vectors viewed in a frame-of-reference convecting at $u_c = 0.55U_e$, $v_c = 0$ (one vector out of 4 in large plot for clarity), showing the growth angle for a single realization of a hairpin packet.

	$\langle\gamma\rangle \pm P_x$	σ_γ
ZPG TBL	4.9 ± 2.3	12.5
$x = 1128$ mm	11.6 ± 2.4	15.4
$x = 1285$ mm	11.3 ± 1.8	11.6
$x = 1509$ mm	11.0 ± 1.8	11.3

Table 5.9: Ensemble average of growth angle at different streamwise positions and ZPG TBL. σ_γ is the standard deviation of γ distribution in figure 5.45.

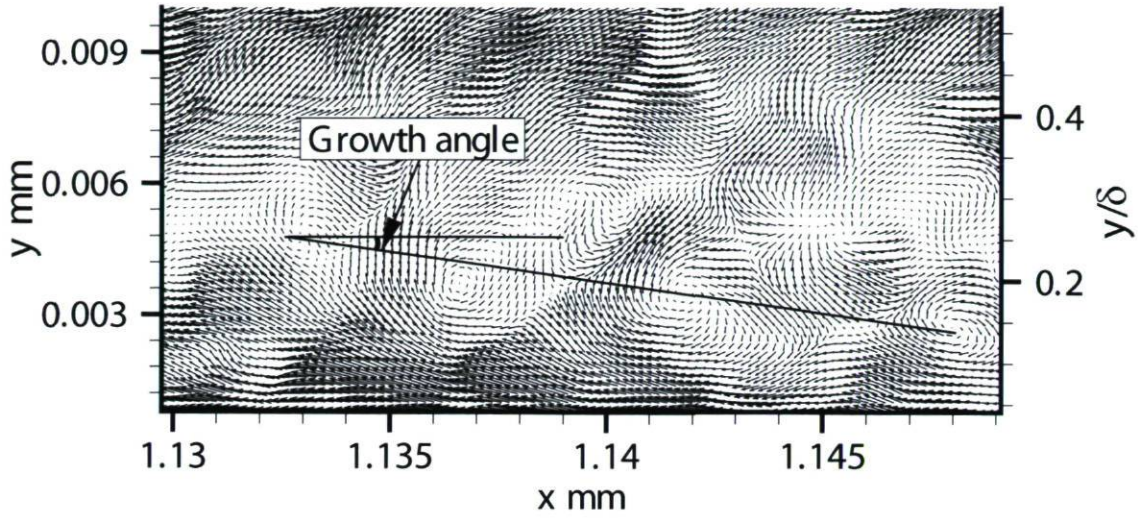

Figure 5.44: Streamwise wall-normal instantaneous field in region $x = 1128 - 1185$ mm, velocity vector field shown using Galilean decomposition (vectors viewed in a frame-of-reference convecting at $u_c = 0.46U_e$, $v_c = 0.53V_e$), showing a hairpin packet with negative growth angle in x-direction.

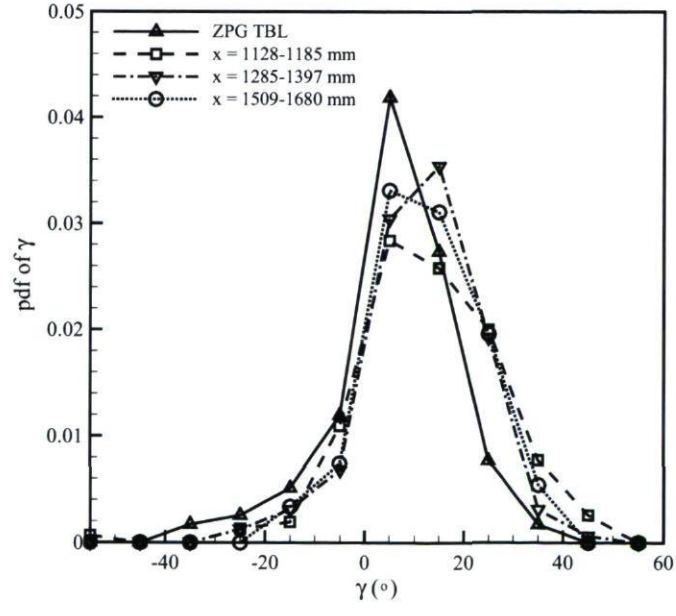

Figure 5.45: Probability density functions of growth angle for all streamwise positions and ZPG TBL.

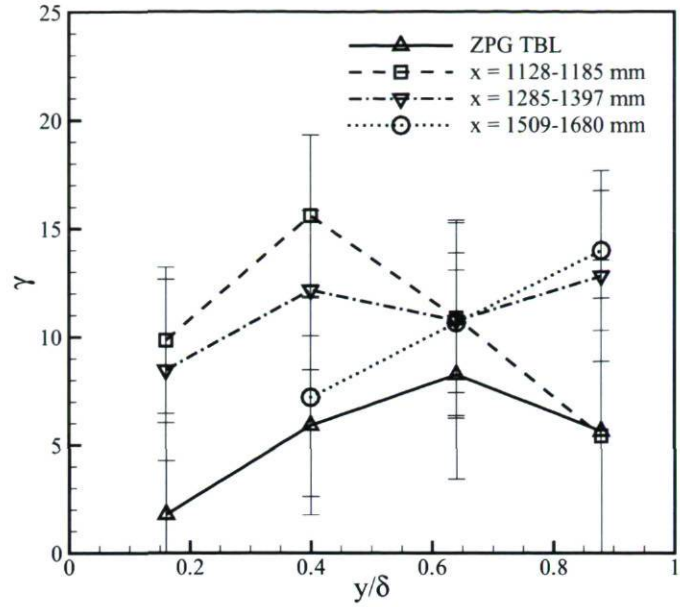

Figure 5.46: Variation of growth angle in wall-normal direction at different streamwise positions and ZPG TBL. Each point is an average over an interval of 0.24 of y/δ in region $y/\delta = 0.04 - 1.00$. The points are at the center of the intervals. The error bars indicate the random uncertainty which is calculated based on the number of realizations in each interval.

Figure 5.46 presents the ensemble average of growth angle as a function of y/δ. It is important to mention that the probability event of hairpin packets is not constant in wall-normal direction as shown in figure 5.23. Each point in figure 5.46 is computed on an interval of 0.24 of y/δ, i.e. 0.16 is related to $0.04 \leq y/\delta \leq 0.28$, in region $y/\delta = 0.04 - 1.00$. The ensemble average of γ is calculated in each interval to acquire one point in this figure. The points are at the center of intervals. The error bars indicate the random uncertainty which is calculated based on the number of realizations in each interval. The associated height of each packet is taken as the height of the last hairpin head in the streamwise direction. The last hairpin in a hairpin packet is usually the parent hairpin.

5.3.4 Hairpin Parameters Before and After Separation

The purpose of the present section is to study the parameters of hairpin vortices before and after the separation point. As mentioned before, the middle of xy plane at the last streamwise position, $x = 1509 - 1680$ mm, is at the separation point ($x = 1615$ mm). It is worth recalling that only PIV data for upper region ($y/\delta > 0.2$) is available at this streamwise position. To study the characteristics of hairpin vortices, the xy plane

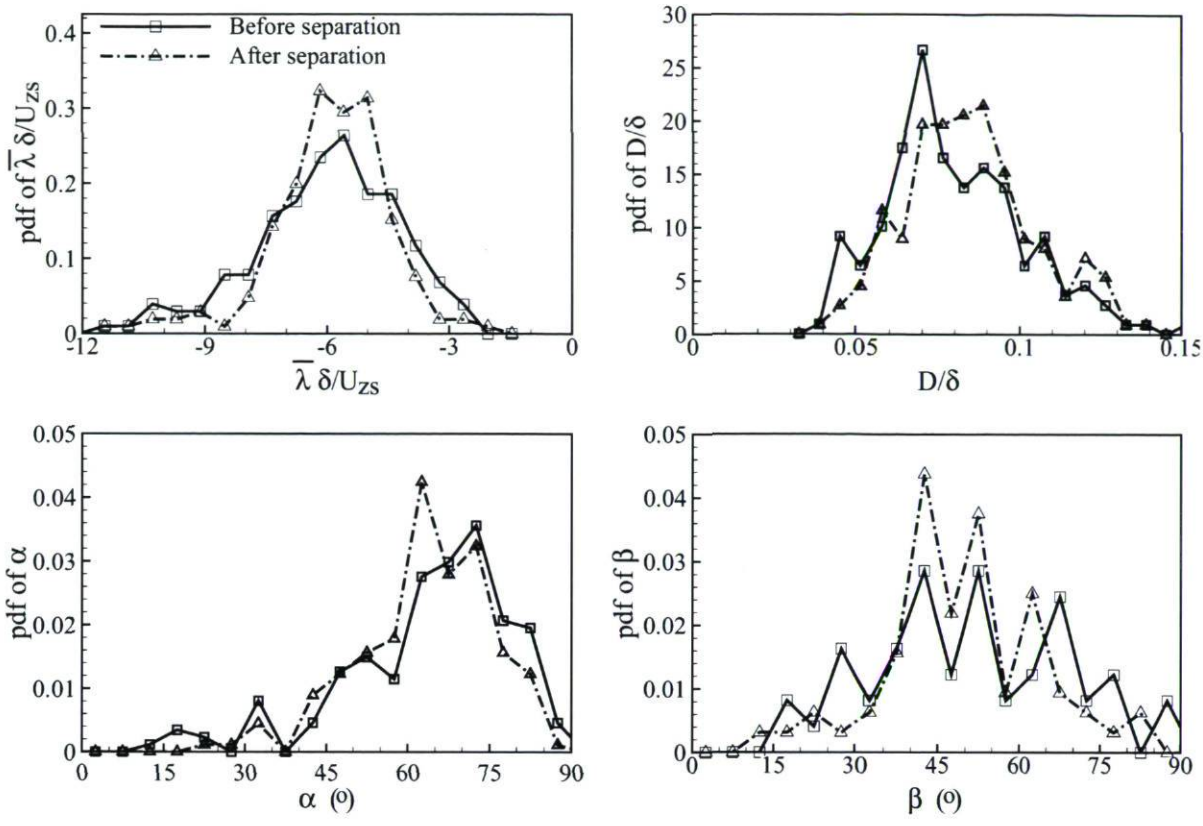

Figure 5.47: Hairpin parameters before and after separation point for $y/\delta > 0.2$.

is divided into two regions in x-direction. The first part includes the region before the separation point, x = 1509-1615 mm, and the second region is in the detachment zone (x = 1615-1680 mm). Then, the different parameters of hairpins are calculated for both regions separately. Figure 5.47 and table 5.10 present the obtained results of hairpin parameters for both regions, before and after separation point.

These results show that the hairpin parameters remain essentially the same before and after the separation point. The hairpin vortices are not affected by the detachment of the flow at least in region just after detachment. Since the results presented are only available for the upper region, the recirculating region near the wall is not included. Hence, the hairpin structures at the begining of the separated shear layer appear to be similar to those just upstream of detachment.

	Before separation		After separation	
	mean	σ	mean	σ
$\langle\bar{\lambda}\rangle$	-6.0	1.8	-6.0	1.5
$\langle D/\delta\rangle$	0.008	0.002	0.008	0.002
$\langle\alpha\rangle$	64	16	64	13
$\langle\beta\rangle$	52	18	50	114

Table 5.10: Average hairpin parameters before and after the separation point for $y/\delta > 0.2$. σ is the standard deviation of the parameter.

5.3.5 Two-point Correlations

Before discussing the results of two-point correlations or linear stochastic estimations it is worth noting that all the instantaneous velocity fields at each streamwise position are accounted for in the two point correlations, conditionally averaged velocity fields and linear stochastic estimations, while only fifty instantaneous velocity fields were used to compute the hairpin and hairpin packet statistics of the previous section. In addition, all the spanwise vortices are included in the results of the present treatment. It is worth mentioning that since the main objective of this work is to explore the instantaneous structures of the APG TBL using PIV, this PIV data are less ideal for the statistical analysis presented hereafter. The number of instantaneous fields (number of realizations) are 1600, 885 and 770 for the first, second and last streamwise positions respectively. Since a large number of realizations is needed for good statistical convergence of correlations and conditional averages, these are not sufficient even for the first streamwise position. Even so, the statistical results are informative as it will be seen in the following.

Since hairpin packet organization is a dominant and robust feature of the present flow, the statistics of the flow should be affected by the imprint of these structures. However, the imprint of coherent structures can be destroyed in the averaging process if variations between instantaneous realizations of packets are large enough.

The instantaneous imprint of hairpin packet signature in xy-plane was previously presented (section 5.2.4) when the measurement plane cross the heads of hairpin vortices (the mid-plane of a hairpin vortex, see figure 5.1-a). In this section two-point spatial correlation coefficients between prograde swirling strength and itself (equation 5.7) are calculated in order to explore the spatial characteristics of hairpin packets. Since the hairpin packet organization is a dominant and robust feature of APG TBL,

it is expected to see correlated areas of negative swirling strength (associated with prograde vortices) below/upstream and above/downstream of the reference position. The population of prograde vortices is approximately constant in y-direction from $y/\delta = 0.1$ to $y/\delta = 0.8$, so several reference heights are chosen at $y/\delta = 0.2$, 0.3, 0.4, 0.5 and 0.6 to calculate the correlation coefficient $\rho_{\lambda_p\lambda_p}$. Since large extent dimensions (especially in streamwise direction) are required to detect the hairpin packet parameters, the two-point correlation is calculated in a bounding box of width 1.3δ and height 0.35δ around the reference position.

$$\rho_{\lambda_p\lambda_p} = \frac{\langle \lambda^p_{ci}(x_{ref}, y_{ref}) \lambda^p_{ci}(x_{ref} + r_x, y) \rangle}{\lambda^p_{rms}(x_{ref}, y_{ref}) \lambda^p_{rms}(x_{ref} + r_x, y)} \tag{5.7}$$

where λ^p_{rms} is the root-mean-square of λ^p_{ci}. λ^p_{ci} is the swirling strength of prograde vortices described in Section 4.3.

Figure 5.48 presents the two-point correlation coefficient $\rho_{\lambda_p\lambda_p}$ at the first streamwise position ($x = 1128 - 1185$ mm) for the reference point at $y/\delta = 0.5$. It is worth mentioning that the acquired results at all reference points are similar to this figure but are not shown for brevity. This figure shows that the correlation coefficient is one (maximum) at the reference point and near zero elsewhere except in special areas in both upstream and downstream of the reference point. Although the correlation is not well converged, the correlated areas of swirling strength grow upwards in the streamwise direction at an angle of approximately 14^o. This orientation is similar to the average growth angle of hairpin packets (see table 5.9) which is around $11^o \pm 2.5^o$. In addition, the mean streamwise spacing between the cores of correlated swirling strength clusters is about 0.2δ, which is approximately equal to the hairpin streamwise spacing, $\Delta x/\delta$, presented in table 5.8 (0.145 ± 0.007). Since the two-point correlations is not well converged, the presented streamwise spacing here is only a rough estimate. The two-point spatial correlation is consistent with the features of hairpin packets observed in the instantaneous velocity fields (section 5.2.4) and the results of Zhou et al. (1996, 1999) and Adrian et al. (2000).

5.3.6 Linear Stochastic Estimation

Statistical evidence of hairpin packets using linear stochastic estimation (LSE) has been reported by Christensen and Adrian (2001) in turbulent channel flow and Hambleton et al. (2006) in ZPG TBL. They found a series of vortices which are located along an inclined line (about 12^o) with respect to the wall using the conditionally averaged flow

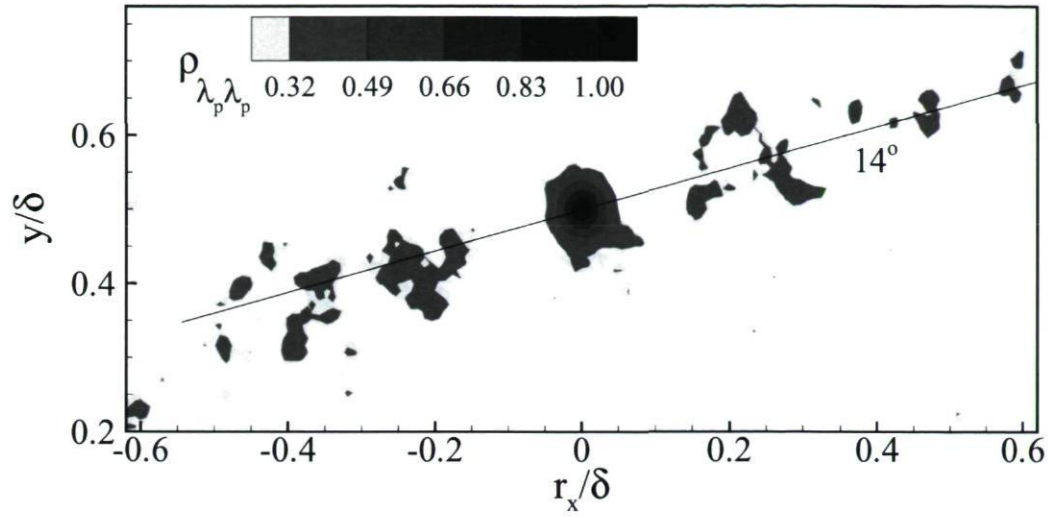

Figure 5.48: Two-point spatial correlation coefficient between λ_{ci}^p and λ_{ci}^p, $\rho_{\lambda_p\lambda_p}$ at $y_{ref} = 0.5\delta$ at the first streamwise position where the number of sample is 1600. Cut off at $\rho_{\lambda_p\lambda_p} = 0.3$.

field associated with a prograde vortex. The same question of Christensen and Adrian (2001) can be posed here: what is the average fluctuating velocity field associated with a single spanwise prograde vortex core (believed to frequently be a hairpin head)? Therefore, LSE will be used to estimate the conditional average of the velocity field, $\langle \boldsymbol{u'}(\boldsymbol{x}+\boldsymbol{r}) \,|\lambda_{ci}^p(\boldsymbol{x})\rangle$ where $\boldsymbol{u'} = (u', v')$ and $\boldsymbol{x} = (x, y)$, given the presence of a prograde vortex core. For the case of the streamwise velocity component, the linear estimate can be defined as

$$\langle u'(\boldsymbol{x}+\boldsymbol{r}) \,|\lambda_{ci}^p(\boldsymbol{x})\rangle \approx \frac{\langle \lambda_{ci}^p(\boldsymbol{x}) u'(\boldsymbol{x}+\boldsymbol{r})\rangle}{\langle \lambda_{ci}^p(\boldsymbol{x}) \lambda_{ci}^p(\boldsymbol{x})\rangle} \lambda_{ci}^p(\boldsymbol{x}) \tag{5.8}$$

where λ_{ci}^p is signed swirl where $\lambda_{ci} < 0$ (prograde swirl), u' is the streamwise component of instantaneous velocity fluctuation and the angled brackets indicate ensemble average over all the available instantaneous fields. This equation allows one to reconstruct the average velocity behaviour associated with a given value of $\lambda_{ci}^p(\boldsymbol{x})$ at $\boldsymbol{x}$. To estimate the conditionally averaged velocity field given a vortex core it is necessary to compute the two-point correlation functions between swirling strength and velocity. The two-point correlation between swirling strength and the velocity fluctuation can be defined as follows

$$\rho_{\lambda u}(\boldsymbol{x}+\boldsymbol{r}) = \frac{\langle \lambda_{ci}^p(\boldsymbol{x}) u'(\boldsymbol{x}+\boldsymbol{r})\rangle}{\lambda_{rms}^p(\boldsymbol{x}) u'_{rms}(\boldsymbol{x}+\boldsymbol{r})} \tag{5.9}$$

where λ^p_{rms} and u'_{rms} are the root-mean-square of λ^p_{ci} and u' respectively, and other parameters as in equation 5.8. In this study, $\rho_{\lambda u}$ and $\rho_{\lambda v}$ are calculated from all instantaneous velocity fields at each streamwise position (1600, 885 and 770 are the number of instantaneous fields for the first, second and third streamwise positions respectively). They are therefore not well converged for the last two positions and even for the first position.

Figure 5.49 illustrates the iso-regions of $\rho_{\lambda u}$ and of $\rho_{\lambda v}$ in region $x = 1128-1185$ mm which is associated with the linear stochastic estimation of figure 5.50-a. The maximum value of correlation functions for both wall-normal and streamwise components occur close to the reference point as expected. The contour of zero value of $\rho_{\lambda u}$ inclined in the x-direction separates the regions of negative and positive $\rho_{\lambda u}$. $\rho_{\lambda u}$ is negative below this contour and positive above. Additionally the contour of zero value of $\rho_{\lambda u}$ is inclined about 13^o with respect to the x-direction which is consistent with the typical growth angle of hairpin packets. These characteristics of $\rho_{\lambda u}$ are consistent with the idea that the head of hairpin vortices lie along an inclined line and a region of relatively uniform low-momentum fluid is created by the collective induction of the vortices. $\rho_{\lambda v}$ is positive to the left of and negative to the right of the reference position. Moreover, the correlated zone below the reference point is bigger than the correlated zone above the event location for the streamwise correlation function. Similarly the correlated zone is bigger to the left of the reference location than to the right for the wall-normal correlation function. As indicated by Christensen and Adrian (2001) these behaviours are consistent with the $Q2$ events induced by the head and legs of hairpin vortices (see section 5.2.1).

Since the conditional average estimation is only a function of unconditional two-point spatial correlation data, equation 5.8 allows to reconstruct the average velocity behaviour associated with a given value of λ_{ci} at $\boldsymbol{x}$=(x_{ref},y_{ref}). It is worth noting that the conditionally averaged velocity field would be the same for all values of $\lambda_{ci} < 0$, because the values of the velocity vectors within a given field estimate are only amplified or attenuated by the chosen value of λ_{ci}.

The conditionally-averaged velocity field obtained via the linear stochastic estimate given a negative swirl event (prograde core) at $y/\delta = 0.5$ is shown in figure 5.50. It is worth mentioning that all vectors were set to unit magnitude by normalizing each with its magnitude because the stochastically estimated velocity field is strongest around the reference point. Thus the velocity vectors tend to be very small away from the reference point. These direction velocity fields in the xy plane reveal general features similar to those presented in Christensen and Adrian (2001) for turbulent channel flow and Hambleton et al. (2006) for a ZPG TBL. As expected, a strong prograde swirl is

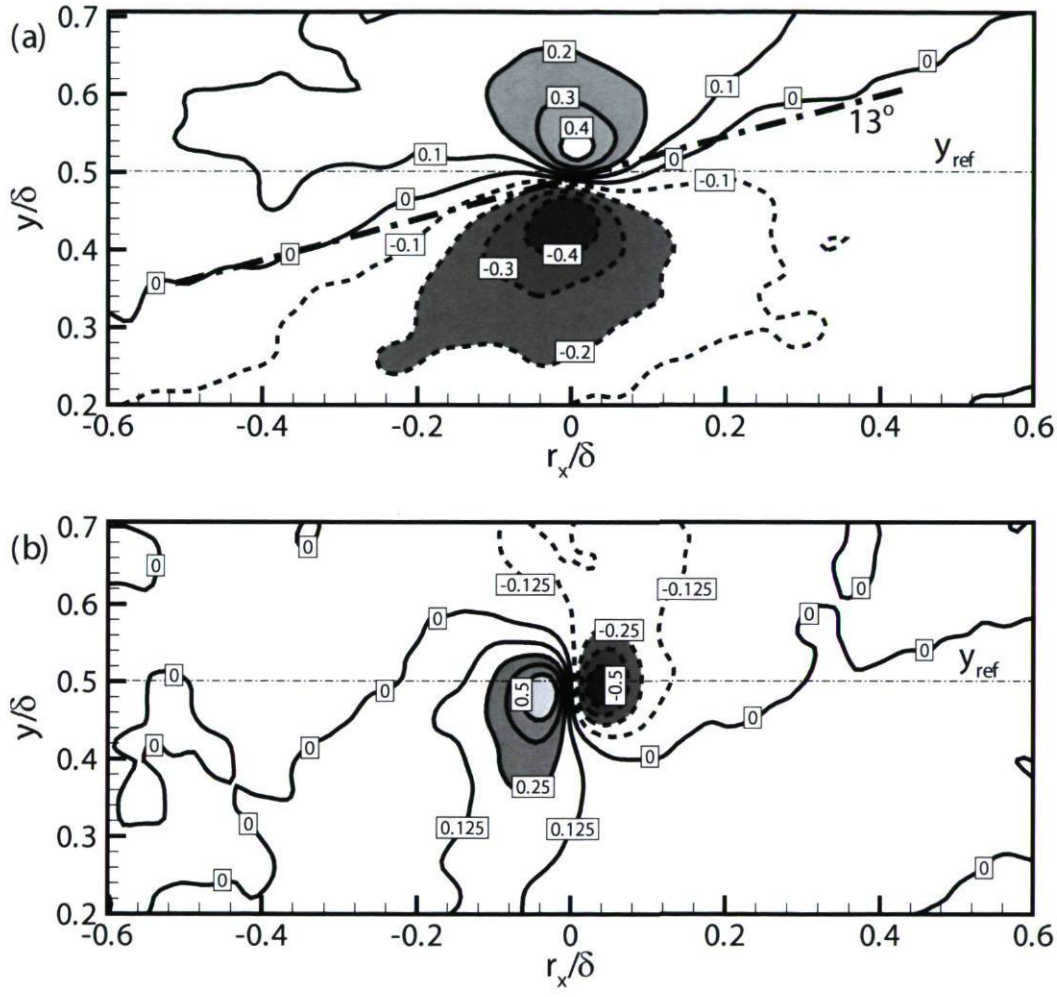

Figure 5.49: Two-point correlation coefficients between velocity and swirling strength in region $x = 1128 - 1185$ mm for $y_{ref} = 0.5\delta$, a) ρ_{λ_u}, b) ρ_{λ_v}.

centered at the condition point (shown by a cross). This swirling motion is accompanied by swirling motions that occur both upstream and downstream of the condition point, except for $x = 1285 - 1397$ mm where no swirling motion exists downstream. This exception could be due to the lack of statistical convergence. The swirling motions are smeared both upstream and downstream of the reference point as shown in figure 5.50. This smeared appearance is probably due to the variation of the relative position of the vortices naturally varies slightly from packet to packet. In other words, if the relative position of vortices was fixed from packet to packet, the swirling motions would appear much more circular.

The stochastically estimated velocity fields shown in figure 5.50 also illustrate a prograde core as the head of hairpin and a $Q2$ event just upstream and below the head. So this swirling motion would be consistent with the hairpin vortex signature. Comparing the results of the stochastically estimated velocity fields of figure 5.50 and the instantaneous fields shown in figures 5.13 and 5.43 and the results of two-point spatial correlations shown in figure 5.48 present a clear qualitative similarity between them. The correlated vortices within the conditionally averaged pattern lie along a line which is inclined from the wall at an angle of about 13^o for the first and second streamwise positions and 20^o for the last one. These angles are approximately equal to those found via the hairpin detection method (table 5.9) except at the last streamwise position. The major difference is that the vortex spacing is not the same in stochastically estimated field. The streamwise spacing is about 0.3-0.4δ for the stochastically estimated velocity fields, while the mean value of $\Delta x/\delta$ is about 0.15δ (table 5.8).

5.3.7 Conditionally-Averaged Velocity Fields

Before presenting the results of conditionally-averaged velocity fields, it is useful to look at the measurement plane and its prospect association with a hairpin vortex signature. For this reason following Natrajan et al. (2007), a hypothetical model of an omega-shaped hairpin vortex is shown in figure 5.51 together with two measurement planes. It is important to note that the hairpin vortices are not necessarily always of an omega shape. If the measurement plane crosses the hairpin vortex at its center, a velocity pattern like figure 5.2 should usually be observed as explained in section 5.2.1. If the measurement plane crosses the neck of the hairpin a prograde vortex above and downstream of the retrograde core would be detected as shown in figure 5.51. To investigate if such scenario occurs frequently, conditionally-averaged velocity fields associated with the presence of a retrograde vortex core are computed. Since the largest population of retrograde vortices occurs in the range $0.15 < y/\delta < 0.35$ (figure 4.13), the reference height for the calculation of the conditionally-averaged velocity fields was chosen at

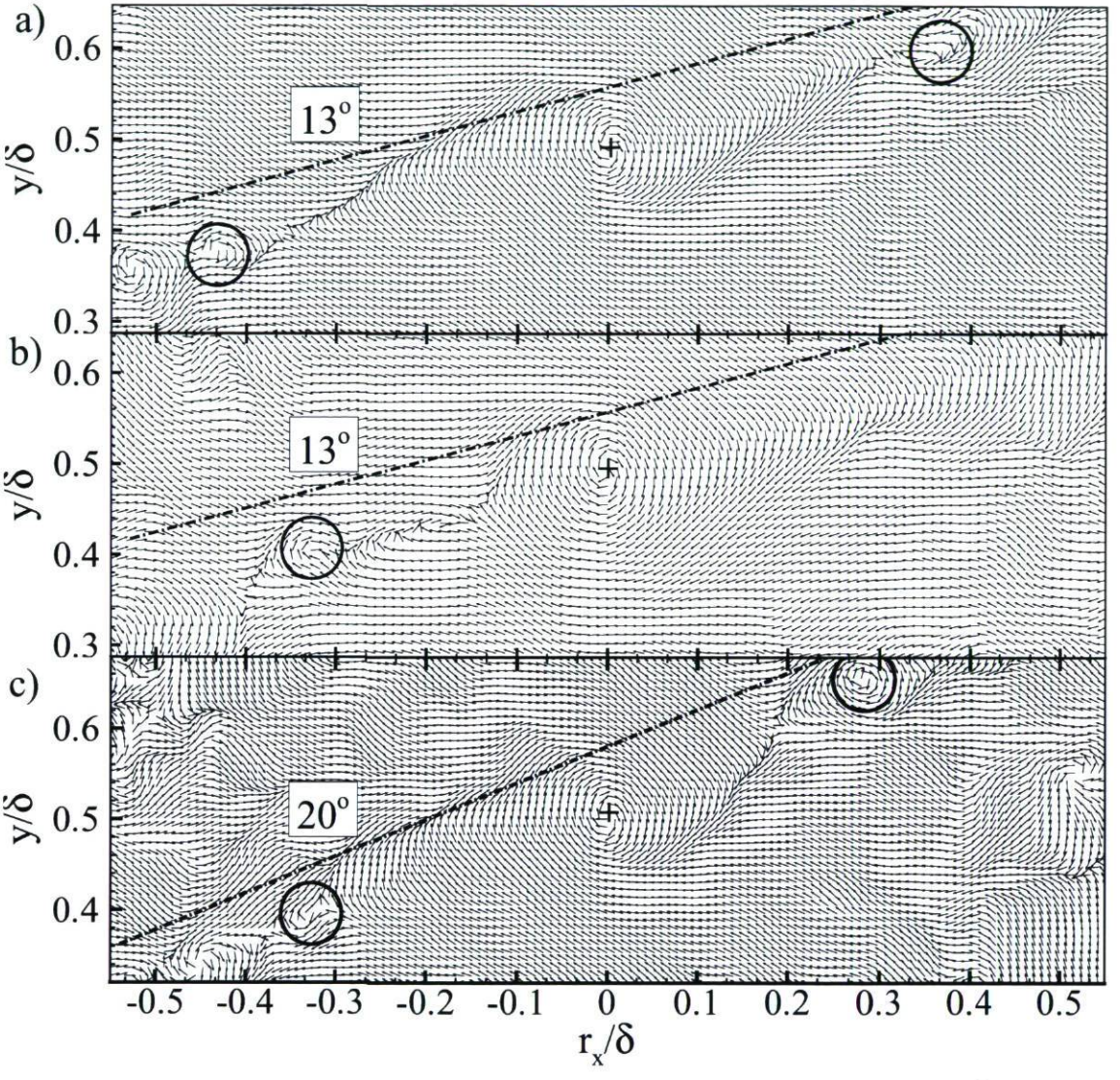

Figure 5.50: Direction field from linear stochastic estimation of velocity based on negative signed swirl at $y/\delta = 0.5$ ($\langle \boldsymbol{u}'(\boldsymbol{x}+\boldsymbol{r}) \,|\lambda_{ci}^{p}(\boldsymbol{x})\rangle$), a) $x = 1128 - 1185$ mm, b) $x = 1285 - 1397$ mm, c) $x = 1509 - 1680$ mm. Vectors have been normalized to unity by their respective magnitudes to highlight swirling motions away from the event location.

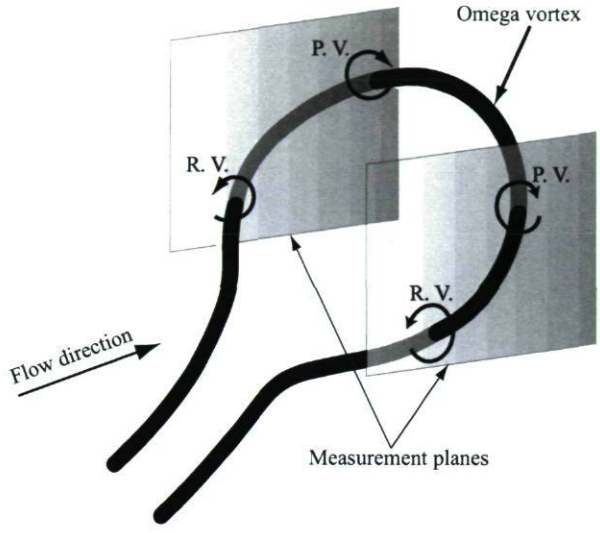

Figure 5.51: Schematic of an omega-shaped hairpin vortex signature which is sliced through one shoulder by streamwise-wall-normal measurement planes. R.V., retrograde vortex, and P.V., prograde vortex. Adapted from schematic of Natrajan et al. (2007).

$y/\delta = 0.25$. The conditional-averages of velocity are done within a bounding box of width 0.22δ and of height 0.2δ centered at each identified retrograde vortex core located at $y/\delta = 0.25$. The advection velocity of the vortex is removed from the instantaneous velocity field within the local bounding box, yielding the local velocity field in the moving reference frame of the retrograde core. The decomposed velocity fields ($u - u_c$ and $v - v_c$) within the bounding box are sorted into four different ensembles based on the orientation of its closest prograde core. The angular orientation of the closest prograde core is $0^o \leq \alpha < 90^o$ for the first quadrant, $90^o \leq \alpha < 180^o$ for the second quadrant, $180^o \leq \alpha < 270^o$ for the third quadrant and $270^o \leq \alpha < 360^o$ for the fourth quadrant. Then the conditional ensemble averages are calculated for each orientation subset.

Figures 5.52-5.54 illustrate the conditionally-averaged velocity fields for retrograde vortices which are centered at $y/\delta = 0.25$ for all streamwise positions. The subplots (a) in figures 5.52-5.54 include the conditionally-averaged velocity fields for which the closest prograde vortex to the identified retrograde core is in the first quadrant. These subplots reveal a well-defined prograde vortex above and downstream of the retrograde spanwise vortex. It is important to mention that the convection velocities of the prograde and retrograde vortices are not exactly the same within the bounding box and that these vortices change in shape and location (prograde one) from one realisation to another. Therefore, the conditionally-averaged prograde core can appear as a deformed vortex. In order to further clarify the averaging effect, conditionally-averaged swirling strength is also computed for each quadrant. For instance, figure 5.55-a corresponds to figure 5.52-a. It is clearly seen that the maximum position of conditionally-averaged

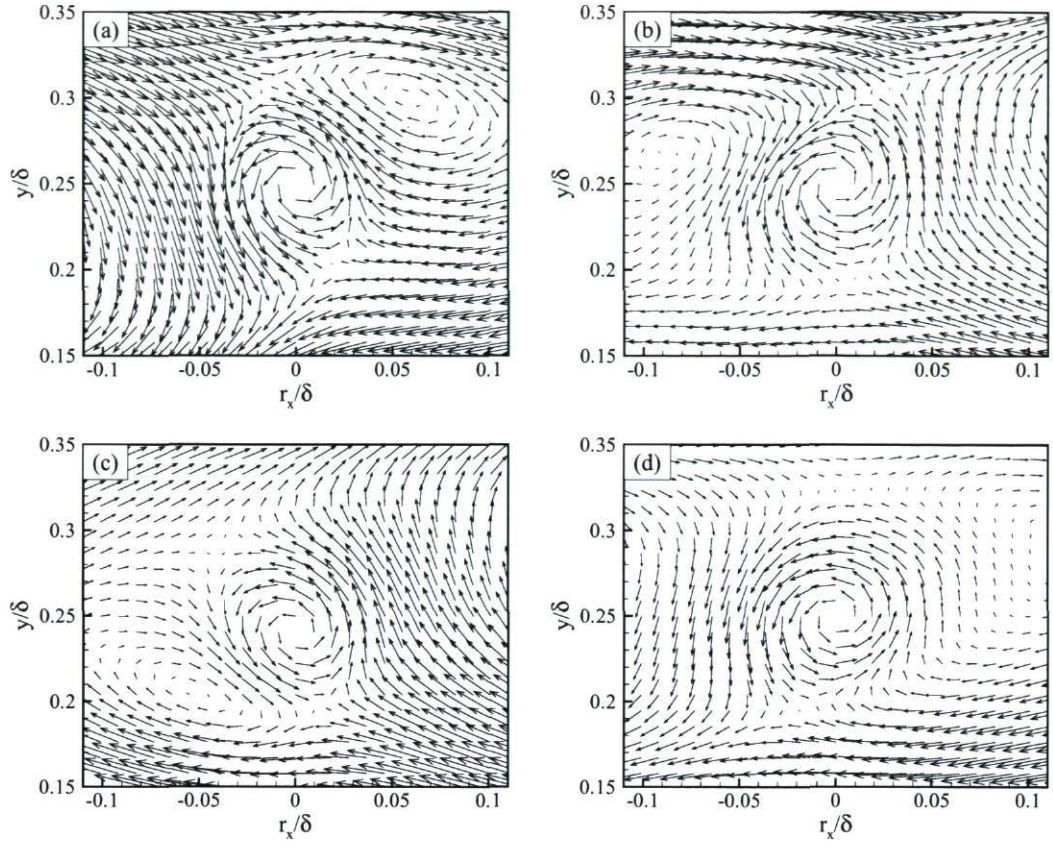

Figure 5.52: Conditionally-averaged velocity fields given a retrograde vortex at $y/\delta = 0.25$ for which its closest prograde vortex is located in quadrants: a) one, b) two, c) three and d) four, in region $x = 1128 - 1185$ mm.

swirling strength is above and upstream of the revealed prograde core in the velocity pattern. The orientation angle of λ_{max} is about 66^o ($\theta \approx 66^o$). This orientation is roughly consistent with the average of neck angle noted in table (5.5). The conditional-averages are also consistent with the model shown in figure 5.51. Moreover, similar velocity signatures are observed in many instantaneous velocity fields at different heights. For instance figure 5.56 shows two examples of similar events at $y/\delta \approx 0.5$. Another feature is the distance between the conditionally-averaged prograde and retrograde cores. This distance is about 0.07δ. The found distance, 0.07δ, is consistent with the results of Natrajan et al. (2007) for the ZPG TBL, 0.058δ.

In the quadrants two and four (the subplots b and d in figures 5.52-5.54), the conditionally-averaged velocity fields are devoid of prograde vortices. It can be supposed that most prograde vortices are randomly orientated with respect to their closest retrograde neighbour in the second and fourth quadrants. These results confirm the expected velocity pattern associated with the model of hairpin vortex signature shown in figure 5.51 and they are also consistent with the results reported by Natrajan et al.

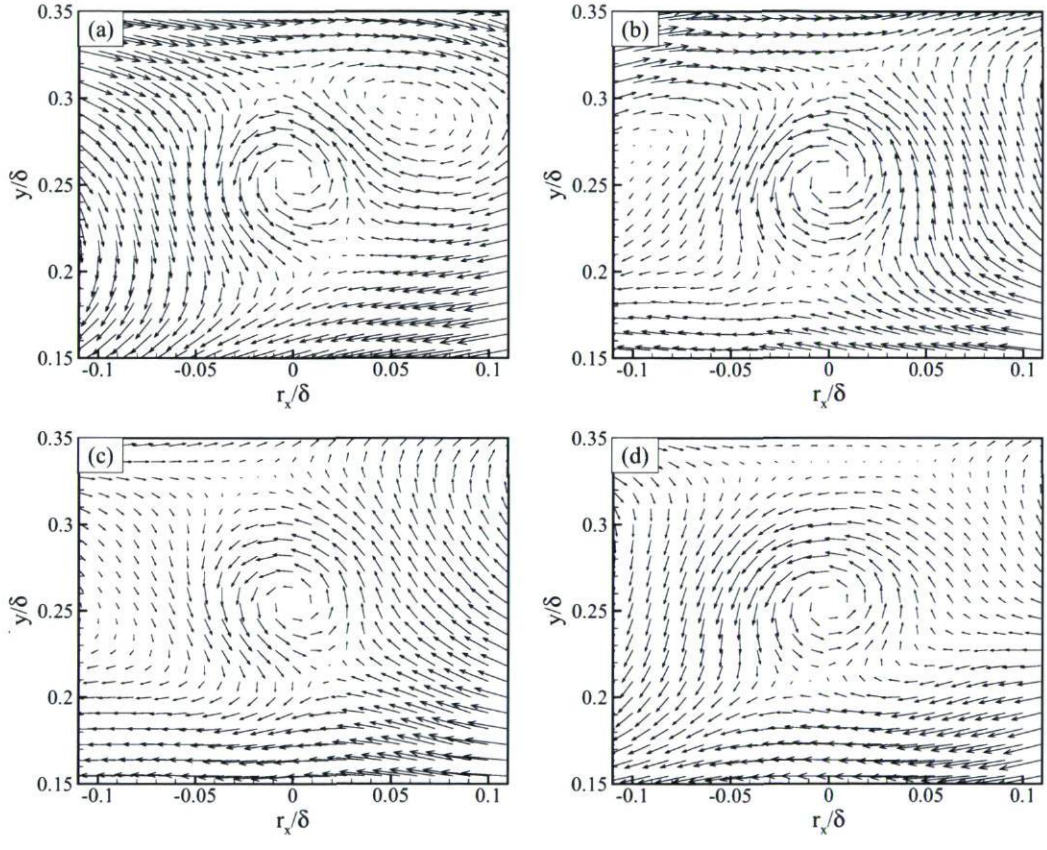

Figure 5.53: As figure 5.52 but in region $x = 1285 - 1397$ mm.

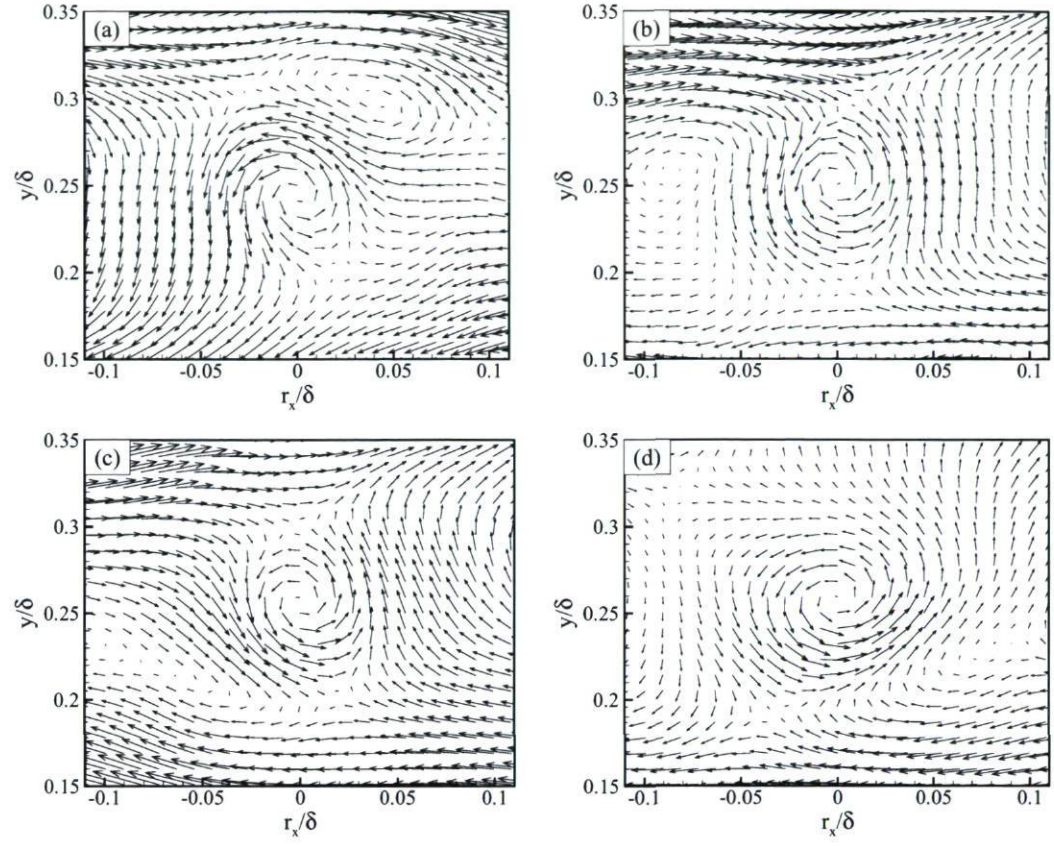

Figure 5.54: As figure 5.52 but in region $x = 1509 - 1680$ mm.

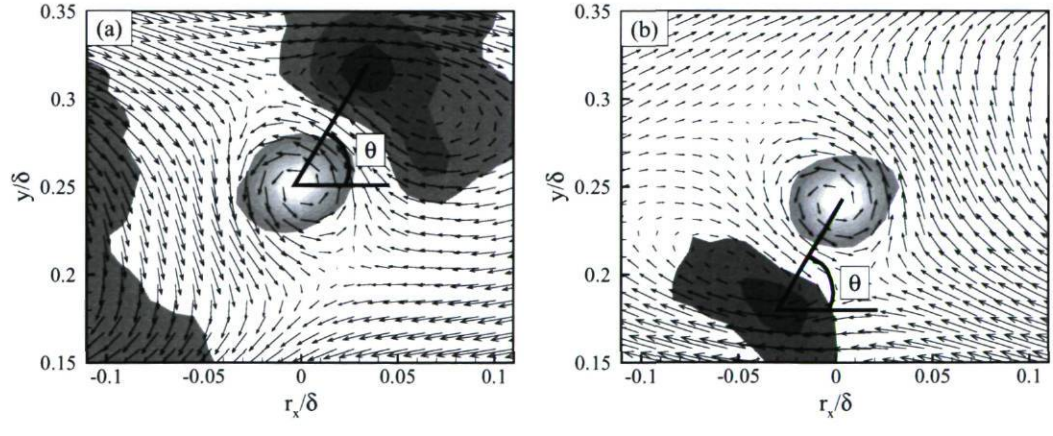

Figure 5.55: Conditionally-averaged velocity fields given a retrograde vortex at $y/\delta = 0.25$ for which its closest prograde vortex is located in quadrants a) one and b) three and iso-regions of conditionally-averaged swirling strength, in region $x = 1128 - 1185$ mm.

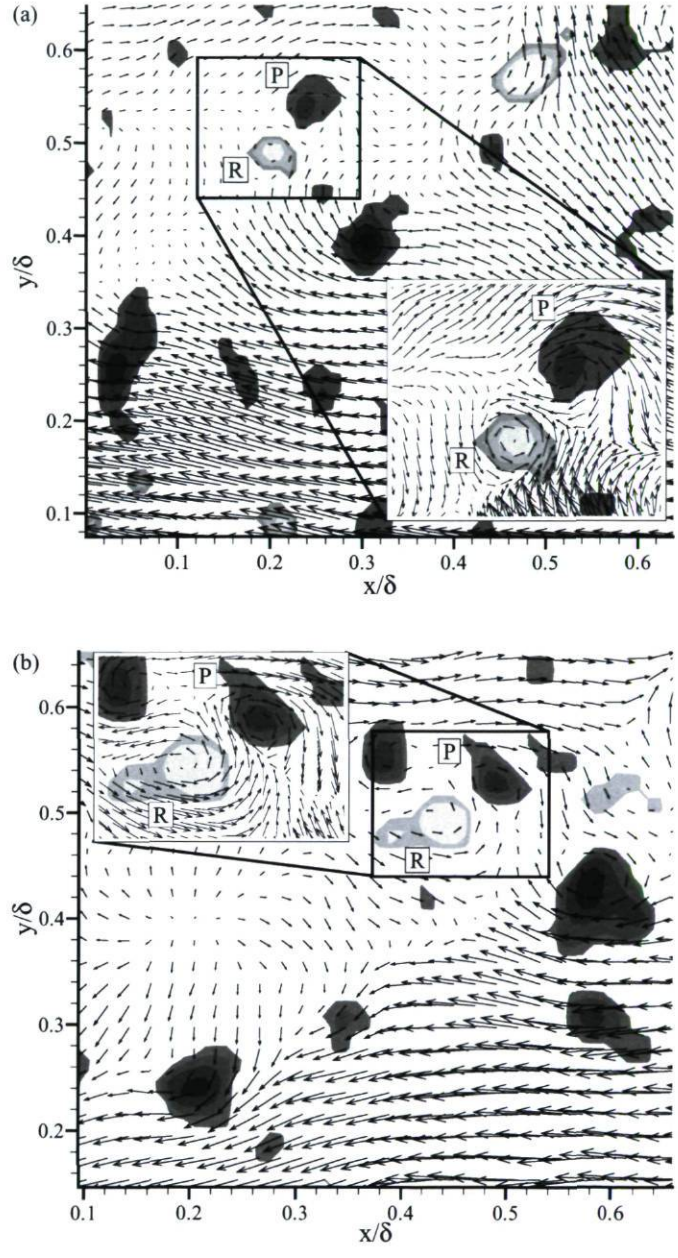

Figure 5.56: Examples of prograde vortex (labeled P) in first quadrant with respect to the retrograde core (labeled R): a) in region $x = 1128 - 1185$ mm, $u_c = 0.80U_e$, $v_c = -1.3V_e$, b) in region $x = 1285 - 1397$ mm, $u_c = 0.61U_e$, $v_c = 0.55V_e$, (one vector out of 4 in large plots for clarity and iso-regions of swirling strength are superimposed).

(2007) for the ZPG TBL.

Based on the hypothetical model, a well-defined prograde vortex above and downstream of the retrograde spanwise vortex (subplots a in figures 5.52-5.54) would be caused by the of omega-shaped hairpin vortices as they occur frequently everywhere. It is important to note that this prograde vortex either is the effect of presence of hairpins or the effect of other structures. Furthermore, a well-defined prograde vortex also occurs in quadrant three, below and upstream of the reference point, at the first streamwise position as shown in figure 5.52-c. According to Natrajan et al. (2007), this prograde vortex can be explained by two possible scenarios. First, this prograde vortex is the imprint of detached ring-like structures. When an omega-shaped hairpin vortex travels downstream, the head and shoulders of this hairpin move up and expand, while its legs squeeze in the inner region. This may leads to detachment of its omega portion (legs detach from the head and shoulder), and the detached omega portion may form a ring-like structure. Furthermore, this pattern, retrograde/prograde pairs in the quadrant-three orientation, would be also represented two different vortical structures. For instance, if a hairpin vortex exists below and downstream of an omega-shaped hairpin structure within a hairpin packet, this pattern (retrograde/prograde pairs in the quadrant-three orientation) can occurr. In this case, the retrograde vortex would be a part of the omega-shaped hairpin structure and the prograde vortex would represent the head of the upstream hairpin vortex. In the second and third streamwise positions, there is not a well-defined prograde vortex in the quadrant three. This could be due to the lack of statistical convergence, or these scenarios (ring-like structures and existence of a hairpin vortex below and downstream of an omega-shaped hairpin structure) are less frequent in these locations.

Even if retrograde vortices are often related to prograde vortices the inverse is not expected. For instance, this is not the case when the measurement plane crosses the mid-plane of a hairpin vortex (figure 5.1-a). The expected velocity pattern in a streamwise/wall-normal cross-section for the hairpin vortex signature is mentioned in section 5.2.1. In fact, isolated prograde structures are expected most of the time since they outnumber retrograde vortices (see section 4.6.1). To explore this idea, similar conditional averages are also computed around identified prograde vortices instead of retrograde vortices. Figures 5.57-5.59 illustrate conditionally-averaged velocity fields given a prograde vortex at $y/\delta = 0.25$. The subplots a to d are related to closest retrograde vortex which is oriented in quadrant one to four relative to prograde vortex at event location. The conditionally-averaged velocity fields are devoid of retrograde vortices. Any preferred orientation of a retrograde vortex with respect to a prograde vortex does not therefore occur frequently enough to leave an imprint in the conditionally-averaged velocity fields. These results are consistent with those of Natrajan et al. (2007) for the

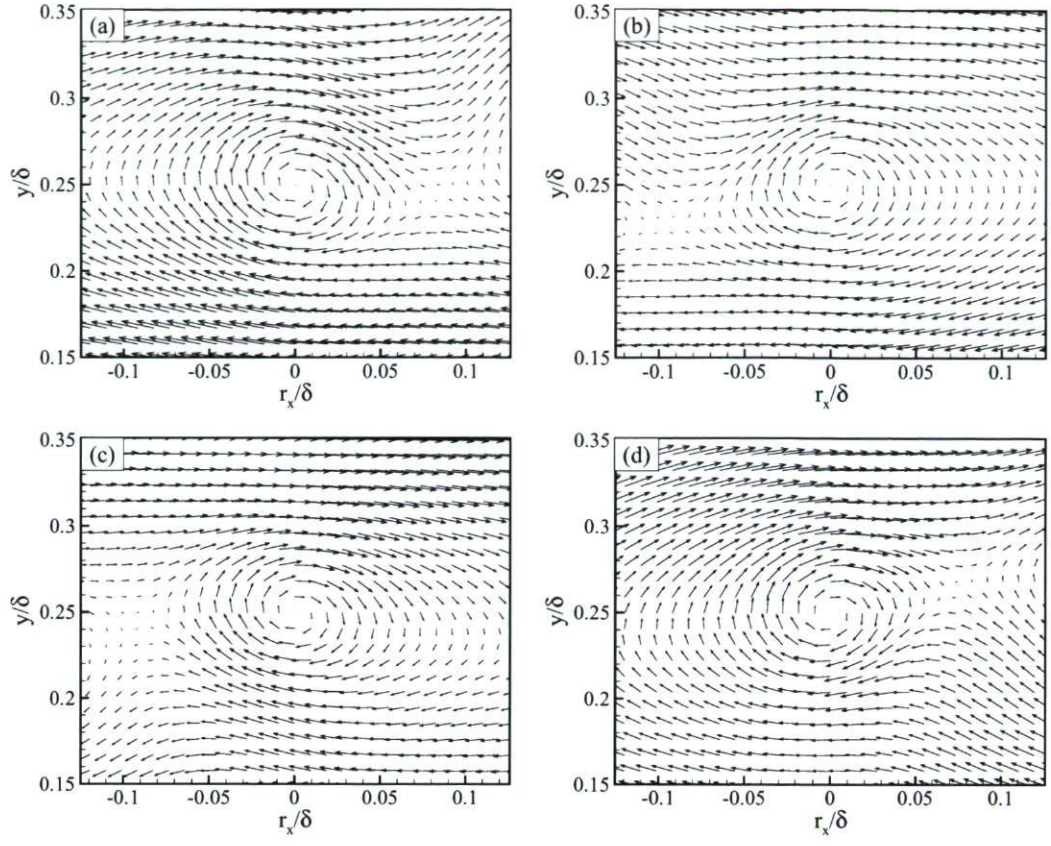

Figure 5.57: Conditionally-averaged velocity fields given a prograde vortex at $y/\delta = 0.25$ for which its closest retrograde vortex is located in quadrants: a) one, b) two, c) three and d) four, in region $x = 1128 - 1185$ mm.

ZPG TBL.

5.4 Discussion of Results

Hairpin vortex signatures are found throughout the lower and upper regions for all streamwise locations and for all of the PIV realizations. In addition the hairpin vortex signatures generally appear in groups of hairpins, with individual hairpins within one group traveling at nearly the same convection velocity, so that they form a traveling packet of hairpin vortices. Since hairpin packets propagate with small velocity dispersion, the streamwise spacing and arrangement of the individual hairpins within a packet remain coherent for long times. It is found experimentally that packets of hairpin vortices sometimes extend over a length of 2δ and contain 3 to 12 vortices. It is worth recalling that the number of hairpins per packet is usually underestimated in xy-plane

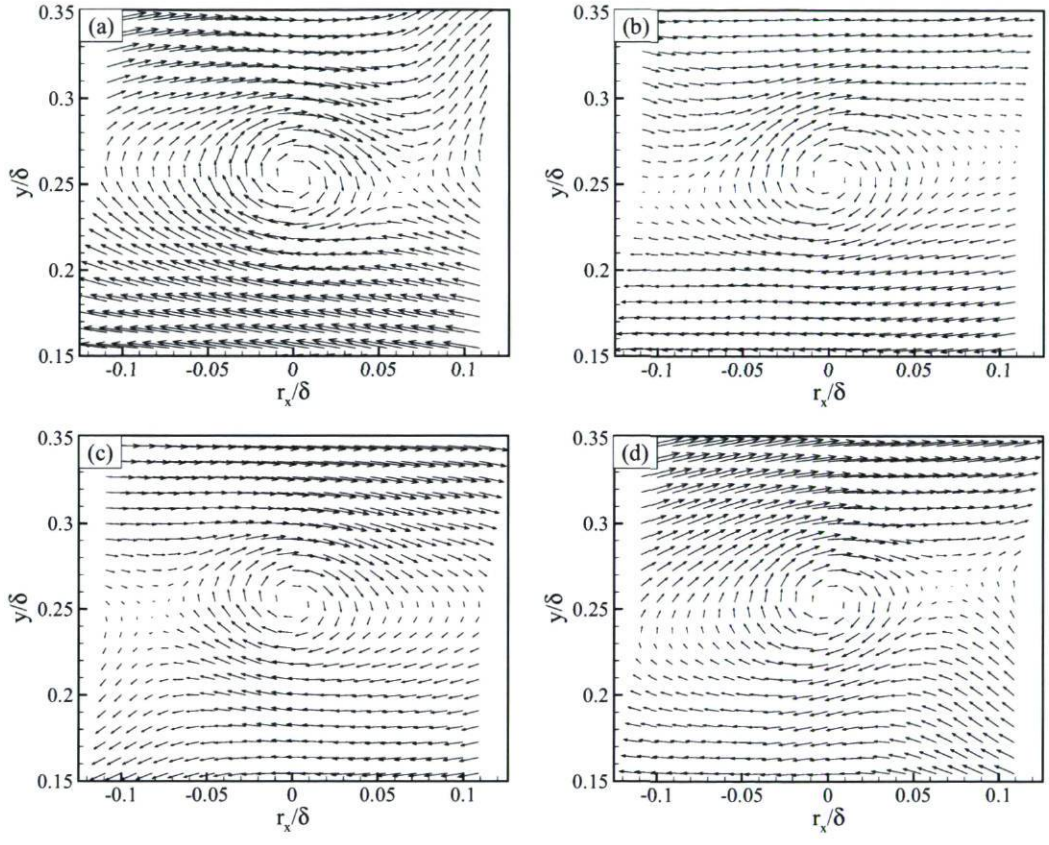

Figure 5.58: As figure 5.57 but in region $x = 1285 - 1397$ mm.

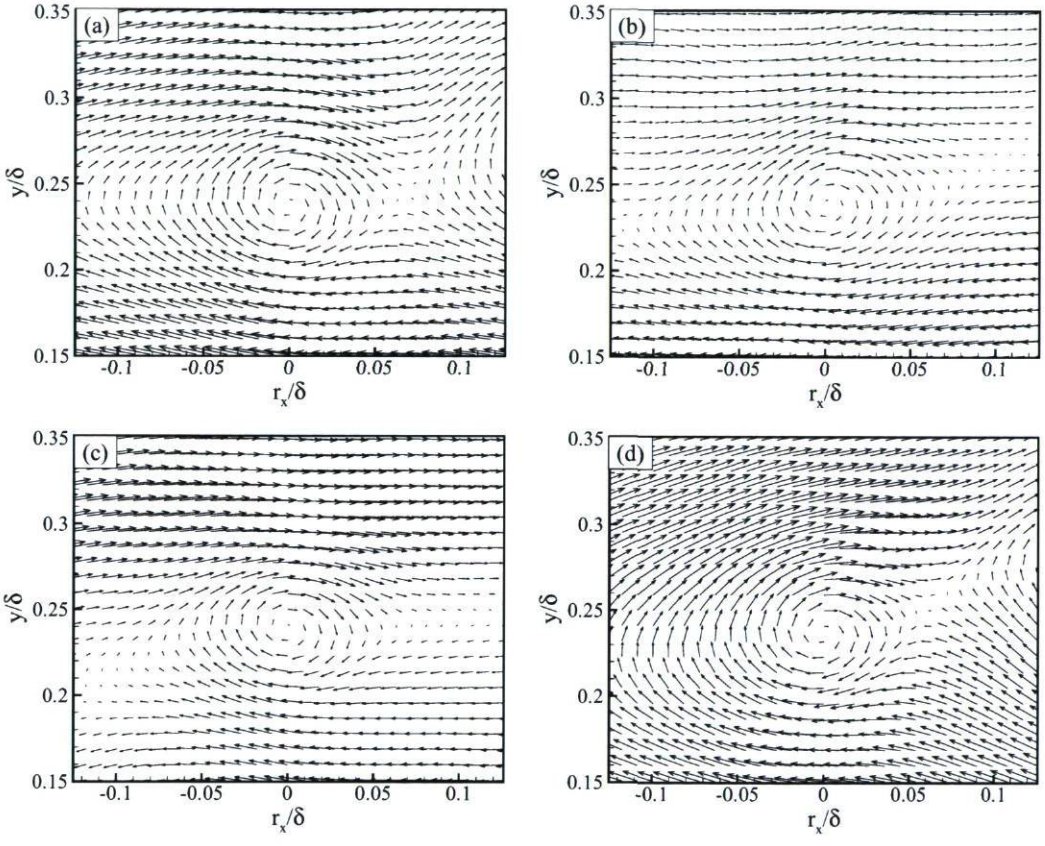

Figure 5.59: As figure 5.57 but in region $x = 1509 - 1680$ mm.

because the hairpin vortices within a packet are not typically aligned in the streamwise direction and are sometimes twisted at small or large angles in the spanwise direction (see section 5.2.4).

Moreover, it can be drawn from the present experimental observations that despite the presence of a very different pressure environment in this flow in comparison to the ZPG TBL, the gross features of the hairpin vortices and hairpin packets remain essentially the same and qualitatively agree well with available results for canonical wall-bounded turbulent flows even as separation is approached.

Now we turn our attention to the differences between the characteristics of hairpin vortices and hairpin packets in those flows. As found and explained in sections 5.3.2 and 5.3.3, the neck and growth angles are larger in the APG TBL than in the ZPG TBL (67^o vs. 60^o for α and 11^o vs. 5^o for γ). These differences can probably be explained by the fact that the mean strain rates are different in those flows. The absolute values of the mean velocity gradients, $\partial U/\partial x$ and $\partial V/\partial y$, are more important in the upper region of APG TBL than in that of a ZPG TBL. Hairpin vortices are more stretched when $\partial V/\partial y$ increases. This is probably why, the neck angle is higher in the present flow in comparison to the ZPG TBL. Furthermore, the hairpin vortices are decelerated when -$\partial U/\partial x$ increases. Two parameters of hairpin packets, $\Delta x/\delta$ and γ, are affected by this phenomenon. First, the streamwise spacing would become shorter for higher value of -$\partial U/\partial x$ because of decelerating effect. In fact, when the effect of the streamwise and wall-normal velocities gradients (-$\partial U/\partial x$ and $\partial V/\partial y$) becomes more pronounced, the hairpin vortices are increasingly stretched in the wall-normal direction, while the spatial streamwise spacing in the streamwise direction between them decreases. It is important to mention that the streamwise spacing may also be affected by swirl intensity and asymmetric/symmetric population of hairpin vortices. The stretching of hairpins in y-direction and decrease spatial spacing in x-direction can effect on hairpin packet inclination (growth angle). Moreover, it was found that the neck angle is approximately constant in wall-normal direction for the present flow, whereas it decreases slightly on the ZPG turbulent boundary layer (figure 5.35). This result contradicts the result of Adrian et al. (2000) that believed the neck angle increases with increasing distance from the wall. In fact, Adrian and co-workers believe that the head takes a near vertical orientation in the upper regions of the boundary layer, while near the wall it takes a more conventional angle.

Although the neck angles increase with the effect of the adverse pressure gradient, the ISL has roughly the same inclination in both APG and ZPG turbulent boundary layers. Moreover, the ensemble average of β is larger in the upper region (table 5.7) than in the lower region. It can be because of the nature of sweep, $Q4$, events in

different regions, as the ISL angle is affected by the $Q4$ inclination. It can be supposed that the high-speed regions are more inclined near the wall (resulting in lower values of β) and more horizontal far from the wall (resulting in higher value of β). Finally, the inclination angle of the neck of hairpin vortices is found to be larger than the ISL angles. This result is consistent with the scenario proposed by Adrian et al. (2000).

The swirl intensity of hairpin heads scaled by U_{zs}/δ is slightly lower in APG TBL compared to the ZPG TBL, especially close to the wall. In addition, it is lower for the last streamwise position in comparison to the other ones for the present flow. Another feature is the form of the profile of $\langle\bar{\lambda}\rangle\,\delta/U_{zs}$ in y-direction for those flows. In the ZPG case, $\langle\bar{\lambda}\rangle\,\delta/U_{zs}$ is maximum near the wall and monotonically decreases in wall-normal direction, while $\langle\bar{\lambda}\rangle\,\delta/U_{zs}$ has a maximum value around $y/\delta = 0.5 - 0.6$ and then decreases near the wall. Such behaviours are consistent with those of the Reynolds stresses as shown in figure 3.29. The link between hairpin vortices and the Reynolds stresses and turbulence production is further discussed in chapter 6.

Besides the effect of $\partial U/\partial x$, the decrease of the streamwise spacing can also be related to the swirl intensity as previously mentioned. Zhou et al. (1999) found that stronger hairpins, hairpins with higher swirl intensity, generate newer ones sooner than weaker hairpins. Furthermore, the newly generated hairpin would be faster repelled because of stronger vortex induction. The streamwise spacing would also be affected by the swirl intensity effect as the swirl intensity is lower at the last streamwise position of the present flow than in the first one. For the same reasons $\Delta x/\delta$ is higher for the ZPG TBL compared to the present flow. The diameter of hairpin heads scaled by δ was also found to be bigger in ZPG TBL (table 5.4), but see chapter 6 regarding the effect of mesh width and interrogation window width on the diameter of vortices. The acquired results also show that D/δ is slightly smaller at the last streamwise position in comparison to other ones for the present flow. It means that the size of vortices are affected by pressure gradient, at least near the detachment point. As the mean flow evolves rapidly in this strong APG TBL, especially near the separation point, it is possible that the turbulent structures respond with a certain delay to the changes of the mean flow.

Chapter 6

Conclusions and Recommendations

In this study, PIV data are taken in streamwise/wall-normal planes of an adverse-pressure-gradient turbulent boundary layer at three streamwise positions to study the turbulence structures in the outer region. These positions go from a position near the pressure peak up to the separation point in order to study the evolution of the turbulence structures in the adverse-pressure-gradient zone. The last streamwise station covers the position of detachment of the boundary layer. The principle contribution of the present study is the detailed characterization of the spanwise vortices and the hairpin vortices. The vortices are detected using the local criteria based on λ_{ci} proposed by Zhou et al. (1999).

Inspection of the contour plots of swirling strength reveals that prograde and retrograde vortex cores densely populate the entire boundary layer. The hairpin vortices and hairpin packets are also found throughout the boundary layer in the adverse pressure gradient zone. The evidence presented here is believed to be the first experimental study that offers strong quantitative support for the existence of hairpin vortices in a strong adverse-pressure-gradient turbulent boundary layer at high Reynolds number.

There are several similarities between the results obtained for the present flow and the available results for the canonical wall-bounded turbulent flows. A primary conclusion drawn from the present experimental observations is that despite the presence of a very different pressure environment in this flow in comparison to the ZPG TBL, the gross features of the spanwise vortices, hairpin vortices and hairpin packets remain essentially the same in the outer region ($y/\delta > 0.2$) and qualitatively agree well with available results for canonical wall-bounded turbulent flows even as separation is approached. Like in many recent PIV studies in ZPG TBL, hairpin vortex signatures frequently occur in groups. In fact, the APG turbulent boundary layer contains

a collection of randomly located hairpins and hairpin packets. Since hairpin packets propagate with small velocity dispersion, the streamwise spacing and arrangement of the individual hairpins within a packet remain coherent for long times. As in the ZPG TBL case, it is found that packets of hairpin vortices sometimes extend over a length of 2δ and contain 3 to 12 vortices in this study. It is worth recalling that the number of hairpins per packet is usually underestimated in xy-plane measurements because the hairpin vortices within a packet are not perfectly aligned in the streamwise direction.

The wall-normal trends of probability of occurrence of spanwise prograde vortices reveal that the largest populations of prograde vortices occur near the wall with a sharp decrease as one moves away from the wall. In addition, near the wall, this probability has higher values in the ZPG TBL compared to the present flow, and it also decreases in the streamwise direction of the present flow. In the upper region, the probability continues to decrease monotonically for $y/\delta > 0.1$ in ZPG case, but at a much slower rate than near the wall. This is also the case for the first streamwise position of the present flow, but at a slower rate than the ZPG TBL, while this trend changes for the other two locations. The probability of occurrence of prograde vortices slightly increases in the upper region, with a maximum around $y/\delta = 0.6 - 0.7$ in the last two streamwise locations. Furthermore, contrary to the near wall trend, this probability increases slightly in the streamwise direction within the upper region of the present flow. In contrast, the probability of occurrence of retrograde vortices is small and very similar for both flows. The wall-normal trends of probability of occurrence of hairpin vortices are roughly similar to those of prograde vortices but they are more pronounced. It means that the probability of occurrence of hairpins, close to the wall, decreases in the streamwise direction of the present flow. Additionally, this probability decreases with distance from the wall for the ZPG TBL and the first streamwise position of the present flow, while it increases and has a maximum in the upper region for the last location. The probabilities of occurrence of spanwise vortices and hairpins are therefore affected by the pressure gradient. The maximum population of these vortices shifts from near the wall to the outer region when the boundary layer is subjected to an adverse pressure gradient.

The forms of the probability density functions of swirling strength and vortex average swirl intensity of the spanwise vortices are very similar to those found by Wu and Christensen (2006) in a ZPG TBL. In addition, an astonishing outcome is that they remain fairly similar at the different streamwise locations. It means that although the vortices change in size and swirl intensity in absolute terms, the distributions of the swirling strength normalized by the standard deviation of the distribution are almost unaffected by the varying strong adverse pressure gradient conditions. Wu and Christensen (2006) also found that the probability density functions of the

swirling strength of spanwise vortices display both Reynolds-number and flow insensitivity. Therefore, the shape of the distributions of swirling strength of spanwise vortices are almost independent of y, Reynolds number, flow type and pressure gradient. Contrarily to the swirling strength scaled by its root-mean-square, the probability density functions of swirl intensity scaled by the Zagarola-Smits time scale, $\bar{\lambda}\delta/U_{zs}$, for both spanwise vortices and hairpin vortices are affected by the pressure gradient. The pdfs of $\bar{\lambda}\delta/U_{zs}$ of the hairpin heads are broader for the ZPG TBL case. The wall-normal trends of $\langle\bar{\lambda}\rangle\,\delta/U_{zs}$ indicate that the swirl intensity of hairpin heads has higher value in the ZPG case in comparison to the present flow. The swirl intensity also decreases in the streamwise direction of the present flow except at the second streamwise position which is slightly lower than the last location. This exception may be due to the effect of spatial resolution on swirl intensity as the spatial resolution at the second streamwise position is slightly lower than the other ones. The shapes of the profiles are also different. In the ZPG TBL, $\langle\bar{\lambda}\rangle\,\delta/U_{zs}$ is maximum near the wall and monotonically decreases in wall-normal direction, while for the present flow it increases in wall-normal direction up to $y/\delta = 0.5 - 0.7$ and then decreases. In addition $\langle\bar{\lambda}\rangle\,\delta/U_{zs}$ decreases in the streamwise direction in the region below $y/\delta = 0.5 - 0.7$ while it remains approximately constant above that region. Similar behaviour is also found for all spanwise, prograde and retrograde, vortices. Finally, higher swirl intensity for the hairpin heads than the prograde spanwise vortices was found, which is consistent with the results of Haidari and Smith (1994) and Zhou et al. (1999).

It is found that the size of the vortices scales well with boundary layer thickness, δ, except near the wall for both spanwise and hairpin vortices. The diameter of vortices decreases near the wall, for $y/\delta \leq 0.1$, while it is roughly constant for $y/\delta > 0.1$. Although the results show higher diameter of vortices scaled by δ for the ZPG TBL in comparison to the present flow, these differences could be due to the effect of mesh width and interrogation window width on the size of vortices. However, taking into account these effects, it is found that the diameter of vortices scaled by δ decreases slightly in the streamwise direction of the present flow. Since the mean flow evolves rapidly in this strong APG TBL, it is therefore possible that the turbulent structures respond with a certain delay to the changes of the mean flow. As a result, the increase in size of the vortices in the streamwise direction does not follow the boundary layer coarsening in the adverse pressure gradient region. Moreover, the average diameter of all prograde spanwise vortices is smaller than that of the hairpin heads. Hence, the hairpin vortices associated with hairpin packets are usually the largest vortical structures in boundary layers.

Turning our attention to the orientations of individual hairpins, the average inclination angle with respect to the wall of the upper neck part of hairpins is about 70^o and

60^o for the present flow and ZPG TBL respectively. These values are consistent with the results of Zhou et al. (1999). It is worth recalling that a characteristic tilt of 45^o is sometimes quoted for hairpin inclination for canonical turbulent wall flows. This angle value represents usually a rough estimate for the complete hairpin (legs and necks) orientation while the present results are obtained from direct measurements and they apply only to the upper neck part. The aforementioned hairpin inclination differences between the ZPG TBL and the present strong APG flow (70^o vs. 60^o) can probably be explained by the fact that the mean strain rates are different in both flows. The velocity gradients $-\partial U/\partial x$ and $\partial V/\partial y$ are much more important in the outer region of a strongly decelerated flow than in that of a ZPG TBL. Consequently, tilting and wall-normal stretching of the legs and necks of the hairpins should also be more important in the present flow in comparison to ZPG TBL, leading to more inclined hairpins. Finally, the results show that the neck angle is approximately constant in y-direction for the present flow, whereas it decreases slightly in the ZPG turbulent boundary layer. This latter result contradicts the result reported by Adrian et al. (2000) that believed the neck angle increases with increasing distance from the wall. Adrian and co-workers believe that the head takes a near vertical orientation in the upper regions of the boundary layer, while near the wall it takes a more conventional angle.

The streamwise spacing between two vortex cores, in both cases of spanwise vortices and hairpin heads, is also affected by pressure gradient. The acquired results show smaller streamwise spacing when scaled by δ in the present flow compared to the ZPG TBL. Moreover the streamwise spacing decreases in the streamwise direction for the present flow. Since $-\partial U/\partial x$ is much more important in the outer region of a strongly decelerated flow than in that of a ZPG TBL, the hairpin vortices probably decelerate in the APG TBL case as they travel downstream. In other words, the streamwise distance between neighbour hairpins would decrease when the effect of $-\partial U/\partial x$ is more important. Furthermore, streamwise spacing may be affected by swirl intensity (in relation to hairpin generation and mutual repulsion mechanisms) and the proportion of asymmetric hairpins as discussed in section 5.3.3.

Similar to the neck inclination of the individual hairpins, the growth angles of hairpin packets are also higher in the present APG TBL when compared to ZPG TBL (11^o vs. 5^o). Since the longer, usually most downstream hairpins in a hairpin packet are also normally the older ones, the increased titling and stretching of hairpins in the APG TBL also implies that the growth angle should be larger.

Since hairpin packets are commonly observed in the instantaneous realizations of the present flow, conditional statistics of the flow should be affected in some manner by the imprint of hairpin vortex signatures. The results of conditionally-averaged velocity fields

are consistent with the omega-shaped hairpin vortex signature. The orientation between the retrograde/prograde vortices in the imprint of conditionally-averaged velocity fields is approximately equal to the neck angle of hairpin vortices. Moreover, both two-point spatial correlations between the swirling strength of prograde/prograde vortices and linear stochastic estimation reveal also imprints which are qualitatively similar to the hairpin packets found in the instantaneous fields. For instance, the velocity pattern obtained by linear stochastic estimation reveals a group of prograde vortices which lie along a line which is inclined from the wall at an angle approximately equal to the measured growth angles of the hairpin packets. Several enhanced correlated areas of two-point correlations between swirling strength of prograde/prograde vortices also grow upwards in the streamwise direction at an angle approximately equal to the average growth angle of the hairpin packets. Additionally, the streamwise spacing between the correlated areas is consistent with those found for the hairpins. Finally, these results are consistent with the reported results for canonical wall turbulent flows.

We turn now our attention to the link between the hairpin characteristics and Reynolds stresses and turbulence production. First, the trends observed for the probability of occurrence of hairpins and swirl intensity in the present flow and ZPG TBL are consistent with those of the Reynolds stresses. For instance, in the ZPG TBL, Reynolds stresses are maximum close to the wall, while they have a maximum value around $y/\delta = 0.6$ for the present flow. Additionally, the Reynolds stresses decrease in the streamwise direction of the present flow. This suggests the strong link between the hairpin vortices and the Reynolds stresses, although the Reynolds stresses are second-order moments which are not solely the result of vortices. However, the differences in levels of the Reynolds stresses between the two flows are slightly different to those of the probability of occurrence and swirl intensity of hairpins. The decrease of hairpin population and swirl intensity near the wall in the APG case is not as strong as the decrease of Reynolds stresses. Even in the outer region, Reynolds stresses are much higher in the ZPG TBL than in the present flow which is consistent with the difference of swirl intensity of hairpin heads in those flows, while it is not consistent with the trends hairpin population. This later point may be related to the high value of Reynolds stresses near the wall in the ZPG TBL, which is the result of hairpin vortices and other types of structures. So, the near wall turbulence energy may also affect the Reynolds stresses in the outer region. In fact, the near wall region transfers much more turbulent energy to the upper region in the ZPG TBL case, while this is much less the case for the present flow.

The tendency of swirl intensity and hairpin population of the hairpin heads are also consistent with the difference of turbulence production between the ZPG TBL and the present flow in the lower region of the boundary layer. As found, the turbulence

production normalized by the Zagarola-Smits scales is much higher in the ZPG TBL than in the present flow in the lower region of boundary layer. This may be related to, at least in part, the swirl intensity of hairpin vortices as the hairpin packets are responsible, at least in part, for the turbulence production. In addition, near the wall the decrease in the streamwise direction of the present flow of the swirl intensity and the hairpin population are consistent with the variation of turbulence production. It would be possible that the hairpin vortices are more detached in the present flow as separation is approached compared to ZPG TBL case. Since turbulence production is in some cases affected by the hairpin vortices, this detachment of hairpins can affect the turbulence production in the lower region.

As is so often the case with research in the field of wall-bounded turbulent flows, in the present study many unanswered questions remain. In spite of the success achieved in the investigation of hairpin vortices and hairpin packets and on how they are affected by the pressure gradient, there remain very critical gaps in knowledge. First, this study does not provide information on the spanwise characteristics of hairpins and hairpin packets. This investigation is currently being done by another PhD student in the fluid mechanics laboratory. Next, the near-wall structures could not be investigated as it needs higher spatial resolution and different types of measurements to interpret and detect the fine structures. The creation and evolution of hairpin vortices and of hairpin packets have not been investigated too. Hopefully, future works would include the study of fine structures, especially close the wall, and of the time evolution of hairpin vortices and packets. The hope is that this study can serve as a building block for any such future work that would add to the knowledge base on adverse-pressure-gradient turbulent boundary layers.

Chapter 7

Bibliography

E. W. Adams and J. P. Johnston. Flow structure in the near-wall zone of a turbulent separated flow. *AIAA journal*, 26(8):933–939, 1988.

R. J. Adrian. Hairpin vortex organization in wall turbulence. *Physics of Fluids*, 19: 041301, 2007.

R. J. Adrian, S. Balachandar, and Z. C. Liu. Spanwise growth of vortex structure in wall turbulence. *KSME Int. Journal*, 15(1741), 2001.

R. J. Adrian, C. D. Meinhart, and C. D. Tomkins. Vortex organization in the outer region of the turbulent boundary layer. *Journal of Fluid Mechanics*, 422:1–54, 2000.

K. P. Angele and B. Muhammad-Klingmann. PIV measurements in a weakly separating and reattaching turbulent boundary layer. *European Journal of Mechanics/B Fluids*, 25(2):204–222, 2006.

P. S. Bernard and J. M. Wallace. Vortex kinematics, dynamics, and turbulent momentum transport in wall bounded flows. *Self-sustaining mechanisms of wall turbulence(A 98-17710 03-34), Southampton, United Kingdom, Computational Mechanics Publications (Advances in Fluid Mechanics Series).*, 15:65–81, 1997.

R. F. Blackwelder. The bursting process in turbulent boundary layers. *Coherent Structure of Turbulent Boundary Layers*, 1978.

R. F. Blackwelder. An experimental model for near-wall structure. *Self-sustaining mechanisms of wall turbulence(A 98-17710 03-34), Southampton, United Kingdom, Computational Mechanics Publications(Advances in Fluid Mechanics Series.*, 15:49–64, 1997.

R. F. Blackwelder and H. Eckelmann. Streamwise vortices associated with the bursting phenomenon. *Journal of Fluid Mechanics*, 94(03):577–594, 1979.

R. F. Blackwelder and R. E. Kaplan. On the wall structure of the turbulent boundary layer. *Journal of Fluid Mechanics*, 76(01):89–112, 1976.

D. G. Bogard and W. G. Tiederman. Burst detection with single-point velocity measurements. *Journal of Fluid Mechanics*, 162:389–413, 1986.

M. H. Buschmann and M. Gad-el Hak. Structure of turbulent boundary layers with zero pressure gradient. In *4 th AIAA Theoretical Fluid Mechanics Meeting*, page 4813, 2005.

J. Carlier and M. Stanislas. Experimental study of eddy structures in a turbulent boundary layer using particle image velocimetry. *Journal of Fluid Mechanics*, 535: 143–188, 2005.

L. Castillo and W. K. George. Similarity analysis for turbulent boundary layer with pressure gradient: outer flow. *AIAA journal*, 39(1):41–47, 2001.

L. Castillo and X. Wang. Similarity analysis for nonequilibrium turbulent boundary layers. *ASME Journal of Fluids Engineering*, 126:827–834, 2004.

L. Castillo, X. Wang, and W. K. George. Separation criterion for turbulent boundary layers via similarity analysis. *ASME Journal of Fluids Engineering*, 126:297–304, 2004.

P. Chakraborty, S. Balachandar, and R. J. Adrian. On the relationships between local vortex identification schemes. *Journal of Fluid Mechanics*, 535:189–214, 2005.

S. I. Chernyshenko and M. F. Baig. The mechanism of streak formation in near-wall turbulence. *Journal of Fluid Mechanics*, 544:99–131, 2005.

M. S. Chong, J. Soria, A. E. Perry, J. Chacin, B. J. Cantwell, and Y. Na. Turbulence structures of wall-bounded shear flows found using dns data. *Journal of Fluid Mechanics*, 357:225–247, 1998.

K. T. Christensen and R. J. Adrian. Statistical evidence of hairpin vortex packets in wall turbulence. *Journal of Fluid Mechanics*, 431:433–443, 2001.

K. T. Christensen, Y. Wu, R. J. Adrian, and W. Lai. Statistical imprints of structure in wall turbulence, 2004. *AIAA Paper*, 2004.

F. H. Clauser. The turbulent boundary layer. *Advances in Applied Mechanics*, 4(1): 1–51, 1956.

H. W. Coleman and W. G. Steele. *Experimentation and uncertainty analysis for engineers.* Wiley-Interscience, 1999.

R. Cucitore, M. Quadrio, and A. Baron. On the effectiveness and limitations of local criteria for the identification of a vortex. *European Journal of Mechanics/B Fluids*, 18(2):261–282, 1999.

D. B. De Graaff and J. K. Eaton. Reynolds-number scaling of the flat-plate turbulent boundary layer. *Journal of Fluid Mechanics*, 422:319–346, 2000.

C. J. Delo, R. M. Kelso, and A. J. Smits. Three-dimensional structure of a low-reynolds-number turbulent boundary layer. *Journal of Fluid Mechanics*, 512:47–83, 2004.

T. L. Doligalski and J. D. A. Walker. The boundary layer induced by a convected two-dimensional vortex. *Journal of Fluid Mechanics*, 139:1–28, 1984.

O. Flores, J. Jimenez, and J. C. Del Alamo. Vorticity organization in the outer layer of turbulent channels with disturbed walls. *Journal of Fluid Mechanics*, 591:145–154, 2007.

B. Ganapathisubramani. *Investigation of turbulent boundary layer structure using stereoscopic particle image velocimetry.* PhD thesis, University of Minnesota, USA, 2004.

B. Ganapathisubramani, N. Hutchins, W. T. Hambleton, E. K. Longmire, and I. Marušic. Investigation of large-scale coherence in a turbulent boundary layer using two-point correlations. *Journal of Fluid Mechanics*, 524:57–80, 2005.

B. Ganapathisubramani, E. K. Longmire, and I. Marušic. Characteristics of vortex packets in turbulent boundary layers. *Journal of Fluid Mechanics*, 478:35–46, 2003.

B. Ganapathisubramani, E. K. Longmire, and I. Marušic. Experimental investigation of vortex properties in a turbulent boundary layer. *Physics of Fluids*, 18:055105, 2006.

A. H. Haidari and C. R. Smith. The generation and regeneration of single hairpin vortices. *Journal of Fluid Mechanics*, 277:135–162, 1994.

W. T. Hambleton, N. Hutchins, and I. Marušic. Simultaneous orthogonal-plane particle image velocimetry measurements in a turbulent boundary layer. *Journal of Fluid Mechanics*, 560:53–64, 2006.

T. J. Hanratty and D. V. Papavassiliou. The role of wall vortices in producing turbulence. *Self-sustaining mechanisms of wall turbulence(A 98-17710 03-34), Southampton, United Kingdom, Computational Mechanics Publications(Advances in Fluid Mechanics Series.*, 15:83–108, 1997.

M. R. Head and P. Bandyopadhyay. New aspects of turbulent boundary-layer structure. *Journal of Fluid Mechanics*, 107:297–338, 1981.

J. C. R. Hunt, A. A. Wray, and P. Moin. Eddies, stream, and convergence zones in turbulent flows. report ctr-s88. *Center for Turbulence Research*, pages 193–208, 1988.

N. Hutchins, W. T. Hambleton, and I. Marušic. Inclined cross-stream stereo particle image velocimetry measurements in turbulent boundary layers. *Journal of Fluid Mechanics*, 541:21–54, 2005.

T. Indinger, M. H. Buschmann, and M. Gad-el Hak. Mean-velocity profile of turbulent boundary layers approaching separation. *AIAA journal*, 44(11):2465, 2006.

J. Jeong and F. Hussain. On the identification of a vortex. *Journal of Fluid Mechanics*, 285:69–94, 1995.

J. Jiménez, G. Kawahara, M. P. Simens, M. Nagata, and M. Shiba. Characterization of near-wall turbulence in terms of equilibrium and bursting solutions. *Physics of Fluids*, 17:015105, 2005.

S. Julien. Nouvelle approche expérimentale pour l'étude de couches limites décollées. Master's thesis, Laval University, canada, 2004.

S. Kida and H. Miura. Identification and analysis of vortical structures. *European Journal of Mechanics/B Fluids*, 17(4):471–488, 1998.

H. T. Kim, S. J. Kline, and W. C. Reynolds. The production of turbulence near a smooth wall in a turbulent boundary layer. *Journal of Fluid Mechanics*, 50(01): 133–160, 1971.

J. Kim. Evolution of a vortical structure associated with the bursting event in a channel flow. *Turbulent Shear Flows 5* (ed. F. Durst, B. E. Launder, J. L. Lumley, F. W. Schmidt and J. H. Whitelaw), 1987.

J. Kim. On the structure of pressure fluctuations in simulated turbulent channel flow. *Journal of Fluid Mechanics*, 205:421–451, 1989.

J. Kim, P. Moin, and R. D. Moser. Turbulent statistics in fully developed channel flow at low reynolds number. *Journal of Fluid Mechanics*, 177(01):133–166, 1987.

K. Kim, H. J. Sung, and R. J. Adrian. Effects of background noise on generating coherent packets of hairpin vortices. *Physics of Fluids*, 20:105107, 2008.

S. J. Kline, W. C. Reynolds, F. A. Schraub, and P. W. Runstadler. The structure of turbulent boundary layers. *Journal of Fluid Mechanics*, 30(04):741–773, 1967.

L. S. G. Kovasznay, V. Kibens, and R. F. Blackwelder. Large-scale motion in the intermittent region of a turbulent boundary layer. *Journal of Fluid Mechanics*, 41 (02):283–325, 1970.

P. A. Krogstad and P. E. Skare. Influence of a strong adverse pressure gradient on the turbulent structure in a boundary layer. *Physics of Fluids*, 7(8):2014–2024, 1995.

F. C. Li, Y. Kawaguchi, K. Hishida, and M. Oshima. Investigation of turbulence structures in a drag-reduced turbulent channel flow with surfactant additive by stereoscopic particle image velocimetry. *Experiments in Fluids*, 40(2):218–230, 2006.

Z. C. Liu, C. C. Landreth, R. J. Adrian, and T. J. Hanratty. High resolution measurement of turbulent structure in a channel with particle image velocimetry. *Experiments in Fluids*, 10(6):301–312, 1991.

O. Lögdberg, K. Angele, and P. H. Alfredsson. On the scaling of turbulent separating boundary layers. *Physics of Fluids*, 20:075104, 2008.

T. S. Luchik and W. G. Tiederman. Time-scale and structure of ejections and bursts in turbulent channel flows. *Journal of Fluid Mechanics*, 174:529–554, 1987.

Y. Maciel, K. S. Rossignol, and J. Lemay. Self-similarity in the outer region of adverse-pressure-gradient turbulent boundary layers. *AIAA journal*, 44(11):2450–2464, 2006a.

Y. Maciel, K. S. Rossignol, and J. Lemay. A study of a turbulent boundary layer in stalled-airfoil-type flow conditions. *Experiments in Fluids*, 41(4):573–590, 2006b.

M. Manhart, N. Peller, and C. Brun. Near-wall scaling for turbulent boundary layers with adverse pressure gradient. *Theoretical and Computational Fluid Dynamics*, 22 (3):243–260, 2008.

I. Marušic and A. E. Perry. A wall-wake model for the turbulence structure of boundary layers. part 2. further experimental support. *Journal of Fluid Mechanics*, 298:389–407, 1995.

C. D. Meinhart and R. J. Adrian. On the existence of uniform momentum zones in a turbulent boundary layer. *Physics of Fluids*, 7(4):694–696, 1995.

G. L. Mellor and D. M. Gibson. Equilibrium turbulent boundary layers. *Journal of Fluid Mechanics*, 24(02):225–253, 1966.

J. P. Monty, J. A. Stewart, R. C. Williams, and M. S. Chong. Large-scale features in turbulent pipe and channel flows. *Journal of Fluid Mechanics*, 589:147–156, 2007.

Y. Na and P. Moin. Direct numerical simulation of a separated turbulent boundary layer. *Journal of Fluid Mechanics*, 374:379–405, 1998.

Y. Nagano, T. Tsuji, and T. Houta. Structures of turbulent boundary layer subjected to adverse pressure gradient. *International Journal of Heat and Fluid Flow*, 19: 563–572, 1998.

V. K. Natrajan, Y. Wu, and K. T. Christensen. Spatial signatures of retrograde spanwise vortices in wall turbulence. *Journal of Fluid Mechanics*, 574:155–167, 2007.

M. Osterlund, B. Lindgren, and A. V. Johansson. Flow structures in zero pressure gradient turbulent boundary layers at high reynolds number. *European Journal of Mechanics/B Fluids*, 22(4):379–390, 2003.

A. Pageau. Mesures du frottement pariétal avec une sonde à deux fils. Departement de Génie Mécanique, Université Laval, canada. Technical report, 2004.

R. L. Panton. Review of wall turbulence as described by composite expansions. *Applied Mechanics Reviews*, 58:1, 2005.

A. Perry and W. Schofield. Mean velocity and shear stress distribution in turbulent boundary layers. *Physics of Fluids*, 16(12):2068–2074, 1973.

A. E. Perry, M. E. Chong, and B. J. Cantwell. A general classification of three-dimensional flow fields. *Phys. Fluids A*, 2(5):765–777, 1990.

A. E. Perry and M. S. Chong. On the mechanism of wall turbulence. *Journal of Fluid Mechanics*, 119:173–217, 1982.

A. E. Perry and I. Marušic. A wall-wake model for the turbulence structure of boundary layers. part 1. extension of the attached eddy hypothesis. *Journal of Fluid Mechanics*, 298:361–388, 1995.

S. Pronchick. *Experimental investigation of the turbulent flow behind a backward facing step.* PhD thesis, Stanford University, California, 1983.

M. Raffel, C. Willert, and J. Kompenhans. *Particle image velocimetry a practical guide.* Springer, 1998.

S. K. Robinson. *Kinematics of turbulent boundary layer structure.* PhD thesis, Stanford University, California, 1990.

S. K. Robinson. Coherent motions in the turbulent boundary layer. *Annual Review of Fluid Mechanics*, 23(1):601–639, 1991.

K. S. Rossignol. Étude PIV d'une couche limite turbulente en condition de décrochage aérodynamique. Master's thesis, Laval University, canada, 2006.

J. Rotta. Über die Theorie der turbulenten Grenzschichten, Mitt. Max Planck Inst. Strömungsforsch., Göttingen, No.1, 1950; translated as "On the theory of turbulent boundary layers". 1344, 1953.

S. Sanghi and N. Aubry. Mode interaction models for near-wall turbulence. *Journal of Fluid Mechanics*, 247:455–488, 1993.

W. Schoppa and F. Hussain. Coherent structure generation in near-wall turbulence. *Journal of Fluid Mechanics*, 453:57–108, 2002.

R. L. Simpson, Y. T. Chew, and B. G. Shivaprasad. The structure of a separating turbulent boundary layer. part 1. mean flow and reynolds stresses. *Journal of Fluid Mechanics*, 113:23–51, 1981.

M. Skote and D. S. Henningson. Direct numerical simulation of a separated turbulent boundary layer. *Journal of Fluid Mechanics*, 471:107–136, 2002.

M. Skote, D. S. Henningson, and R. Henkes. Direct numerical simulation of self-similar turbulent boundary layers in adverse pressure gradients. *Flow, turbulence and combustion*, 60(1):47–85, 1998.

C. R. Smith and S. P. Metzler. The characteristics of low-speed streaks in the near-wall region of a turbulent boundary layer. *Journal of Fluid Mechanics*, 129:27–54, 1983.

C. R. Smith and J. D. A. Walker. Sustaining mechanisms of turbulent boundary layer: The roll of vortex development and interactions, self-sustaining mechanism of wall turbulence. *Computational Mechanics Publication*, pages 13–47, 1997.

P. R. Spalart. Direct simulation of a turbulent boundary layer up to rθ= 1410. *Journal of Fluid Mechanics*, 187:61–98, 1988.

V. Suponitsky, J. Cohen, and P. Z. Bar-Yoseph. The generation of streaks and hairpin vortices from a localized vortex disturbance embedded in unbounded uniform shear flow. *Journal of Fluid Mechanics*, 535:65–100, 2005.

T. Theodorsen. Mechanism of turbulence. In *Proc. 2nd Midwestern Conf. on Fluid Mechanics*, pages 1–19, 1952.

S. Toh and T. Itano. Interaction between a large-scale structure and near-wall structures in channel flow. *Journal of Fluid Mechanics*, 524:249–262, 2005.

C. D. Tomkins and R. J. Adrian. Spanwise structure and scale growth in turbulent boundary layers. *Journal of Fluid Mechanics*, 490:37–74, 2003.

A. Venisse. Suppression des non-uniformités dans une couche limite en gragradient de pression adverse conduisant au d ecollement. Master's thesis, Laval University, canada, 2004.

R. J. Volino, M. P. Schultz, and K. A. Flack. Turbulence structure in rough-and smooth-wall boundary layers. *Journal of Fluid Mechanics*, 592:263–293, 2007.

J. Westerweel. Efficient detection of spurious vectors in particle image velocimetry data. *Experiments in Fluids*, 16(3):236–247, 1994.

J. Westerweel. Theoretical analysis of the measurement precision in particle image velocimetry. *Experiments in Fluids*, 29(7):3–12, 2000.

J. Westerweel and F. Scarano. Universal outlier detection for PIV data. *Experiments in Fluids*, 39(6):1096–1100, 2005.

Y. Wu and K. T. Christensen. Population trends of spanwise vortices in wall turbulence. *Journal of Fluid Mechanics*, 568:55–76, 2006.

M. V. Zagarola and A. J. Smits. Mean-flow scaling of turbulent pipe flow. *Journal of Fluid Mechanics*, 373:33–79, 1998.

J. Zhou, R. J. Adrian, and S. Balachandar. Autogeneration of near-wall vortical structures in channel flow. *Physics of Fluids*, 8:288–290, 1996.

J. Zhou, R. J. Adrian, S. Balachandar, and T. M. Kendall. Mechanism for generating coherent packets of hairpin vortices in channel flow. *Journal of Fluid Mechanics*, 387:353–396, 1999.

Appendix A

Gaussian Filtering

A.1 Brief Description

The Gaussian smoothing operator is a convolution operator that is employed to remove noises from images or data. The Gaussian filter is the filter type that results in the most gradual pass band roll-off and the lowest group delay. As the name states, the Gaussian filter is derived from the same basic equation used to derive the Gaussian distribution. The significant characteristic of the Gaussian filter is that the step response contains no overshoot at all.

A.2 Gaussian Distribution

One-dimensional Gaussian distribution has the form:

$$g(x) = \frac{1}{\sigma\sqrt{2\pi}}\exp\left(-\frac{x^2}{2\sigma^2}\right) \tag{A.1}$$

where σ is the standard deviation of the Gaussian distribution. We have also assumed that the distribution has a mean of zero (i.e. it is centered at $x = 0$). The distribution is illustrated in figure A.1.

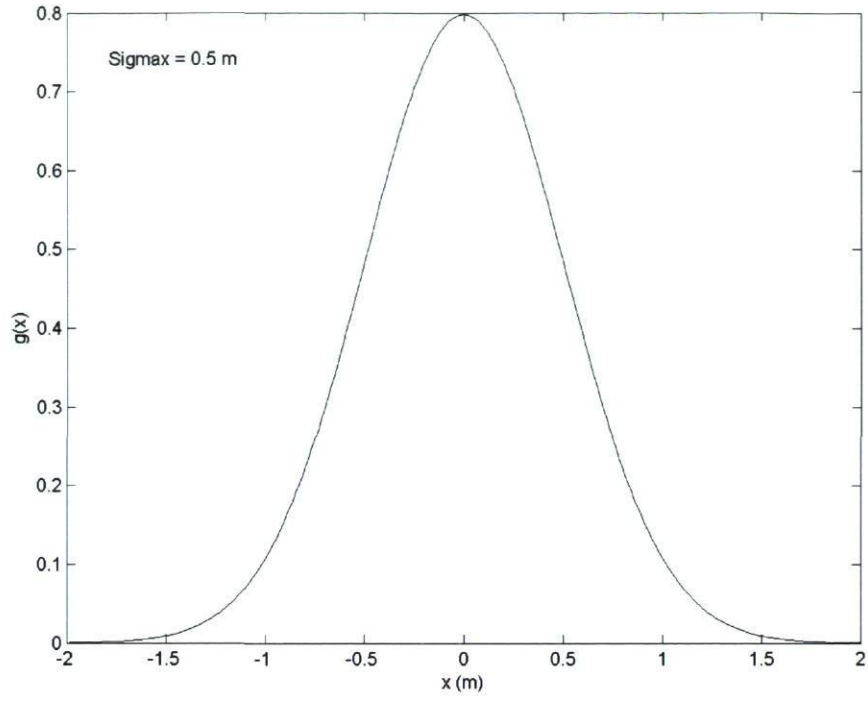

Figure A.1: Centered one dimensional Gaussian distribution with $\sigma = 0.5$.

The two-dimensional Gaussian distribution has the following form

$$g(x) = \frac{1}{2\pi\sigma_x\sigma_y}\exp\left(-\frac{x^2}{2\sigma_x^2} - \frac{y^2}{2\sigma_y^2}\right) \tag{A.2}$$

The idea of Gaussian smoothing is to use this two-dimensional distribution to smooth images or data and remove details and noise. Since the PIV data of present study is stored as a collection of discrete data we need to produce a discrete approximation for the Gaussian function before we can perform the smoothing.

Once a suitable kernel has been calculated, then the Gaussian smoothing can be performed by convolution or in Fourier space.

A.3 Properties of the Gaussian Filter

The degree of smoothing is determined by the standard deviation of the Gaussian function (Larger standard deviation of Gaussian function, of course, removes fewer

noise compared to smaller standard deviation of Gaussian distribution).

One of the principal justifications for using the Gaussian function, as a smoothing filter, is due to its frequency response. Most convolution-based smoothing filters act as low pass frequency filters. This means that their effect is to remove high spatial or temporal frequency components from the data. The frequency response of a convolution filter, i.e. its effect on different spatial frequencies, can be seen by taking the Fourier transform of the filter.

A.4 Fourier Transform

A.4.1 Brief Description

The Fourier Transform is an important image and data processing tool which is used to decompose an image or data into its sine and cosine components. In the case of spatially evolving data, the output of the transformation represents the data in the Fourier, frequency or wave number domain, while the input data is the spatial domain equivalent. In the Fourier domain of data, each point represents a particular spatial frequency or wave number contained in the spatial domain of data.

A.4.2 Discrete Fourier Transform

The discrete Fourier transform (DFT) of a function with infinite limits can not be computed. Anyway the temporal or spatial domain is always finite in practical applications. Moreover, since the discrete data is olny interpreted in the present study, we focus on discussing the Discrete Fourier Transform here.

Finite Fourier transform:

$$F(w_x, w_y) = \int_0^Y \int_0^X f(x,y) e^{-2\pi i(w_x x + w_y y)} dxdy \qquad \begin{cases} 0 \leq x \leq X \\ 0 \leq y \leq Y \end{cases} \tag{A.3}$$

where $k_x = 2\pi w_x$ and $k_y = 2\pi w_y$ as k_x and k_y are the wave numbers in x and y directions respectively. w_x and w_y are the spatial frequencies (cycle per meter).

Discretization of spatial domain:

For a continuous function $f(x, y)$ consider the discrete form as $f(x_m, y_n)$ where:

$$\begin{aligned} x_m &= (m-1)\Delta x & m &= 1, 2, 3, \ldots, N_x \\ y_n &= (n-1)\Delta y & n &= 1, 2, 3, \ldots, N_y \\ \Delta x &= \tfrac{X}{N_x} \\ \Delta y &= \tfrac{Y}{N_y} \end{aligned} \tag{A.4}$$

The DFT is the sampled Fourier Transform and therefore does not contain all frequencies forming an image or data-set, but it contains a set of samples which is large enough to fully describe the spatial domain of data. The number of spatial frequencies corresponds to the number of data points in the spatial domain, i.e. the data in the spatial and Fourier domain are of the same size.

Discretization of frequency domain:

If we define the sampling frequency as $w_{Dx_s} = \frac{1}{\Delta x}$ and $w_{Dy_s} = \frac{1}{\Delta y}$ then we can determine a signal character for the frequencies of w_{Dx} and w_{Dy} as follow

$$\begin{aligned} \Delta w_{Dx} &= \tfrac{w_{Dx_s}}{N_x} = \tfrac{1}{N_x \Delta x} \\ \Delta w_{Dy} &= \tfrac{w_{Dy_s}}{N_y} = \tfrac{1}{N_y \Delta y} \end{aligned} \tag{A.5}$$

then

$$\begin{aligned} w_{Dx} &= (l_x - 1)\Delta w_{Dx} \\ w_{Dy} &= (l_y - 1)\Delta w_{Dy} \end{aligned} \tag{A.6}$$

So, the DFT of discrete function, $f(x_m, y_n)$, can be defined as follow

$$F(w_{Dx}, w_{Dy}) = \Delta x \Delta y \sum_{m=1}^{N_x} \sum_{n=1}^{N_y} f(x_m, y_n) \exp\left(-2\pi i \left[\frac{(l_x - 1)(m-1)}{N_x} + \frac{(l_y - 1)(n-1)}{N_y}\right]\right) \tag{A.7}$$

Because of discretization, the DFT is periodic with periods (see figures A.2, A.5 and A.9) as follow

$$\begin{aligned} P_{wx} &= \tfrac{1}{\Delta x} \\ P_{wy} &= \tfrac{1}{\Delta y} \end{aligned} \tag{A.8}$$

Thus $F(w_{Dx}, w_{Dy})$ is unique in the range:

$$\begin{aligned} 0 \leq w_{Dx} \leq \tfrac{w_{Dx_s}}{2} \quad &\Rightarrow \quad \begin{cases} 0 \leq w_{Dx} \leq \tfrac{1}{2\Delta x} & \text{if } N_x \text{ even} \\ 0 \leq w_{Dx} < \tfrac{1}{2\Delta x} & \text{if } N_x \text{ odd} \end{cases} \\ 0 \leq w_{Dy} \leq \tfrac{w_{Dy_s}}{2} \quad &\Rightarrow \quad \begin{cases} 0 \leq w_{Dy} \leq \tfrac{1}{2\Delta y} & \text{if } N_y \text{ even} \\ 0 \leq w_{Dy} < \tfrac{1}{2\Delta y} & \text{if } N_y \text{ odd} \end{cases} \end{aligned} \tag{A.9}$$

which correspond to

$$\begin{cases} l_x = 1, 2, 3, \ldots, \tfrac{N_x}{2} + 1 & \text{for } N_x \text{ even} \\ l_x = 1, 2, 3, \ldots, \tfrac{N_x - 1}{2} + 1 & \text{for } N_x \text{ odd} \\ l_y = 1, 2, 3, \ldots, \tfrac{N_y}{2} + 1 & \text{for } N_y \text{ even} \\ l_y = 1, 2, 3, \ldots, \tfrac{N_y - 1}{2} + 1 & \text{for } N_y \text{ odd} \end{cases} \tag{A.10}$$

Because of periodicity, the remaining values that are, $\frac{N_x}{2} - 1$, $\frac{N_y}{2} - 1$ for even N_x, N_y and $\frac{N_x+1}{2} - 1$, $\frac{N_y+1}{2} - 1$ for odd N_x, N_y, correspond to the negative range of w_{Dx} and w_{Dy}. So:

$$\begin{aligned} w_{Dx} &= -\tfrac{N_x + 1 - l_x}{N_x \Delta x} \\ w_{Dy} &= -\tfrac{N_y + 1 - l_y}{N_y \Delta y} \end{aligned} \tag{A.11}$$

where

$$\begin{cases} l_x = \frac{N_x}{2} + 2, \frac{N_x}{2} + 3. \ldots N_x & \text{for } N_x \text{ even} \\ l_x = \frac{N_x - 1}{2} + 2, \frac{N_x - 1}{2} + 3. \ldots N_x & \text{for } N_x \text{ odd} \\ l_y = \frac{N_y}{2} + 2, \frac{N_y}{2} + 3. \ldots N_y & \text{for } N_y \text{ even} \\ l_y = \frac{N_y - 1}{2} + 2, \frac{N_y - 1}{2} + 3. \ldots N_y & \text{for } N_y \text{ odd} \end{cases} \tag{A.12}$$

If w_{Dx} is written as $w_{l_x - 1}$, we have the following sequence for even N_x values

$$w_0 = 0, w_1 = \frac{1}{N_x \Delta x}, w_2 = \frac{2}{N_x \Delta x}, \ldots w_k = \frac{k}{N_x \Delta x} \ldots w_{N_x/2} = \frac{1}{2\Delta x}$$

and

$$w_{\frac{N_x}{2}+1} = -w_{\frac{N_x}{2}-1}, w_{\frac{N_x}{2}+2} = -w_{\frac{N_x}{2}-2}, \ldots, w_{N_x - 1} = -w_1$$

On the other hand, the amplitude of $F(w_{Dx}, w_{Dy})$ is changed due to discretization, and it is equal $\Delta x \Delta y \, |F(w_x, w_y)|$. In the other words, the coefficients of Δx and Δy is the scaling factors used to approximate the equivalent of the continuous Fourier transform. It is because of periodicity due to discretization.The other effect of discretization is periodicity.

The fast Fourier transform (FFT) is used in the DFT area. A FFT is an efficient algorithm to compute the discrete Fourier transform and its inverse. FFTs are of great importance to a wide variety of applications, from digital signal processing, to solve partial differential equations for quickly multiplying large integers. The two-dimensional DFT is given by equation A.7.

Where $f(x_m, y_n)$ is the data in the spatial domain and the exponential term is the basis function corresponding to each point $F(w_{Dx}, w_{Dy})$ in the Fourier space. The equation can be interpreted as the value of each point $F(w_{Dx}, w_{Dy})$ is obtained by multiplying the spatial data with the corresponding base function and summing the result.

In a similar way, the Fourier data can be re-transformed to the spatial domain. The

inverse Fourier transform is given as follow

$$f(x_m, y_n) = \Delta w_{Dx} \Delta w_{Dy} \sum_{l_x=1}^{N} \sum_{l_y=1}^{N} F(w_{Dx}, w_{Dy}) \exp\left(2\pi i \left[\frac{(l_x-1)(m-1)}{N_x} + \frac{(l_y-1)(n-1)}{N_y}\right]\right) \tag{A.13}$$

Which is the discrete equivalent of the following function

$$f(x, y) = \int_0^{w_{ys}} \int_0^{w_{xs}} F(w_x, w_y) \exp\left(2\pi i (w_x x + w_y y)\right) dw_x dw_y \tag{A.14}$$

Note: The scaling factors, Δw_x and Δw_y, have to be used because the DFT is employed with Δx and Δy. The scaling factors for DFT and inverse DFT can be written as follow

Scaling factor for DFT		Scaling factor for inverse DFT
1	$\longleftrightarrow$	$\frac{1}{N_x N_y}$
$\Delta x \Delta y$	$\longleftrightarrow$	$\Delta w_{Dx} \Delta w_{Dy} = \frac{1}{N_x \Delta x} \frac{1}{N_y \Delta y}$

A double sum has to be calculated for each data point to obtain the results for the above equations. However, because the Fourier Transform is separable, it can be written as follow

$$F(w_{Dx}, w_{Dy}) = \Delta w_{Dy} \sum_{n=1}^{N_y} P(w_{Dx}, y_n) \exp\left(-\frac{2\pi i}{N_y}(l_y-1)(n-1)\right) \tag{A.15}$$

where

$$P(w_{Dx}, y_n) = \Delta w_{Dx} \sum_{m=1}^{N_x} f(x_m, y_n) \exp\left(-\frac{2\pi i}{N_x}(l_x-1)(m-1)\right) \tag{A.16}$$

Using these two formulas, the spatial domain data is first transformed into an intermediate data using N_X one-dimensional Fourier Transforms. This intermediate data is then transformed into the final data, again using N_y one-dimensional Fourier Transforms. Expressing the two-dimensional Fourier Transform in terms of a series of $N_x + N_y$ one-dimensional transforms decreases the number of required computations.

The ordinary one-dimensional DFT has actually complex even with these computational savings. This can be reduced if the Fast Fourier Transform (FFT) is employed to compute the one-dimensional DFTs. This is a significant improvement, in particular for large digital images and large amount of data.

The Fourier Transform produces a complex number valued output data which can be displayed with two series of data, either with the real and imaginary part or with magnitude and phase. In image and data processing, often the magnitude of the Fourier Transform is only displayed, as it contains most of the information of the geometric structure of the spatial domain data. However, if we want to re-transform the Fourier image into the correct spatial domain after some processing in the frequency domain, we must make sure to preserve both magnitude and phase of the Fourier data.

The Fourier domain data has a much greater range than the data in the spatial domain. Hence, to be sufficiently accurate, its values are usually calculated and stored in float values.

A.5 Filtering

If we have a sampled signal of $f(x)$ and we want to filter it by $g(x)$, the response of filtering ($f_{filter}(x)$) is:

$$f_{filter}(x) = f(x) * g(x) = \int_{-\infty}^{\infty} f(u)g(x-u)du \tag{A.17}$$

This convolution can be done by multiplying the Fourier transform of $f(x)$ and $g(x)$. Thus the following operations should be done to caculate this convolution:

1. Calculating the Fourier transform of $f(x)$ and $g(x)$ that the results are $F(w_x)$ and $G(w_x)$ in spectral domain.

2. Multiplying the results in step 1 to obtain the filtered $f(x)$ in Fourier transform ($F_{filter}(w_x)$).

$$F_{filter}(w_x) = F(w_x)G(w_x) \tag{A.18}$$

3. Calculating the inverse Fourier transform of $F_{filter}(w_x)$ that results the filtered

$f_{filter}(x)$ in spatial domain.

$$f_{filter}(x) = \int_{-\infty}^{\infty} F_{filter}(w_x) e^{2\pi i w_x x} dw_x \tag{A.19}$$

A.5.1 Digital Filtering

As the discrete form of data is used here, we discus the digital filtering. If the discrete form of $f(x)$ is written as $f(x_m)$ where $x_m = (m-1)\Delta x$ and $m = 1, 2, \ldots, N_x$, a similar definition applies for $g(x_m)$, then the $f_{filter}(x_m)$ can be obtained as follow

$$f_{filter}(x_m) = f(x_m) * g(x_m) = \sum_{l_x=1}^{N_x} f((l_x - 1)\Delta x) g\left([(m-1) - (l_x - 1)]\Delta x\right) \tag{A.20}$$

This operation can be done using DFT as follow

$$F(w_{Dx}) = \Delta x \sum_{m=1}^{N_x} f(x_m) \exp\left(-\frac{2\pi i}{N_x}(l_x - 1)(m-1)\right) \tag{A.21}$$

$$G(w_{Dx}) = \Delta x \sum_{m=1}^{N_x} g(x_m) \exp\left(-\frac{2\pi i}{N_x}(l_x - 1)(m-1)\right) \tag{A.22}$$

where

$$l_x = 1, 2, 3, \ldots, N_x$$

Then:

$$F_{filter}(w_{Dx}) = F(w_{Dx}) G(w_{Dx}) \tag{A.23}$$

and the $f_{filter}(x)$ can be calculated by inverse DFT as follow

$$f_{filter}(x_m) = \Delta w_{Dx} \sum_{l_x=1}^{N_x} F_{filter}(w_{Dx}) \exp[\frac{2\pi i}{N_x}((l_x - 1)(m-1))] \tag{A.24}$$

A.6 Computational Method

The computational method includes the following steps:

1. Since in the FFT, calculations are based on variations of signals around zero values and regarding the fact that u and v have significant deviations from zero, we are have to use u' and v' those have variations around zero. Then their filtered values, u'_{filter} and v'_{filter}, should add to U and V values to obtain filtered u and v ($u_{filter} = U + u'_{filter}$, $v_{filter} = V + v'_{filter}$).

   The u' and v' are obtained as follow

$$u' = u - \overline{U} \tag{A.25}$$

$$v' = v - \overline{V} \tag{A.26}$$

2. Next the DFT of u' and v' are calculated as it is explained in the section of A.5.1 (it is done by two-dimensional FFT).

$$U'_D(w_{Dx}, w_{Dy}) = \sum_{n=1}^{N_y} \sum_{m=1}^{N_x} \exp\left(-2\pi i \left[\frac{(m-1)(l_x-1)}{N_x} + \frac{(n-1)(l_y-1)}{N_y}\right]\right) u'(x_m, y_n) \tag{A.27}$$

   where

$$1 \leq l_x \leq N_x$$

$$1 \leq l_y \leq N_y$$

3. In this step the Gaussian distribution in spectral domain is caculated as follow

$$f(x) = e^{-ax^2} \longrightarrow F(w_x) = \int_{-\infty}^{\infty} e^{-ax^2} e^{-2\pi i w_x x} dx = \sqrt{\frac{\pi}{a}} e^{-(2\pi w_x)^2/4a} \tag{A.28}$$

   so for the following Gaussian distribution:

$$g(x) = \frac{1}{\sigma_x \sqrt{2\pi}} \exp\left(-\frac{x^2}{2\sigma_x^2}\right) \tag{A.29}$$

the Fourier transform of $g(x)$ is obtained as follow

$$G(w_x) = \exp\left(-\frac{(2\pi)^2 w_x^2 \sigma_x^2}{2}\right) \tag{A.30}$$

and for 2-D Gaussian distribution we have:

$$g(x,y) = \frac{1}{2\pi\sigma_x\sigma_y}\exp\left(-\left[\frac{x^2}{2\sigma_x^2} + \frac{y^2}{2\sigma_y^2}\right]\right) \tag{A.31}$$

$$G(w_{Dx}, w_{Dy}) = \exp\left(-\left[\frac{(2\pi)^2 w_{Dx}^2 \sigma_x^2}{2} + \frac{(2\pi)^2 w_{Dy}^2 \sigma_y^2}{2}\right]\right) \tag{A.32}$$

The standard deviation in spectral domain is obtained with the following equations

$$\sigma_{wx} = \frac{1}{2\pi\sigma_x}$$

$$\sigma_{wy} = \frac{1}{2\pi\sigma_y}$$

so equation A.32 can be written as:

$$G(w_{Dx}, w_{Dy}) = \exp\left(-\left[\frac{w_{Dx}^2}{2\sigma_{wx}^2} + \frac{w_{Dy}^2}{2\sigma_{wy}^2}\right]\right) \tag{A.33}$$

We use this definition such that $|G(0,0)| = 1$, so during the filtering the amplitude of the u' and v' will not be changed. On the other hand due to periodicity of the DFT we calculate the $G(w_{Dx}, w_{Dy})$ for $l_x = 1, 2, \ldots, \frac{N_x}{2}+1$ and $l_y = 1, 2, \ldots, \frac{N_y}{2}+1$ if N_x and N_y are even. Therefore

$$G(w_{Dx}, w_{Dy}) = \begin{cases} \exp\left(-\left[\frac{w_{Dx}^2}{2\sigma_{wx}^2} + \frac{w_{Dy}^2}{2\sigma_{wy}^2}\right]\right) & \begin{cases} 1 \le l_x \le \frac{N_x}{2}+1 \\ 1 \le l_y \le \frac{N_y}{2}+1 \end{cases} \\ \exp\left(-\left[\frac{(w_{Dx}-1/\Delta x)^2}{2\sigma_{wx}^2} + \frac{(w_{Dy}-1/\Delta y)^2}{2\sigma_{wy}^2}\right]\right) & \begin{cases} \frac{N_x}{2}+2 \le l_x \le N_x \\ \frac{N_y}{2}+2 \le l_y \le N_y \end{cases} \end{cases} \tag{A.34}$$

4. To filter u' and v' we multiply $U'(w_{Dx}, w_{Dy})$ by $G(w_{Dx}, w_{Dy})$ as follow

$$U'_{filter}(w_{Dx}, w_{Dy}) = U'(w_{Dx}, w_{Dy})G(w_{Dx}, w_{Dy}) \tag{A.35}$$

5. Finally we calculate the inverse Fourier transform of the result in the latter step. TConsequently, the filtered u' and v' in spatial domain are obtained and can be derived as follow

$$u'_{filter}(x_m, y_n) = \frac{1}{N_x N_y} \sum_{l_y=1}^{N_y} \sum_{l_x=1}^{N_x} \exp\left(2\pi i \left[\frac{(m-1)(l_x-1)}{N_x} + \frac{(n-1)(l_y-1)}{N_y}\right]\right) U'(w_{Dx}, w_{Dy}) \tag{A.36}$$

6. The filtered u and v are obtained by adding the u'_{filter} and v'_{filter} to U and V.

The values of σ_x and σ_y are chosen 0.014δ.

A.7 Examples

In this section, some examples of Gaussian distribution and filtered data are presented. The variables are as follow in this section:

- $\sigma_{w_{Dx}} = \frac{1}{2\pi\sigma_x} = 522.7$ (cycle/m)
- $\sigma_{w_{Dy}} = \frac{1}{2\pi\sigma_y} = 522.7$ (cycle/m)
- $\sigma_{k_{Dx}} = \frac{1}{\sigma_x} = 3284$ (rad/m)
- $\sigma_{k_{Dy}} = \frac{1}{\sigma_y} = 3284$ (rad/m)
- $N_x = 300$, $N_y = 127$
- $\Delta x = 1.91\ e^{-004}$ m, $\Delta y = 1.9291\ e^{-004}$ m
- $\Delta w_{Dx} = \frac{1}{N_x \Delta x} = 17.5$ (rad/m), $\Delta w_{Dy} = \frac{1}{N_y \Delta y} = 40.8$ (rad/m)
- $\Delta k_{Dx} = \frac{2\pi}{N_x \Delta x} = 110.2$ (rad/m), $\Delta w_{Dy} = \frac{2\pi}{N_y \Delta y} = 256.5$ (rad/m)

Figures A.3 to A.10 show the Gaussian distribution, filtered data and unfiltered data in spatial and spectral domain.

A.7.1 Examples of Test of Fourier Transform

The Gaussian distribution in spectral domain corresponds to a Gaussian distribution in spatial domain can be acquired using different methods. The motivation of this section is to obtain the Gaussian distribution in spectral domain using different methods and to compare the acquired results by these methods. The used methods are analytical solution, DFT series and function of Matlab (FFT for one-dimensional and FFT2 for two-dimensional Gaussian distribution). Figures A.11 to A.13 show the obtained the Gaussian distribution in spectral domain using different methods. The collapse of different results confirm that the Fourier transform of Gaussian distribution using different methods are always the same and identical.

- Analytic solution is the analytic Fourier transform of the function.
- Series function uses the summation in the DFT formulation (see equations A.13 and A.7).
- Matlab function is the function FFT (for one-dimensional distribution) or FFT2 (for two-dimensional distribution) uses the Fast Fourier transform.

A.7.2 Examples of Filtered and Unfiltered Velocity Fields

In this section there are some examples of the filtered velocity fields that are filtered by Gaussian filtering and unfiltered velocity fields (see figures A.14 and A.15).

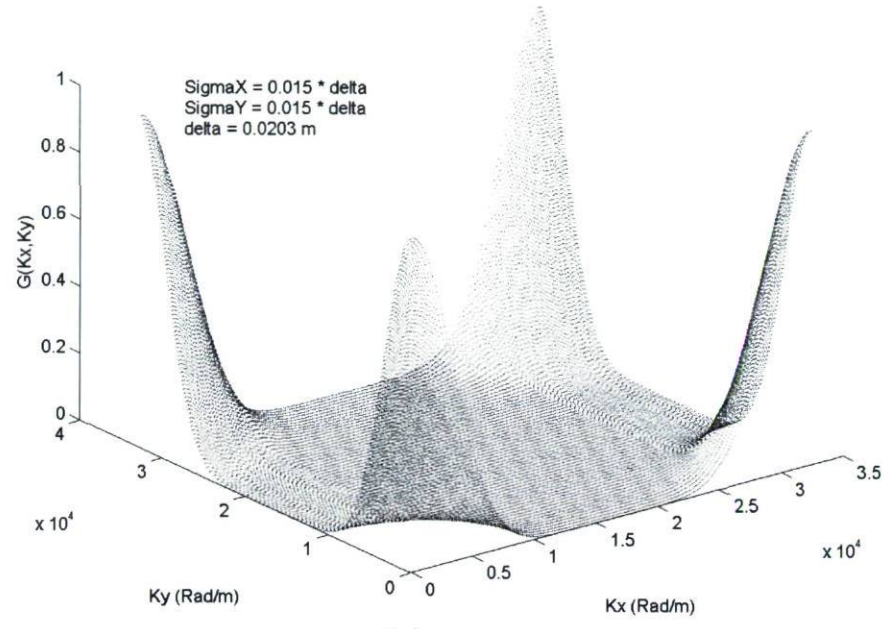

(a)

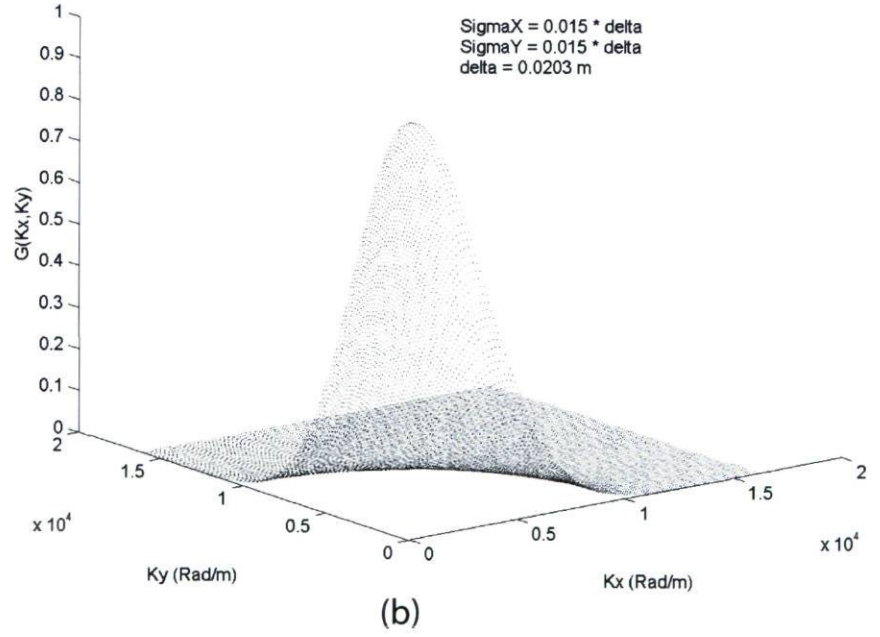

(b)

Figure A.2: Centered two-dimensional Gaussian distribution in spectral domain: a) whole Gaussian distribution, b) First quarter of Gaussian distribution ($\sigma_x = \sigma_y = 0.0003$).

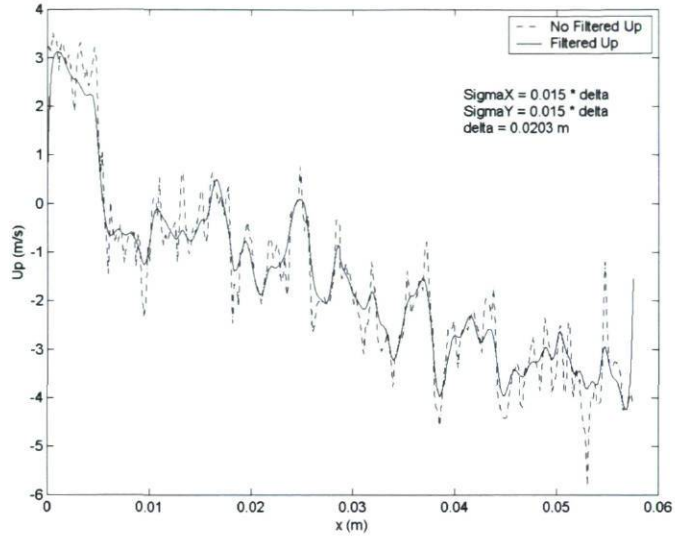

Figure A.3: Filtered and unfiltered of streamwise fluctuation profile, u', in streamwise direction.

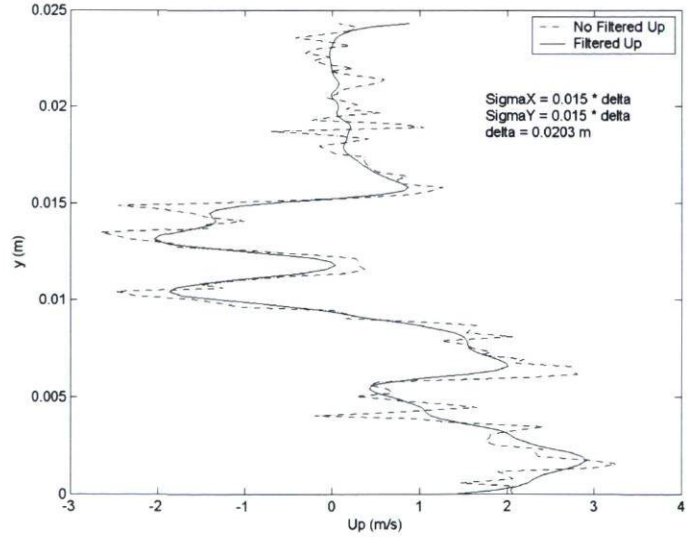

Figure A.4: Filtered and unfiltered of streamwise fluctuation profile, u', in wall-normal direction.

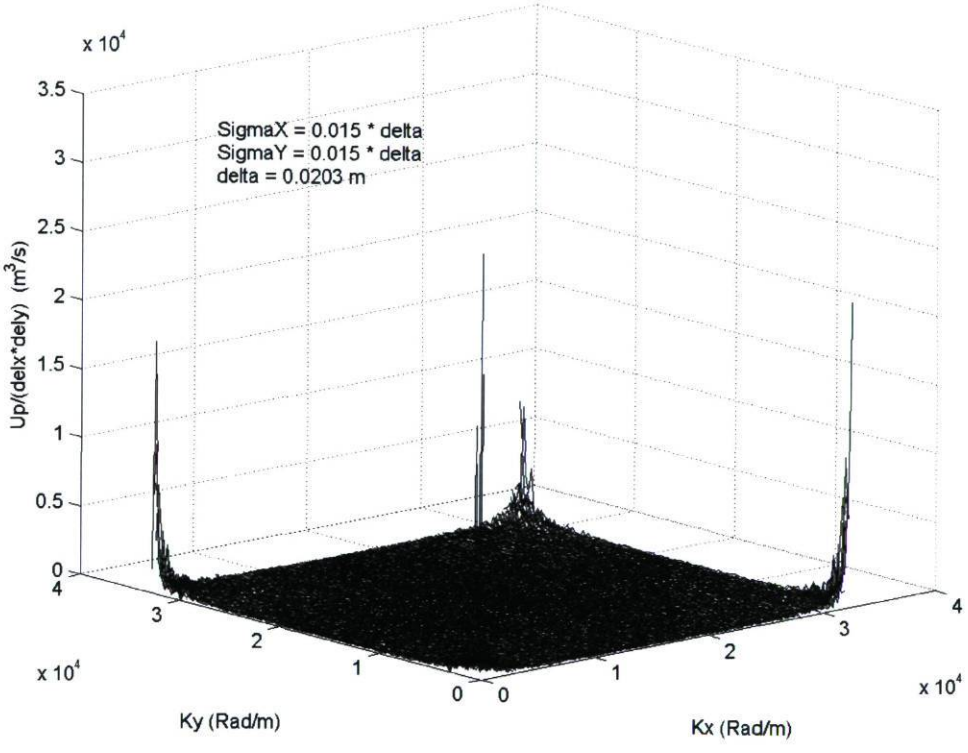

Figure A.5: Filtered streamwise fluctuation distribution, u', in spectral domain.

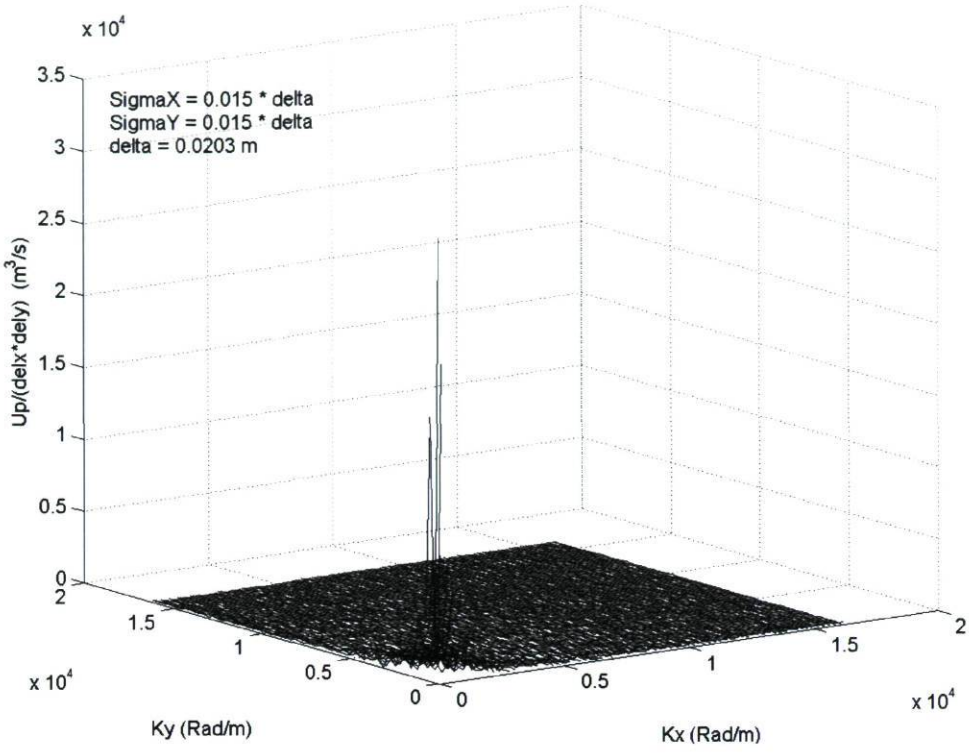

Figure A.6: First quarter of filtered streamwise fluctuation distribution, u', in spectral domain.

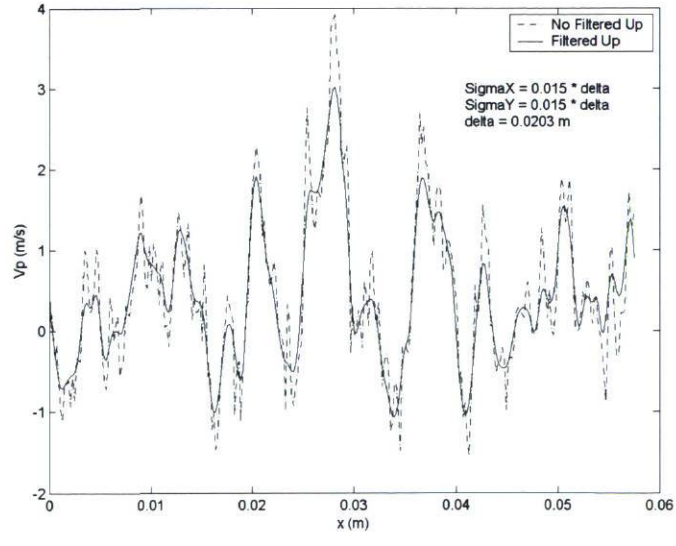

Figure A.7: Filtered and unfiltered of wall-normal fluctuation profile, v', in streamwise direction.

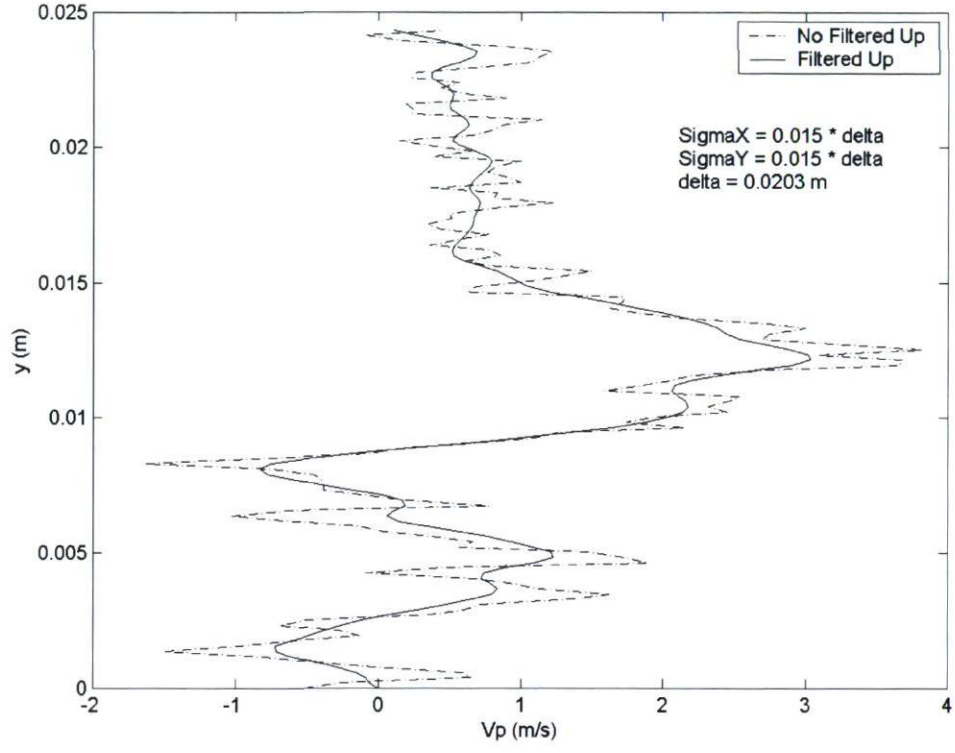

Figure A.8: Filtered and unfiltered of wall-normal fluctuation profile, v', in wall-normal direction.

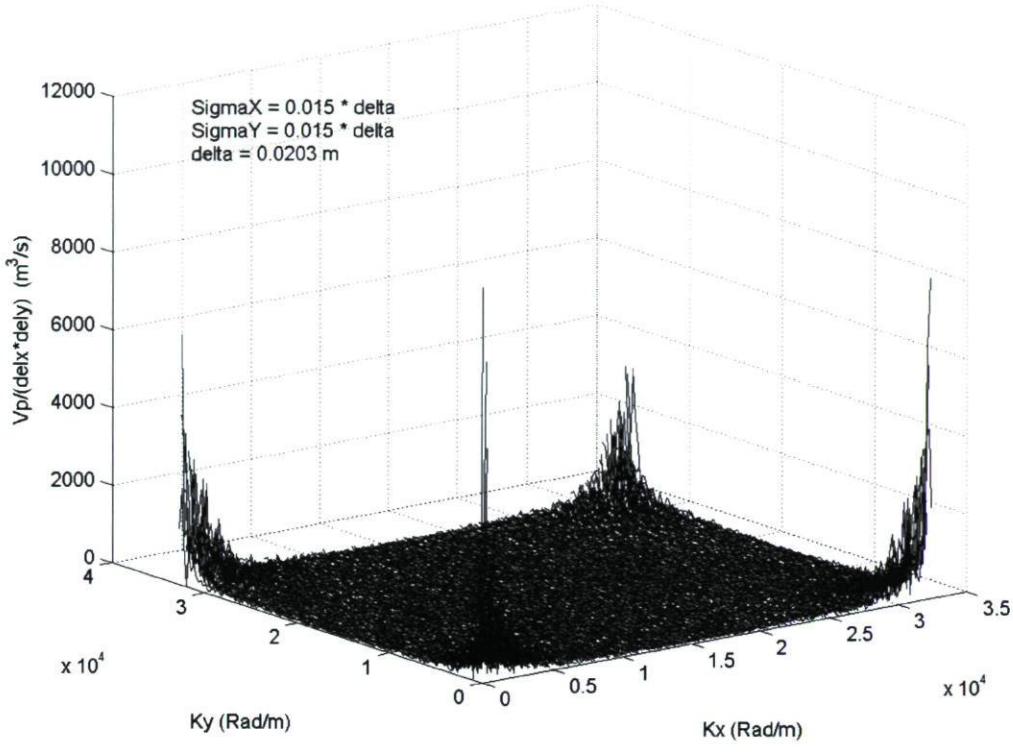

Figure A.9: Filtered wall-normal fluctuation distribution, v', in spectral domain.

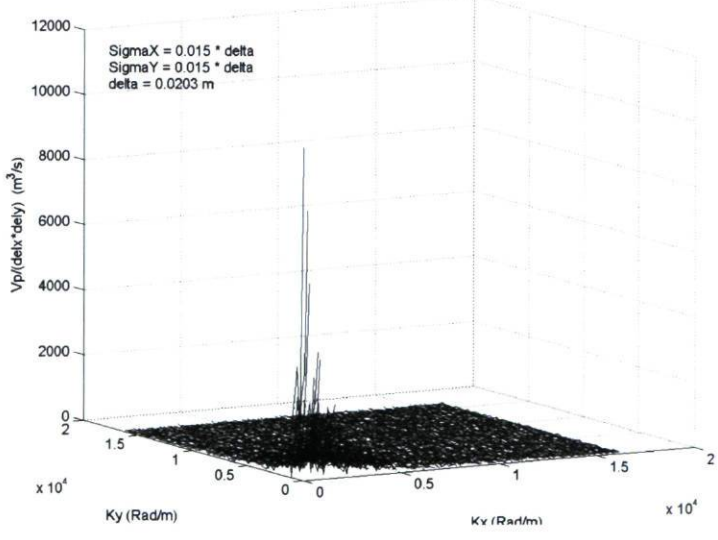

Figure A.10: First quarter of filtered wall-normal fluctuation distribution,v', in spectral domain.

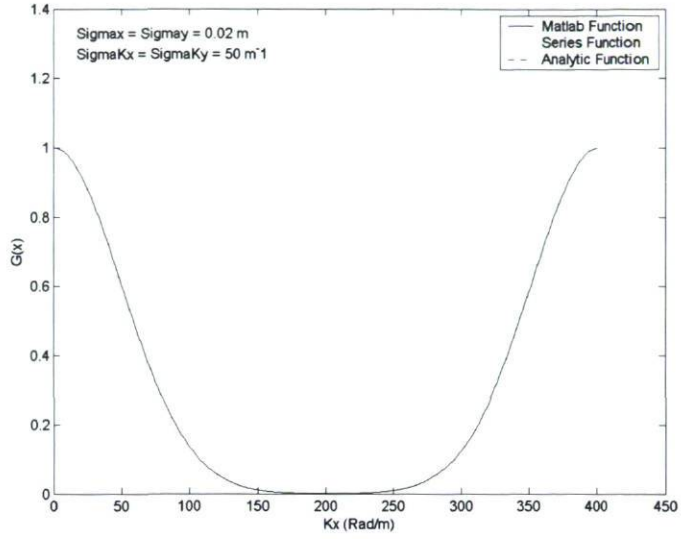

Figure A.11: Centered one-dimensional Gaussian distribution in spectral domain $G(w_x) = e^{-\frac{w_x^2}{2\sigma_{wx}^2}}$.

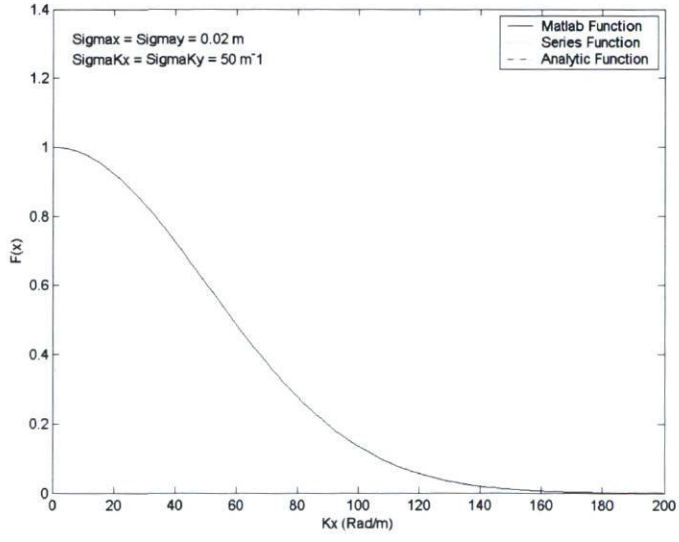

Figure A.12: First quarter of one-dimensional Gaussian distribution in spectral domain $G(w_x) = e^{-\frac{w_x^2}{2\sigma_{wx}^2}}$.

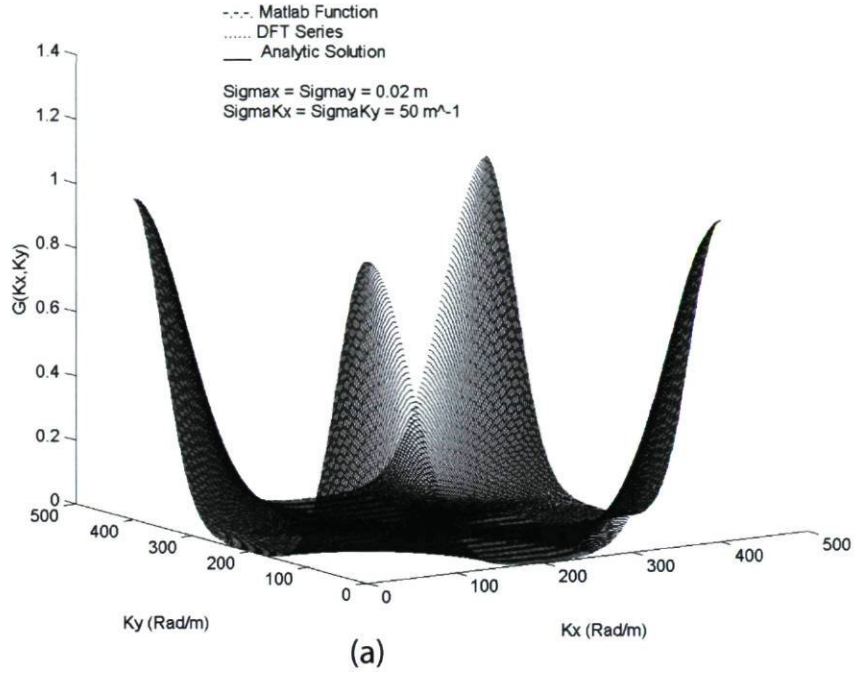

Figure A.13: Centered two-dimensional Gaussian distribution in spectral domain ($G(w_x, w_y) = e^{-\left(\frac{w_x^2}{2\sigma_{wx}^2}+\frac{w_y^2}{2\sigma_{wy}^2}\right)}$), a)whole distribution, b) First quarter of Gaussian distribution.

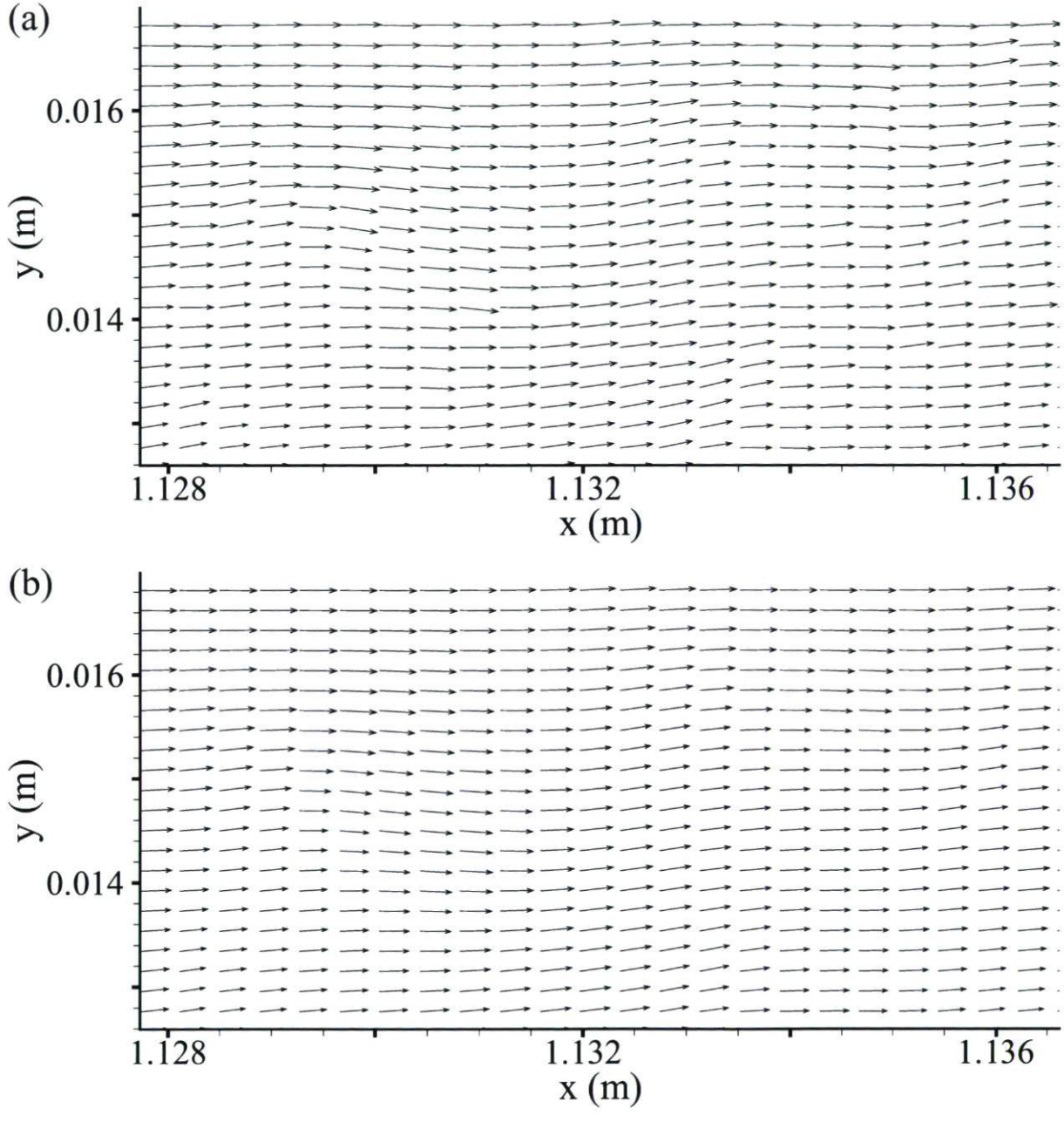

Figure A.14: Velocity vector field (one vector out of 2 for clarity), a) unfiltered velocity field, b) filtered velocity field. The filter bandwidth is 0.028δ ($\sigma = 0.014\delta$).

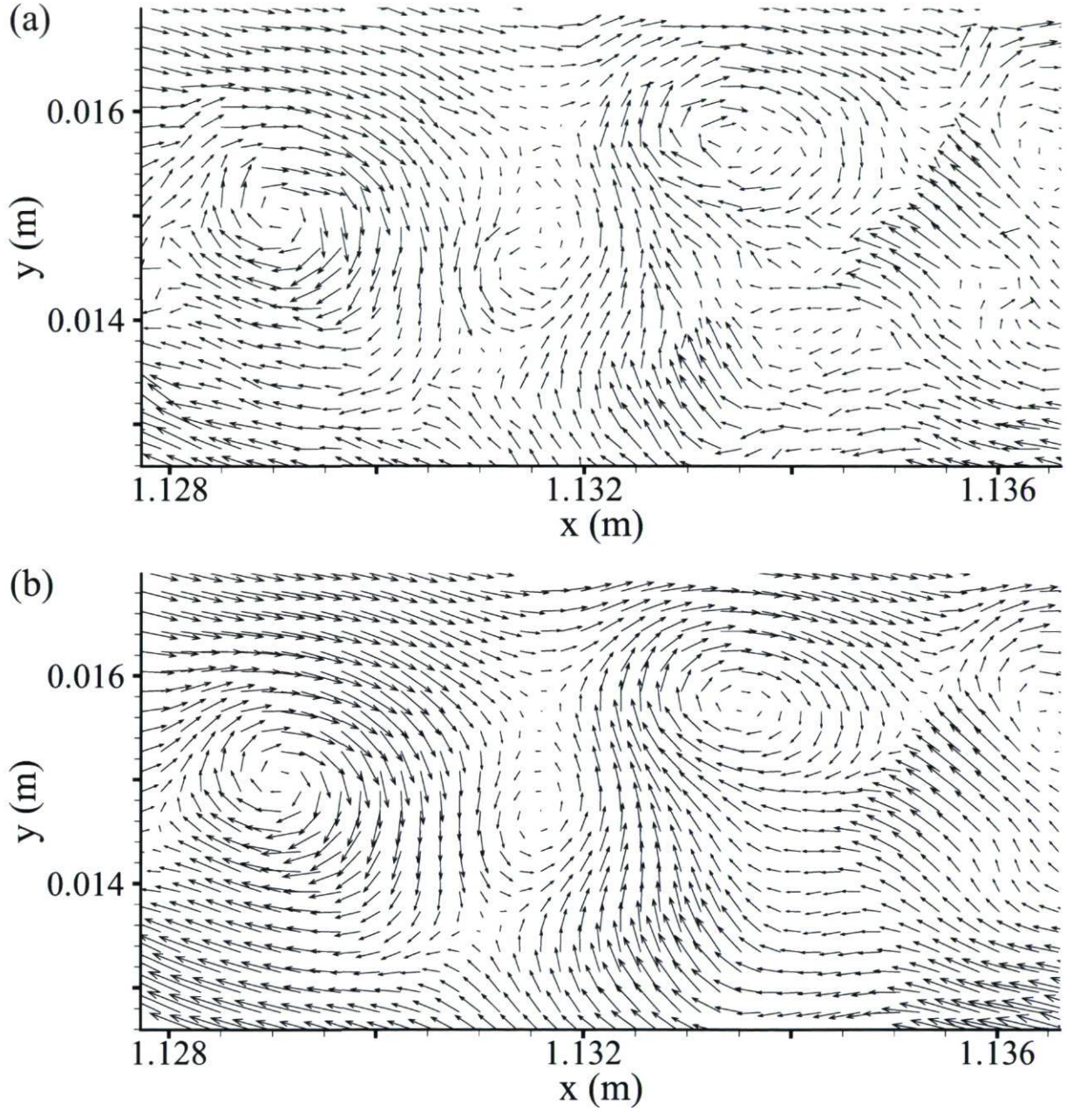

Figure A.15: Velocity vector field shown using Galilean decompositions, same position and same field as figure A.14, a) unfiltered velocity field, b) filtered velocity field. The filter bandwidth is 0.028δ ($\sigma = 0.014\delta$).

Appendix B

Mathematical and Physical meaning of λ_{ci}

The mathematical discription and physical meaning of λ_{ci}, defined by Zhou et al. (1999), is presented in this appendix. First of all, the local velocity field around a point can be expressed by the position vector $\boldsymbol{r}$ in linear order as equation B.1.

$$\boldsymbol{u}(\boldsymbol{r}+\delta\boldsymbol{r}) = \boldsymbol{u}(\boldsymbol{r}) + D\delta\boldsymbol{r} + O(||\delta\boldsymbol{r}||^2) \tag{B.1}$$

where D is the velocity gradient tensor ($\nabla\boldsymbol{u}$). Its characteristic equation is given by

$$\lambda^3 + P\lambda^2 + Q\lambda + R = 0 \tag{B.2}$$

where $P = -trace(D) = -div(\boldsymbol{u})$, $Q = \frac{1}{2}[P^2 - trace(DD)]$ and $R = \frac{1}{3}[P^3 + 3PQ - trace(DDD)]$ are invariants of the velocity gradient tensor. The discriminant for this characteristic equation is

$$\Delta \equiv \left(\frac{1}{2}\tilde{R}\right)^2 + \left(\frac{1}{3}\tilde{Q}\right)^3 \tag{B.3}$$

where $\tilde{R} \equiv R + \frac{2}{27}P^3 - \frac{1}{3}PQ$ and $\tilde{Q} \equiv Q - \frac{1}{3}P^2$.

If Δ is positive, then the velocity gradient tensor has a real eigenvalue and a pair of

conjugated complex eigenvalues. Zhou et al. (1999) decomposed the velocity gradient tensor D in cartesian coordinates as

$$D \equiv [d_{ij}] = [\boldsymbol{v}_r \;\; \boldsymbol{v}_{cr} \;\; \boldsymbol{v}_{ci}] \begin{bmatrix} \lambda_r & & \\ & \lambda_{cr} & \lambda_{ci} \\ & -\lambda_{ci} & \lambda_{cr} \end{bmatrix} [\boldsymbol{v}_r \;\; \boldsymbol{v}_{cr} \;\; \boldsymbol{v}_{ci}]^{-1} \tag{B.4}$$

where λ_r is the real eigenvalue corresponding to eigenvector $\boldsymbol{v}_r$ and $\lambda_{cr} \pm \lambda_{ci} i$ are the conjugate pair of complex eigenvalues with complex eigenvectors $\boldsymbol{v}_{cr} \pm \boldsymbol{v}_{ci} i$.

In a local (curvilinear) coordinate (y_1, y_2, y_3) system defined by the three vectors $\boldsymbol{v}_r$, $\boldsymbol{v}_{cr}$, $\boldsymbol{v}_{ci}$, the local streamlines can then be expressed as

$$\begin{cases} y_1(t) = C_r exp\lambda_r t, \\ y_2(t) = exp\lambda_{cr} t[C_c^1 cos(\lambda_{ci} t) + C_c^2 sin(\lambda_{ci} t)], \\ y_3(t) = exp\lambda_{cr} t[C_c^2 cos(\lambda_{ci} t) - C_c^1 sin(\lambda_{ci} t)], \end{cases} \tag{B.5}$$

where C_r, C_c^1, and C_c^2 are constants. The local flow may be stretched or compressed along the axis $\boldsymbol{v}_r$ as shown in figure B.1, while the flow is swirling on the plane spanned by the $\boldsymbol{v}_{cr}$ and $\boldsymbol{v}_{ci}$. Furthermore, the rotation rate is quantified by λ_{ci}, and therefore Zhou and co-workers used the imaginary part of the complex eigenvalue pair as the local swirling strength of the vortex. If λ_{ci} is equal to zero then there is no swirling motion or local circular streamline.

The iso-contours of λ_{ci} were employed to visualize vortices by Zhou and co-workers. Since Q and λ_{ci} criteria yield comparable vortex-identification results of Chernyshenko and Baig (2005), Wu and Christensen (2006) also employed λ_{ci} to indentify the spanwise vortices in a two-dimensional experimental PIV data. The λ_{ci} criteria for vortex identification has also been applied to the present experimental PIV data. The two-dimensional form of the velocity gradient tensor can be written as

$$\nabla \boldsymbol{u} = \begin{bmatrix} \partial u/\partial x & \partial u/\partial y \\ \partial v/\partial x & \partial v/\partial y \end{bmatrix} \tag{B.6}$$

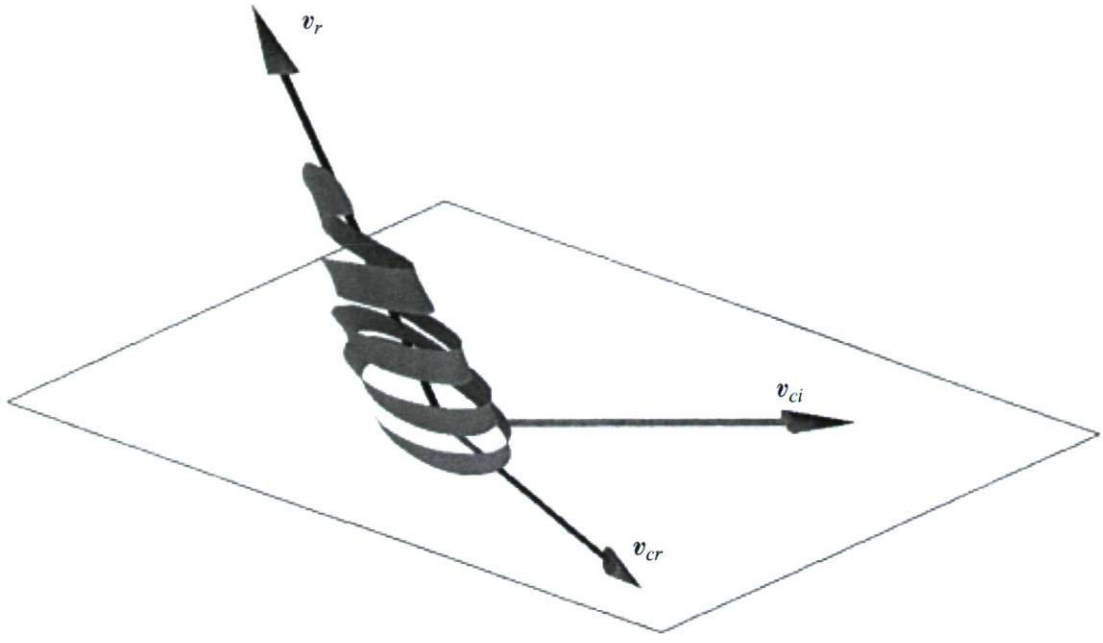

Figure B.1: The local streamline pattern in the coordinates of eigenvectors of the velocity gradient tensor in the neighbourhood of a vortex core (Zhou et al., 1999).

the discriminant for this characteristic equation is

$$\Delta = trace(\nabla \boldsymbol{u})^2 - 4det(\nabla \boldsymbol{u}) \tag{B.7}$$

λ_{ci} is the imaginary part of conjugate pair of the complex eigenvalues of $\nabla \boldsymbol{u}$ as mentioned before and it is not zero when $\Delta > 0$.

Appendix C

Mesh Dependency of Population Density of Vortices

A brief description of mesh dependency of population density, a parameter used by some researchers, is presented in this appendix. In fact, the population density of vortices is strongly dependent on the relative grid spacing of the velocity field, while the probability trends of vortices is mesh independent.

To illustrate the mesh dependency of vortex population density we will consider the limiting case shown in figure C.1. In this case, the area of fine mesh is $\frac{1}{4}$ of the coarse mesh size. A bounding box, to calculate the population density, is chosen to cover the four mesh nodes in the coarse mesh and nine mesh nodes of fine mesh. A schematic vortex is also shown to calculate its area. The population density is obtained based on equation C.1.

$$\rho_\lambda = \frac{N_\lambda}{A_b} \tag{C.1}$$

where ρ_λ is the population density, N_λ is the number of nodes of the λ_{ci} cluster within the bounding box and A_b is the area the bounding box ($A_\lambda = N_b dA$, where N_b is the number of nodes within the bounding box).

In the presented case, N_λ is 9 for the coarse mesh and 37 for the fine mesh. So ρ_λ

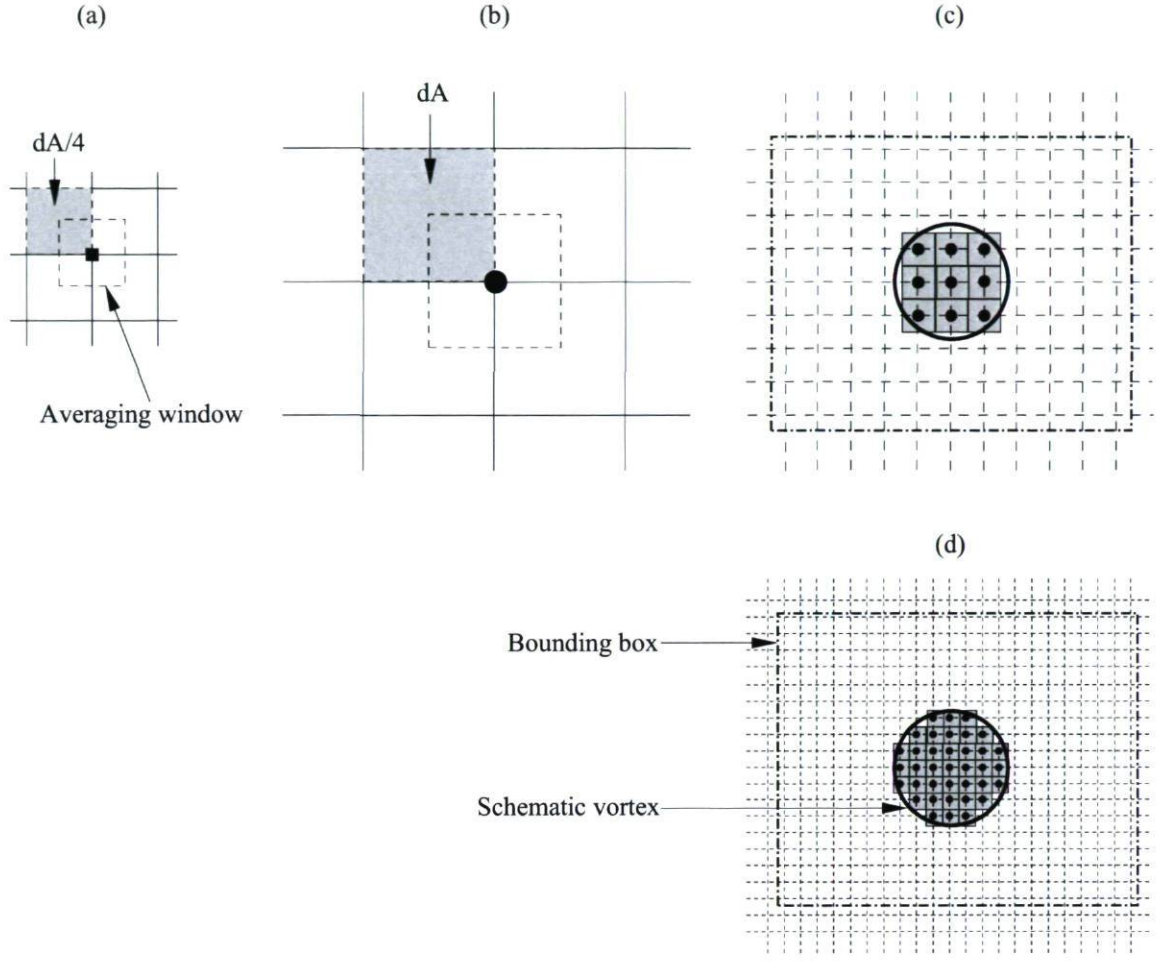

Figure C.1: Arithmetic average of each node of the grid for a) fine mesh, b) coarse mesh, c, d) schematic vortex and bounding box.

is obtained as follows

$$\begin{cases} \text{Fine mesh} & \rho_\lambda = \frac{N_\lambda}{A_\lambda} = \frac{37}{(22\times18)dA/4} = \frac{37}{A_b} \\ \text{Coarse mesh} & \rho_\lambda = \frac{N_\lambda}{A_\lambda} = \frac{9}{(11\times9)dA} = \frac{9}{A_b} \end{cases} \tag{C.2}$$

Since we divide the number of nodes by the surface, vortex population density increases as the mesh refinement increases as shown in equation C.2. This problem has also been confirmed with our data in an adverse-pressure-gradient TBL where the boundary layer thickens rapidly. The vortex population density was found to vary greatly in short distances because the relative mesh refinement (wrt δ) was also varying

rapidly. The problem comes from the fact that we have to use an averaging window with a discretized surface. It becomes therefore impossible to compare the vortex population density quantitatively between different experiments or different streamwise stations if the mesh size is not the same.

The streamwise-wall-normal planes cover roughly 3δ in the streamwise direction and 1.3δ in the wall-normal one. Over 3δ, the boundary layer thickness can grow by 20% to 30%. When considering one plane, the absolute number of vortices remains fairly constant everywhere in the outer region in both x and y, except of course close to the wall and at the outer edge. But because the relative grid spacing varies in the streamwise direction due to the strong variation of δ, the population density artificially grows by as much as 70% from one end of the plane to the other. This growth is much more important than the one between planes which are roughly 6δ apart. This is why the population density is not an appropriate parameter because of the issue of strong streamwise dependency of the trends. We should therefore use a pointwise definition (probability of occurrence of a vortex at a given x, y location) instead of a vortex population surface density.

Appendix D

Random Errors

D.1 Systematic and Random Uncertainties

This is the inescapable fact that every time you repeat a measurement, you will get a slightly different value. The values will be distributed about the mean (average) value, and the way they are distributed can be used to establish the statistical uncertainty of the measurement.

There are two basic kinds of uncertainties, systematic and random uncertainties. Systematic uncertainties are those due to faults in the measuring instruments or in the techniques used in the experiments, and cause a measurement to be skewed in a certain direction, i.e., consistently large or consistently small. Random uncertainties are associated with unpredictable variations in the experimental conditions under which the experiment is being performed, or are due to a deficiency in defining the quantity being measured. Random errors may be reduced by improving the measurement or the technique, but they cannot be eliminated. The size of the random uncertainty may be obtained only by making a set of repeated, independent observations. This sort of uncertainty cannot be eliminated but can be reduced by making lots of measurements and averaging. There is no general procedure for estimating the magnitude of systematic uncertainties as there is for random uncertainties.

If an experiment has low systematic uncertainty it is said to be accurate. If an experiment has low random uncertainty it is said to be precise. Obviously an experiment can be precise but inaccurate or accurate but imprecise. When thinking about uncertainty, it is important to remember these associations, so they are worth repeating:

- Random uncertainty decreases the precision of an experiment.
- Systematic uncertainty decreases the accuracy of an experiment.

The mean of a set of numbers is defined as the sum of all the numbers divided by the number of them. In mathematical language, if we have N observations and x_i represents any one of the observations (i.e. i can have any integer value from 1 to N), then the arithmetic mean, which we designate by the symbol, $\bar{x}$, is given by

$$\bar{x} = \frac{\sum_{i=1}^{N} x_i}{N} \tag{D.1}$$

Having obtained a mean or "best" value, $\bar{x}$, it is important to have a way of stating quantitatively how much the individual measurements are scattered about the mean. For a precise experiment we expect all measurements to be quite close to the mean value. The extent of scatter about the mean value gives us a measure of the precision of the experiment, and thus, a way to quantify the random uncertainty.

A widely accepted quantitative measure of scatter is the sample standard deviation, S_x. For the special case where all data points have equal weight, the sample standard deviation is defined by the equation,

$$S_x = \sqrt{\frac{\sum_{i=1}^{N}(x_i - \bar{x})^2}{N-1}} \tag{D.2}$$

Although this equation may not be intuitive, inspection of it reveals that S_x becomes larger if there is more scatter of the data about the mean. This is because $(x_i - \bar{x})^2$ for any particular i will on the average increase with greater scatter of the data about the mean so that $\sum(x_i - \bar{x})^2$ increases. Note that S_x has the same units as x_i or $\bar{x}$ since the square root of the sum of squares of differences between x_i and $\bar{x}$ is taken.

The standard deviation S_x defined by equation D.2 provides the random uncertainty estimate for any variable x. Intuitively we expect the mean value of the measurements to have less random uncertainty than any one of the individual measurements. It can be shown that the standard deviation of the mean value of a set of measurements $S_{\bar{x}}$, when all measurements have equal statistical weight, is given by

$$S_{\bar{x}} = \sqrt{\frac{\sum_{i=1}^{N}(x_i - \bar{x})^2}{N(N-1)}} = \frac{S_x}{\sqrt{N}} \tag{D.3}$$

Note that $S_{\bar{x}}$ is necessarily smaller than S_x. When we speak of the uncertainty S of a set of measurements made under identical conditions, we mean that number $S_{\bar{x}}$ and not S_x. It is most important that we distinguish properly between standard deviation associated with individual data points, S_x, and standard deviation of the mean of a set of data points, $S_{\bar{x}}$.

D.2 Confidence Intervals in Sample Populations

Random uncertainties always occur and have the effect of producing different results (within a certain narrow range) for successive measurements of a given quantity. It is important to try to minimise random uncertainties as much as possible by careful attention to the experimental procedure and by reading all instruments as accurately as possible. If a set of readings of a particular quantity has been taken, the average value or arithmetic mean is obviously more reliable than an individual value. Do not, however, average widely differing values as these may indicate a peculiar non-random error in a certain experiment and show that the experiment should be repeated. The rigorous way to estimate random uncertainty in a quantity is to measure the quantity a large number of times and to examine the spread in values obtained using rigorous statistical methods.

To calculate confidence intervals in sample populations, suppose that N readings of an experiment have a Gaussian distribution population with a mean value $\bar{x}$ and standard deviation S_x. If one more reading x_i is taken, the interval of 95% confidence that this reading would fall within the interval can be obtained as follows (Coleman and Steele, 1999)

$$\tau = \frac{x_i - \bar{x}}{S_x} \tag{D.4}$$

where τ can be obtained form table A.1 of Coleman and Steele (1999). For instance $\tau = 1.96$ for 95% confidence (for the Prob(τ) = 0.95 in the table A.1). So, the probability expression can be written as follow

$$Prob\left(-1.96 \leq \frac{x_i - \bar{x}}{S_x} \leq 1.96\right) = 0.95 \tag{D.5}$$

or

$$Prob(\bar{x} - 1.96S_x \leq x_i \leq \bar{x} + 1.96S_x) = 0.95 \tag{D.6}$$

So, based on equation D.6, 95% of the measuring data lies within $\pm 1.96S_x$ of the

mean $\bar{x}$. In other words, a single reading will fall within the $\pm 1.96 S_x$ with 95% confidence.

Turning now our point of view in determining a 95% confidence interval around a single reading x_i. Indeed, we expect to have an interval around x_i that the mean value of distribution of x_i ($\bar{x}$) within this interval lies at a confidence level of 95%. In other words, we can say with 95% confidence that the mean value of x_i is within $\pm 1.96 S_x$ of a single reading from that distribution. This can be obtained by rearranging the equation D.6 as follow

$$Prob(x_i - 1.96 S_x \leq \bar{x} \leq x_i + 1.96 S_x) = 0.95 \tag{D.7}$$

Finally the random uncertainty, P, can be calculated as

$$P_x = t S_x \tag{D.8}$$

$$P_{\bar{x}} = t S_{\bar{x}} = \frac{t S_x}{\sqrt{N}} \tag{D.9}$$

where t can be obtained from table A.2 of Coleman and Steele (1999).